

FLOW AND SEGREGATION BEHAVIOR OF FLUIDIZED SYSTEMS

By

AKHIL ARUN RAO

A DISSERTATION PRESENTED TO THE GRADUATE SCHOOL
OF THE UNIVERSITY OF FLORIDA IN PARTIAL FULFILLMENT
OF THE REQUIREMENTS FOR THE DEGREE OF
DOCTOR OF PHILOSOPHY

UNIVERSITY OF FLORIDA

2011

© 2011 Akhil Arun Rao

To my family and friends for their encouragement and support throughout graduate school

ACKNOWLEDGMENTS

My sincere gratitude goes to my advisor, Dr. Jennifer Curtis for her constant guidance, supervision and encouragement. Her perspective has helped me gain a panoramic view on research. I also appreciate the intellectual advice provided by Dr. Carl Wassgren and Dr. Bruno Hancock throughout the course of my PhD. I would also like to thank Dr. Mark Pepple and Deepak Rangarajan without whom getting some of the experimental data would have been difficult. Deepak Rangarajan and I have worked together to obtain the data for the 1.5 mm glass particles (Chapter 3). I am also grateful for all my friends, roommates and office colleagues, and the pedantic lunch table discussion with them that kept me energized. Finally, I am indebted to my family and friends back home (in India). I shall cherish their love and support forever.

TABLE OF CONTENTS

	<u>page</u>
ACKNOWLEDGMENTS.....	4
LIST OF TABLES.....	8
LIST OF FIGURES.....	10
LIST OF ABBREVIATIONS.....	15
ABSTRACT.....	21
CHAPTER	
1 INTRODUCTION	23
Dilute Turbulent Fluid-Solid Fluidized Flows	23
Gas-Solid Flows	23
Liquid-Solid Flows	26
Fluidized Beds	27
Binary Segregation.....	27
Wall Effects	29
2 FLUIDIZED DILUTE TURBULENT GAS-SOLID FLOW	30
Background.....	30
Fluctuating Interaction Terms	30
Drag Relation	32
Solid-Phase Stress Description.....	33
Mathematical Model.....	33
Fluid Stress (τ_{rz}).....	34
Drag Force (F_D)	36
Granular Energy Dissipation (γ).....	38
Solid-Phase Stress (σ_{rz} , σ_{rr} , $\sigma_{\theta\theta}$).....	38
Granular Energy Flux (q_{pTr})	39
Fluctuating Interaction/Coupling Terms (I_k , I_T).....	41
Fluctuating Energy Transfer (FET) Model for the Fluctuating Interaction/Coupling Terms	47
Boundary Conditions	50
Numerical Solution.....	51
Benchmark Data Sets.....	53
Results and Discussion.....	54
Comparing the Various Models for Interaction Terms and Cross- Correlations.....	55
Comparing the Various Models for Drag Terms	62

Comparing the Various Models for Solid Stress Terms.....	62
Summary	63
3 FLUIDIZED DILUTE TURBULENT LIQUID-SOLID FLOW	88
Background.....	88
Experimental Setup	90
Flow Loop.....	90
PDPA System.....	92
Single-Phase Validation	92
Particles and Laser Settings.....	93
Two-Phase Data Validation	94
Eulerian Two-Fluid Models for Dilute Turbulent Liquid-Solid Flows	95
High ST, Inertia-Dominated Flow Regime ($ST > 40$)	95
Low ST, Viscous Dominated Flow Regime ($ST < 5$).....	97
Intermediate ST, Transitional Flow Regime ($5 < ST < 40$).....	98
Results and Discussion.....	100
High ST, Inertia-Dominated Flow Regime	101
Low ST, Viscous-Dominated Flow Regime	102
Intermediate ST, Transitional Flow Regime.....	102
Summary	105
4 BINARY SEGREGATION IN FLUIDIZED BED	120
Background.....	120
Experiments.....	124
Particles and Their Preparation	124
Experimental Setup	125
Experimental Procedure	126
Segregation Index.....	127
Results and Discussion.....	128
Mixture Types.....	129
Type A mixtures	130
Type B mixtures	132
Type C mixtures.....	132
Type D mixtures.....	134
Type E mixtures	134
Type F mixtures	134
Type G mixtures.....	135
Classification Diagram.....	135
Experiments Validating Minimal Wall Effects	138
Effect of column H/D on Binary Segregation in Fluidized Bed	139
Summary	140

5	EFFECT OF COLUMN DIAMETER AND BED HEIGHT ON MINIMUM FLUIDIZATION VELOCITY.....	156
	Background.....	156
	Experimental Setup	157
	Theory.....	160
	Results and Discussion.....	167
	Summary	169
6	CONCLUSIONS AND RECOMMENDATIONS.....	175
	Dilute Turbulent Fluid-Solid Fluidized Flows	175
	Fluidized Beds – Segregation of Binary Mixtures and Wall Effects.....	178
APPENDIX		
A	DILUTE-TURBULENT FLUID-SOLID FLOW PROGRAM	181
B	RAW FLUID-SOLID DATA.....	227
C	FIGURES FOR FLUIDIZED BED BINARY MIXTURES.....	233
	LIST OF REFERENCES	248
	BIOGRAPHICAL SKETCH.....	254

LIST OF TABLES

<u>Table</u>	<u>page</u>
2-1	Closure relations employed in the published gas-solid flow models 65
2-2	Summary of experimental data..... 71
2-3	Time scale used in FET model for the different experimental data..... 72
2-4	Percentage Error in Predicted Gas Velocity Fluctuations Using the Various Combinations of Different Interaction Terms and Velocity Cross Correlations ... 85
2-5	Percentage Error in Predicted Solid Velocity Fluctuations Using the Various Combinations of Different Interaction Terms and Velocity Cross Correlations ... 85
2-6	Percentage error in predicted gas velocity fluctuations using the various drag relations 85
2-7	Percentage error in predicted gas velocity fluctuations using the various solid stress closures..... 87
3-1	PDPA settings 110
3-2	Summary of experimental data..... 111
3-3	Summary of model equations in the high, low and intermediate <i>ST</i> flow regimes..... 112
4-1	Summary of published work 141
4-2	Experimental material and properties – present study..... 142
4-3	Experimental mixtures and their properties – present study 142
4-4	Details of mixtures and their properties – published work and present study ... 144
5-1	Experimental materials and properties 170
B-1	Raw data for $d = 1.5$ mm, $m = 0.0175$ and $V_{fzcl} = 3.07$ m/s..... 227
B-2	Raw data for $d = 1.5$ mm, $m = 0.0425$, $V_{fzcl} = 2.96$ m/s and run 1 227
B-3	Raw data for $d = 1.5$ mm, $m = 0.0425$, $V_{fzcl} = 2.96$ m/s and run 2 228
B-4	Raw data for $d = 1.5$ mm, $m = 0.0425$, $V_{fzcl} = 2.96$ m/s and run 3 228
B-5	Raw data for $d = 1.5$ mm, $m = 0.0425$, $V_{fzcl} = 2.96$ m/s and run 4 229

B-6	Raw data for $d = 1.5$ mm, $m = 0.075$ and $V_{fzcl} = 3.04$ m/s.....	229
B-7	Raw data for $d = 1.5$ mm, $m = 0.0175$ and $V_{fzcl} = 5.03$ m/s.....	230
B-8	Raw data for $d = 1.5$ mm, $m = 0.0425$ and $V_{fzcl} = 4.90$ m/s.....	230
B-9	Raw data for $d = 1.5$ mm, $m = 0.075$ and $V_{fzcl} = 5.04$ m/s.....	231
B-10	Raw data for $d = 1.5$ mm, $m = 0.0175$ and $V_{fzcl} = 7$ m/s.....	231
B-11	Raw data for $d = 1.5$ mm, $m = 0.0425$ and $V_{fzcl} = 7.06$ m/s.....	232
B-12	Raw data for $d = 1.5$ mm, $m = 0.075$ and $V_{fzcl} = 7.02$ m/s.....	232

LIST OF FIGURES

<u>Figure</u>	<u>page</u>
2-1	Suspended particles enclosed in a box 65
2-2	Profile for the fluctuating energy transfer 66
2-3	Program flow chart 67
2-4	Comparison of solutions using various number of grids 68
2-5	Comparison between the Bolio <i>et al.</i> code and the code used in the present study 69
2-6	Comparison of prediction in the fluctuation velocity between (a) Benavides and van Wachem and (b) present study 69
2-7	Comparison between the MFIX code and the present study 70
2-8	Present model predictions compared to Tsuji <i>et al.</i> 243 μm particles 73
2-9	Present model predictions compared to Tsuji <i>et al.</i> 500 μm particles 74
2-10	Present model predictions compared to Tsuji <i>et al.</i> 1420 μm particles 74
2-11	Present model predictions compared to Tsuji <i>et al.</i> 2780 μm particles 75
2-12	Present model predictions compared to Jones <i>et al.</i> 70 μm particles 76
2-13	Present model predictions compared to Sheen <i>et al.</i> 77
2-14	Louge <i>et al.</i> cross-correlation predictions compared to Tsuji <i>et al.</i> 78
2-15	Koch and Sangani cross-correlation predictions compared to Tsuji <i>et al.</i> 78
2-16	Wylie <i>et al.</i> cross-correlation predictions compared to Tsuji <i>et al.</i> 79
2-17	Simonin cross-correlation predictions compared to Tsuji <i>et al.</i> 79
2-18	Sinclair and Mallo cross-correlation predictions compared to Tsuji <i>et al.</i> 80
2-19	FET model predictions compared to Tsuji 243 μm particles 80
2-20	Louge <i>et al.</i> cross-correlation predictions compared to Tsuji 243 μm particles .. 81
2-21	Koch and Sangani cross-correlation predictions compared to Tsuji 243 μm particles 81

2-22	Wylie <i>et al.</i> cross-correlation predictions compared to Tsuji 243 μm particles....	82
2-23	Simonin cross-correlation predictions compared to Tsuji 243 μm particles	82
2-24	Sinclair and Mallo cross-correlation predictions compared to Tsuji 243 μm particles	83
2-25	Comparing the magnitudes of βk_{sg} (a), I_k (b) and I_T (c) for the various interaction term models for the case of 243 μm particles with $m = 3.2$	84
2-26	Comparing the magnitudes of F_D (a) and β (b) for the various drag models for 243 μm particles with $m = 3.2$	86
2-27	Comparing the magnitudes of μ_s/μ_f (a) and λ/μ_f (b) for the various solid stress models for 243 μm particles with $m = 3.2$	86
3-1	Effect of ST on the solid path in the fluid	107
3-2	Flow loop	108
3-3	Comparing single-phase fluctuating velocity to the single-phase k - ϵ turbulence model ($v'_{fz} = \sqrt{k}$)	109
3-4	Solid fluctuating velocity measurement for $d = 1.5$ mm, $m = 0.0425$ and $V_{fzcl} \sim 3$ m/s (averaged over four runs)	111
3-5	Mean velocity (V_{fz} and V_{sz}) measurement for $d = 2.32$ mm compared to flow predictions for high ST case	113
3-6	k , T measurements for $d = 2.32$ mm compared to flow prediction for high ST case	113
3-7	Mean velocity (V_{fz} and V_{sz}) measurements for $d = 0.5$ mm compared to flow predictions for low ST case	114
3-8	Fluctuating velocity (v'_{fz} and v'_{sz}) measurements for $d = 0.5$ mm compared to flow predictions for low ST case	115
3-9	Mean velocity (V_{fz} and V_{sz}) measurements for $d = 1$ mm compared to flow predictions for intermediate ST case	116
3-10	Fluctuating velocity (v'_{fz} and v'_{sz}) measurement for $d = 1$ mm compared to flow predictions for intermediate ST case	117
3-11	Mean velocity (V_{fz} and V_{sz}) measurement for $d = 1.5$ mm compared to flow predictions for intermediate ST case	118

3-12	Fluctuating velocity (v_{fz}' and v_{sz}') measurement for $d = 1.5$ mm compared to flow predictions for intermediate ST case.....	119
4-1	Schematic of the experiment.....	143
4-2	Typical pressure drop profiles and segregation index behavior for a Type A mixture 50G385-50G083.....	146
4-3	Process of fluidization for a homogeneous binary mixture which fluidizes at two points	147
4-4	Typical pressure drop profiles and segregation index behavior for a Type B mixture 75S328-25G328.....	148
4-5	Typical pressure drop profiles and segregation index behavior for a Type C mixture 50G195-50G083.....	149
4-6	Pressure drop profiles for the mixture 75G231-25G116 from an initially mixed state.....	150
4-7	Typical pressure drop profiles and segregation index behavior for a Type D mixture 50G165-50G083.....	151
4-8	Mixture type diagram.....	152
4-9	Correlation for the minimum fluidization velocity ratio and the Archimedes number ratio.....	153
4-10	Segregation profiles for the mixture 75G231-25G116	153
4-11	Segregation profiles of 25G116-75G231 at $V^*=2.3$	154
4-12	Segregation profiles of 50G138-50G328 at $V^*=2.5$	154
4-13	Segregation profiles of 50G138-50G275 at $V^*=3$	155
4-14	Segregation profiles of 70G116-30P275 at $V^*=3.1$	155
5-1	Example of a pressure drop profile (fluidization and defluidization) using G231 particles in the 1.6 cm diameter column	170
5-2	Re_{p-mf} as a function of H/D , for different glass particles in the column $D=1.6$ cm.....	171
5-3	Re_{p-mf} as a function of H/D , for different glass particles in the column $D=2.4$ cm.....	171
5-4	Re_{p-mf} as a function of H/D , for polystyrene particles in the column $D=1.6$ cm.....	172

5-5	Re_{p-mf} as a function of H/D , for polystyrene particles in the column $D=2.4$ cm.	172
5-6	Sketch showing the fluidized bed coordinate system.	173
5-7	A schematic showing how the vertical stress in the bed varies with bed depth at different fluid velocity V_1 , V_2 and V_3 .	173
5-8	The minimum fluidization velocity as a function of the column diameter using the experimental data from Liu <i>et al.</i>	174
5-9	Comparison of the curves from equation 5-30 to the experimental data and existing correlations.	174
C-1	Pressure drop profiles and segregation index behavior for a Type A mixture 50G550-50G083.	233
C-2	Pressure drop profiles and segregation index behavior for a Type A mixture 50G462-50G083.	234
C-3	Pressure drop profiles and segregation index behavior for a Type A mixture 50G550-50G116.	235
C-4	Pressure drop profiles and segregation index behavior for a Type A mixture 50G385-50G083.	236
C-5	Pressure drop profiles and segregation index behavior for a Type A mixture 50G462-50G116.	237
C-6	Pressure drop profiles and segregation index behavior for a Type B mixture 50G328-50G083.	238
C-7	Pressure drop profiles and segregation index behavior for a Type B mixture 50G275-50G083.	239
C-8	Pressure drop profiles and segregation index behavior for a Type C mixture 50G231-50G083.	240
C-9	Pressure drop profiles and segregation index behavior for a Type C mixture 50G195-50G083.	241
C-10	Pressure drop profiles and segregation index behavior for a Type D mixture 50G165-50G083.	242
C-11	Pressure drop profiles and segregation index behavior for a Type D mixture 50G138-50G083.	243
C-12	Pressure drop profiles and segregation index behavior for a Type D mixture 50G116-50G083.	244

C-13	Pressure drop profiles and segregation index behavior for a Type B mixture 13S328-87P328.....	245
C-14	Pressure drop profiles and segregation index behavior for a Type B mixture 75S328-25G328.	246
C-15	Pressure drop profiles and segregation index behavior for a Type E mixture 70G116-30P275.	247

LIST OF ABBREVIATIONS

a_E	Ergun equation coefficient [kg m^{-4}]
A_{ht}	area of heat transfer [m^2]
$A_{PL}, B_{PL}, C_{PL}, D_{PL}$	coefficients based on e for Peirano and Leckner ⁵¹
A_{SO}, B_{SO}	parameter based on ν for Syamlal and O'Brien model ⁴⁹
b_E	Ergun equation coefficient [$\text{kg m}^{-3} \text{s}^{-1}$]
c_1	coefficient of vertical stress equation [m^{-1}]
c_2	coefficient of vertical stress equation [$\text{kg m}^{-2} \text{s}^{-2}$]
C_D	friction factor
C_{mix}	composition of mixture
$C_{T1}, C_{T2}, C_{T3}, C_\mu$	constants in k- ϵ model
C_w	coefficient for turbulence generation by vortex shedding
c_β	parameter based on angle between flow direction and slip velocities
d	particle diameter [m]
d_r	ratio of particle diameter of jetsam to flotsam
e	particle-particle coefficient of restitution
e_w	particle-wall coefficient of restitution
E_w	turbulence generation by vortex shedding [$\text{kg m}^{-1} \text{s}^{-3}$]
F, F_0, F_1, F_2, F_3	dimensionless functions based on Re_p and ν for Hill <i>et al.</i> ^{47, 48} model
F_B	stress force on the bottom face [kg m s^{-2}]
F_{bu}	buoyancy force [kg m s^{-2}]
F_D	drag force per unit volume [$\text{kg m}^{-2} \text{s}^{-2}$]
f_D	fluctuating drag force [$\text{kg m}^{-2} \text{s}^{-2}$]
F_d	drag force [kg m s^{-2}]
FET	Fluctuation Energy Transfer

F_F	wall friction force [kg m s^{-2}]
F_T	stress force on the top face [kg m s^{-2}]
$f_{T1}, f_{T2}, f_{T3}, f_\mu$	coefficients in k - ϵ model
F_W	weight of the element [kg m s^{-2}]
g	gravitational acceleration [m s^{-2}]
G_{1k}, G_{1c}	dimensionless functions based on e and T
G_{2k}, G_{2c}	dimensionless functions based on e and T
G_{3k}, G_{3c}	dimensionless functions based on e and T
g_o	radial distribution coefficient
H	bed height [m]
h	instantaneous fixed bed height [m]
h_t	heat transfer coefficient [$\text{kg s}^{-2} \text{K}^{-1}$]
I_k	interaction term in the k equation [$\text{kg m}^{-1} \text{s}^{-3}$]
I_T	interaction term in the T equation [$\text{kg m}^{-1} \text{s}^{-3}$]
k	fluid turbulence kinetic energy [$\text{m}^2 \text{s}^{-2}$]
k_1, k_2, k_1', k_2'	constants for the wall affected Ergun's equation
k_{fb}	coefficient based on ν
k_J	Jassen's proportionality constant
k_{sf}	fluid-solid fluctuating velocity cross-correlation [$\text{m}^2 \text{s}^{-2}$]
LDV	LASER Doppler Velocitometry
m	ratio of solid mass flux to fluid mass flux
M	Mixing Index
MFBs	Micro Fluidized Beds
p	pressure [$\text{kg m}^{-1} \text{s}^{-2}$]
PDPA	phase doppler particle analysis

q_{pT}	granular energy flux [kg s^{-3}]
R	radius of pipe [m]
r	radial component [m]
Re	Reynolds number based on mean flow
Re_p	particle Reynolds number
Re_{p-mf}	particle Reynolds number at minimum fluidization
Re_T	Reynolds number based on T
R_T	turbulent Reynolds number
SI	segregation index
ST	Stokes number
T	granular temperature [$\text{m}^2 \text{s}^{-2}$]
t	Time and Volume Based Averaging [s]
T_f	real temperature of a fluid [k]
TVBA	Time and Volume Based Averaging
U_c	complete fluidization velocity [m s^{-1}]
U_{mf}	minimum fluidization velocity [m s^{-1}]
$U_{mf-lower}$	lower minimum fluidization velocity of the two components [m s^{-1}]
U_r	ratio of minimum fluidization velocity of jetsam to flotsam
U_{TO}	take-over velocity [m s^{-1}]
U_τ	friction velocity [m s^{-1}]
V	average fluid velocity [m s^{-1}]
V^*	ratio of operating velocity to complete fluidization velocity
VBA	Volume Based Averaging
V_f	mean gas velocity [m s^{-1}]
v'_f	fluctuation fluid velocity [m s^{-1}]

V_{fzcl}	fluid center line velocity [m s^{-1}]
V_{rm}	dimensionless velocity based on Re_p and ν for Syamlal and O'Brien model ⁴⁹
V_s	mean solid velocity [m s^{-1}]
V'_s	fluctuation solid velocity [m s^{-1}]
W_{HLK}	dimensionless parameter based on Re_p and ν for Hill <i>et al.</i> ^{47, 48} model
y^+	dimensionless distance from the wall
z	axial component [m]
Z	parameter based on velocity
Greek	
β	drag coefficient [$\text{kg m}^{-3} \text{s}^{-1}$]
β'	FET coefficient [$\text{kg m}^{-3} \text{s}^{-1}$]
ε	dissipation of fluid turbulence [$\text{m}^2 \text{s}^{-3}$]
ϵ	fluidized bed voidage
η	parameter based on e
η_t	ratio of Lagrangian time scale to particle relaxation time scale
θ	azimuthal component
θ'	angle between flow direction and slip velocities
ϑ	sphericity
λ	conductivity of granular temperature modified by inelastic collisions [$\text{kg m}^{-1} \text{s}^{-1}$]
λ'	conductivity of granular temperature modified by inelastic collisions [$\text{kg m}^{-1} \text{s}^{-1}$]
λ_{mfp}	mean free path between particles [m]
μ_b	fluid-phase bulk viscosity [$\text{kg m}^{-1} \text{s}^{-1}$]
μ_{ef}	fluid-phase viscosity modified by particles [$\text{kg m}^{-1} \text{s}^{-1}$]

μ_f	fluid-phase viscosity [$\text{kg m}^{-1} \text{s}^{-1}$]
μ_s	solid-phase viscosity modified for inelastic collisions [$\text{kg m}^{-1} \text{s}^{-1}$]
μ_s'	solid-phase viscosity [$\text{kg m}^{-1} \text{s}^{-1}$]
μ_T	fluid-phase eddy viscosity [$\text{kg m}^{-1} \text{s}^{-1}$]
μ_t	turbulent fluid-phase viscosity for vortex shedding [$\text{kg m}^{-1} \text{s}^{-1}$]
ν	solid volume fraction
ν_0	maximum packing solid volume fraction
ξ_r	parameter based on relative velocity and k
ρ_{avg}	average density of fluid-solid mixture [kg m^{-3}]
ρ_f	fluid density [kg m^{-3}]
ρ_r	ratio of density of jetsam to flotsam
ρ_s	solid density [kg m^{-3}]
σ	solid stress tensor [$\text{kg m}^{-1} \text{s}^{-2}$]
σ^c	collisional solid stress tensor [$\text{kg m}^{-1} \text{s}^{-2}$]
σ_H	horizontal stress due to friction [$\text{kg m}^{-1} \text{s}^{-2}$]
σ^k	kinetic solid stress tensor [$\text{kg m}^{-1} \text{s}^{-2}$]
$\sigma_k, \sigma_\varepsilon$	constants in k - ε model
σ_v	vertical stress [$\text{kg m}^{-1} \text{s}^{-2}$]
τ	fluid stress tensor [$\text{kg m}^{-1} \text{s}^{-2}$]
τ_c	collisional time scale [s]
τ_D	particle relaxation time scale [s]
τ_e	eddy time scale [s]
τ_f	fluid response time scale [s]
τ_L	Lagrangian time scale [s]

τ_p	solid response time scale [s]
τ_{sf}	time scale for FET model [s]
τ^{TUR}	turbulent component of fluid-phase stress [$\text{kg m}^{-1} \text{s}^{-2}$]
γ	dissipation rate of granular energy [$\text{kg m}^{-1} \text{s}^{-3}$]
ϕ	specularity
φ	friction angle between particles and wall
χ	ratio of mass of solid in a unit volume to the mass of fluid in the same volume
ψ	function based on ν
ψ', ψ''	functions based on $\nu, \text{Re}_p, \text{Re}_T$
ω	dampening function

Abstract of Dissertation Presented to the Graduate School
of the University of Florida in Partial Fulfillment of the
Requirements for the Degree of Doctor of Philosophy

FLOW AND SEGREGATION BEHAVIOR OF FLUIDIZED SYSTEMS

By

Akhil Arun Rao

May 2011

Chair: Jennifer S. Curtis
Major: Chemical Engineering

A model for dilute turbulent gas-solid flow with inelastic collisions in an Eulerian framework necessitates many different closures. The various closure models proposed to date in the literature that are required for the fluctuating interaction terms, the solid-fluid fluctuation velocity cross-correlation, the solid stress and the drag formulation are compared. A new interpretation is provided for the fluctuating interaction terms, based on a fluctuating energy transfer mechanism. All the closures are evaluated against benchmark experiments for fully-developed, dilute and turbulent gas-solid flow in a vertical pipe.

The Eulerian model is also extended to the case of dilute turbulent liquid-solid flows in the viscous, transitional and inertial flow regimes. The model is validated with both published experimental data and with new experimental data obtained in this study. These experiments were performed in a three inch vertical pipe, with 1.5 mm diameter glass particles and Re from 2.0×10^5 to 5.0×10^5 . The concentration of solids is varied from 0.7% to 3% by volume.

Experimental investigations of binary mixtures in a gas fluidized bed have also been carried out in this study. Glass and polystyrene particles from 70 μm to 500 μm are fluidized in a micro fluidized bed of diameter 1.6 cm. These investigations exhibit

varied pressure drop profiles and segregation patterns. Different mixture types are mapped on a graph of density ratio versus size ratio. Categorizing binary mixtures in this manner gives a qualitative understanding of how the different mixtures behave upon fluidization.

Further, fluidized bed experiments of particles with mono-sized distributions revealed that the minimum fluidization velocity of particles increases as the diameter of the fluidization column is reduced, or if the height of the bed is increased. It is found that wall friction leads to an enhancement in the minimum fluidization velocity. A new, semi-correlated model is proposed which incorporates Janssen's wall effects in the calculation of the minimum fluidization velocity. The model predictions compare favorably to existing correlations and experimental data.

CHAPTER 1 INTRODUCTION

Fluidized systems are encountered in an enormous number of industrial applications. These applications vary from dilute and low mass loading conditions like pneumatic transport of powders, pulverized coal injection into entrained flow gasifiers, and cyclones, to dense fluidized bed applications like slurry transport, circulating fluidized beds, drying of pharmaceutical powders and fluid-solid catalytic reactions ¹. Although fluidization technology has been around for decades, there are several aspects of fluidization about which not much is known.

Dilute Turbulent Fluid-Solid Fluidized Flows

Gas-Solid Flows

Modeling of gas-solid fluidized flows is essential for designing and optimizing, and for understanding the energy distribution of the various internal processes, in equipment involving such flows. Unfortunately, even for the case of dilute fluid-solid flow there is a lack of fundamental understanding of the effect of the solid phase on the flow of fluid phase and vice versa. The experimental data considered in the present work for fully developed dilute turbulent gas-solid flow in a vertical pipe ^{2, 3, 4, 5} is in the inertia dominated flow regime, as most pneumatic transportation applications exhibit this flow regime. The flow regime of fluid-solid flows is determined by the Stokes number (ST) of the particles.

Louge *et al.* ⁶ developed an Eulerian two-fluid model for dilute turbulent gas-solid flow with particle-particle interactions for the inertia dominated flow regime. They were the first to use a single k -equation model to describe gas-phase turbulence. This model was further developed by Bolio *et al.* ⁷ who employed a two-equation k - ϵ model to

describe the gas-phase turbulence. Simonin⁸ and Benavides and van Wachem⁹ have suggested models along similar lines. All these models are able to describe the mean velocity profiles of the gas and solid phases well.

The granular temperature behavior for particles with low particle Reynolds numbers ($Re_p \sim 10$, Re_p is based on particle diameter and slip velocity) is also captured fairly well by these models, with some deviations from the experimental data of Tsuji^{**} for 243 μm polystyrene beads. According to these data, as the mass loading (ratio of the solid mass flux to the fluid mass flux, m) increases, the granular temperature decreases. Furthermore, for smaller mass loadings ($m \sim 1$) the granular temperature is virtually independent of the radial position, while for larger loadings ($m \sim 3-5$) the granular temperature increases towards the wall. This behavior suggests that for larger loadings (but still dilute-phase flow), particles tend to concentrate at the center of the pipe. These trends are correctly predicted by the models. Unfortunately, granular temperature data for large and intermediate Re_p are not available in the literature.

In contrast, all of these models under predict the gas-phase turbulence in the presence of the particles. In fact, these models also predict that large particles ($d > 400 \mu\text{m}$) exhibit turbulence dampening, contrary to experimental observations as summarized by Gore and Crowe¹⁰. Further, Hestroni¹¹ showed that particles with small Re_p (~ 10) exhibit turbulence dampening, while particles with large Re_p (~ 1000) cause turbulence enhancement of the gas phase due to vortex shedding. Particles with intermediate Re_p (~ 100) show in-between behavior, exhibiting turbulence enhancement at the core of the pipe and turbulence dampening at the wall. The present study further

^{**} Tsuji Y. Private Communication 1993.

advances the work of Bolio *et al.* ⁷ and corrects for the deficiencies in these other gas-solid flow models.

To generate reliable predictions for gas-solid flow in an Eulerian framework, it is critically important to have accurate closure models. In particular, the gas-particle turbulent interactions, the effect of the presence of particles on gas-phase turbulence and vice versa, must be appropriately described. For state-of-the-art Eulerian, dilute gas-solid flow models with particle-particle interactions, there are several important forces/interactions requiring constitutive modeling. The flow models vary from one another in the following key aspects.

- The fluctuating interaction/coupling terms in the gas-phase turbulent kinetic energy and granular temperature equations which includes the gas-solid fluctuating velocity cross-correlation
- The drag relation
- The solid-phase stress description

Although the closure models for the above terms have evolved over time, there is no single combination of closures for an Eulerian model, for dilute turbulent gas-solid flow with particle-particle interactions that is generally accepted. In the present study, different models for the various closures are compared against the benchmark data sets of Tsuji *et al.* ², Jones *et al.* ³, Sheen *et al.* ⁴, and Lee and Durst ⁵. Further, a novel but simple interpretation for the fluctuating interaction term is suggested which leads to improved flow predictions and match the experimental data favorably as compared to the other models. Also, a new combination of various closures models is proposed such that there is minimum error between the predictions and the experimental data.

Liquid-Solid Flows

For the case of liquid-solid fluidized flows, all of the three flow regimes – namely viscous-dominated flow regime, inertia-dominated flow regime and the transitional flow regime – have industrial applications. However, very little experimental data are available and even fewer modeling studies have been carried out. Reliable and detailed measurements of the of liquid-solid flow behavior are difficult as intrusive techniques disrupt flow behavior, and, due to the lack of data, model predictions cannot be validated.

Alajbegovic *et al.*¹² used laser-Doppler anemometer and a single-beam γ -ray densitometer, non-intrusive techniques, to study a system of water laden with ceramic particles of size 2.32 mm. Pepple¹³ used the phase-Doppler particle analyzer (PDPA) to measure the mean and fluctuating velocities of glass particles of size 0.5 and 1 mm. The experiments performed herein, extend the work of Pepple¹³ to obtain velocity data for 1.5 mm glass particles. The data for the 0.5 mm glass¹³ show viscous-dominated flow behavior, the 1 mm¹³ and the 1.5 mm (present study) glass exhibit transition flow regime behavior, and 2.32 mm ceramic particles¹² provide data for the inertia-dominated flow regime.

Modeling attempts of liquid-solid fluidized flows are rare. Hadinoto and Curtis¹⁴ extended the work of Bolio *et al.*⁷ to include fluid lubrication effects and employed their gas-solid model to generate flow predictions corresponding to the operating conditions in the liquid-solid data of Alajbegovic *et al.*¹². However, the Hadinoto and Curtis¹⁴ model is prescribed for only particles with high inertia and is neither appropriate to describe the experimental data of Pepple¹³ nor the experimental data obtained in the present study. The new combination of closure models for gas-solid flows, proposed in

this work, is extended to describe the inertia dominated flow data of Alajbegovic *et al.*¹². The closures for solid stress and fluctuating interaction term are changed to that proposed by Chen and Wood¹⁵ to describe the viscous dominated flow, and a bridge model between the above two models is used to describe the intermediate flow regime.

On increasing the loading of the solid phase (volume fraction of solids > 10%), dense fluid-solid flow is observed, and the correlations of the fluctuating solid volume fraction and fluctuating velocity govern the flow behavior. Dense fluid-solid flows have not been studied in this work. Dense fluid-solid flows in vertical pipes transition to fluidized beds at lower fluidization velocities.

Fluidized Beds

Binary Segregation

Fluidized bed operations are gaining a lot of interest as they involve intimate contact between a fluid stream and a dense mixture of various solid materials leading to good heat and mass transfer coefficients. An enormous amount of research on fluidized beds with monosized particles has been carried out and the flow patterns of such systems are well studied¹. In the industry however, monosized particles are rarely used and mixtures of particle with various sizes and densities are generally used. A common, observable phenomenon associated with multi-solid beds is that they may segregate when subjected to fluidization. Segregation is primarily due to particle size and/or density differences.

The segregation tendency of a powder mixture influences the overall process efficiency. Much experimental data exist in the literature concerning fluidized bed segregation, yet the current understanding of the mechanisms controlling multi-solid fluidization segregation is very poor, even for two component particle mixtures. In fact,

for a simple binary mixture fluidized by a gas, there are a variety of pressure drop profiles that have been observed and the different pressure drop profiles lead to different segregation patterns. For example, Formisani *et al.*¹⁶ presented several binary mixtures having large density and/or size ratios that fluidize at two different velocity points, while Joseph *et al.*¹⁷ has reported mixtures which fluidize at a single velocity point, just like a mono-component powder. Marzocchella *et al.*¹⁸ studied an extremely disparate mixture that mixes well at low velocities, just beyond the point of fluidization, but segregates at larger velocities. Complicating matters further, the phenomenon of layer inversion has also been observed in fluidized mixtures containing smaller, denser particles and coarser, less dense particles¹⁹.

In the present study, an attempt is made to categorize the various gas fluidized binary mixture types reported by various authors. In addition, a correlation between the

minimum fluidization velocity ratio, $U_r = \frac{U_{mf-jetsam}}{U_{mf-flotsam}}$, and the density ratio, $\rho_r = \frac{\rho_{s-jetsam}}{\rho_{s-flotsam}}$

and size ratio, $d_r = \frac{d_{jetsam}}{d_{flotsam}}$ is proposed that can be used to distinguish between these

mixture types, the observed pressure drop profiles, and segregation patterns. Cases in which the particle size d_r and density ratio ρ_r (the causes for U_r) aid each other, ρ_r and d_r are sufficient to give an idea of the level of disparity and, hence, make conclusions about the mixture's pressure drop or segregation behavior. But, in some cases where the particle size and density ratio oppose each other, it is difficult to gauge the level of disparity (nature of its pressure drop and segregation behavior) based only on ρ_r and d_r . Thus, using U_r as a measure of disparity will be beneficial in such cases.

Wall Effects

As stated earlier, fluidized bed operations have become more popular in industry, and, hence, there is a drive to study these beds in greater detail at laboratory scales. Reducing the size of fluidized beds is gaining interest because of the better gas distribution and operability at smaller scales. Micro fluidized Beds (MFB), which were first proposed by Potic *et al.*²⁰, have even better mixing and heat transfer capabilities, making them a useful tool for studying various processes like drying, mixing or segregation^{21, 22, 23, 24}, as well as reaction kinetics²⁵. For example, MFBs are used to investigate fluidization segregation in the pharmaceutical industry where active ingredients are expensive and difficult to obtain during the early stages of development.

One parameter of particular interest when working with fluidized beds is the minimum fluidization velocity. Experimental data obtained in the present study indicate that the minimum fluidization velocity increases as the column diameter is decreased or if the fixed bed height is increased. Many correlations exist for calculating the minimum fluidization velocity²⁶⁻³⁹ but none of the correlations include the effect of the bed height or diameter of the column (wall effects), factors which are likely to be of interest when MFBs are considered. Hence, a correlation is developed which encompasses the effect of aspect ratio and the ratio of column diameter to particle diameter to predict the elevation in the minimum fluidization velocity.

CHAPTER 2 FLUIDIZED DILUTE TURBULENT GAS-SOLID FLOW

Background

Eulerian two-fluid model for dilute turbulent gas-solid flows, as discussed in Chapter 1, requires closure models for the following relations

- The fluctuating interaction term and the fluid-solid fluctuating velocity cross-correlation within it
- The drag
- The solid stress

In the literature, many different closures have been suggested for each of these terms.

Fluctuating Interaction Terms

Louge *et al.*⁶ suggested an approximation for closing the fluctuating Interaction term. The fluctuating interaction term they proposed was based on the gas turbulence, granular temperature, and the gas-solid velocity cross-correlation. Time and volume based averaging (TVBA) was used for developing expressions for the fluctuating interactions. Louge *et al.*⁶ closed the gas-solid velocity cross-correlation, modifying Koch⁴⁰, in which it was assumed that a dilute gas-solid suspension at very small particle Reynolds number in the limit where solid body collisions determine the particle velocity distribution function. TVBA and the modified Koch⁴⁰ gas-solid velocity cross-correlation were also used by Bolio *et al.*⁷ and then tested by Benavides and van Wachem⁹. Along similar lines, Igci *et al.*⁴¹ used a cross-correlation expression developed by Koch and Sangani⁴², but Igci *et al.*⁴¹ neglected gas-phase turbulence in their analysis. More recently, Hadinoto and Curtis¹⁴ used TVBA for the interaction term and applied a closure model for the gas-solid velocity cross-correlation developed by Wylie *et al.*⁴³ for particles with high inertia and moderate fluid inertia. Both the Koch and

Sangani ⁴² and Wylie *et al.* ⁴³ closure models are extensions of the original Koch ⁴⁰ model, wherein the most important assumption is that the inertia of the fluid is negligible and the solid particle interactions occur for particles in viscous fluids with small particle Reynolds number. Bolio *et al.* ⁶, Benavides and van Wachem ⁹ and Hadinoto and Curtis ¹⁴ observed that the above-mentioned closure models could not predict the phenomenon of turbulence enhancement and under predicted the gas-phase turbulence in the presence of particles.

A closure model for the gas-solid velocity cross-correlation based on time scales was developed by Simonin ⁸ which is discussed later (in the Mathematical Model section). He too used TVBA to develop closure models to describe these fluctuating interaction terms. The NETL-MFIX code (Multiphase Flows with Interphase Exchanges) employs Simonin ⁸ closure model to simulate dilute, turbulent gas-solid phase flow. Benavides and van Wachem ⁹ have also tested the Simonin ⁸ closure. Predictions from the MFIX code, as well as the work of Benavides and van Wachem ⁹, again showed that the Simonin ⁸ model cannot predict the phenomenon of turbulence enhancement and under predicts the gas-phase turbulence in the presence of particles.

Benavides and van Wachem ⁹ and Hadinoto and Curtis ¹⁴ also test a simple closure model for the gas-solid velocity cross-correlation developed by Sinclair and Mallo ⁴⁴. This model assumes the fluid-solid fluctuation velocity cross-correlation to be a geometric mean of the gas-phase turbulence and the granular temperature.

Finally, Crowe ⁴⁵ developed a different form for the fluctuating interaction term. The Crowe ⁴⁵ form includes additional generation based on the square of the relative velocity between the two phases. Volume based averaging (VBA) was used to develop

new relations for the fluctuating interaction terms in contrast to most of the other models which have used TVBA to develop expressions for the fluctuating interaction terms. Only Zhang and Reese⁴⁶ have used the Crowe⁴⁵ formulation, along with a modified Koch and Sangani⁴² model for the fluid-solid velocity cross-correlation, and observed a good match with available experimental data.

A new closure model for the fluctuating interactions is introduced in this study based on a fluctuating energy transfer (FET) mechanism by analogy to a heat transfer mechanism. In this new closure, the Sinclair and Mallo⁴⁴ model is used for the gas-solid fluctuating velocity cross-correlation. Gas-solid flow predictions based on this closure compare more favorably to experimental data for gas turbulence and granular temperature than all of the previously published models. This new model is capable of predicting the gas-phase turbulence behavior associated with a wide range of particle sizes such as turbulence dampening in the presence of particles, turbulence enhancement as well as in-between turbulence behavior.

Drag Relation

Wen and Yu³⁹ is probably the most widely used and accepted particle drag model. However, Hadinoto and Curtis¹⁴ showed that the choice of the drag model may affect the predicted mean and fluctuating velocity profiles in dilute gas-solid flow for small and low density particles at low velocities. In the present study, flow predictions employing the (1) Wen and Yu³⁹ drag model, based on experimental correlation, the (2) Hill *et al.*^{47, 48} drag model, based on theory and Lattice – Boltzman simulations, and the (3) Syamlal and O'Brien drag model⁴⁹ also based on experimental correlation, are investigated and compared.

Solid-Phase Stress Description

Two different closures for the solid-phase stress are considered in this study. Both of these originate from the kinetic theory for granular flow. The Lun *et al.*⁵⁰ granular flow theory was the first fundamental description for the solid-phase stress based on analogy with molecular collisions in a dense gas. The second model, based on the work of Peirano and Leckner⁵¹, includes the effect of gas-phase turbulence and the effect of the interstitial fluid in the description for the solid-phase stress.

Table 2-1 summarizes the closures used by the various dilute, turbulent gas-solid flow models in the literature. As outlined above, several model formulations obtained by combining the different interaction/coupling term formulations along with the various gas-solid velocity cross-correlations, three different drag force models, and two different solid-phase stress models, are compared and tested against benchmark experimental data provided by Tsuji *et al.*², Jones *et al.*³, Sheen *et al.*⁴, and Lee and Durst⁵. These data sets were obtained under the conditions of fully-developed, dilute, turbulent gas-solid flow in a vertical pipe using laser Doppler velocimetry. The mean and fluctuating velocity profiles of the gas and solid phases have been reported in these experiments. After evaluating all the combinations of the models, Table 2-1 puts forth the final model which yielded minimum error when compared to the various data sets.

Mathematical Model

The continuum equations for an Eulerian description of dilute, turbulent fluid-solid flow have been well documented in many studies. The two-fluid equations used in this work follow those given in Bolio *et al.*⁷. The simplified equations are also consistent with the ones employed in MFIx and Benavides and van Wachem⁹.

Gas Phase Momentum Balance (z-component),

$$0 = \frac{1}{r} \frac{\partial}{\partial r} (r\tau_{rz}) - F_{Dz} - \frac{dp}{dz} + \rho_f g. \quad (2-1)$$

Solid Phase Momentum Balance (z-component),

$$0 = -\frac{1}{r} \frac{\partial}{\partial r} (r\sigma_{rz}) + F_{Dz} + (\rho_s - \rho_f)\nu g. \quad (2-2)$$

Solid Phase Momentum Balance (r-component),

$$0 = \frac{1}{r} \frac{\partial}{\partial r} (r\sigma_{rr}) - \frac{\sigma_{\theta\theta}}{r}. \quad (2-3)$$

Granular Energy Balance,

$$0 = -\frac{1}{r} \frac{\partial}{\partial r} (rq_{PTr}) - \sigma_{rz} \frac{\partial V_{sz}}{\partial r} - \gamma + I_T. \quad (2-4)$$

Transport Equations for k - ε ,

$$0 = \frac{1}{r} \frac{\partial}{\partial r} \left[r(1-\nu) \left(\frac{\mu_{ef}}{\rho_f} + \frac{\mu_T}{\sigma_k \rho_f} \right) \frac{\partial k}{\partial r} \right] + (1-\nu) \frac{\mu_T}{\rho_f} \left(\frac{\partial V_{fz}}{\partial r} \right)^2 - (1-\nu) \varepsilon + I_k, \quad (2-5)$$

$$0 = \frac{1}{r} \frac{\partial}{\partial r} \left[r(1-\nu) \left(\frac{\mu_{ef}}{\rho_f} + \frac{\mu_T}{\sigma_\varepsilon \rho_f} \right) \frac{\partial \varepsilon}{\partial r} \right] + (1-\nu) c_{T1} f_{T1} \frac{\varepsilon}{k} \frac{\mu_T}{\rho_f} \left(\frac{\partial V_{fz}}{\partial r} \right)^2 - (1-\nu) c_{T2} f_{T2} \frac{\varepsilon^2}{k} + (1-\nu) c_{T3} f_{T3} \frac{\varepsilon}{k} I_k. \quad (2-6)$$

Equation 2-1 to equation 2-6 presents the Bolio *et al.*⁷ governing equations for the simplified case of fully-developed, dilute, turbulent gas-solid flow in a vertical pipe of radius (R).

Fluid Stress (τ_{rz})

The total fluid stress (τ_{rz}) has two components. First, there is the viscous fluid component in which the intrinsic fluid viscosity (μ_f) is affected by the presence of the solids. The effect on μ_f for very dilute solids concentration cases is given by Batchelor and Green⁵².

$$\tau_{rz} = (\mu_{ef} + \mu_T) \frac{\partial V_{fz}}{\partial r}, \quad (2-7)$$

$$\mu_{ef} = \mu_f \left(1 + 2.5\nu + 7.6\nu^2\right) \left(1 - \frac{\nu}{\nu_0}\right). \quad (2-8)$$

The second component in the total fluid stress is the turbulent contribution (Reynold Stress) which is simplified using an eddy viscosity closure. For the two-equation k - ε turbulence model, the eddy viscosity is described based on the turbulent kinetic energy (k) and its dissipation rate (ε).

$$\mu_T = \frac{c_\mu f_\mu \rho_f k^2}{\varepsilon}, \quad (2-9)$$

$$c_{T1}=1.4, c_{T2}=1.8, c_{T3}=1.2, c_\mu=0.09, \sigma_k=1.4, \sigma_\varepsilon=1.3, f_{T1}=1^7,$$

$$f_{T2} = \left[1 - \frac{2}{9} \exp\left\{-\left(\frac{R_T}{6}\right)^2\right\}\right] \left[1 - \exp\left\{-\frac{y^+}{5}\right\}\right]^2, \quad (2-10)$$

$$f_\mu = \left[1 - \exp\left(-\frac{y^+}{70}\right)\right] \left[1 + \frac{3.45}{\sqrt{R_T}}\right], \quad (2-11)$$

where,

$$y^+ = \frac{U_\tau \rho_f}{\mu_f} (R - r) \quad (2-12)$$

and

$$R_T = \frac{\rho_f k^2}{\mu_{ef} \varepsilon}. \quad (2-13)$$

The turbulence model coefficients (c_{T1} , c_{T2} , c_{T3} , c_μ , σ_k , σ_ε , f_{T1} , f_{T2} and f_μ) are the same as given in Bolio *et al.*⁷ and are summarized in equation 2-9 to equation 2-13.

Drag Force (F_D)

The drag force is proportional to the relative velocity and to the drag coefficient β , which is a function of the solids volume fraction (ν), and particle Reynolds number.

$$F_{Dz} = \beta(V_{fz} - V_{sz}). \quad (2-14)$$

Three drag models considered in this study: Wen and Yu³⁹, Hill *et al.*^{47, 48}, and Syamlal and O'Brien⁴⁹.

$$\beta = \frac{3}{4} \frac{\rho_g}{d} C_D \frac{\nu}{(1-\nu)^{2.65}} |V_{fz} - V_{sz}|, \quad (2-15)$$

$$C_D = \frac{24}{\text{Re}_p} (1 + 0.15 \text{Re}_p^{0.687}) \text{ for } \text{Re}_p < 1000, \quad (2-16)$$

$$C_D = 0.44 \text{ for } \text{Re}_p > 1000, \quad (2-17)$$

$$\text{Re}_p = \frac{(1-\nu) \rho_f d |V_{fz} - V_{sz}|}{\mu_f}. \quad (2-18)$$

Equation 2-15 to equation 2-18 provide details for the Wen and Yu³⁹ model.

$$\beta = 18 \mu_f (1-\nu) \nu \frac{F}{d^2}, \quad (2-19)$$

$$F = 1 + \frac{3}{8} \text{Re}_p \text{ for } \nu \leq 0.01 \text{ and } \text{Re}_p \leq \frac{F_2 - 1}{3/8 - F_3}, \quad (2-20)$$

$$F = F_0 + F_1 \text{Re}_p^2 \text{ for } \nu > 0.01 \text{ and } \text{Re}_p \leq \frac{F_3 + \sqrt{F_3 - 4F_1(F_0 - F_2)}}{2F_1}, \quad (2-21)$$

$$F = F_2 + F_3 \text{Re}_p \text{ for } \nu \leq 0.01 \text{ and } \text{Re}_p > \frac{F_2 - 1}{3/8 - F_3}, \quad (2-22)$$

$$F = F_2 + F_3 \text{Re}_p \text{ for } \nu > 0.01 \text{ and } \text{Re}_p > \frac{F_3 + \sqrt{F_3 - 4F_1(F_0 - F_2)}}{2F_1}, \quad (2-23)$$

$$F_0 = (1 - w_{HLK}) \left[\frac{1 + 3\sqrt{\nu/2} + (135/64)\nu \ln(\nu) + 17.14\nu}{1 + 0.681\nu - 8.48\nu^2 + 8.16\nu^3} \right] + w_{HLK} \left[10 \frac{\nu}{(1-\nu)^3} \right] \quad (2-24)$$

for $\nu < 0.4$,

$$F_1 = \frac{1}{40} \sqrt{\frac{2}{\nu}} \text{ for } \nu < 0.1, \quad (2-25)$$

$$F_2 = (1 - w_{HLK}) \left[\frac{1 + 3\sqrt{\nu/2} + (135/64)\nu \ln(\nu) + 17.89\nu}{1 + 0.681\nu - 11.03\nu^2 + 15.41\nu^3} \right] + w_{HLK} \left[10 \frac{\nu}{(1-\nu)^3} \right] \quad (2-26)$$

for $\nu < 0.4$,

$$F_3 = 0.9531\nu + 0.03667 \text{ for } \nu < 0.0953, \quad (2-27)$$

$$w_{HKL} = \exp[-10(0.4 - \nu)/\nu], \quad (2-28)$$

$$Re_p = \frac{(1-\nu)\rho_f d |V_{fz} - V_{sz}|}{2\mu_f}. \quad (2-29)$$

Equation 2-19 to equation 2-29 provide the details for the Hill *et al.*^{47, 48} model.

$$\beta = \frac{3\nu\rho_f}{4V_m^2 d} \left(0.63 + 4.8\sqrt{V_m/Re_p} \right)^2 |V_{fz} - V_{sz}|, \quad (2-30)$$

$$V_m = 0.5 \left(A - 0.06Re_p + \sqrt{(0.06Re_p)^2 + 0.12Re_p(2B_{SO} - A_{SO}) + A^2} \right), \quad (2-31)$$

$$A_{SO} = (1-\nu)^{4.14} \quad (2-32)$$

and

$$B_{SO} = (1-\nu)^{2.65}, \quad (2-33)$$

$$Re_p = \frac{\rho_f d |V_{fz} - V_{sz}|}{\mu_f}. \quad (2-34)$$

Equation 2-30- 2-34 provides the details for Syamlal and O'Brien⁴⁹ model.

Granular Energy Dissipation (γ)

Granular energy is dissipated due to inelastic collisions of particles with a restitution coefficient (e). This granular energy dissipation is given by Lun *et al.*⁵⁰ and is a function of the radial distribution function (g_0), the solid volume fraction (ν), and granular temperature (T).

$$\gamma = \frac{48}{\sqrt{\pi}} \eta (1 - \eta) g_0 \nu^2 \frac{\rho_s}{d} T^{3/2}, \quad (2-35)$$

where

$$T = \frac{1}{3} \left(\overline{v_{si}^2} \right), \quad (2-36)$$

$$\eta = \frac{(1 + e)}{2}, \quad (2-37)$$

$$g_0 = \frac{V_0^{1/3}}{V_0^{1/3} - \nu^{1/3}}. \quad (2-38)$$

Solid-Phase Stress (σ_{rz} , σ_{rr} , $\sigma_{\theta\theta}$)

The solid-phase stresses have two contributions: the kinetic (or translational) part (σ^k) and the collisional part (σ^c). Bolio *et al.*⁷ modified the Lun *et al.*⁵⁰ stress expressions so that the kinetic contribution remains bounded in finite-sized domains and dampens according to a function ω proportional to the mean free path of the particles.

Consequently,

$$\sigma = \omega \sigma^k + \sigma^c, \quad (2-39)$$

where,

$$\omega = \frac{1}{1 + \lambda_{mfp} / R}, \quad (2-40)$$

and the mean free path, λ_{mfp} is

$$\lambda_{mfp} = \frac{d}{6\sqrt{2}\nu}. \quad (2-41)$$

The descriptions for the normal solid-phase stresses (σ_{rr} , $\sigma_{\theta\theta}$) are very similar in Lun *et al.*⁵⁰ and Peirano and Leckner⁵¹, with the primary difference being with the presence of the damping function ω in the Lun *et al.*⁵⁰ formulation. In the present study, the Bolio *et al.*⁷ expressions have been followed for the normal solid stress when the Lun *et al.*⁵⁰ model is used.

$$\sigma_{rr} = \sigma_{\theta\theta} = \rho_s(\omega G_{1k} + G_{1c})T \text{ (for }^{50}), \quad (2-42)$$

$$\sigma_{rr} = \sigma_{\theta\theta} = \rho_s(G_{1k} + G_{1c})T \text{ (for }^{51}), \quad (2-43)$$

where,

$$G_{1k} = \nu, \quad (2-44)$$

$$G_{1c} = 4\eta\nu^2 g_0. \quad (2-45)$$

The shear stress for the solid phase is expressed as a product of the solid-phase viscosity (μ_s), and the solid velocity strain.

$$\text{Shear stress } \sigma_{rz} = -\mu_s \frac{\partial V_{sz}}{\partial r}. \quad (2-46)$$

Granular Energy Flux (q_{pTr})

Similar to the solid-phase shear stress, the granular energy flux is expressed as a product of the granular (or pseudo-thermal) conductivity (λ), and the gradient of granular temperature.

$$q_{pTr} = -\lambda \frac{\partial T}{\partial r}. \quad (2-47)$$

The expressions for the solids viscosity (μ_s) and conductivity (λ) given by Lun *et al.*⁵⁰ and Peirano and Leckner⁵¹ are quite different.

$$\mu_s = \mu_s' (\omega G_{2k} + G_{2c}), \quad (2-48)$$

$$\mu_s' = \frac{5\sqrt{\pi}}{96} \rho_s d \sqrt{T}, \quad (2-49)$$

$$G_{2k} = \frac{1}{\eta(2-\eta)g_0} \left[1 + \frac{8}{5} \eta \nu g_0 (3\eta - 2) \right], \quad (2-50)$$

$$G_{2c} = \frac{8\nu}{5(2-\eta)} \left[1 + \frac{8}{5} \eta \nu g_0 (3\eta - 2) \right] + \frac{768\nu^2 g_0 \eta}{25\pi}. \quad (2-51)$$

Equation 2-48 to equation 2-51 detail the Lun *et al.*⁵⁰ expressions for μ_s .

$$\mu_b = \frac{256\mu_s \nu^2 g_0}{5\pi}. \quad (2-52)$$

Equation 2-52 gives the Lun *et al.*⁵⁰ expressions for μ_b .

$$\lambda = \lambda' (\omega G_{3k} + G_{3c}), \quad (2-53)$$

$$\lambda' = \frac{25\sqrt{\pi}}{128} \rho_s d \sqrt{T}, \quad (2-54)$$

$$G_{3k} = \frac{8}{\eta(41-33\eta)g_0} \left[1 + \frac{12}{5} \eta^2 \nu g_0 (4\eta - 3) \right], \quad (2-55)$$

$$G_{3c} = \frac{96\nu}{5(41-33\eta)} \left[1 + \frac{12}{5} \eta^2 \nu g_0 (4\eta - 3) + \frac{16}{5\pi} \eta \nu g_0 (41\eta - 33) \right]. \quad (2-56)$$

Equation 2-53 to equation 2-56 detail the Lun *et al.*⁵⁰ expressions for λ .

$$\mu_s = \nu \rho_s (G_{2k} + G_{2c}), \quad (2-57)$$

$$G_{2k} = \left[\frac{2}{3} k_{sg} \eta_t + T(1 + A_{PL} \nu g_0) \right] \left(\frac{2}{\tau_D} + \frac{B_{PL}}{\tau_c} \right)^{-1}, \quad (2-58)$$

$$G_{2c} = \frac{8}{5} \nu g_0 \eta \left(G_{2k} + d \sqrt{\frac{T}{\pi}} \right). \quad (2-59)$$

Equation 2-57 to equation 2-59 detail the Peirano and Leckner⁵¹ expressions for μ_s .

$$\mu_b = \frac{5}{3} \nu \rho_s G_{2c}. \quad (2-60)$$

Equation 2-60 gives the Peirano and Leckner⁵¹ expression for μ_b .

$$\lambda = \nu \rho_s (G_{3k} + G_{3c}), \quad (2-61)$$

$$G_{3k} = \left[\frac{9}{10} k_{sg} \eta_t + \frac{3}{2} T (1 + C_{PL} \nu g_0) \right] \left(\frac{9/5}{\tau_D} + \frac{D_{PL}}{\tau_c} \right)^{-1}, \quad (2-62)$$

$$G_{3c} = \frac{18}{5} \nu g_0 \eta \left(G_{3k} + \frac{5}{9} d \sqrt{\frac{T}{\pi}} \right). \quad (2-63)$$

where,

$$\begin{aligned} A_{PL} &= 2/5(1+e)(3e-1), \\ B_{PL} &= (1+e)(3-e)/5, \\ C_{PL} &= (1+e)^2(2e-1)/100, \\ D_{PL} &= (1+e)(49-33e)/100. \end{aligned} \quad (2-64)$$

Equation 2-61 to 2-64 detail the Peirano and Leckner⁵¹ expressions for λ .

Here τ_D is the drag time and τ_c is the time between collisions, η_t is the ratio of Lagrangian time scale to the particle relaxation time scale and k_{sf} is the fluid-solid fluctuation velocity cross-correlation (these variables are discussed in the next section).

Fluctuating Interaction/Coupling Terms (I_k , I_T)

Louge *et al.*⁶ used TVBA and simplified the fluctuating interaction/coupling terms to the following form,

$$I_k = -\beta(1-\nu) \left(2k - \overline{v_{fi}' v_{si}'} \right), \quad (2-65)$$

$$I_T = \beta(1-\nu) \left(\overline{v_{fi}' v_{si}'} - 3T \right), \quad (2-66)$$

where l_k represents the interaction coupling between granular temperature and the gas-phase turbulence equation and l_T is the interaction coupling between the gas-phase turbulence and the granular energy balance equation. For the sake of convenience, the cross-correlation of the gas and solid fluctuating velocities $\overline{v_{fi}' v_{si}'}$ will be denoted as k_{sf} hereafter.

The description for k_{sf} is probably the most controversial point amongst the different closures required for gas-solid flow modeling in an Eulerian framework. This controversy is due to the fact that there is a lack of fundamental understanding of the nature concerning the fluid-solid interactions at the level of the velocity fluctuations.

In the gas-solid flow model of Louge *et al.*⁶, the authors modified Koch⁴⁰ who rigorously derived an expression for k_{sf} .

$$k_{sf} = \frac{4}{\sqrt{\pi}} \frac{d}{\rho_s} \frac{\beta(1-\nu)}{\nu} \frac{(V_{tz} - V_{sz})^2}{\sqrt{T}}. \quad (2-67)$$

However, the system under consideration by Koch⁴⁰ was assumed to have negligible fluid inertia with particles suspended in a viscous fluid. Consequently, the Koch⁴⁰ expression for k_{sf} lacks the effect of gas-phase turbulence on the cross-correlation. Hence, the expressions for fluid-solid fluctuating interactions that have evolved from the Koch⁴⁰ model may not be appropriate in the case of turbulent gas-solid flow.

Igci *et al.*⁴¹ employed the work of Koch and Sangani⁴², an extension of the Koch⁴⁰ model, in a system where the fluid turbulence was again neglected. Koch and Sangani⁴² model use a ψ factor to summarize the effect of the solids concentration.

$$\beta(1-\nu)k_{sf} = \frac{81\nu\mu_f^2|V_{fz} - V_{sz}|^2}{g_0d^3\rho_f\sqrt{\pi T}}\psi, \quad (2-68)$$

where,

$$\psi = \frac{(1+3\sqrt{\nu/2}+(135/64)\nu\ln(\nu)+17.14\nu)^2}{(1+3.5\sqrt{\nu}+5.9\nu)(1+0.681\nu-8.48\nu^2+8.16\nu^3)^2}. \quad (2-69)$$

The function ψ replaces the solid volume fraction functionality obtained from using the drag term (β) in the work of Louge *et al.*⁶.

Hadinoto and Curtis¹⁴ used another form of the Koch⁴⁰ model based on the work of Wylie *et al.*⁴³. This model included the effect of large particle inertia and moderate fluid inertia obtained by enhancing the ψ factor with a functionality which depends on ν , Re_T , and Re_p .

$$\beta(1-\nu)k_{sf} = \frac{81\nu\mu_f^2|V_{fz} - V_{sz}|^2}{g_0d^3\rho_f\sqrt{\pi T}}\psi', \quad (2-70)$$

where,

$$\psi' = \psi + K_{fb}Re_p\psi'', \quad (2-71)$$

$$K_{fb} = 0.0336 + 0.106\nu + 0.0116(1-\nu)^{-5}, \quad (2-72)$$

$$\psi'' = \left(1 + 2\frac{Re_T^2}{Re_p^2} - \frac{Re_T^4}{Re_p^4}\right)erf\left(\frac{Re_T}{\sqrt{2}Re_p}\right) + \sqrt{\frac{2}{\pi}}\frac{Re_T}{Re_p}\left(1 + \frac{Re_T^2}{Re_p^2}\right)\exp\left(-\frac{Re_d^2}{2Re_p^2}\right), \quad (2-73)$$

$$Re_p = \frac{\rho_f d|V_{fz} - V_{sz}|}{\mu_f}, \quad (2-74)$$

$$Re_T = \frac{\rho_f d\sqrt{T}}{\mu_f}. \quad (2-75)$$

Simonin⁸ developed a model for the gas-solid fluctuation velocity cross-correlation based on the Lagrangian time scale and particle relaxation time scale. The Lagrangian time scale is the time for which the effect of a passing eddy can be felt on the rest of the fluid and is defined as,

$$\tau_L = \frac{\tau_e}{\sqrt{1 + c_\beta \xi_r^2}}, \quad (2-76)$$

where the eddy time scale (τ_e the turn over time of an eddy) is,

$$\tau_e = \frac{3}{2} c_\mu f_\mu \frac{k}{\varepsilon}, \quad (2-77)$$

and,

$$\xi_r^2 = \frac{3|V_f - V_s|^2}{2k}, \quad (2-78)$$

$$c_\beta = 1.8 - 1.35 \cos^2(\theta'). \quad (2-79)$$

The parameter θ' is the angle between the mean fluid and solid velocity. The particle relaxation or the drag time (τ_D) is the time for which the effect of a passing particle can be felt on the neighboring fluid and is defined as,

$$\tau_D = \frac{v\rho_s}{\beta(1-v)}. \quad (2-80)$$

Simonin⁸ assumed that the ratio of the Lagrangian time scale (τ_L) to particle relaxation time (τ_D) is equal to the ratio of the fluctuation energy of the cross-correlation carried by the gas phase to the fluctuation energy carried by the entire mixture. That is,

$$\eta_t = \frac{\tau_L}{\tau_D} = \frac{\rho_f(1-v)k_{sf}}{(2\rho_f(1-v)k + 3\rho_s vT - \rho_{avg}k_{sf})}. \quad (2-81)$$

Equation 2-81 on rearrangement gives,

$$k_{sf} = \frac{\eta_t}{1 + [1 + \chi]\eta_t} [2k + 3\chi T], \quad (2-82)$$

where

$$\chi = \frac{\rho_s \nu}{\rho_f (1 - \nu)}. \quad (2-83)$$

Crowe⁴⁵ argued that it was incorrect to take the averaged flow variables as being local flow variables and to treat the governing equations as if they represented single-phase flow with a local coupling term. Hence, Crowe⁴⁵ suggested a new approach for the development of the governing equations which is not based on temporal and volume averaging, but is based on volume averaging only (VBA). The equations he used for the fluctuation interaction terms I_k and I_T , are different than those normally used by others,

$$I_k = \beta(1 - \nu) |V_f - V_s|^2 + \beta(1 - \nu)(3T - k_{sf}), \quad (2-84)$$

$$I_T = \beta(1 - \nu)(k_{sf} - 3T). \quad (2-85)$$

This formulation includes an additional generation term which is proportional to the square of the relative velocity between the two phases (equation 2-84), arising due to the new averaging technique. This additional generation helps predict the enhanced fluid turbulence. The model of Zhang and Reese⁴⁶ employs equation 2-84 and equation 2-85 for the fluctuating interaction terms along with a modified Koch and Sangani⁴² model to describe the cross-correlation between the fluid and solid fluctuating velocity,

$$k_{sf} = |V_f - V_s|^2 \frac{\tau_c}{\tau_D}, \quad (2-86)$$

where the collision time τ_c is the time between collisions and is defined as,

$$\tau_c = \frac{d}{24\nu g_0} \sqrt{\frac{\pi}{T}}. \quad (2-87)$$

Zhang and Reese⁴⁶ showed good predictions when compared with the Tsuji *et al.*² data.

Sinclair and Mallo⁴⁴ developed a simple model for the cross-correlation of fluid-solid velocity fluctuations using a simple geometric mean,

$$k_{sf} = \sqrt{6kT}. \quad (2-88)$$

Equation 2-88 is obtained by assuming that the correlation of the fluctuating gas velocity and the fluctuating drag force ($\overline{v_{fi}' \cdot f_{Di}}$) divided by the gas fluctuation velocity is equal to the correlation of the fluctuating solid velocity and the fluctuating drag force ($\overline{v_{si}' \cdot f_{Di}}$) divided by the fluctuating solid velocity, *i.e.*,

$$\frac{\overline{v_{fi}' \cdot f_{Di}}}{(\overline{v_{fi}' \cdot v_{fi}'})^{1/2}} \cong -\frac{\overline{v_{si}' \cdot f_{Di}}}{(\overline{v_{si}' \cdot v_{si}'})^{1/2}}, \quad (2-89)$$

where f_{Di} is the fluctuating drag force. The correlation between fluctuating gas velocity and the fluctuating drag force is generally approximated as I_k , the effect of solids on the gas turbulence, and the correlation of fluctuating solid velocity and the fluctuating drag force is approximated as I_T , the effect of gas turbulence on the granular temperature.

Thus equation 2-89 can be interpreted as,

$$\frac{I_k}{\sqrt{2k}} = -\frac{I_T}{\sqrt{3T}}. \quad (2-90)$$

Substituting equation 2-65 and equation 2-66 into equation 2-90 gives,

$$\frac{\beta(2k - k_{sf})}{\sqrt{2k}} = \frac{\beta(k_{sf} - 3T)}{\sqrt{3T}}. \quad (2-91)$$

Equation 2-91 on simplification gives equation 2-88.

Fluctuating Energy Transfer (FET) Model for the Fluctuating Interaction/Coupling Terms

To develop the new fluctuating interaction model (FET model), we consider the hypothetical situation where:

- Particles are enclosed and suspended freely in a box (Figure 2-1) with no gravitational acceleration.
- The fluid has negligible viscosity; hence, there is no momentum, diffusion and no turbulence dissipation.
- The collisions of the particles are elastic; consequently, there is no dissipation due to collisions.
- The diffusion of particle momentum is also negligible.
- There are no wall effects.

Now, assume that at the start of an experiment the particles are stationary but the gas has an evenly distributed turbulent energy given by k . In this situation, the gas-phase turbulence will initiate some velocity fluctuations in the particle phase that will continue to grow. In this hypothetical situation, the gas-phase turbulent kinetic energy and granular energy equations will reduce to,

$$\rho_f(1-\nu)\frac{\partial k}{\partial t} = -I_k = -\beta'(1-\nu)(2k - k_{sf}), \quad (2-92)$$

$$\frac{3}{2}\rho_s\nu\frac{\partial T}{\partial t} = I_T = \beta'(1-\nu)(k_{sf} - 3T). \quad (2-93)$$

Equation 2-92 and equation 2-93 are analogous to the case of simple heat transfer between two fluids. The interaction terms are similar to convection heat transfer where $(2k - k_{sf})$ and $(k_{sf} - 3T)$ are analogous to temperature differences $(T_{f1} - T_{f12})$ and $(T_{f12} - T_{f2})$, respectively (T_{f1} and T_{f2} are the bulk temperatures of the two fluids and T_{f12} is the temperature at the interface), and $\beta'(1-\nu)$ is analogous to the heat transfer coefficient

multiplied by the surface area ($h_t A_{ht}$). For the defined hypothetical situation, the energy lost by the gas phase is equal to the energy gained by the solid phase,

$$\frac{3}{2} \rho_s v \frac{\partial T}{\partial t} = -\rho_f (1-v) \frac{\partial k}{\partial t}. \quad (2-94)$$

Figure 2-2 shows how the difference in the magnitude of the velocity fluctuations causes a transfer of energy from one phase to another, similar to the transfer of heat from one fluid phase to another. This picture of the energy transfer is consistent with the assumption of interpenetrating continua of the two phases and the use of the two-fluid model. The energy exchange will continue until the fluctuations equalize, that is,

$$k_{sf} = 2k = 3T.$$

Typical units of $\beta'(1-v)$ are $M^1 L^{-3} T^{-1}$ and so $\frac{\rho_f}{\beta'(1-v)}$ is a time scale (τ_{sf}) over which the transfer of fluctuation energy occurs. In the following sections it will be shown that for particles exhibiting turbulence dampening, the time scale for fluctuation energy transfer is τ_D , while for particles showing in-between behavior and turbulence enhancement, the time scale for fluctuation energy transfer is τ_c . This behavior occurs because, for particles exhibiting turbulence dampening, the mechanism of the fluid being pulled along by the particles causes the transfer of fluctuation energy. On the other hand, particles showing in-between behavior and turbulence enhancement, the change in direction of individual solid particles and the corresponding disturbance caused by the particle wake are responsible for the transfer of the fluctuation energy.

Finally, to describe the vortex shedding phenomenon associated with gas-phase turbulent enhancement, the fluctuating interaction/coupling term, I_k (equation 2-92) is enhanced by the wake effect E_w as given by Lun⁵³.

$$E_w = 12 \frac{C_w \mu_t k}{d^2}, \quad (2-95)$$

$$\text{Re}_p = \frac{\rho_f d |V_{fz} - V_{sz}|}{\mu_f}, \quad (2-96)$$

$$\mu_t = 0.017 \text{Re}_p \mu_f \text{ for } 150 \leq \text{Re}_p < 310, \quad (2-97)$$

$$\mu_t = 1.2 + 0.0000 \text{Re}_p^2 \mu_f \text{ for } 310 \leq \text{Re}_p < 610, \quad (2-98)$$

$$\mu_t = 0.029 \text{Re}_p \mu_f \text{ for } \text{Re}_p \geq 610, \quad (2-99)$$

$$C_w = 10/3 \text{ for } 150 \leq \text{Re}_p < 310, \quad (2-100)$$

$$C_w = 24/3 \text{ for } \text{Re}_p \geq 310. \quad (2-101)$$

Equation 2-95 to equation 2-101 detail the vortex shedding term. The coefficient C_w is slightly modified from what was originally prescribed in Lun⁵³ in order to produce a better fit to the experimental data. Thus, the following equations represent the complete fluctuating interaction/coupling terms for the new model,

$$I_k = -\frac{\rho_f}{\tau_{sf}} (2k - k_{sf}) + E_w, \quad (2-102)$$

$$I_T = \frac{\rho_f}{\tau_{sf}} (k_{sf} - 3T). \quad (2-103)$$

where, τ_{sf} is the time scale for the fluctuation energy transfer ($\tau_{sf} = \tau_D$, for particles which show turbulence damping and $\tau_{sf} = \tau_c$, for particles which show in-between behavior and turbulence enhancement).

A couple of observations can be made about the cross-correlation k_{sf} :

- According to the new model and from the heat transfer analogy, k_{sf} must lie between $2k$ and $3T$.

- At the wall, as the instantaneous fluid velocity becomes zero due to the no-slip condition, the cross-correlation k_{sf} must also become zero.

Keeping these two conditions in mind, the Sinclair and Mallo⁴⁴ model is used for the cross-correlation k_{sf} since it is the only closure that is consistent with both conditions.

Boundary Conditions

Appropriate boundary conditions are also of prime importance to generate reliable flow predictions. At the center of the pipe, the symmetry boundary condition is used for all the flow variables. For the solid phase, boundary conditions at the wall for shear stress (σ_{rz}) and the flux of granular energy (q_{pT}) follow Johnson and Jackson⁵⁵.

For the fluid phase at the wall, two sets of conditions were employed in this study. The first set of conditions is based on a low Reynolds number k - ϵ turbulence model as used by Bolio *et al.*⁷ where turbulent transport equations for the fluid phase are integrated to the wall. For low Reynolds number k - ϵ turbulence model, the mean and fluctuating fluid velocities are zero (no-slip boundary condition). Dissipation of gas turbulence at the wall is given by,

$$\rho_f \epsilon = \mu_{ef} \frac{\partial^2 k}{\partial r^2} + I_k. \quad (2-104)$$

The second set of boundary conditions for the fluid phase employ wall functions for the fluid phase and follow the MFIX code⁵⁴. These conditions assume some fluid velocity slip at the wall. Also, the wall conditions for k and ϵ are modified to be consistent with this approximation. The wall functions for the fluid-phase were used only when the code was being validated against the MFIX code and the results of Benavides and van Wachem⁹. For all the figures and tables in the present study, the low Reynolds

number k - ε turbulence model is used (*i.e.*, no-slip boundary condition along with equation 2-104).

Numerical Solution

To solve the governing equations numerically, one operating condition for the fluid phase and one for the solid phase are required. In the code developed for the present study, two options are available for the operating condition on the fluid phase: the centerline fluid velocity or the fluid flow rate. The choice of which to use is made based on the conditions specified in the experimental data. For the solid phase, solid mass loading m is used to specify the operating condition. The solid loading m is defined as,

$$m = \frac{\int \rho_s v V_{sz} r dr}{\int \rho_f (1-v) V_{fz} r dr} \quad (2-105)$$

The governing equations including the closure models, boundary and operating conditions are solved using a combination of marching and iterative schemes as described in the following paragraph.

The continuum equations are discretized using the finite volume method approach described in Patankar and Spadling⁵⁶. Approximately one hundred discrete grid points were distributed in a non-uniform pattern throughout the domain cross-section with higher grid resolution near the wall. Bolio *et al.*⁷ showed that sixty grid points were sufficient to generate a grid-independent solution.

Figure 2-3 depicts the flow chart for the code. First, a guess of single phase dimensionless fluid velocity V_{fz} , gas turbulence k , and gas-phase dissipation ε at a specific Re (where $Re = \frac{\rho_f V_{fzcl} 2R}{\mu_f}$ and V_{fzcl} is the centerline fluid velocity) are given as

input to the code. The code then perturbs the Re towards the direction of the desired

operating velocity and generates the new single-phase profiles for the perturbed Re in an iterative scheme. The operating condition is solved along with the discretized version of the single-phase gas momentum equation. The operating condition provides an additional equation which allows the pressure drop (∇p) to be treated as an unknown parameter. Thus, a pressure drop guess is not needed. The perturbations in Re are made until the operating Re is achieved (*i.e.*, the operating velocity is achieved). At this point, an assumption is made that the fluid profile at very low solids loading will match the single phase profiles. Further, the guessed profiles for v , V_{sz} , and T are considered to be independent of r (the radial co-ordinate). The single phase profiles along with the guess for v , V_{sz} and T are taken as guesses for the very dilute case of two-phase profiles. Like the fluid operating condition, the solid operating condition is solved along with the solid phase momentum balance (r-component) equation for the solid volume fraction profiles. The simulated flow profiles are used as a guess for the very dilute case. The loading is increased in small discrete steps (profiles for each loading step were calculated in an iterative scheme) until the two-phase flow operating conditions are obtained. Thus, in this fashion, a stable numerical solution is obtained.

The program is written in a modular fashion so that it is simple to toggle amongst the various closure models and boundary conditions (Appendix A details the Matlab program). Hence, the program developed herein has the ability to easily reproduce the predicted flow patterns (with slight differences arising due to the numerical technique used) given in Bolio *et al.* ⁷ (Figure 2-5), Benavides and van Wachem ⁹ (Figure 2-6), and MFIx (following the work of Simonin ⁸, Figure 2-7). Therefore, this code provides a useful tool to compare various dilute turbulent gas-solid models against the same

benchmark experimental data sets on the same platform. Unfortunately, the code is unable to reproduce the results of Zhang and Reese ⁴⁶ even after consultation with the authors.

Figure 2-4 compares the solutions obtained from the model using Wen and Yu ³⁹ drag relation, Peirano and Leckner ⁵¹ solid stress and FET model (with Sinclair and Mallo ⁴⁴ cross-correlation) for a variety of number of grids. Although it is determined that fifty grids are sufficient to get a grid independent solution, ninety nine grids are used for all simulation runs.

Benchmark Data Sets

As stated earlier, the data under consideration are for pneumatic transport of solids by gas (air) in a vertical pipe. These flows are dilute and turbulent, and the flow profiles are fully developed. The data sets of Tsuji *et al.* ², Jones *et al.* ³, Lee and Durst ⁵, and Sheen *et al.* ⁴ span various sizes of polystyrene and glass bead particles (70 – 3000 μm) with Re approximately between 10,000 and 30,000 and mass loadings varying between 0 to 5.

Since the experimental data by Tsuji *et al.* ² is the most widely cited, the data sets for 243 μm and 500 μm are chosen here as a standard by which all the previously published models, as well as the present model, will be evaluated. However, all of the models have been evaluated against all the experimental data summarized in Table 2-2, and it is observed that the model utilizing the combination of Syamlal and O'Brien ⁴⁹ drag force relation, the Peirano and Leckner ⁵¹ solid stress model, and the FET closure compare more favorably to the data than the other models. The values for the coefficient of restitution of particle-particle/particle-wall collisions and the specularity

factor are the same as those given in Bolio *et al.*⁷ and are approximately similar to the values employed in the other published gas-solid flow models.

Results and Discussion

From the simulations, profiles of the gas and solid mean velocities V_{fz} and V_{sz} , along with the profiles of the gas turbulent kinetic energy k and the granular temperature T are obtained. Since experimental data report values for the axial solid velocity fluctuations v_{sz}' , these values need to be extracted from the predicted granular temperature T . To convert T to v_{sz}' , isotropic solid velocity fluctuations are assumed. Measurements of axial and radial solid velocity fluctuations show that this assumption is a reasonable one for dilute gas-solid flow⁵⁷,

$$v_{sz}' = \sqrt{T}. \quad (2-106)$$

For the gas velocity fluctuations, Sheen *et al.*⁴ has shown that the gas turbulence is not isotropic in pipe flows. Consequently, it is assumed that the radial and azimuthal fluctuations in velocity v_{fr}' and $v_{f\theta}'$ respectively, are approximately half of the axial velocity fluctuations⁴,

$$v_{fr}' = v_{f\theta}' = \frac{v_{fz}'}{2}, \quad (2-107)$$

which results in

$$v_{fz}' = \sqrt{k}. \quad (2-108)$$

Figures 2-8 to 2-11 compare the predicted profiles of the new model (which incorporates the Wen and Yu³⁹ drag force, the Peirano and Leckner⁵¹ solids stress, the new FET model for the interaction between the gas and particle velocity fluctuations, and the Sinclair and Mallo⁴⁴ model for the solid-gas velocity cross-correlation) to the

experimental data of Tsuji *et al.* ². Figures 2-12 and 2-13 compare the predicted profiles from the same model to the Jones *et al.* ³ and Sheen *et al.* ⁴ data, respectively. In all of these predictions, when the Stokes number ($ST = \frac{d^2 V_{fzcl} \rho_s}{18 \mu_f (2R)}$) is less than 100, the particle relaxation time scale τ_D is used as the time scale for the fluctuation energy transfer. When ST is less than 100, the mechanism of the fluid being pulled along by the particles causes the transfer of the fluctuation energy. On the other hand, when ST is greater than 100, the particle collision time scale τ_c is used because the change in direction of the individual solid particles and the corresponding disturbance in the particle wake are responsible for the transfer of the fluctuation energy. Finally, if $Re_p > 150$ (large particles with large relative velocity), E_w is activated. When Re_p is greater than 150, the turbulent boundary layer detaches from the particle surface and vortices are generated in the wake of the solid particles, enhancing gas-phase turbulence. Table 2-3 summarizes the time scales used by the FET model for the various experimental data (detailed in Table 2-2).

Overall, the simulation results for the mean gas and solid velocities, as well as the fluctuating gas and solid velocities, favorably match the experimental data with this proposed model. The predictions for gas-solid flow shown in Figure 2-11 for 2780 μm particles are not as good as the other cases. This discrepancy is likely due to an inadequate description for vortex shedding with such large particles.

Comparing the Various Models for Interaction Terms and Cross-Correlations

The different models for the interaction terms are compared using the gas-phase turbulence and granular temperature data for the 243 μm and 500 μm particles of Tsuji

*et al.*². These experimental data are used as the standard for uniformly comparing model predictions since most (all but Zhang and Reese⁴⁶) of the other closure models do not predict gas-phase turbulence enhancement in the presence of large particles (1.42 mm and 2.78 mm).

In order to focus this comparison on the effect of the model predictions from the various descriptions for interaction terms and the cross-correlation, the same drag force relation³⁹ and the same solid-phase stress⁵¹ are used in generating the model predictions. Furthermore, only the gas fluctuation velocity (v_{fz}') and the solid fluctuation velocity (v_{sz}') are compared, as variations in the predicted mean gas and solid velocity profiles are negligible.

Figures 2-14, 2-15, 2-16, 2-17 and 2-18 compare the predictions of v_{fz}' profile using Louge *et al.*⁶, Koch and Sangani⁴², Wylie *et al.*,⁴³ Simonin⁸, and Sinclair and Mallo⁴⁴ cross-correlation (TVBA is used for interaction terms, I_k and I_T) respectively, to the data of Tsuji *et al.*². Most models are able to capture the very dilute mass loading flow cases but underpredict the cases with higher mass loading.

Figures 2-19 compare the predictions of v_{sz}' profile using FET model (using Sinclair and Mallo,⁴⁴ cross-correlation). Further, Figures 2-20, 2-21, 2-22, 2-23 and 2-24 compare the predictions of v_{sz}' profile using Louge *et al.*⁶, Koch and Sangani⁴², Wylie *et al.*⁴³, Simonin⁸, and Sinclair and Mallo⁴⁴ cross-correlation (TVBA is used for interaction terms, I_k and I_T) respectively, to the data of Tsuji^{**}. In the case of v_{sz}' profile, most models again underpredict the solid fluctuating velocity.

^{**} Tsuji Y. Private Communication 1993.

Figure 2-25a compares the magnitude of the βk_{sf} (where β is calculated from the Wen and Yu³⁹ drag correlation and k_{sf} is calculated from the various cross-correlations) for the various combinations of interaction terms and the cross-correlation models for the Tsuji *et al.*² case of 243 μm particles with a solids loading of 3.2. Similarly, I_k (equation 2-102), along with the generation $(1-\nu)\mu_T\left(\frac{\partial V_{tz}}{\partial r}\right)^2$ (calculated using FET model only) are compared in Figure 2-25b, and I_T (equation 2-103), along with the rate of granular energy dissipation (equation 2-35, calculated again using FET model only) are compared in Figure 2-25c.

From Figure 2-25b, it is observed that the generation is very small at the core of the pipe and sharply rises toward the wall. For the FET model, the I_k term dominates at the core of the pipe, and the remaining two terms, the generation and the dissipation ε (not shown in Figure 2-25b), play an important role near the wall of the pipe. Since I_k dominates at the core of the pipe, the gas-phase turbulence k largely depends on the interaction term. While, at the wall the gas-phase turbulence depends on the generation and the dissipation.

Further, from Figure 2-25c, the FET model predicts that I_T will be negative and all three terms, in the granular energy balance equation, granular temperature generation (not shown Figure 2-25c), dissipation, and interaction play equally important roles throughout the pipe. No one term dominates at any point.

In cases in which the Louge *et al.*⁶, Koch and Sangani⁴², and Wylie *et al.*⁴³ cross-correlation models (these models use TVBA for I_k and I_T) are used, the error in predicating the gas-phase turbulence profile (Figures 2-14, 2-15 and 2-16 respectively)

increases as the mass loading increases, especially at the core of the pipe. This result is because the magnitude βk_{sf} in equation 2-65 is underestimated, and consequently, I_k is small compared to the gas-phase generation (Figure 2-25b), even at the center of the pipe. Additionally, the I_T values estimated from Louge *et al.*⁶, Koch and Sangani⁴², and Wylie *et al.*⁴³ models are more negative than what is predicted from the FET model resulting in relatively poorer model predictions (Figures 2-20, 2-21 and 2-22). All the cross-correlation models that contain a square of the relative velocity $(V_{fz} - V_{sz})^2$ produce a profile for k_{sf} that increase rapidly near the wall as the relative velocity between the gas and solid phases is very large. However, βk_{sf} must be zero at the wall (as $k_{sf} = 0$, no slip condition).

Although the Simonin⁸ cross-correlation model yields values for I_k which dominate the k -equation at the pipe center, the predictions of shape and magnitude of the fluctuation gas velocity (Figure 2-17 and 2-23) are not as good as those obtained from the FET model (which uses the Sinclair and Mallo⁴⁴ model for cross-correlation), especially for higher mass loading. These predictions are because the Simonin⁸ model predicts too much turbulence damping since the I_k values obtained from it are smaller than those from the FET model (Figure 2-25b). On the other hand, the Sinclair and Mallo⁸ closure (using TVBA for I_k and I_T) predicts the order of magnitude of k and T profiles well, but fails to predict the shape of the k profile correctly (Figure 2-18 and 2-24).

As mentioned earlier, the code was unable to reproduce the results of Zhang and Reese⁴⁶ even after consultation with the authors. Stable model solutions could not be obtained for the Tsuji *et al.*² 243 μm particles, and the model predictions for the 500 μm

particles were poor. The additional generation term $\beta(1-\nu)(V_{fz} - V_{sz})^2$ in equation 2-84 produces values for I_k which are up to two orders of magnitude larger than the typical range of values for I_k and yields an unrealistically large increase in the gas-phase turbulence resulting in unstable solutions in some cases.

Based on Figure 2-25b and 2-25c, all the models predict I_k to be positive, which is a net generation of gas turbulence at the core of the pipe, while I_T is negative which is a net dissipation of granular temperature. The interaction term I_T in the granular temperature equation behaves as dissipation, taking energy from the solid phase and transferring it to the fluid phase resulting in a generation of gas-phase turbulence. This idea goes well with the concept of the fluctuation energy transfer mechanism.

It is observed experimentally that for small particles ($d < 300 \mu\text{m}$ or $40 < ST < 100$), the solid velocity fluctuations are larger than the fluid velocity fluctuations at the core of the pipe. Furthermore, for such particles, if the solids loading increases, the magnitude of the solid velocity fluctuations reduces due to enhanced particle-particle collisions and larger inelastic dissipation γ . The reduction in the granular temperature T (solid velocity fluctuations) tends to further dampen the gas-phase turbulence through the energy coupling terms (I_k, I_T). Hence, higher the mass loading, more is the gas-phase turbulence dampening (Figures 2-8b and 2-8c). Flow predictions employing the FET interaction model are able to reproduce these experimental observations and trends very well.

For the case of very large particles ($d > 800 \mu\text{m}$ or $\text{Re}_p > 150$, Figure 2-10b and 2-11), with a large degree of slip ($V_{fz} - V_{sz}$), the vortex shedding E_w overpowers the effect of the interaction term I_k in the k-equation which results in a high gas-phase turbulence.

Also, as the solids mass loading increases, more vortex shedding takes place, this further enhances the gas-phase turbulence. The predicted fluid velocity fluctuations employing the FET model are greater than the solid velocity fluctuations ($2k > 3T$) resulting in a net dissipation of the fluid-phase velocity fluctuations and a net generation for the solid phase. Thus, a counter effect is seen in these cases with larger particles in which increases in solid mass loading reduces T by increasing γ , but this effect is offset by the increase in I_T . Overall, the granular temperature T slowly increases as the solids mass loading increases. Unfortunately, solid velocity fluctuation data are not available for these larger particles to validate these model predictions.

The intermediate particle sizes ($300 \mu\text{m} < d < 800 \mu\text{m}$ or $ST > 100$ and $Re_p < 150$, Figure 2-9b) display flow behavior between the two extremes, where the gas turbulence is enhanced at the core of the pipe but dampened at the wall as compared to single-phase flow. Also, the simulations incorporating the FET interaction term model predict that the solid velocity fluctuations are greater than the fluid fluctuations at low solid mass loadings, but the fluid fluctuations become greater than those of the solid as the mass loading increases. Again, there are no solid fluctuation data to validate these model predictions for the solid-phase fluctuations, but the model favorably matches the experimental gas-phase fluctuation data.

All of these predicted qualitative trends obtained by using the FET interaction term model, along with the Sinclair and Mallo⁴⁴ cross-correlation, are in line with the well-known work of Gore and Crowe¹⁰. These authors suggest that for small particles, drag is responsible for the turbulence transfer between the phases and turbulence damping. In the FET model, the drag time scale τ_D is used as the time scale for energy transfer

for small particles. Furthermore, Hestroni¹¹ showed that particles with intermediate Re_p display in-between behavior (i.e., gas-phase turbulence enhancement in the core of the pipe and dampening at the wall). In the FET model, this behavior occurs when τ_c is the time scale, but vortex shedding is not activated (i.e., $ST > 100$ but $Re_p < 150$). Hestroni¹¹ also showed that for very large Re_p , vortex shedding is responsible for enhanced turbulence as is seen in the cases in which $Re_p > 150$. The vortex shedding, in the present study is described using E_w .

The FET model predictions for particle sizes ranging from 70 – 3000 μm with a wide range of mass loadings compare very well with the experimental data. Hence, the FET model along with the Sinclair and Mallo⁴⁴ cross-correlation is recommended over the other previously proposed closure models for the interaction terms and the solid-gas fluctuating velocity cross-correlation.

Gas-phase turbulence and granular temperature predictions using different fluctuation Interaction terms are compared in Table 2-4 and Table 2-5, respectively. These tables provide the percentage error values of the predictions from the experimental data. The percentage error for the gas phase is defined as

$$\%error = \frac{\sqrt{\sum_j (v'_{fzj}{}^{expt} - v'_{fzj}{}^{sim})^2}}{\sum_j v'_{fzj}{}^{expt}} * 100, \quad (2-109)$$

where $v'_{fzj}{}^{expt}$ is the j^{th} experimental value of the fluctuating gas velocity and $v'_{fzj}{}^{sim}$ is the predicted value of the fluctuating gas velocity at the same radial position r at its corresponding j^{th} experimental value. Percentage error for the solid fluctuating velocity predictions is similarly defined for the solid phase.

Comparing the Various Models for Drag Terms

Flow predictions using different drag force relations are compared in Table 2-6 which provides the percentage error values of the predictions from the experimental data. To compare the different drag relations, the FET interaction model, along with the Sinclair and Mallo⁴⁴ cross-correlation and the Perino and Leckner⁵¹ solid stress model were employed. Figure 2-26 shows that the magnitude of the drag force based on the Wen and Yu³⁹ and Syamlal and O'Brien⁴⁹ models for the case of 243 μm particles and $m = 3.2$ of Tsuji *et al.*² are very similar. The Hill *et al.*^{47, 48} drag relation predicts a drag force magnitude slightly smaller than the other two models. The percentage error values in Table 2-6 for the Hill *et al.*^{47, 48} drag relation are slightly larger than the other two models, suggesting that the Hill *et al.*^{47, 48} drag relation may under predict the drag coefficient β and thereby under predict the drag force.

Hadinoto and Curtis¹⁴ studied the effect of the various drag relations for particles with low inertia on two-phase flow predictions. They observed some influence in the predictions of the slip velocity due to changes in the drag model; however, no such effect is seen in the present study, since the particles studied herein have large inertia. Hence, the effect of the choice of the drag model is not that significant. Since the predicted flow profiles found by changing the drag models are similar, the Wen and Yu³⁹ model, a robust and widely used closure, is recommended for the case of dilute, turbulent, gas-solid flow models.

Comparing the Various Models for Solid Stress Terms

Figure 2-27 compares the magnitude of the solid phase viscosity μ_s and solid phase conductivity λ using the Lun *et al.*⁵⁰ and the Peirano and Leckner⁵¹ solid stress closures for the case of 243 μm particles and $m = 3.2$ in the experiments of Tsuji *et al.*².

The FET interaction model and the Wen and Yu³⁹ drag relation were employed in this comparison. Both the solid viscosity μ_s and conductivity λ values, as predicted by the Lun *et al.*⁵⁰ model, are insensitive to the radial position r . Both the μ_s and λ are primarily functions of the granular temperature, which is essentially constant over the pipe cross-section. In contrast, the predicted solid viscosity and conductivity from the Peirano and Leckner⁵¹ solid stress closure exhibit some dependency on the radial position r , as this solid stress model incorporates a direct effect of the fluid on the μ_s and λ values.

Table 2-7 shows that the two solid stress closures produce similar error in the model predictions from the experimental data. Furthermore, the detailed shape of the mean and fluctuating solid and gas profiles obtained from the two solid stress closures are hardly different. Since the Peirano and Leckner⁵¹ solid stress closure directly incorporates fluid effects, it is chosen over the Lun *et al.*⁵⁰ solid stress closure. It is anticipated that this direct incorporation of fluid effects may yield improved flow predictions in situations involving liquid-solid systems.

Summary

Experimental data considered in the present Chapter is for high ST gas-solid flows in the inertia dominated regime. The flow behavior in this regime, for a wide range of particle sizes from 70 μm to 3 mm, fluidized at $\text{Re} \sim 3 \times 10^4$, is predicted using an Eulerian model. The Eulerian two-fluid model for dilute turbulent gas-solid flows with particle-particle interaction (must be considered in inertia dominated flow regime) requires many closures. The fluid phase stresses which are enhanced by gas-phase turbulence are closed using the eddy viscosity assumption which in turn is computed with the help of a standard two equation $k-\epsilon$ model. While granular kinetic theory is used

to compute the solid-phase stresses. Two different granular kinetic theory models^{50, 51} are compared in the present study.

The drag force behaves as the interaction between the fluid and solid phases at the mean level. To compute this force innumerable models are suggested in the literature. However, only three models (Wen and Yu³⁹, Hill *et al.*^{47, 48} and Syamlal and O'Brien⁴⁹) are compared in the present study as changing these models did not affect the predictions much.

The interaction term at the fluctuating velocity level is not well understood and so a new model (FET model) is proposed. Using the FET model, along with the Sinclair and Mallo⁴⁴ gas-solid fluctuating velocity cross-correlation expression, in the Eulerian model improves the prediction capabilities of the Eulerian model. Also, for the large particles the Lun⁵³ vortex shedding model is included in the Eulerian model to capture the enhanced turbulence.

When the combination of the Syamlal and O'Brien⁴⁹ drag relation, the Peirano and Leckner⁵¹ solid stress closure, the FET model for fluctuating interaction terms and the Sinclair and Mallo⁴⁴ gas-solid fluctuating velocity cross-correlation expression are used, minimum error in prediction of the various velocity profiles is obtained. This model has the capability to describe and predict flow behavior of not only gas-solid flows (at high ST), but also of liquid-solid flows in the inertia dominated flow regime (Chapter 3).

Table 2-1. Closure relations employed in the published gas-solid flow models

Model	Interaction Term (I_k, I_T)	Cross - Correlation (k_{sf})	Drag Force (F_D)	Solid Stress (μ_s, λ)
Bolio <i>et al.</i> ⁷	TVBA	Louge <i>et al.</i> ⁶	Wen & Yu ³⁹	Lun <i>et al.</i> ⁵⁰
MFIX	TVBA	Simonin ⁸	Syamlal & O'Brien model ⁴⁹	Peirano & Leckner ⁵¹
Zhang & Reese ⁴⁶	VBA, Crowe ⁴⁵	Zhang & Reese ⁴⁶	Zhang & Reese ⁴⁶	Peirano & Leckner ⁵¹
Benavides & van Wachem ⁹	TVBA	Louge <i>et al.</i> ⁶ , Simonin ⁸ , Sinclair & Mallo ⁴⁴	Wen & Yu ³⁹	Peirano & Leckner ⁵¹
Present study	TVBA	Louge <i>et al.</i> ⁶ , Koch & Sangani ⁴² , Wiely <i>et al.</i> ⁴³ , Simonin ⁸ , Sinclair & Mallo ⁴⁴	Wen & Yu ³⁹ , Syamlal & O'Brien model ⁴⁹ , Hill <i>et al.</i> ^{47, 48}	Lun <i>et al.</i> ⁵⁰ , Peirano & Leckner ⁵¹
	VBA, Crowe ⁴⁵	Zhang & Reese ⁴⁶		
	FET	Sinclair & Mallo ⁴⁴		
New proposed model	FET	Sinclair & Mallo ⁴⁴	Syamlal & O'Brien model ⁴⁹	Peirano & Leckner ⁵¹

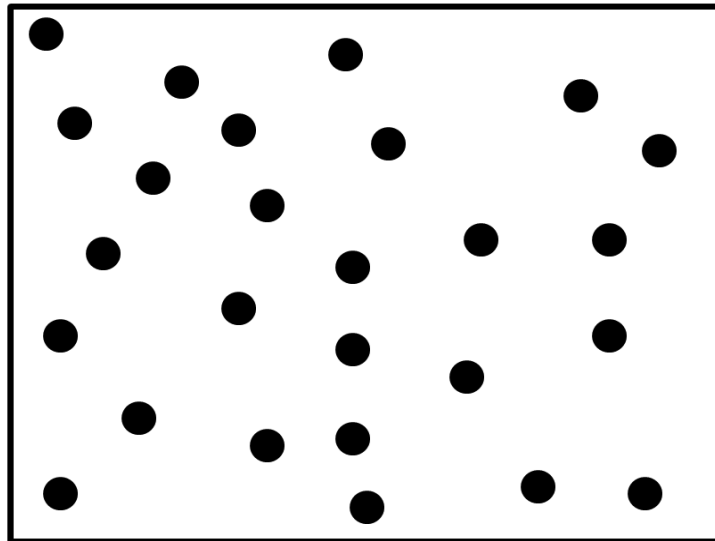


Figure 2-1. Suspended particles enclosed in a box

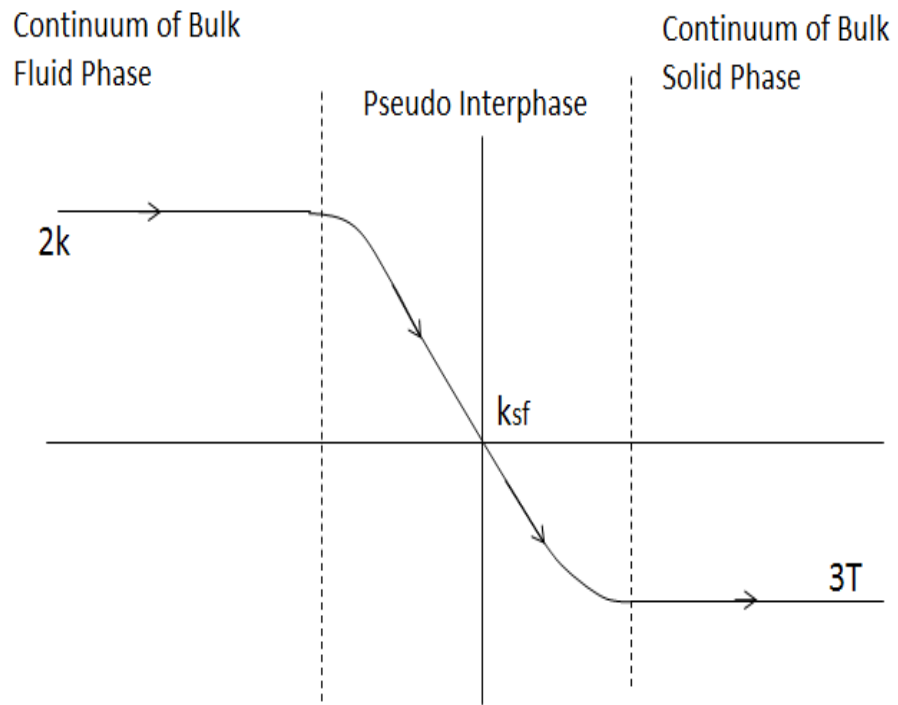


Figure 2-2. Profile for the fluctuating energy transfer

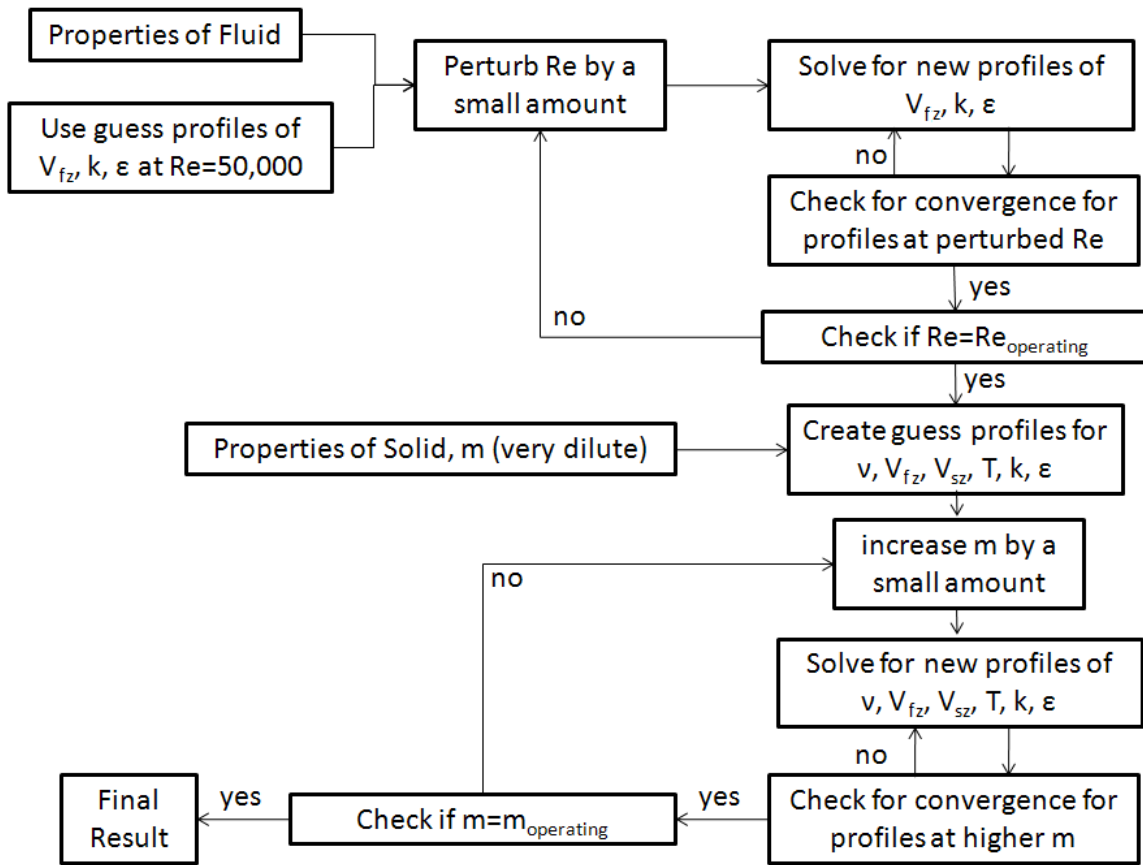


Figure 2-3. Program flow chart

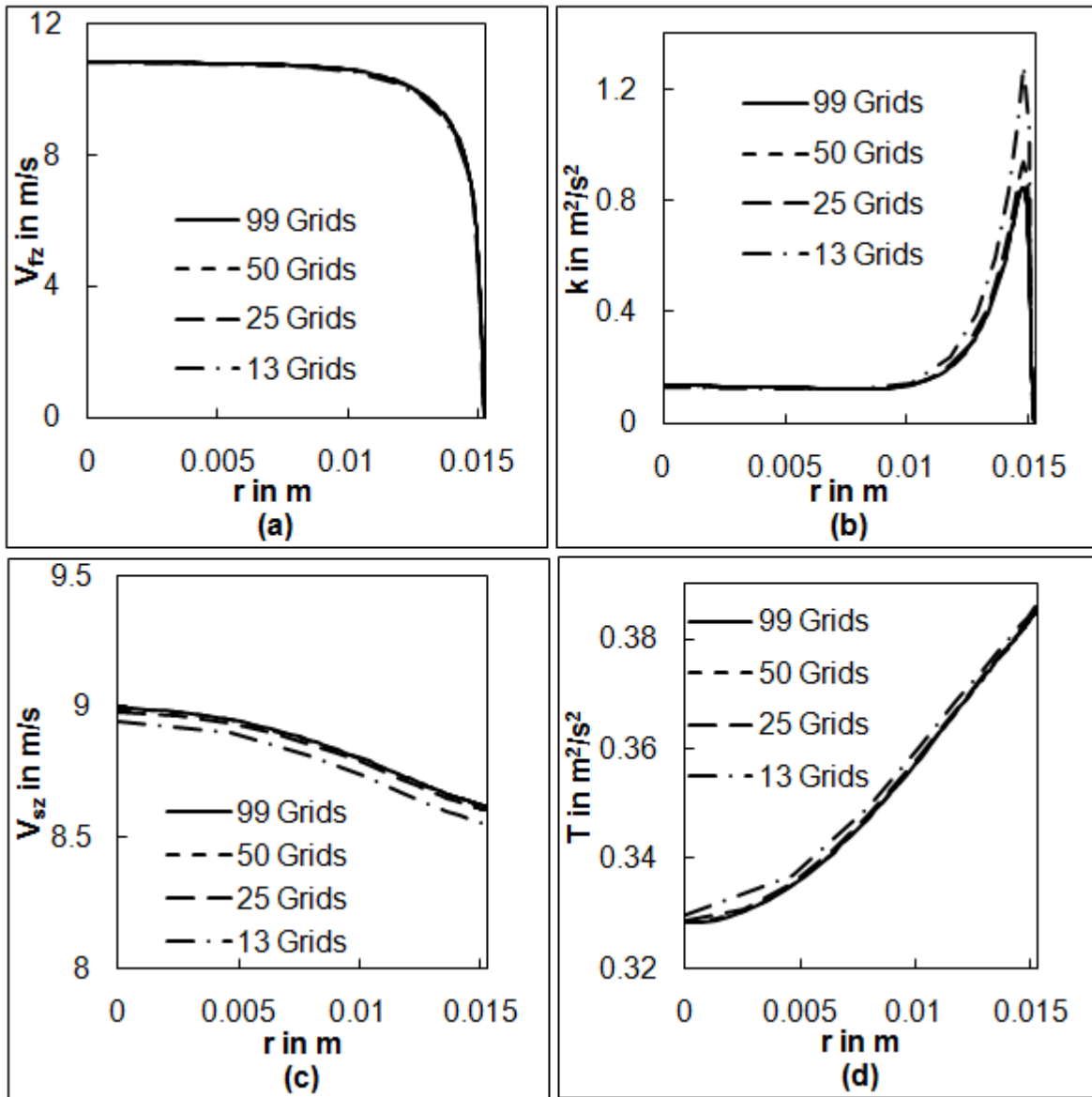


Figure 2-4. Comparison of solutions using various number of grids, (a) fluid mean velocity, (b) gas-phase turbulence (c) solid mean velocity (d) granular temperature, for the case of polystyrene particles $d = 200 \mu\text{m}$, $V_{fzcl} = 11.3 \text{ m/s}$ and $m = 3.2$

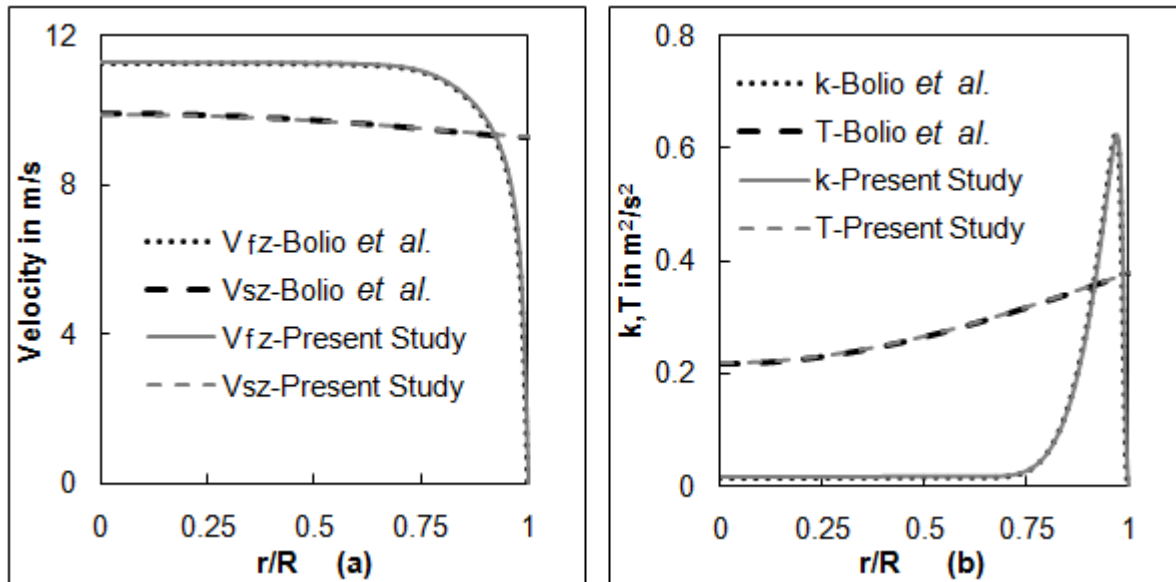


Figure 2-5. Comparison between the Bolio *et al.*⁷ code and the code used in the present study, (a) mean velocity profiles, (b) gas-phase turbulence and granular temperature profiles, for the case of polystyrene particles $d = 200 \mu\text{m}$, $V_{fzcl} = 11.3 \text{ m/s}$ and $m = 3.2$

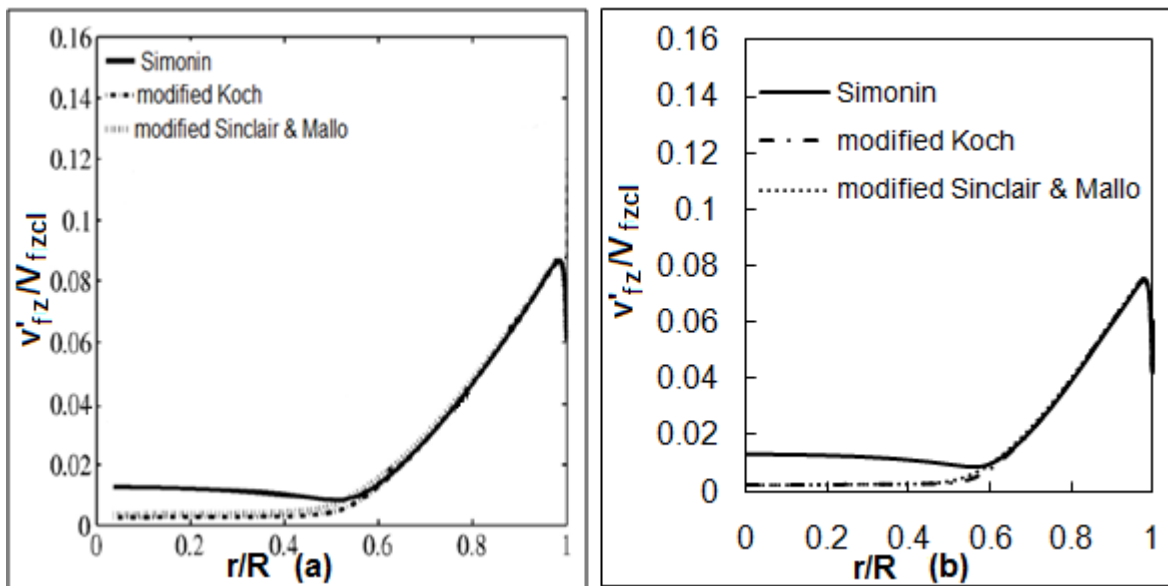


Figure 2-6. Comparison of prediction in the fluctuation velocity between (a) Benavides and van Wachem⁹ and (b) present study for the case of polystyrene particles $d = 200 \mu\text{m}$, $V_{fzcl} = 10.8 \text{ m/s}$ and $m = 3.2$

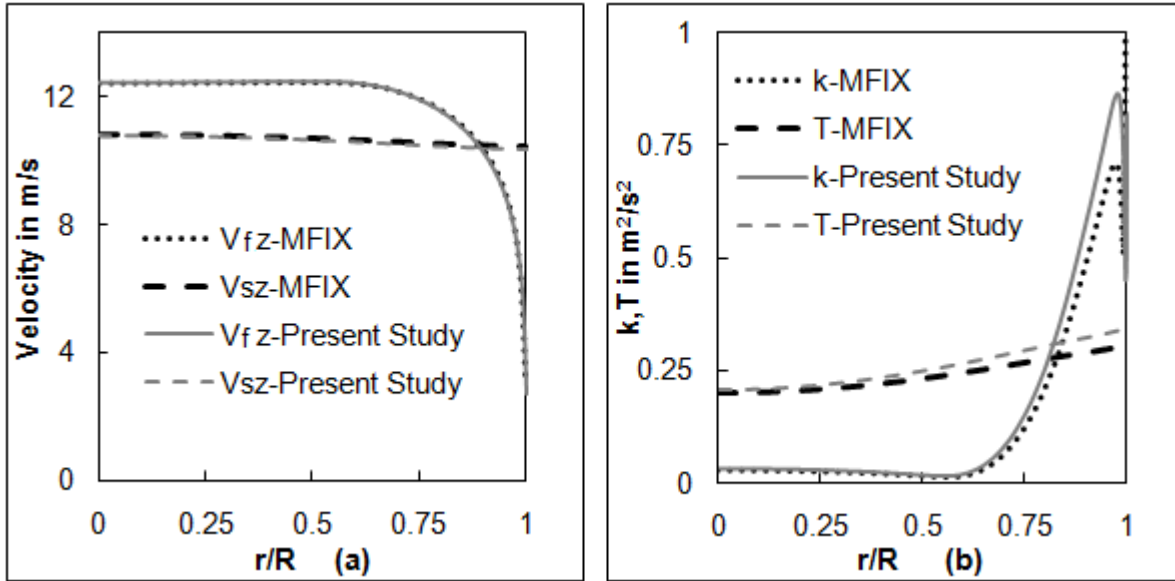


Figure 2-7. Comparison between the MFIX code and the present study, (a) mean velocity profiles, (b) gas-phase turbulence and granular temperature profiles for the case of polystyrene particles $d = 243 \mu\text{m}$, $V_{fzcl} = 12.4 \text{ m/s}$ and $m = 3.2$

Table 2-2. Summary of experimental data

Data	Size μm	Density kg/m ³	Mass Loading			V _{fzcl} (m/s)			R mm	e, ew, φ	Profiles Provided
			Cases			Cases					
			1	2	3	1	2	3			
Tsuji <i>et al.</i> ²	243	1020	0.5	1.3	3.2	13.1	12.8	10.8	15.25	0.9, 0.9, 0.002	V _{fz} , V _{fz'} , V _{sz'}
	500	1020	0.7	1.3	3.4	12.2	13.3	10.7			V _{fz} , V _{fz'}
	1420	1030	0.6	2	2	13.4	12.8	13.2			V _{fz} , V _{fz'}
	2780	1020	0.6	2.3	3.4	14.5	13.8	14.2			V _{fz} , V _{fz'}
Jones <i>et al.</i> ³	70	2529	1	2	4	18.1	17.6	16.5	7.112	0.94, 0.94, 0.002	V _{fz} , V _{sz} , k, V _{sz'}
Lee & Durst ⁵	400	2500	1.5			5.77			20.9	0.94, 0.94, 0.002	V _{fz} , V _{sz}
	200	2500	1.31			5.84					
Sheen <i>et al.</i> ⁴	275	1020	1.224			8.785			26	0.9, 0.9, 0.002	V _{fz} , V _{sz} , V _{fz'}
	450	1020	0.885			9.22					
	800	1020	1.5			9.686					

For all cases, $\mu_f = 1.8 \cdot 10^{-5}$ Ns/m², $\rho_f = 1.2$ kg/m³ and $v_0 = 0.65$

Table 2-3. Time scale used in FET model for the different experimental data

Experimental Data	Size	Density	$\sim Re_p$	$\sim Stokes$	Time Scale	Vortex Shedding
	μm	kg/m^3	No.	No.		
Tsuji <i>et al.</i> ²	243	1020	45	75	τ_D	no
	500	1020	130	320	τ_c	no
	1420	1030	730	2700	τ_c	yes
	2780	1020	1800	11300	τ_c	yes
Jones <i>et al.</i> ³	70	2529	12	50	τ_D	no
Lee & Durst ⁵	400	2500	90	170	τ_c	no
	200	2500	5	43	τ_D	no
Sheen <i>et al.</i> ⁴	275	1020	30	40	τ_D	no
	450	1020	85	115	τ_c	no
	800	1020	220	380	τ_c	yes

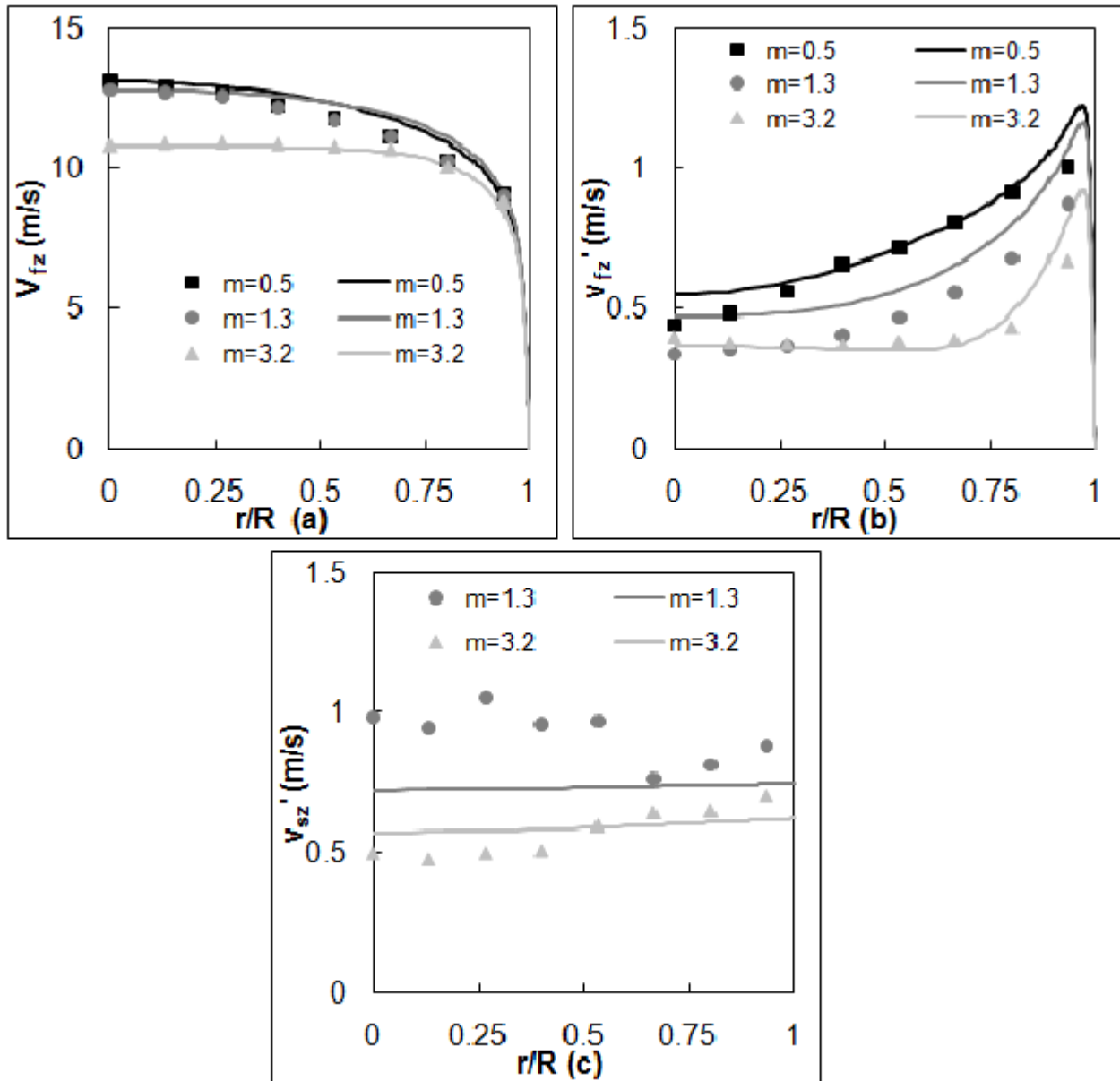


Figure 2-8. Present model predictions compared to Tsuji *et al.*² 243 μm particles

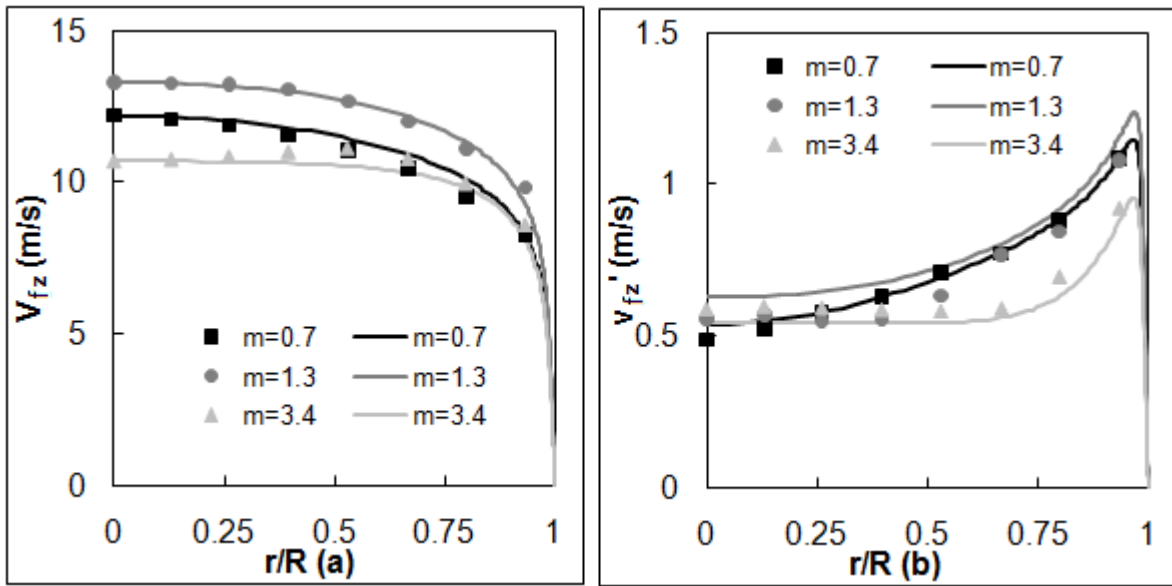


Figure 2-9. Present model predictions compared to Tsuji *et al.*² 500 μm particles

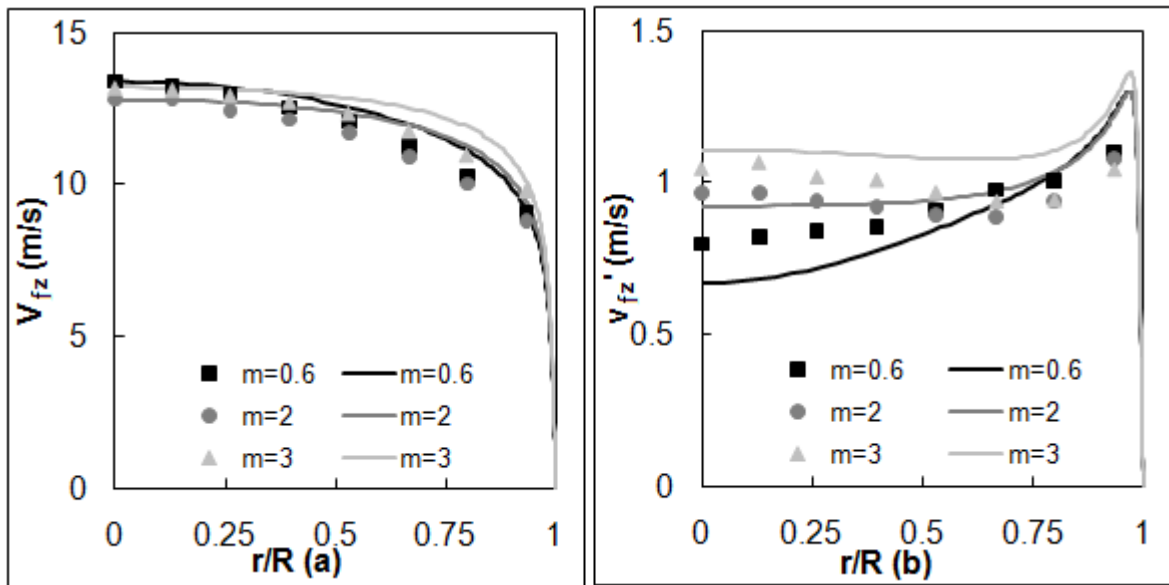


Figure 2-10. Present model predictions compared to Tsuji *et al.*² 1420 μm particles

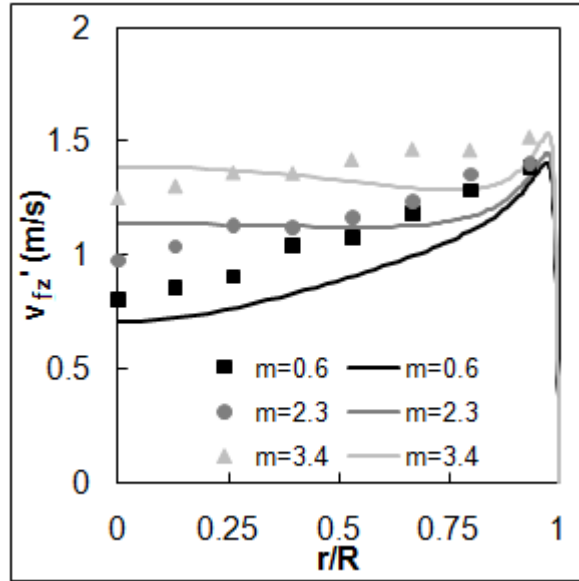


Figure 2-11. Present model predictions compared to Tsuji *et al.*² 2780 μm particles

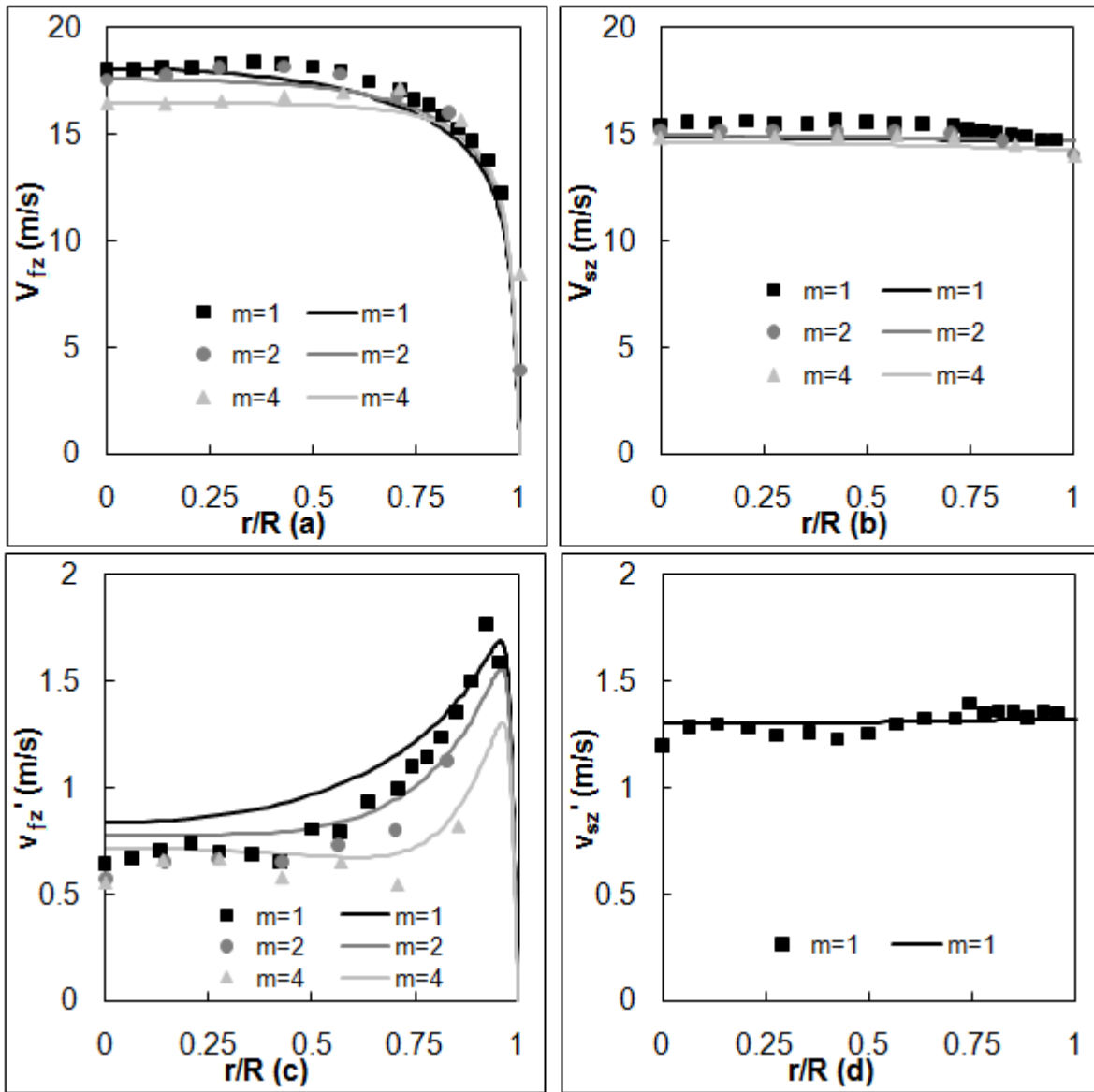


Figure 2-12. Present model predictions compared to Jones *et al.*³ 70 μm particles

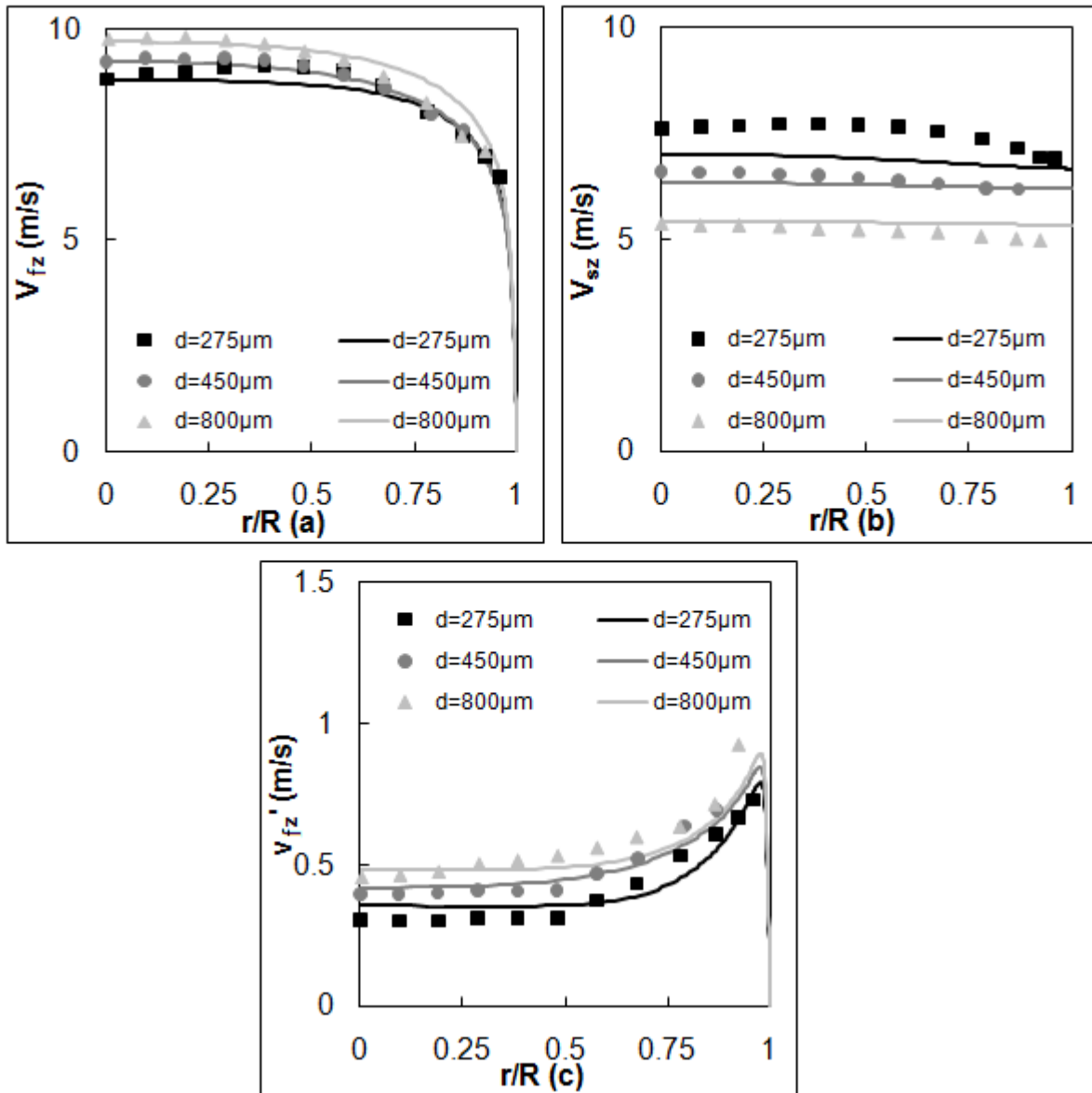


Figure 2-13. Present model predictions compared to Sheen *et al.* ⁴

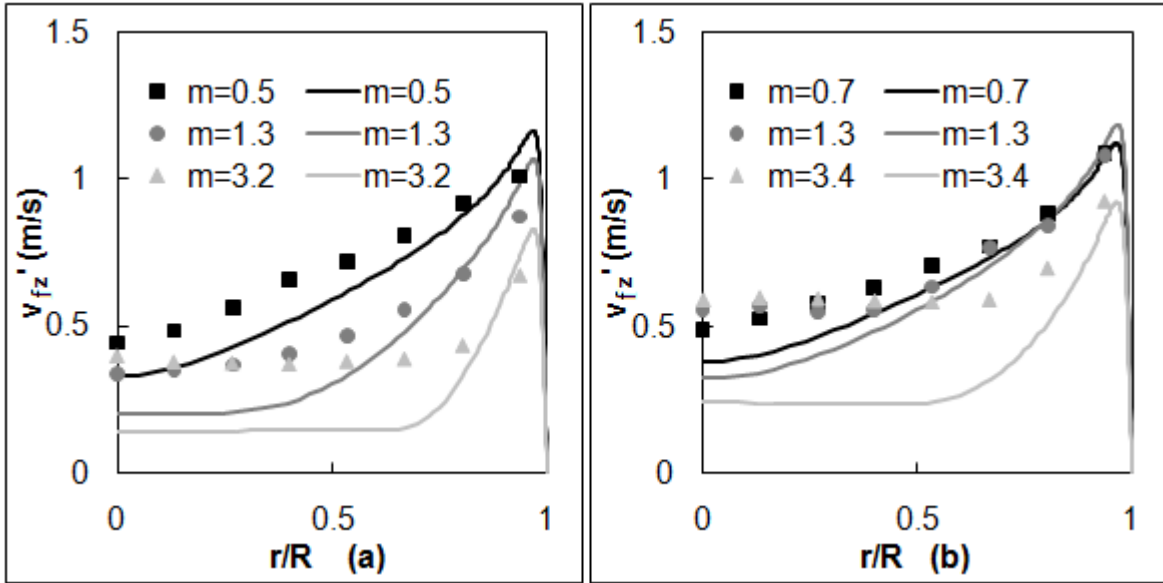


Figure 2-14. Louge *et al.*⁶ cross-correlation predictions compared to Tsuji *et al.*² (a) 243 μm particles, (b) 500 μm particles

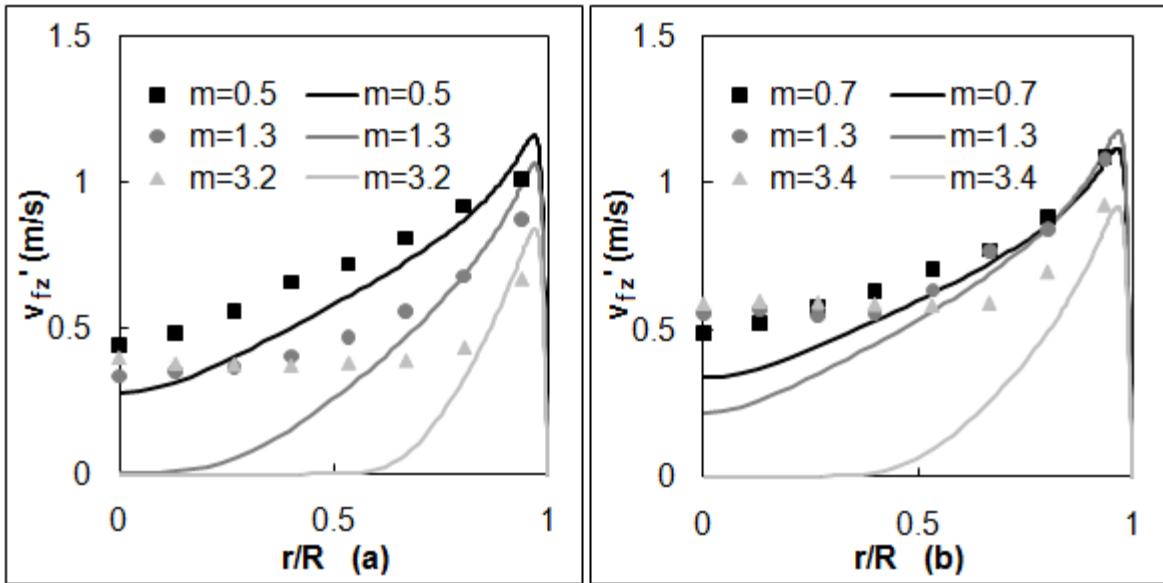


Figure 2-15. Koch and Sangani⁴² cross-correlation predictions compared to Tsuji *et al.*² (a) 243 μm particles, (b) 500 μm particles

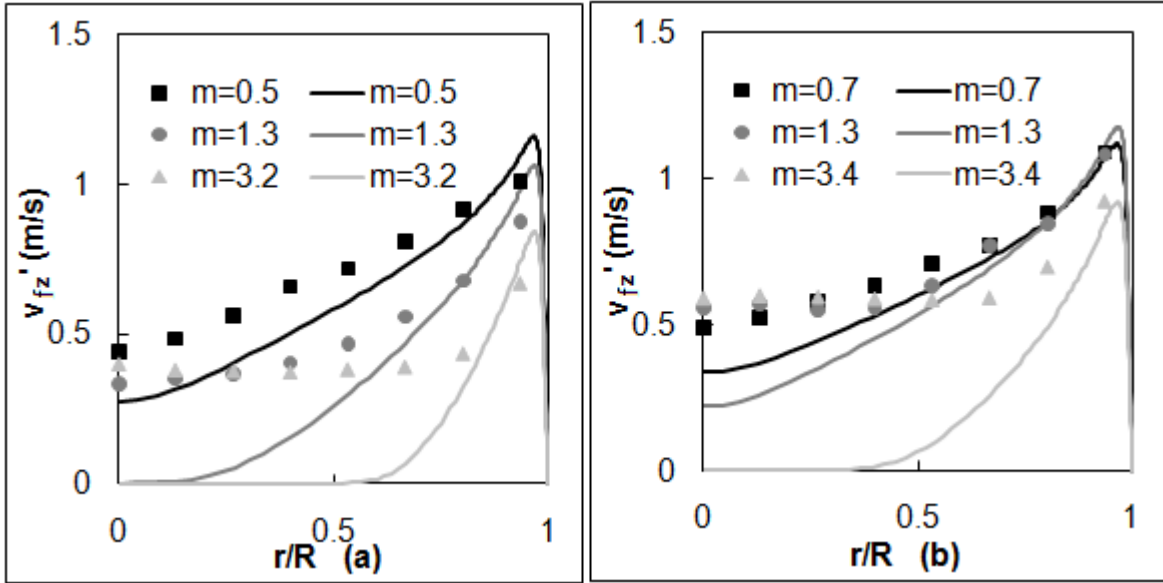


Figure 2-16. Wylie *et al.*⁴³ cross-correlation predictions compared to Tsuji *et al.*² (a) 243 μm particles, (b) 500 μm particles

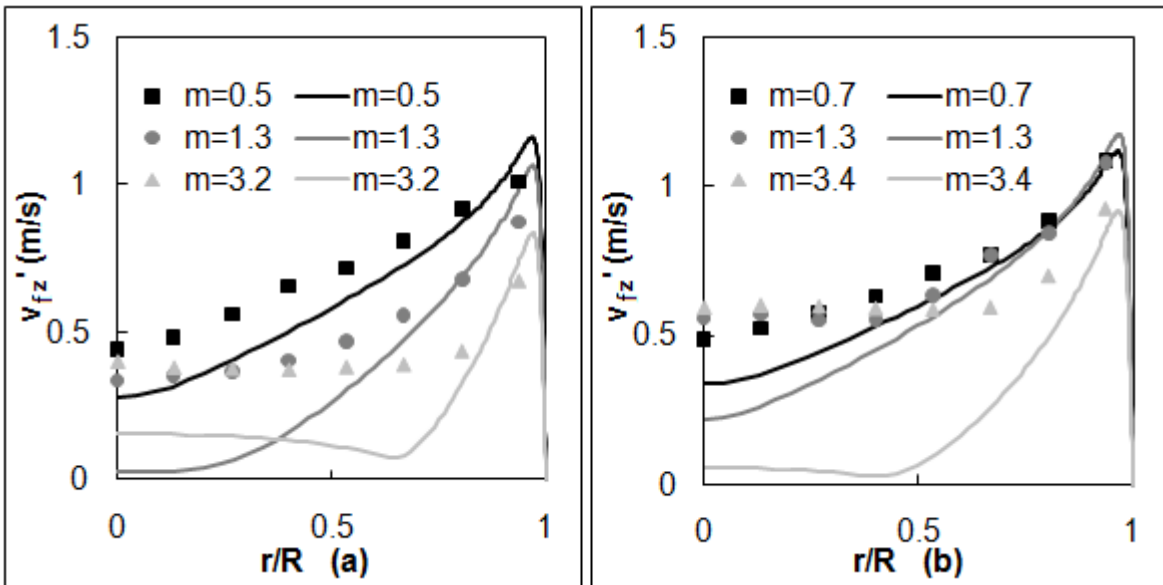


Figure 2-17. Simonin⁸ cross-correlation predictions compared to Tsuji *et al.*² (a) 243 μm particles, (b) 500 μm particles

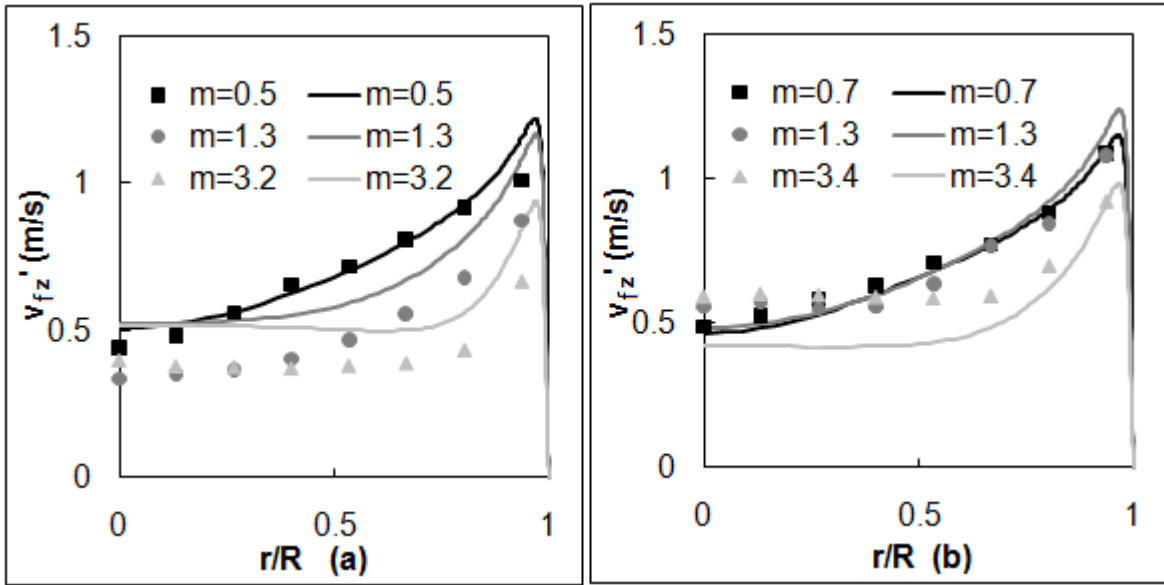


Figure 2-18. Sinclair and Mallo⁸ cross-correlation predictions compared to Tsuji *et al.*²
 (a) 243 μm particles, (b) 500 μm particles

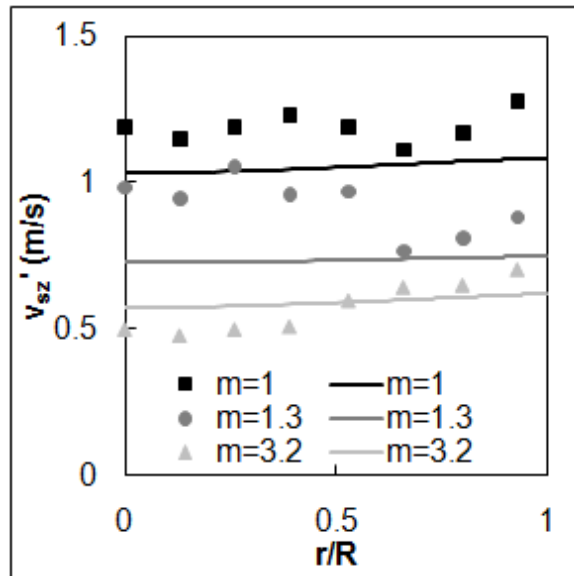


Figure 2-19. FET model predictions compared to Tsuji^{**} 243 μm particles

^{**} Tsuji Y. Private Communication 1993.

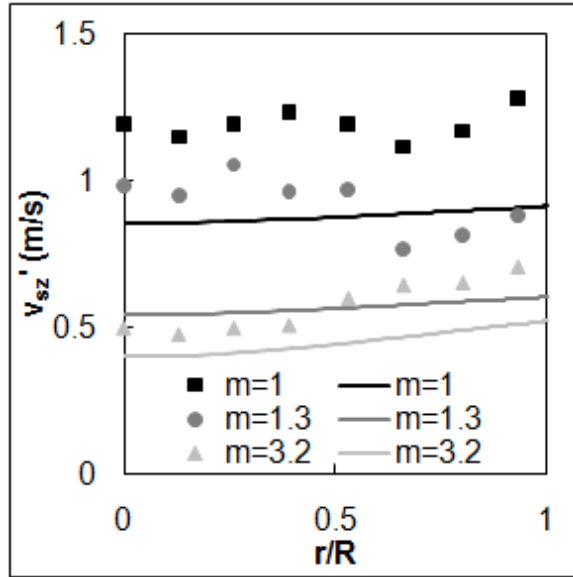


Figure 2-20. Louge *et al.*⁶ cross-correlation predictions compared to Tsuji^{**} 243 μm particles

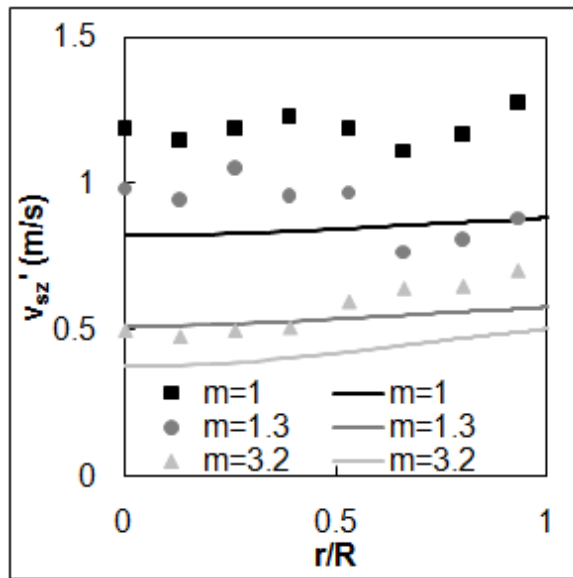


Figure 2-21. Koch and Sangani⁴² cross-correlation predictions compared to Tsuji^{**} 243 μm particles

^{**} Tsuji Y. Private Communication 1993.

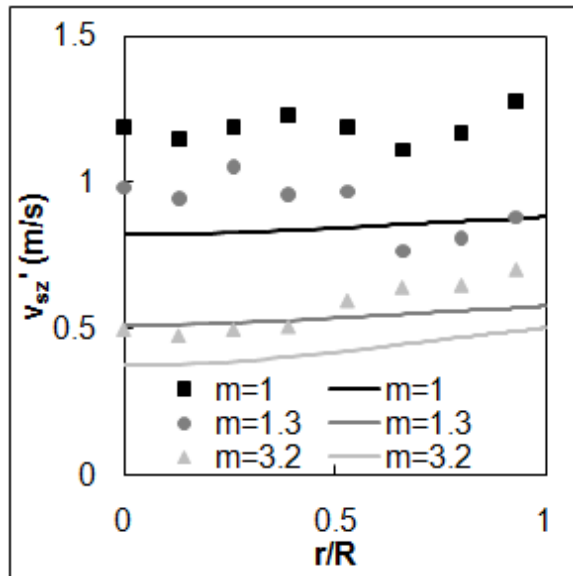


Figure 2-22. Wylie *et al.*⁴³ cross-correlation predictions compared to Tsuji^{**} 243 μm particles

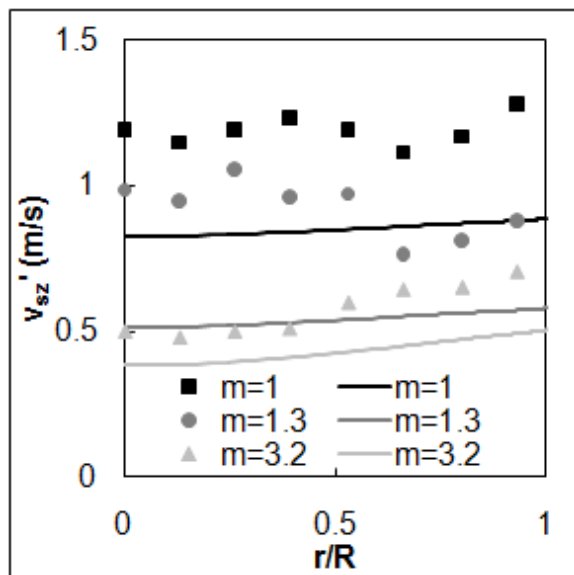


Figure 2-23. Simonin⁸ cross-correlation predictions compared to Tsuji^{**} 243 μm particles

^{**} Tsuji Y. Private Communication 1993.

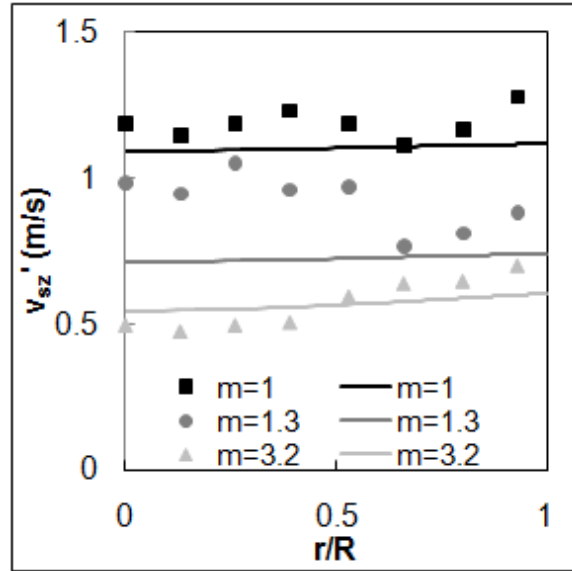


Figure 2-24. Sinclair and Mallo ⁴⁴ cross-correlation predictions compared to Tsuji ^{**} 243 μm particles

^{**} Tsuji Y. Private Communication 1993.

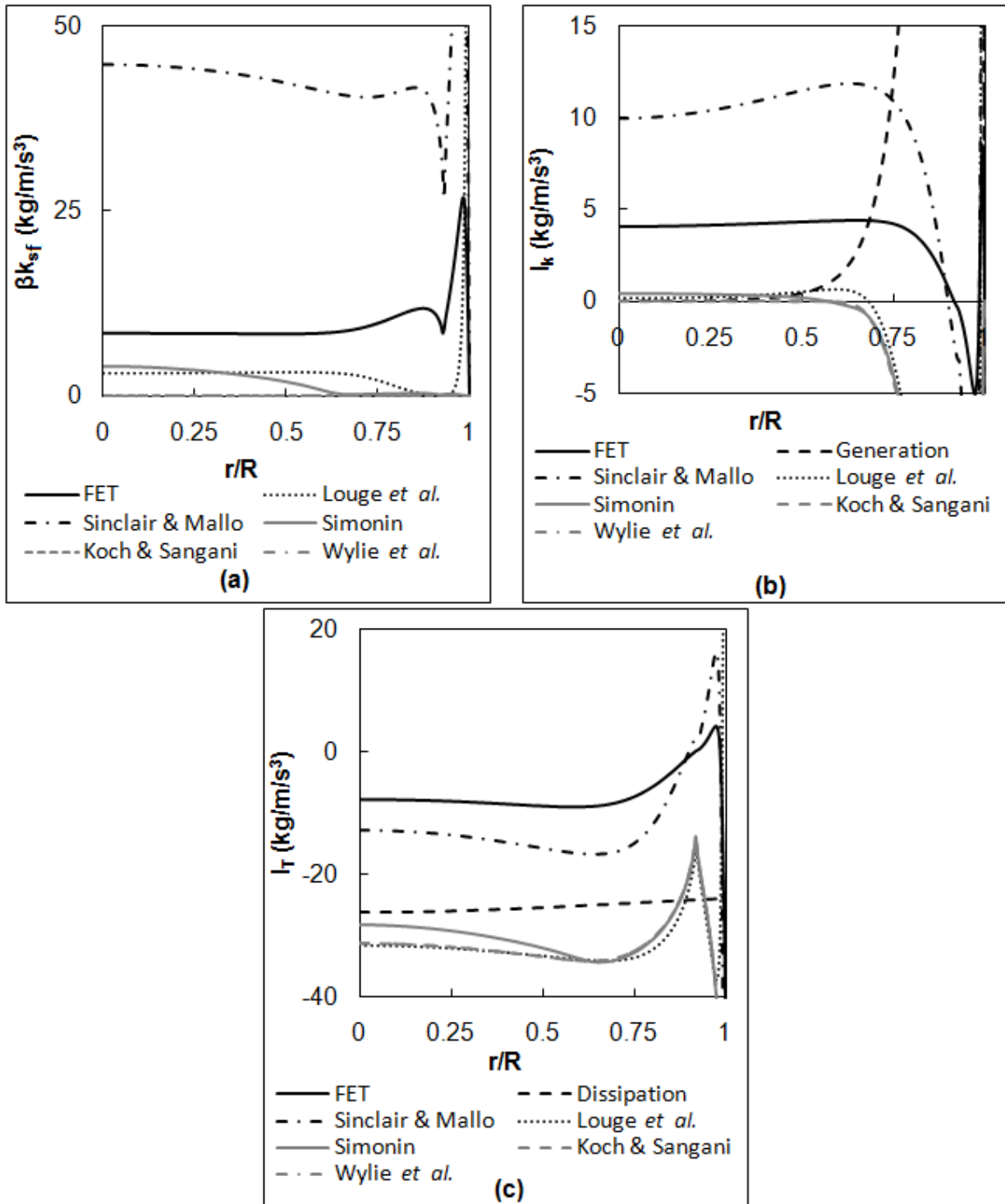


Figure 2-25. Comparing the magnitudes of βk_{sg} (a), I_k (b) and I_T (c) for the various interaction term models for the case of 243 μm particles with $m = 3.2^2$

Table 2-4. Percentage Error in Predicted Gas Velocity Fluctuations Using the Various Combinations of Different Interaction Terms and Velocity Cross Correlations

Interaction term	Cross Correlation	d = 243 μm			d = 500 μm			Average error%
		m=0.5	m=1.3	m=3.2	m=0.7	m=1.3	m=3.4	
FET	Sinclair & Mallo ⁴⁴	3.65	9.14	5.10	1.03	4.30	2.58	4.30
TVBA	Louge <i>et al.</i> ⁶	5.49	8.97	17.57	4.11	6.84	16.70	9.95
TVBA	Koch & Sangani ⁴²	6.53	16.37	26.99	5.15	9.40	25.82	15.04
TVBA	Wylie <i>et al.</i> ⁴³	6.53	16.37	27.00	5.15	9.40	25.83	15.05
TVBA	Simonin ⁸	6.47	15.59	18.69	5.14	9.34	24.36	13.27
TVBA	Sinclair & Mallo ⁴⁴	3.03	11.22	11.42	1.44	3.02	7.86	6.33

Table 2-5. Percentage Error in Predicted Solid Velocity Fluctuations Using the Various Combinations of Different Interaction Terms and Velocity Cross Correlations

Interaction term	Cross Correlation	d = 243 μm			Average error%
		m=0.5	m=1.3	m=3.2	
FET	Sinclair & Mallo ⁴⁴	4.25	8.05	4.29	5.53
TVBA	Louge <i>et al.</i> ⁶	9.41	14.29	8.41	10.70
TVBA	Koch & Sangani ⁴²	10.29	15.29	9.56	11.72
TVBA	Wylie <i>et al.</i> ⁴³	10.29	15.29	9.56	11.72
TVBA	Simonin ⁸	10.22	15.24	9.32	11.59
TVBA	Sinclair & Mallo ⁴⁴	2.87	8.42	3.93	5.07

Table 2-6. Percentage error in predicted gas velocity fluctuations using the various drag relations

Models	d = 243 μm			d = 500 μm			Average error%
	m=0.5	m=1.3	m=3.2	m=0.7	m=1.3	m=3.4	
Wen & Yu ³⁹	3.65	9.14	5.10	1.03	4.30	2.60	4.30
Hill <i>et al.</i> ^{47, 48}	3.76	10.25	8.41	0.88	4.00	4.12	5.24
Syamlal and O'Brien ⁴⁹	3.65	9.05	4.34	1.01	4.22	2.30	4.10

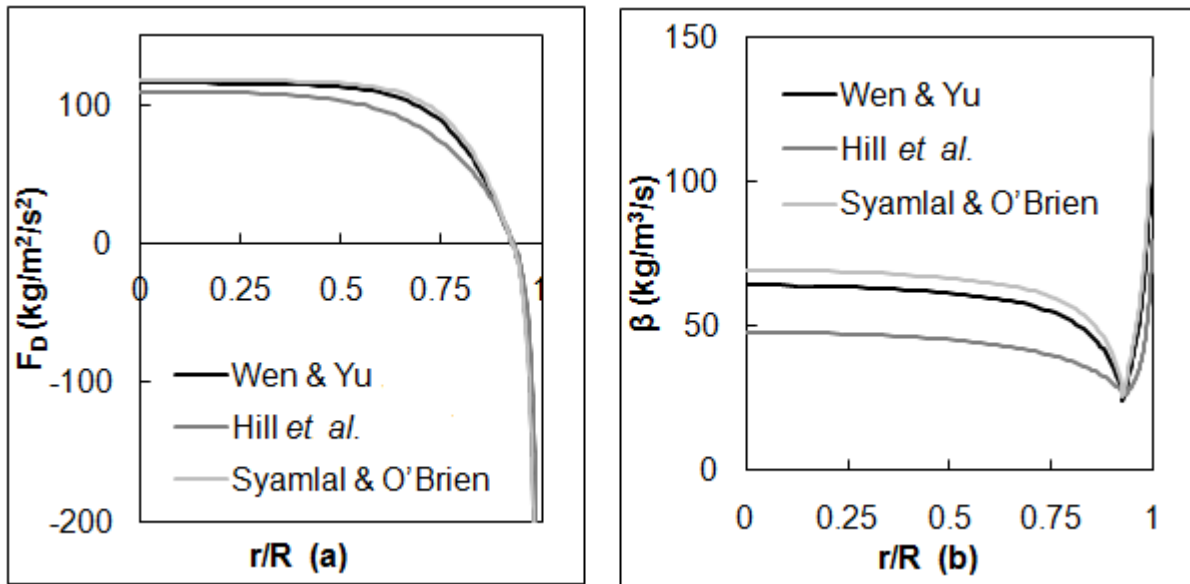


Figure 2-26. Comparing the magnitudes of F_D (a) and β (b) for the various drag models for 243 μm particles with $m = 3.2^2$

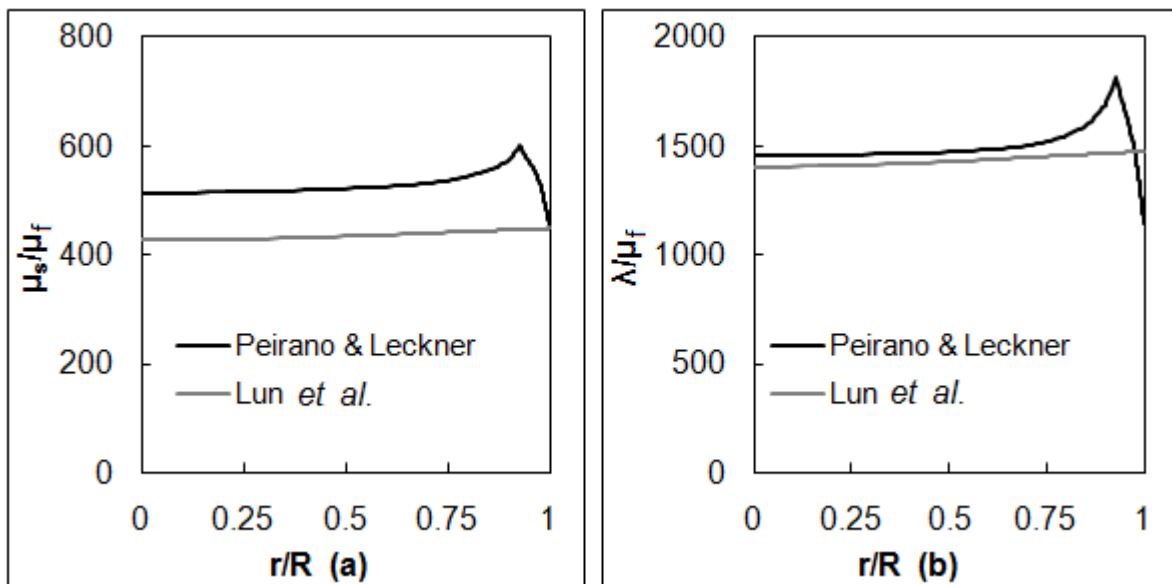


Figure 2-27. Comparing the magnitudes of μ_s/μ_f (a) and λ/μ_f (b) for the various solid stress models for 243 μm particles with $m = 3.2^2$

Table 2-7. Percentage error in predicted gas velocity fluctuations using the various solid stress closures

Models	d = 243 μm			d = 500 μm			Average error%
	m=0.5	m=1.3	m=3.2	m=0.7	m=1.3	m=3.4	
Peirano & Leckner ⁵¹	3.65	9.14	5.10	1.03	4.30	2.58	4.30
Lun <i>et al.</i> ⁵⁰	3.77	9.53	4.97	1.03	4.28	2.71	4.38

CHAPTER 3 FLUIDIZED DILUTE TURBULENT LIQUID-SOLID FLOW

Background

For slurry flows, their dynamic behavior and transportation is a frequent issue in the industry. Flow variables such as mean velocities, fluctuating velocities and volume fraction of both phases are necessary for understanding the physical processes involved and the energy distribution. However, for macro sized particles in a liquid, very little experimental data are available and even fewer modeling studies have been carried out. Reliable and detailed measurements of the two-phase flow behavior are difficult as intrusive techniques disrupt the flow, and due to the lack of data, model predictions cannot be validated.

For gas solid flows; Lee and Durst⁵, Tsuji *et al.*², and Sheen *et al.*⁴ used laser-Doppler velocimeter (LDV), a non-intrusive technique, to successfully measure mean and fluctuating velocities of both phases in a vertical pipe. In liquid-solid flow Alajbegovic *et al.*¹² also used laser-Doppler anemometer and a single-beam Y-ray densitometer to respectively measure the velocities and volume fraction of both phases accurately. Alajbegovic *et al.*¹² studied a system of water ($Re \sim 3 \times 10^4$) laden with ceramic particles of size 2.32 mm with density 2450 kg/m^3 and solid concentration of ~2-3% by volume, in a 30.6 mm diameter vertical pipe.

Pepple¹³ has carried out experiments with glass particles of size 0.5 and 1 mm, and density 2500 kg/m^3 . These particle were fluidized by water at $Re \sim 2 \times 10^5$ - 5×10^5 with a solid concentration ~ 0.7-3% by volume, in a vertical pipe of diameter 78 mm. LDV/Phase-Doppler particle analyzer (PDPA) was used to measure the axial mean and fluctuating velocities of the liquid and solid phases. The experiments performed herein,

extend the work of Pepple¹³. Glass particles of size 1.5 mm and density 2500 kg/m³ were studied in the same experimental setup as that of Pepple¹³ under similar operating conditions (Re ~ 2x10⁵-5x10⁵, solid concentration ~ 0.7-3% by volume and pipe diameter is 78 mm), although a different LASER setup was used. The data obtained in the present study along with the experiments performed by Alajbegovic *et al.*¹² and Pepple¹³ provide benchmarks data sets for a wide range of particle sizes which exhibit either viscous, transitional or collisional flow regimes.

The flow regime of fluid-solid flows depends upon the Stokes number (*ST*) of the particles.

$$ST = \frac{\tau_p}{\tau_f}, \quad (3-1)$$

where τ_p and τ_f are the particle and fluid response times, respectively.

$$\tau_p = \frac{\rho_s d^2}{18\mu_f}, \quad (3-2)$$

$$\tau_f = \frac{D}{V_{fzcl}}, \quad (3-3)$$

here ρ_s is the solid density, d is the particle diameter, μ_f is the intrinsic fluid viscosity, D is the pipe diameter and V_{fzcl} is the center line fluid velocity.

At low *ST* (small and light particles), the solid response time is smaller than the fluid response time, the particles tend to follow the fluid streamlines (Figure 3-1) and the two phase flow is considered to be in a viscous-dominated regime. Chen and Wood¹⁵ have described an Eulerian two-fluid model for dilute turbulent gas-solid flows in which particles tend to emulate the fluid motion.

At high ST , the particle response time is much larger than the fluid response time. The particles have large inertia and they tend to travel in straight lines (Figure 3-1) and collide with each other and the confining vessel. In this case, the flow is considered to be in inertia-dominated flow regime. Hadinoto and Curtis¹⁴ extended the work of Bolio *et al.*⁷ to include fluid lubrication effects and employed their gas-solid model to generate flow predictions corresponding to operating conditions in the liquid-solid data of Alajbegovic *et al.*¹².

Finally, at intermediate ST , particles neither follow the fluid, nor do they travel in straight lines, but instead their path is governed by both fluid eddies and particle inertia. Hence, in this case, particles have curved paths (Figure 3-1). To date no Eulerian two-fluid models have been proposed to describe this flow regime at intermediate ST .

In the present study, two-fluid gas-solid flow models are extended to predict liquid-solid flow behavior. The Chen and Wood¹⁵ model describes liquid-solid flows with low ST (viscous-dominated regime). An Eulerian two-fluid model using the combination of Syamlal and O'Brien⁴⁹ drag force relation, Peirano and Leckner⁵¹ solid stress description, and the FET (Chapter 2) interaction term describes liquid-solid flows with high ST (inertia-dominated regime). For the intermediate ST (transitional regime), a combination of the two-fluid models at the low and high ST limits describes these heterogeneous slurry flows. All the model solutions are validated against the benchmark data sets obtained in the present study and by Alajbegovic *et al.*¹².

Experimental Setup

Flow Loop

The experiments are carried out in a versatile pilot-scale flow loop system. The flow loop was designed in-house with capabilities to handle a wide range of particle

sizes and solid concentrations at very high velocities of about 7 m/s. Enormous amount of time was spent on troubleshooting the flow loop and ensuring the accuracy of the measurements¹³. Figure 3-2 presents the schematic of the flow loop. The loop is constructed with a nominal three inch (78 mm), schedule 40, and type 304, stainless steel pipe. Water from the storage tank can be circulated through the loop via a 50 hp centrifugal pump controlled by a variable frequency drive (ABB model number ACH550-UH-072A-4). The water is first pumped through a venturi eductor which when open entrains particles into the loop. An electromagnetic flow meter which can accurately measure the single-phase volumetric flow rate of the liquid is also installed in the loop. Next, the flow passes through the 3.84 m vertical pipe section and then through the borosilicate glass test-section, 0.91 m in length and an inner diameter of 78 mm. After that, the flow is deposited into a particle separator through a by-pass section (closed during normal operation) and a sampling tank (open during normal operation). A particle screen, mounted on top of the separator, allows only the water to overflow back into the storage tank, while the particles settle in the standpipe arrangement. If the eductor is open, the particles flow back into the loop, and if the eductor is closed the particles collect in the standpipe.

The liquid-solid flow can also be sampled for the purpose of determining the solid mass loading (m). To sample, during normal operation, the drain at the bottom of the sampling tank is closed so that the sample starts collecting in the sampling tank. Next, after a measured time interval, the flow is diverted directly to the particle separator using the by-pass. The volume of water in the tank is measured and the particles are filter out, dried and weighed. The ratio of the weight of the solids collected to the weight of the

water is equal to the mass loading. More information on the design and operation of the flow loop and details on the sampling technique are described in Pepple¹³.

PDPA System

A LDV/PDPA system, laser based non-intrusive technique accurately measures the instantaneous and time averaged velocities of both the fluid and particle phases, as well as the particle diameter with high spatial resolution. It is necessary for the particles to be perfect spheres to get accurate particle size data. The LDV/PDPA system uses an Argon-Ion laser (Spectra-Physics Stabilite 2017 6W laser) and a Bragg-cell to avoid directional uncertainty. The power of each of the probes is 40-50 mV for the laser. The transmitting and receiving optics and the real time signal analyzers are manufactured by TSI/Aerometrics. The transmitting and receiving optics are mounted on a traversing mechanism that can be positioned within 15 μm . A 363 mm focal length transmitting lens and a 300 mm focal length receiver lens are used for the LASER to measure the seed particles in the fluid phase.

Single-Phase Validation

Before two-phase measurements were carried out, single-phase validation is performed to establish a base case. Raw data obtained for the single-phase liquid fluctuating velocity¹³ at three different centerline velocities (3, 5 and 7m/s) are compared to the standard single-phase $k-\epsilon$ turbulence model in Figure 3-3a. There is a consistent difference between the raw data and the single-phase model prediction for the single-phase liquid flow that is not present in single phase gas flow⁵⁸.

Pepple *et al.*⁵⁹ have compared various benchmark measurements of single-phase flows published in the literature using a variety of experimental techniques (hot wire and LDV). The authors observe that there is considerable variation in the values of

single-phase gas and single-phase liquid fluctuating velocity amongst these commonly cited references. These variations exceed the generic errors associated with the measurement techniques. Furthermore, Pepple *et al.*⁵⁹ also show that the fluctuating velocities in water are consistently higher than the fluctuating velocities in air at the same Re. Additionally, the authors also conclude that, in air, the scaled turbulent velocity exhibits no dependency on Re far away from the wall, although the same is not true for water. In fact, in water, the scaled turbulent velocities increase as the Re increases.

In the present work, effects similar to that of Pepple *et al.*⁵⁹ were observed, but instead of changing the parameters of a well established single-phase $k-\epsilon$ turbulence model, all of the experimental data are multiplied by a constant factor of 0.85 to refine the data. Figure 3-3b compares the refined data to the single-phase $k-\epsilon$ turbulence model predictions. Thus, to be consistent, all of the two-phase data are also refined through multiplication with the constant factor of 0.85.

Particles and Laser Settings

Moving on to the two-phase data, soda-lime glass beads of size 1.5 mm (Jaygo Incorporated) in water are measured in this study. For these particles, two traverses across the pipe radius are required. The first measures the solid-phase and the second the fluid-phase. The 1.5 mm particles also require larger fringe spacing, a transmitting lens of focal length 762 mm, and a receiver lens of 1000 mm focal length for accurate size measurements. The relevant optical settings are summarized in Table 3-1. Further information on the optical settings, the LDV/PDPA system and the flow measurements are detailed in Pepple¹³.

Table 3-2 details the various operating conditions – including Stokes numbers, system parameters, and properties of the glass particles used in the present study as well as the ceramic particles in the study by Alajbegovic *et al.*¹².and the glass particles used by Pepple¹³. The values of the particle-particle coefficient of restitution (e) and particle-wall coefficient of restitution (e_w), defined in a liquid⁶⁰ and the value of specularity coefficient (ϕ) are also given in Table 3-2. 27 experiments (0.5 and 1mm, Pepple,¹³ and 1.5 mm, present study) were conducted. For each of the particle size, the mass loading was held constant while the fluid centerline velocity varied. Three mass loading levels (0.0175, 0.0425 and 0.0750) were investigated for each particle size. In Alajbegovic *et al.*¹² study three experiments were conducted, each with a different mass loading and centerline fluid velocity. The raw data for the 1.5 mm particles for the operating conditions described above is presented in Appendix B.

Two-Phase Data Validation

Four replicates were performed to gauge the reproducibility of the measurements of the solid velocity for the case of $d = 1.5$ mm with the operating conditions $m = 0.0425$ and $V_{fzcl} = 3$ m/s. Figure 3-4a shows that the deviation in the mean solid velocity is extremely small (~1%). But Figure 3-4b shows that the deviation in the fluctuating solid velocity is ~5% in the core of the pipe and at the wall it is ~10%. Near the wall, the laser light gets scattered and the resulting signal interferes with the signal from the particles leading to distortion of the velocity peak at the wall. Hence, the data near the wall needs to be sub-ranged appropriately. This sub-ranging may lead to the larger errors near the wall versus the core of the pipe.

Eulerian Two-Fluid Models for Dilute Turbulent Liquid-Solid Flows

The fluid and solid fluctuating velocity data for the 0.5 mm particles ¹³ ($ST \sim 3$) are approximately equal indicating that the particles follow the details of the fluid and hence exhibit viscous-dominated flow behavior. While, for 2.32 mm particles ¹², with $ST > 40$, the solid fluctuating data is lower than that of the fluid indicating an energy loss for the solid particles due to collisions. This exhibits inertia-dominated flow behavior. For the 1 mm ¹³ and 1.5 mm particles ($5 < ST < 30$) however, the solid fluctuating velocity is higher than that of the fluid exhibiting transitional behavior. Thus Stokes numbers 5 and 40 are assumed as the limits of the viscous and inertia regimes, respectively. The experimental data are described in detail in the results and discussion section of this Chapter.

High ST, Inertia-Dominated Flow Regime ($ST > 40$)

The continuum equations for the Eulerian model description of a dilute turbulent liquid-solid flow model are being based on the gas-solid model discussed in Chapter 2. Equation 2-1 to equation 2-6 describe the continuum equations used for the liquid solid flow. The liquid-phase stress τ_{rz} is also described in the same fashion as that for the gas-solid flow (Chapter 2, Mathematical Model, Fluid Stress). The drag force (F_D) equation 2-14 is still valid for the case of liquid-solid flow and for the drag coefficient β is computed using the Syamlal and O'Brien ⁴⁹ (equation 2-30 to equation 2-34) drag relation. For the case of high ST in liquid-solid flow, granular kinetic theory is still applicable and hence, Peirano and Leckner ⁵¹ can be used for computing granular energy dissipation (γ , equation 2-35 to equation 2-38), solid-phase stresses (σ_{rz} , equation 2-46, σ_{rr} and $\sigma_{\theta\theta}$, equation 2-43 to equation 2-45) and granular energy flux

(q_{pTr} , equation 2-47). Equation 2-57 to equation 2-51 are used for calculating μ_s and equation 2-53 to equation 2-64 are used for calculating λ . Finally, the fluctuating interaction terms (I_k and I_T) are based on the FET model (Chapter 2, Mathematical Model, Fluctuating Interaction term) and the liquid solid fluctuating velocity cross-correlation is based on the Sinclair and Mallo⁴⁴ model (equation 2-88).

Liquid solid flows exhibit the phenomenon of vortex shedding at larger Re_p than the gas-solid flow. The only experimental data, of liquid-solid flow, which exhibits vortex shedding has the operating conditions $d = 2.32$ mm, $V_{fzcl} = 1.81$ m/s, $m = 0.0556$ ¹² and $Re_p \sim 540$. The rest of the experimental conditions have Re_p less than 500 and do not exhibit vortex shedding. The Lun⁵³ vortex shedding model is modified for the liquid-solid flow as,

$$E_w = 12 \frac{C_w \mu_t k}{d^2}, \quad (3-4)$$

$$Re_p = \frac{\rho_f d |V_{fz} - V_{sz}|}{\mu_f}, \quad (3-5)$$

$$\mu_t = 0.017 Re_p \mu_f \text{ for } Re_p \geq 500, \quad (3-6)$$

$$C_w = 10/3 \text{ for } Re_p \geq 500. \quad (3-7)$$

For the high ST cases, the boundary conditions follow the gas-solid model (Chapter 2, Boundary Conditions). The fluid centerline velocity (V_{fzcl}) is used as the operating condition for the fluid-phase, and for the solid-phase, solid mass loading m is used as the operating condition.

For the high ST model the solid volume fraction (ν) is calculated from r-component of the solid-phase momentum balance equation (equation 2-3) as the equation of continuity for the solid phase yields a redundant equation.

Low ST , Viscous Dominated Flow Regime ($ST < 5$)

In two phase flows with low ST model, particles are affected by the details of the fluid motion, and particles do not move in straight lines through turbulent eddies. Hence, granular kinetic theory is not appropriate to describe solid-phase fluctuations and the resulting solid-phase stresses. Rather, since the particles follow the details of the fluid motion, it is reasonable to assume that the fluid fluctuations and the solid fluctuations are similar.

$$T \approx k. \quad (3-8)$$

The experimental data obtained in the Peppke¹³ validate this assumption.

In the case of low Stokes number flow, the Chen and Wood¹⁵ expressions can be applied to describe the solid-phase viscosity and the corresponding solid-phase shear stress.

$$\mu_s = \mu_{ef} + \frac{\mu_T}{\left(1 + \frac{\tau_p}{\tau_e}\right)}, \quad (3-9)$$

where τ_e is the time scale of the fluid eddy,

For the fluctuation interaction term l_k , the Chen and Wood¹⁵ equations are also followed.

$$l_k = (1 - \nu)\beta(2k - k_{sf}), \quad (3-10)$$

where k_{sf} is the fluid-solid velocity cross-correlation,

$$k_{sf} = 2k \exp\left(-0.0825 \frac{\tau_p}{\tau_e}\right). \quad (3-11)$$

In the case of low ST flow, the solid continuity equation of Chen and Wood¹⁵ reveal that the solids volume fraction is not a function of the radial position. Hence, the

solids mass loading operating condition (equation 2-105) can be solved to yield the constant value for the solid volume fraction.

$$\frac{(1-\nu)}{\nu} = \frac{\rho_s \int V_{sz} r dr}{m \rho_f \int V_{fz} r dr}, \quad (3-12)$$

which can be rewritten as,

$$\nu = \frac{1}{\left(1 + \frac{\rho_s \int V_{sz} r dr}{m \rho_f \int V_{fz} r dr} \right)}. \quad (3-13)$$

The mean fluid and solid velocities as well as the fluid-phase turbulence, follow the no slip condition at the wall.

Intermediate ST, Transitional Flow Regime ($5 < ST < 40$)

For intermediate ST flow, there are no published modeling studies. For this regime, the modeling framework is similar to the high ST case. However, modifications are made to the granular dissipation (γ), the solid-phase viscosity (μ_s), the solid-phase conductivity (λ) and the time scale for fluctuation energy transfer (τ_{sf}) since traditional granular kinetic theory as originally developed is not fully appropriate to describe the details of the solid motion in this flow regime. While the particles in this regime do have some degree of inertia, it is not large and hence the loss of energy on collisions is not that high. Thus, in the intermediate Stokes number regime, the granular dissipation (γ) is set to zero.

$$\gamma = 0. \quad (3-14)$$

The solid viscosity and the solid conductivity are obtained by using a ST weighted combination of their respective expressions from the low ST model¹⁵ and the high ST model⁵¹.

$$\mu_s = \left(\frac{40 - ST}{40 - 5} \right) \left[\mu_{ef} + \frac{\mu_T}{\left(1 + \frac{\tau_p}{\tau_e}\right)} \right] + \left(\frac{ST - 5}{40 - 5} \right) \left[\nu \rho_s (G_{2k} + G_{2c}) \right], \quad (3-15)$$

$$\lambda = \left(\frac{40 - ST}{40 - 5} \right) \left[\mu_{ef} + \frac{\mu_T}{\sigma_k \left(1 + \frac{\tau_p}{\tau_e}\right)} \right] + \left(\frac{ST - 5}{40 - 5} \right) \left[\nu \rho_s (G_{3k} + G_{3c}) \right]. \quad (3-16)$$

For the time scale for fluctuation energy transfer, a modified expression of the high ST model is developed based on the available experimental data in the intermediate ST flow regime (1 mm and 1.5 mm particles).

$$\frac{\rho_f}{\tau_{sf}} = \left(6.7 * 10^{-7} \text{Re} - 37 \frac{d}{D} + 0.62 \right) (1 - \nu) \beta, \quad (3-17)$$

here Re is the flow Reynolds number

$$\text{Re} = \frac{V_{fzcl} \rho_f D}{\mu_f}. \quad (3-18)$$

The closure for the FET time scale (equation 3-17) is proposed such that, as the diameter of the particle increases, at a constant m and V_{fzcl} , the difference between the fluid and solid fluctuations increase. Also, upon increasing the operating Re , at a constant d and m , the difference between the fluid and solid fluctuating velocity decreases. By including the drag coefficient β in the FET time scale, a mass loading dependency is also obtained. This dependency is such that on increasing the mass

loading, at a constant d and V_{fzcl} , the difference between the fluid and solid fluctuations decreases. All of these qualitative trends are consistent with experimental observations.

Looking to the granular energy balance, the dissipation rate is set to zero, the solid-phase strain is small, and hence the generation term $\left(\sigma_{rz} \frac{\partial V_{sz}}{\partial r} \right)$ is small. Flow predictions in the intermediate ST regime strongly depend on I_T and, consequently, they are dependent on $\frac{\rho_f}{\tau_{sf}}$.

Finally, the solid volume fraction is similarly based on a ST weighted combination of the resulting profiles from the low ST model (equation 3-13) and the high ST model expressions (equation 2-3, where solid-phase normal stress are computed using ⁵¹).

$$v^{\text{Intermediate } ST} = \left(\frac{40 - ST}{40 - 5} \right) \frac{1}{\left(1 + \frac{\rho_s \int V_{sz} r dr}{m \rho_f \int V_{fz} r dr} \right)} + \left(\frac{ST - 5}{40 - 5} \right) v^{\text{High } ST}. \quad (3-19)$$

The boundary conditions applied for intermediate ST flow are similar to those for high ST flow. The only change is that the solid-phase stress and conductivity that appear in the solid velocity and granular temperature boundary condition follow equations 3-15 and 3-16 for the intermediate ST flow as mentioned above.

Table 3-3 presents a summary of the model equations and constitutive relations for the high, low and intermediate ST cases.

Results and Discussion

In Chapter 2 (Results and Discussion), for gas-solid flows it is assumed that fluctuations in velocity are isotropic in all directions for the solid phase, and for the fluid phase the radial and azimuthal fluctuations in velocity v_{fr}' and $v_{f\theta}'$ respectively, are

approximately half of the axial velocity fluctuations. Similar assumptions are made for the liquid-solid flow cases too. Thus enabling the computation of the solid and fluid fluctuating velocities from T (equation 2-106) and k (equation 2-108) profiles, respectively.

Once the axial fluctuating velocity profiles are related to the corresponding k and T profiles, the flow predictions can be directly compared to the experimental data.

High ST , Inertia-Dominated Flow Regime

As indicated in Table 3-2, the data of Alajbegovic *et al.*¹² with $ST > 40$ falls in the inertia-dominated flow regime. Figure 3-5 compares the predicted mean velocities of the fluid and solid phases from the high ST model to the Alajbegovic *et al.*¹² data, while Figure 3-6 compares the fluctuating velocities for the liquid and solid phases.

From the data for the high ST conditions, a visible slip between the mean velocities of the liquid and solid phases (Figure 3-5) is clearly observed. This is indicative of the significant inertia the large particles ($d = 2.32\text{mm}$). The Syamlal and O'Brien⁴⁹ drag force relation captures the slip between the two phases for all the three operating conditions fairly well. In Figure 3-6 the experimental data further indicates that the granular temperature is lower than the liquid-phase turbulence. In the inertia dominated regime, particles with large inertia on collision lose energy, the granular dissipation increases, and, as a result, the granular temperature reduces. The application of the Peirano and Leckner⁵¹ model not only captures the reduction of the granular temperature, but also the shape of the T -profile for all the three operating conditions. This significant slip velocity and reduction of granular temperature are not seen in the experimental data for the viscous or transitional flow regimes.

Low ST, Viscous-Dominated Flow Regime

From the experimental data of 0.5 mm particles¹³ ($ST < 5$), the flow is anticipated to be in viscous-dominated flow regime. Experimental data for the three centerline fluid operating conditions and the highest mass loading conditions, in the core of the pipe, was difficult to obtain (Figure 3-7) since the particle number density associated with these mass loadings was very large, leading to poor signal quality and extremely low data rate. From Figure 3-7, it can be observed that there is marginal slip between the mean liquid and solid phase velocities which is correctly captured by the low ST model. Furthermore, the fluid velocity fluctuation essentially match the solid velocity fluctuation for all of the nine operating conditions (Figure 3-8), indicating that the particles are following the details of the fluid motion. The magnitude and the shape of mean and fluctuating velocity profiles for both phases at all nine operating conditions are well predicted by the Chen and Wood¹⁵ model. In addition, both the experimental data and the flow predictions reveal that there is very little effect on the magnitude and shape of the mean and fluctuating velocities as solid loading is increased from 0.0175 to 0.075 at a constant fluid centerline velocity. Additionally, as the centerline fluid velocity is increased at a constant mass loading, and the magnitude of the liquid and solid velocity fluctuations increase (Figure 3-8). These trends are similar to those observed in single-phase fluid flow.

Intermediate ST, Transitional Flow Regime

Operating conditions associated with the 1 mm¹³ and 1.5 mm particles have ST between 5 and 40, and exhibit transitional flow behavior. Figure 3-9 ($d = 1$ mm) and Figure 3-11 ($d = 1.5$ mm) present the experimental data and model predictions for the mean fluid and solid velocities of 1 mm and 1.5 mm particles, respectively. Figure 3-10

and Figure 3-12 present the corresponding fluctuating fluid and solid velocities.

Although there is a small slip in the mean velocity between the two phases (Figure 3-9 and Figure 3-10) large difference in magnitude in the solid and fluid velocity fluctuations exists (Figure 3-10 and 3-12).

For the 1mm particles, as the solids loading is increased from 0.0175 to 0.075 at a constant velocity, minimal change is seen in the mean velocity profiles (Figure 3-9). However, the magnitude of the difference in velocity fluctuations of both phases tends to decrease with the increasing mass loading (Figure 3-10). As the centerline fluid velocity is increased at constant mass loading, there is no trend in the fluid and solid velocity fluctuations. In most cases, the difference in magnitude between the fluctuation velocities of the two phases decreases while in some cases the difference increases.

The mean velocity behavior of the 1.5 mm particles (Figure 3-11) is similar to that of the 1 mm particles. The solid velocity fluctuations associated with the 1.5 mm particles are significantly larger than those associated with the 1 mm particles and greatly exceed the magnitude of the fluid velocity fluctuations. As the solids mass loading is increased from 0.0175 to 0.075 at a constant velocity, the experimental data show that the magnitude and difference between the velocity fluctuations of both phases changes minimally (Figure 3-12). Also, as the centerline fluid velocity is increased at a constant mass loading, the magnitude of the velocity fluctuations for both phases increases, but the difference between the velocity fluctuations of both phases remains the same (unlike the 1 mm particles).

As the particle size is increased from 0.5 mm to 1mm¹³ and finally to 1.5 mm (at constant m and V_{fzcl}), minimal changes are observed in the mean velocity profiles

(Figure 3-7, 3-9 and 3-11). In fact, in all three cases, marginal slip is observed because the Re is very high. Hadinoto *et al.*⁶¹ experiments showed that as the Re is increased, the slip velocity reduced. This effect is also seen in Alajbegovic *et al.*¹² data (Figure 3-5) and the model also shows same behavior. On the other hand, the fluctuating velocities of both phases show different behavior for the different particle sizes. For the 0.5 mm particles there is no difference between the fluctuating velocities of both phases, while this difference increases dramatically as the particle size increases from 0.5 mm to 1 mm¹³ and then to 1.5 mm with the solid velocity fluctuations exceeding the fluid velocity fluctuations. For the 2.32 mm particles¹², however, the solid velocity fluctuations are lower than that of the fluid.

As mentioned earlier, model predictions in the transitional flow regime are strongly dependent on I_T . The closure proposed for I_T (equation 3-17) is consistent with the following observed flow behaviors:

- As the particle diameter increases, at constant m and V_{fzcl} , the difference between the fluid and solid fluctuations increases
- As the flow Re of flow increases, at constant d and m , the difference between the fluid and solid fluctuations decreases
- As the mass loading increases, at constant d and V_{fzcl} , the difference between the fluid and solid fluctuations decreases. In the fluctuating interaction term, the dependency on the mass loading is through drag coefficient β

Although the model predictions for the magnitude of the solid velocity fluctuations are not in perfect agreement with the experimental measurements, the intermediate ST model is able to capture the shape of the solid velocity fluctuation profile. This agreement indicates that the weighted expressions for the solid-phase viscosity and

conductivity (which govern the shape of this profile) in equation 3-15 and 3-16 work well in this intermediate ST flow regime.

Summary

There are many practical difficulties and limitation due to which accurate measurement of data for liquid-solid turbulent flows is difficult. In this study, LDV/PDPA is used to measure the mean and fluctuating velocity of solid and liquid phases in a versatile, pilot-scale flow loop. The flow loop setup can be used to for measuring flow properties of a wide range of particles (0.5 and 1 mm, Pepple¹³, and 1.5 mm, present study) at a variety of flow rates ($V_{fzcl} = 3$ m/s to 7m/s). The data obtained herein along with the data of 2.32 mm particles¹² and in Pepple¹³ span all three flow regimes (viscous, inertia and transitional flow regimes). The Eulerian two-fluid model for dilute turbulent gas-solid flows with particle-particle interaction described in Chapter 2 is used for predicting velocity profiles of the flows in the inertia dominated regime, Chen and Wood¹⁵ model is used to describe flow in the viscous dominated flow regime, and a bridge model (using expressions from the high and low ST model) is proposed for the transitional flow regime. The predictions obtained for all three regimes compare well against the experimental data

In the industry, generally the solid concentration is ~ 5% by volume for slurries, however the laser based setup can only measure a solid concentration up to 3% by volume, due to signal attenuation and low data rate. Efforts are been made to acquire data for higher mass loading conditions by matching the refractive indices of the liquid and solid phases. Even then, acquiring detailed data for dense liquid-solid flow (solid concentration > 10% by volume) using LDV based technique is difficult. Hence in the present work, dense fluid-solid flows are not studied. Dense fluid-solid flows transition to

fluidized beds at low operating velocities. Fluidized beds have many industrial applications (Chapter 1). Some aspects of fluidized beds have also been studied in Chapter 4 and Chapter 5.

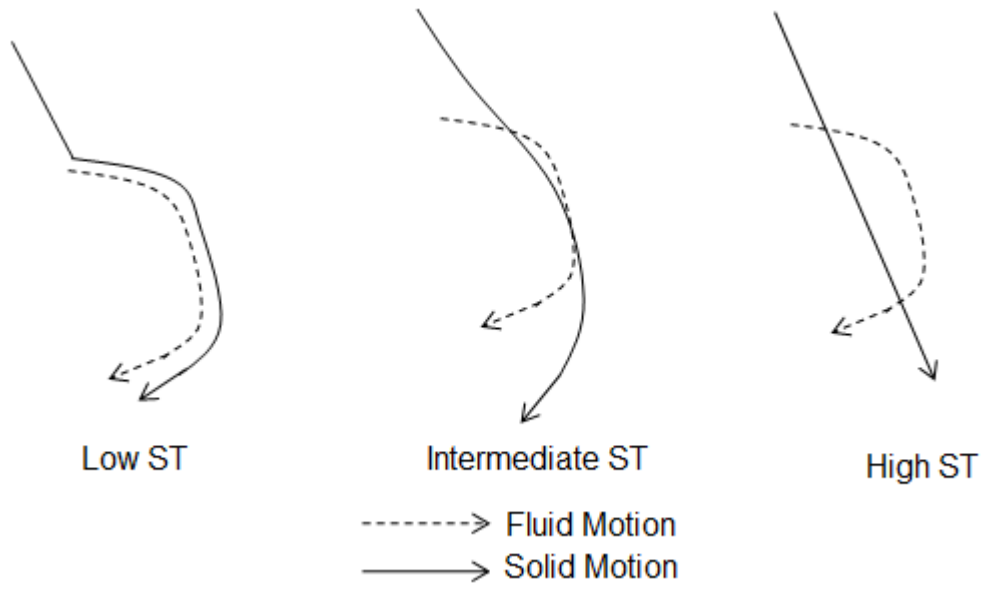


Figure 3-1. Effect of ST on the solid path in the fluid

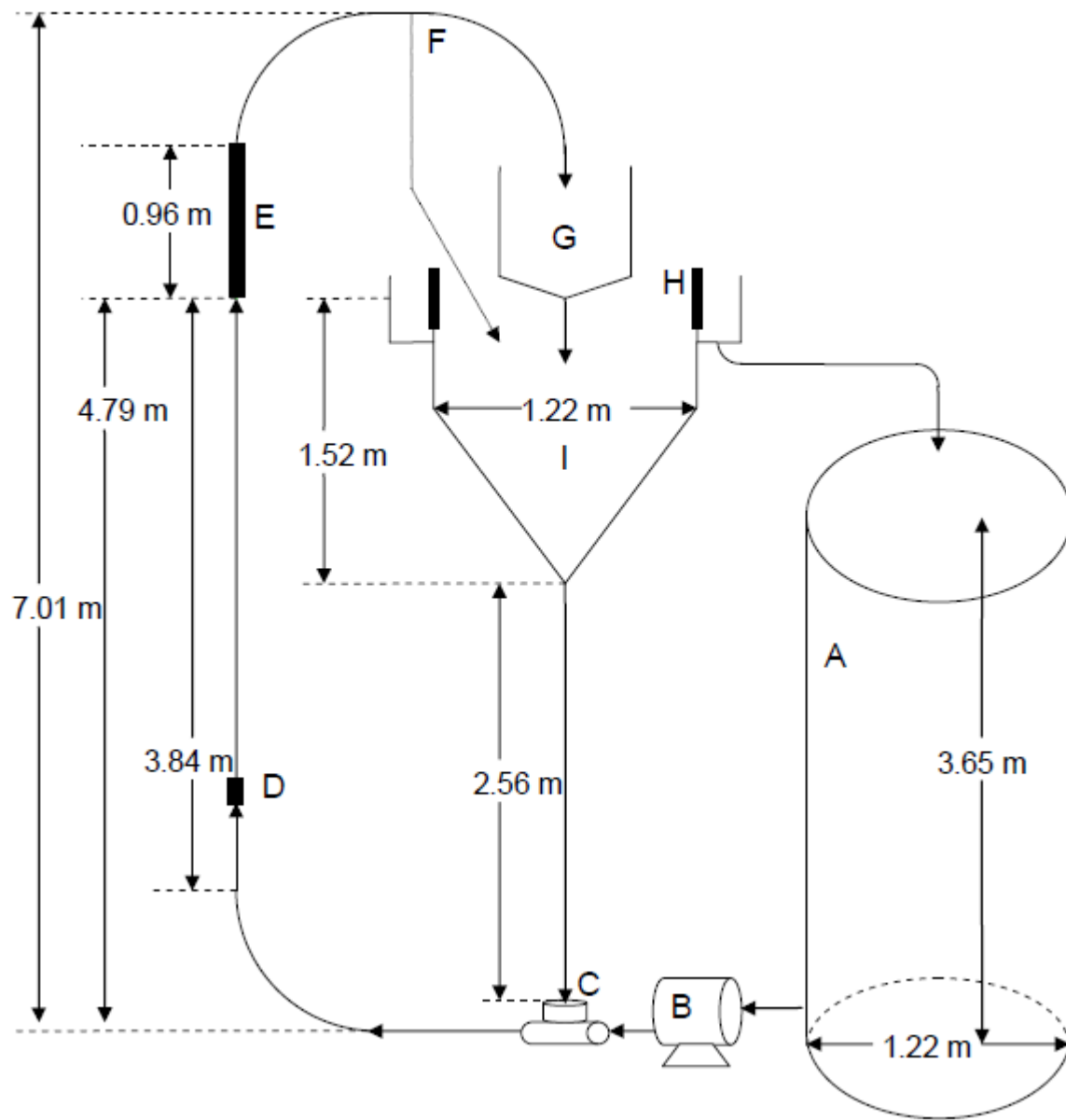


Figure 3-2. Flow loop (A) water tank (B) pump (C) venturi eductor (D) electromagnetic flow meter (E) test section (F) by-pass (G) sampling tank (H) particle screen (I) particle separator (modified from the original in Pepple¹³)

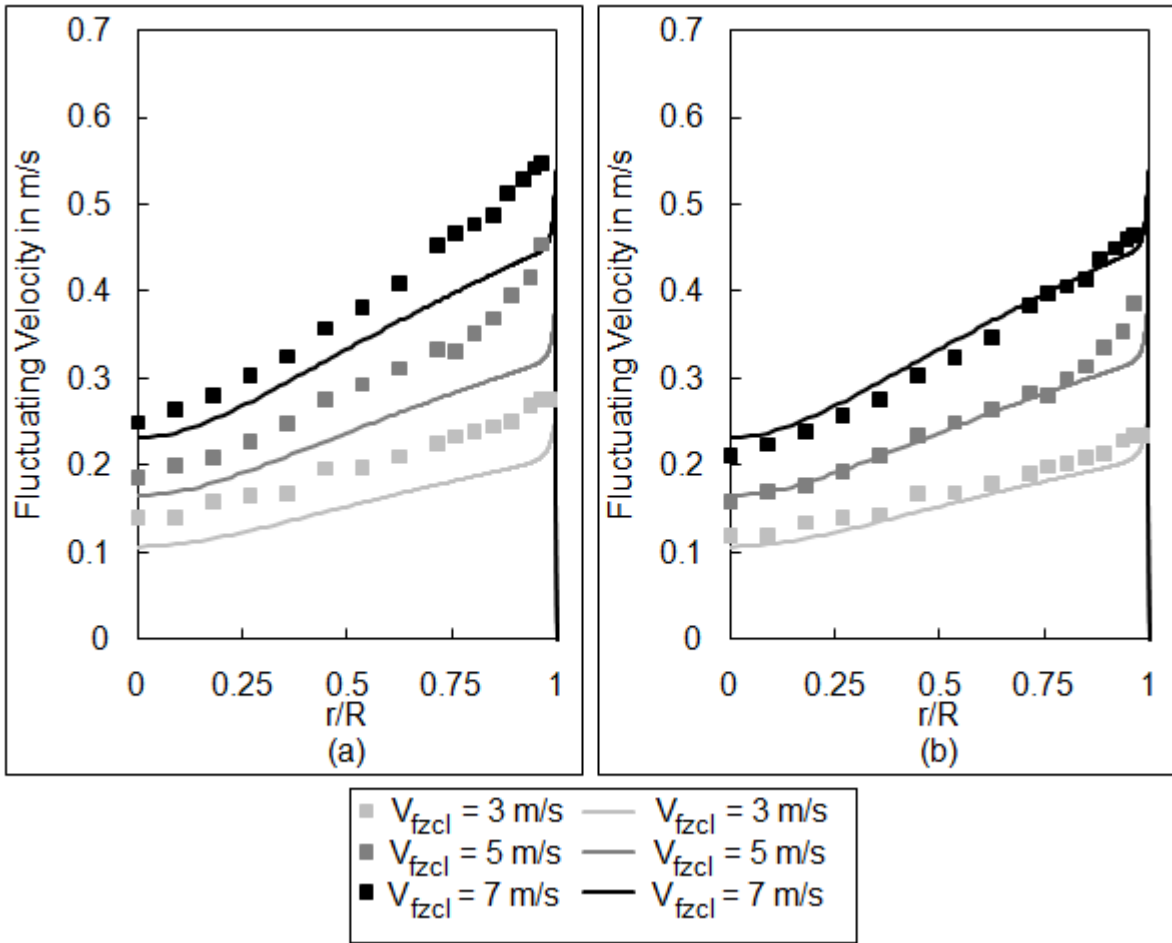


Figure 3-3. Comparing single-phase fluctuating velocity ¹³ to the single-phase $k-\epsilon$ turbulence model ($v'_{fz} = \sqrt{k}$) (a) raw data (b) refined data using the 0.85 factor

Table 3-1. PDPA settings

LASER setup	Liquid < 0.2 mm	Glass 1.5 mm
Transmitting Optics		
Wavelength (nm)	514.5	514.5
Focal Length (mm)	363	762
Fringe Spacing (μm)	3.7	7.8
LASER Beam Diameter (mm)	2.65	2.65
LASER Beam Intersection Angle	7.97	3.78
LASER Beam Separation (mm)	50	50
LASER Beam Waist (μm)	89.7	188
Probe Volume Length (mm)	1.29	5.71
Probe Volume Height (mm)	0.090	0.188
Probe Volume Width (mm)	0.090	0.188
Receiving Optics		
Focal Length in air (μm)	300	1000
Slit Aperture (μm)	150	150
Collection Angle	150	150
Software Setting		
High Pass Filter (MHz)	20	20
Frequency Shift (MHz)	36	36
Sampling Rate (MHz)	10, 20	10, 20
Low Pass Filter (MHz)	5, 10	5, 10
Burst Threshold (mV)	0.2	0.2

Table 3-2. Summary of experimental data

Data	Density kg/m ³	Size mm	Mass Loading (<i>m</i>)	<i>V_{fzcl}</i> in m/s			<i>R</i> mm	<i>~ST</i>	Regime
				Case					
				1	2	3			
Pepple ¹³	2500	0.5	0.0175	3.12	4.93	7.14	78	1.44	Viscous
			0.0425	3.17	5.10	7.03		2.30	Viscous
			0.0750	3.17	5.10	7.30		3.27	Viscous
	2500	1	0.0175	3.11	5.04	7.06	78	5.66	Transitional
			0.0425	3.02	5.03	7.04		8.98	Transitional
			0.0750	3.16	4.68	6.83		12.8	Transitional
Present Study	2500	1.5	0.0175	3.12	5.04	7.00	78	12.5	Transitional
			0.0425	2.97	4.91	7.05		20.5	Transitional
			0.0750	3.04	5.04	7.02		28.9	Transitional
Alajbegovic <i>et al.</i> ¹²	2450	2.32	0.0556		1.81		30.6	43.4	Inertial
			0.0584		2.33			55.8	Inertial
			0.0670		2.83			67.8	Inertial

For all cases: $\mu_f=0.001$ Ns/m², $\rho_f=1000$ kg/m³, $v_o=0.65$, $e=0.54$, $e_w=0.54$, $\phi=0.002$

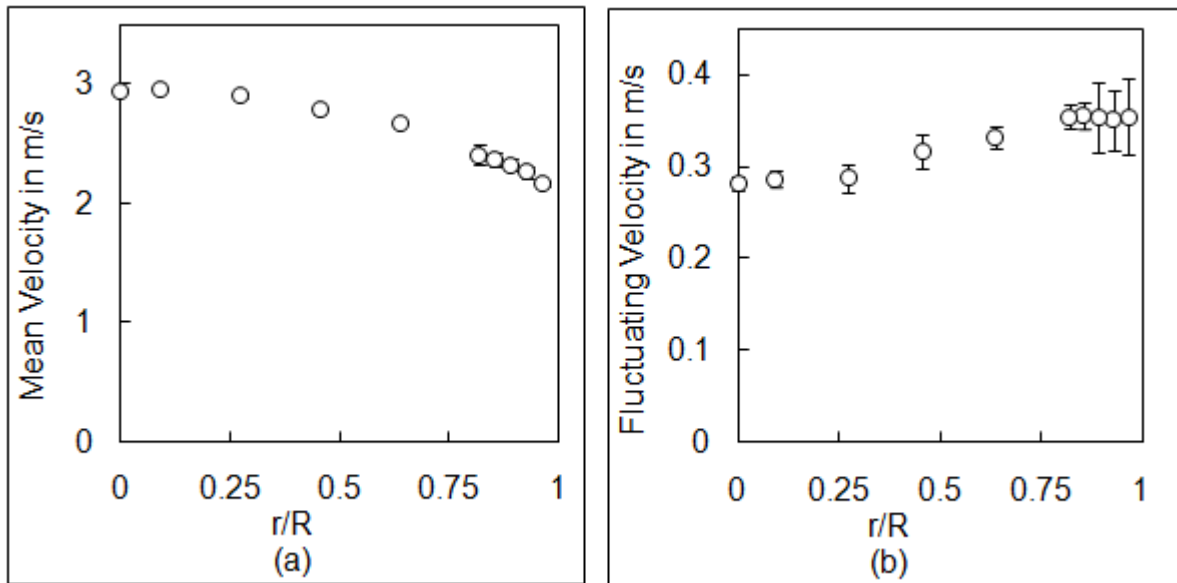


Figure 3-4. Solid fluctuating velocity measurement for $d = 1.5$ mm, $m = 0.0425$ and $V_{fzcl} \sim 3$ m/s (averaged over four runs)

Table 3-3. Summary of model equations in the high, low and intermediate *ST* flow regimes

Variable	High <i>ST</i>	Low <i>ST</i>	Intermediate <i>ST</i>
ν	Eq. 2-3	Solid-phase continuity equation (Chen & Wood ¹⁵)	Eq. 3-19
V_{fz}	Eq. 2-1	Eq. 2-1	Eq. 2-1
V_{sz}	Eq. 2-2	Eq. 2-2	Eq. 2-2
k, ε	Eq. 2-5, Eq. 2-6	Eq. 2-5, Eq. 2-6	Eq. 2-5, Eq. 2-6
T	Eq. 2-4	Eq. 3-8	Eq. 2-4
γ	Eq. 2-35	NA	Eq. 3-14
μ_s, λ	Peirano & Leckner ⁵¹	Eq. 3-9, NA	Eq. 3-15, Eq. 3-16
l_k, l_T	Eq. 2-102, Eq. 2-103	Eq. 3-10, NA	Eq. 2-102, Eq. 2-103
ρ_s/τ_{sf}	ρ_s/τ_D for $40 < ST < 100$ ρ_s/τ_c for $ST > 100$ (FET model)	β	Eq. 3-17
k_{sf}	Eq. 2-86	Eq. 3-11	Eq. 2-86

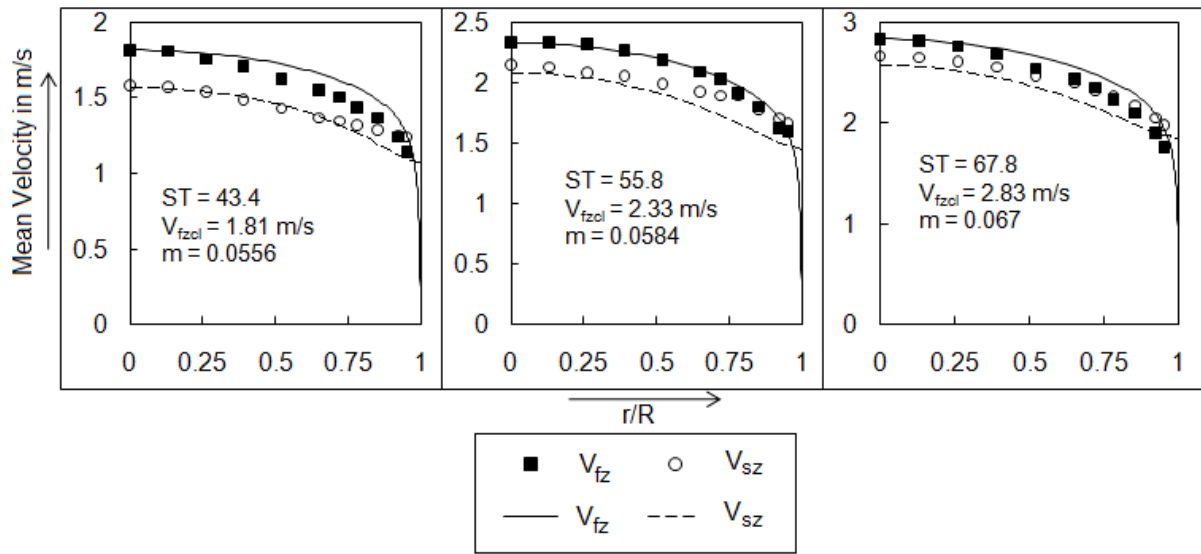


Figure 3-5. Mean velocity (V_{fz} and V_{sz}) measurement for $d = 2.32$ mm¹² compared to flow predictions for high ST case

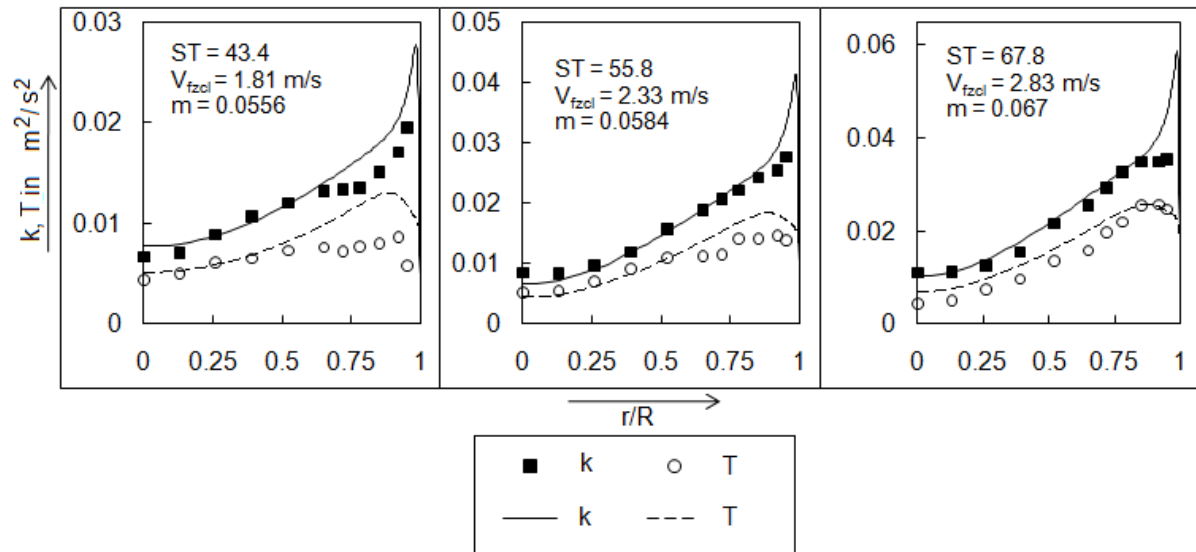


Figure 3-6. k, T measurements for $d = 2.32$ mm¹² compared to flow prediction for high ST case

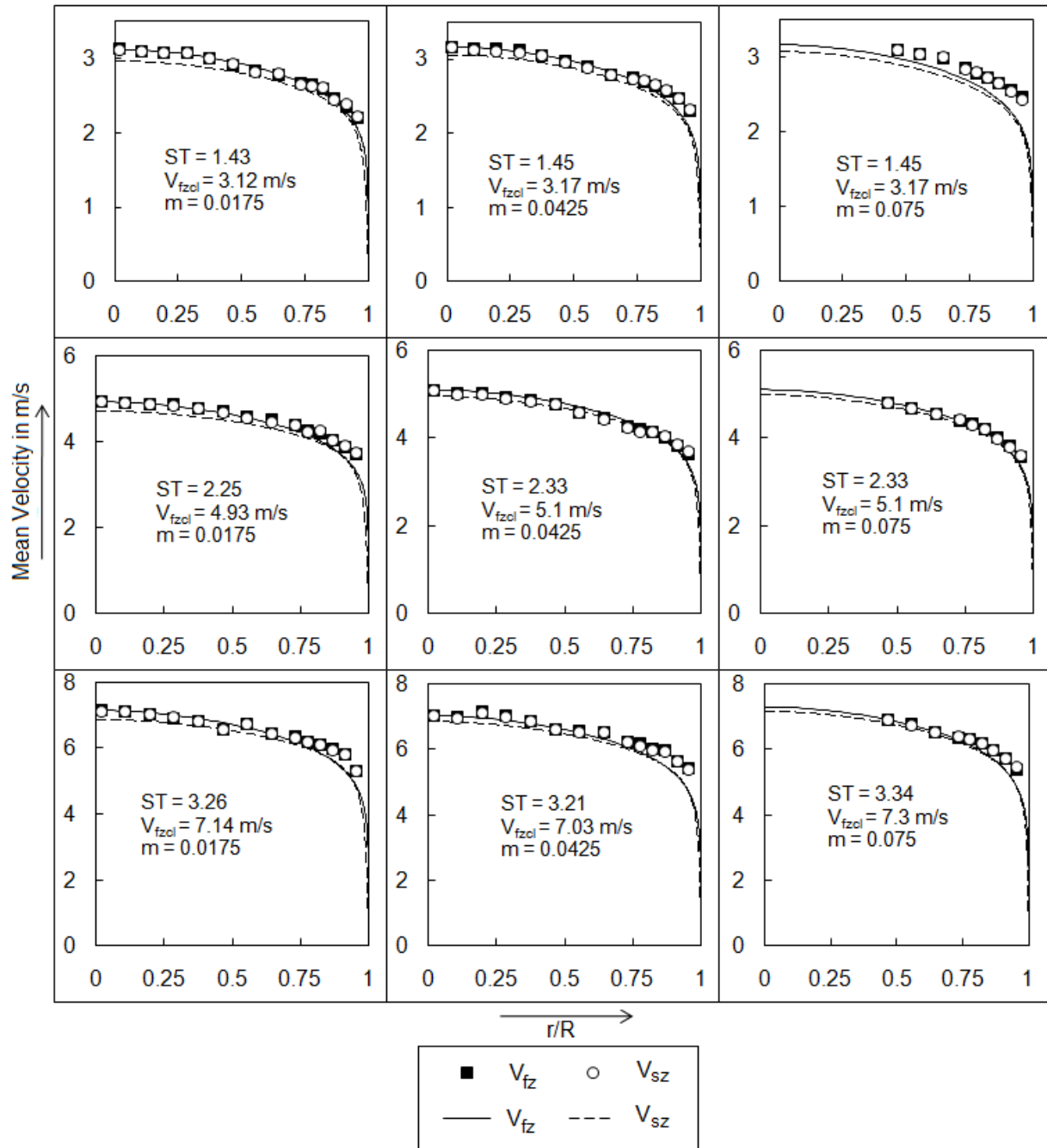


Figure 3-7. Mean velocity (V_{fz} and V_{sz}) measurements for $d = 0.5$ mm¹³ compared to flow predictions for low ST case

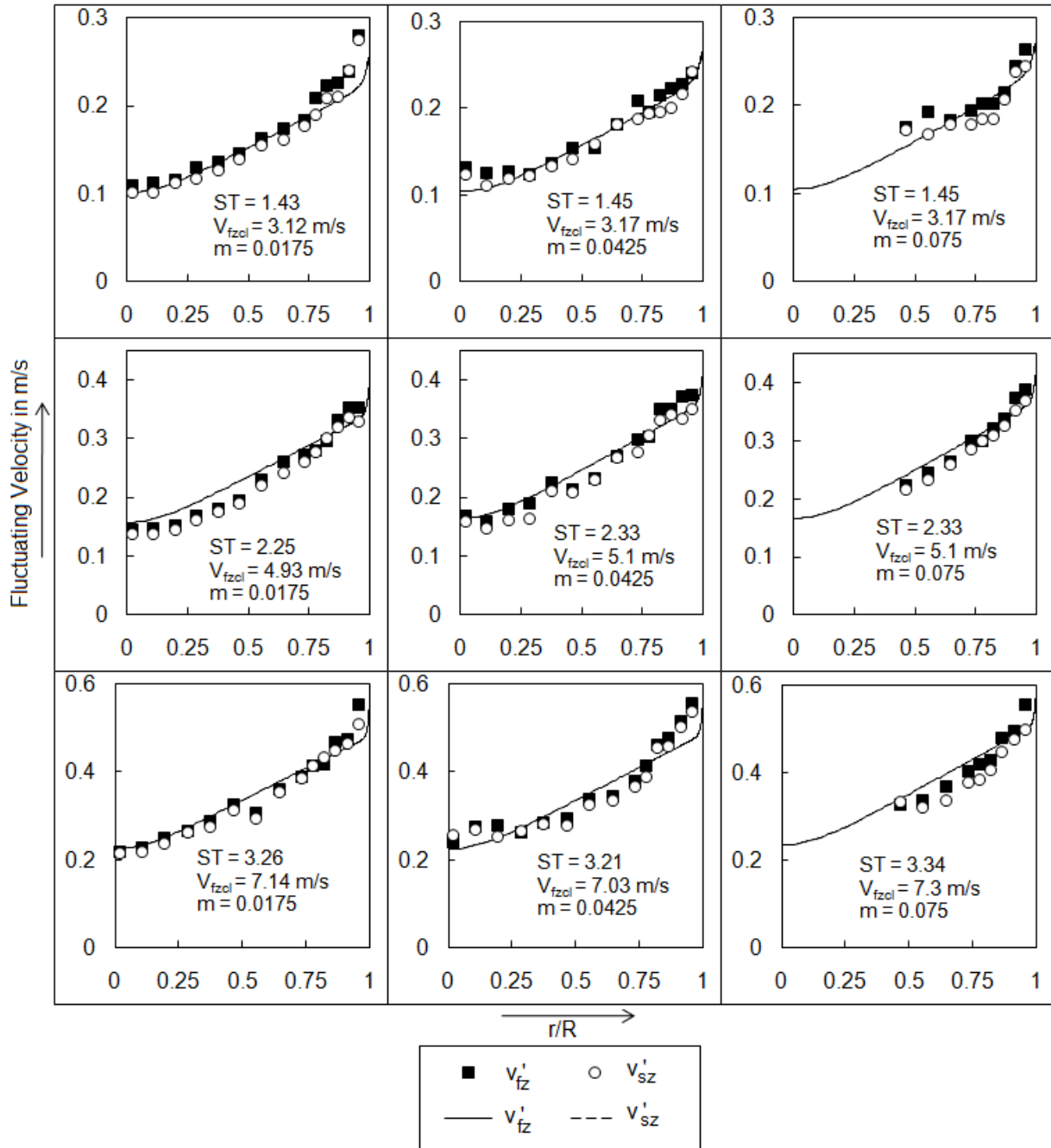


Figure 3-8. Fluctuating velocity (v'_{fz} and v'_{sz}) measurements for $d = 0.5$ mm¹³ compared to flow predictions for low ST case

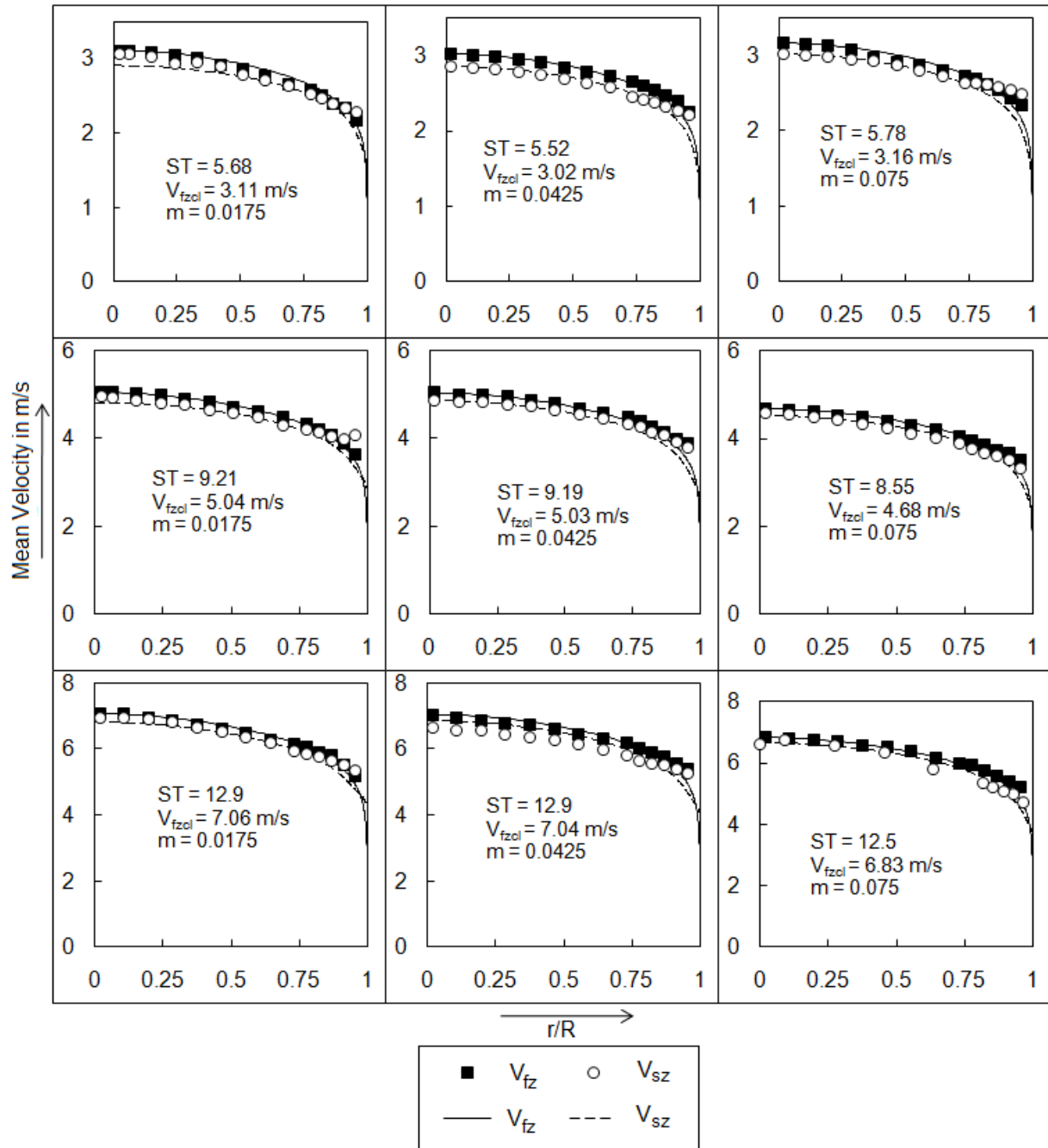


Figure 3-9. Mean velocity (V_{fz} and V_{sz}) measurements for $d = 1 \text{ mm}^{13}$ compared to flow predictions for intermediate ST case

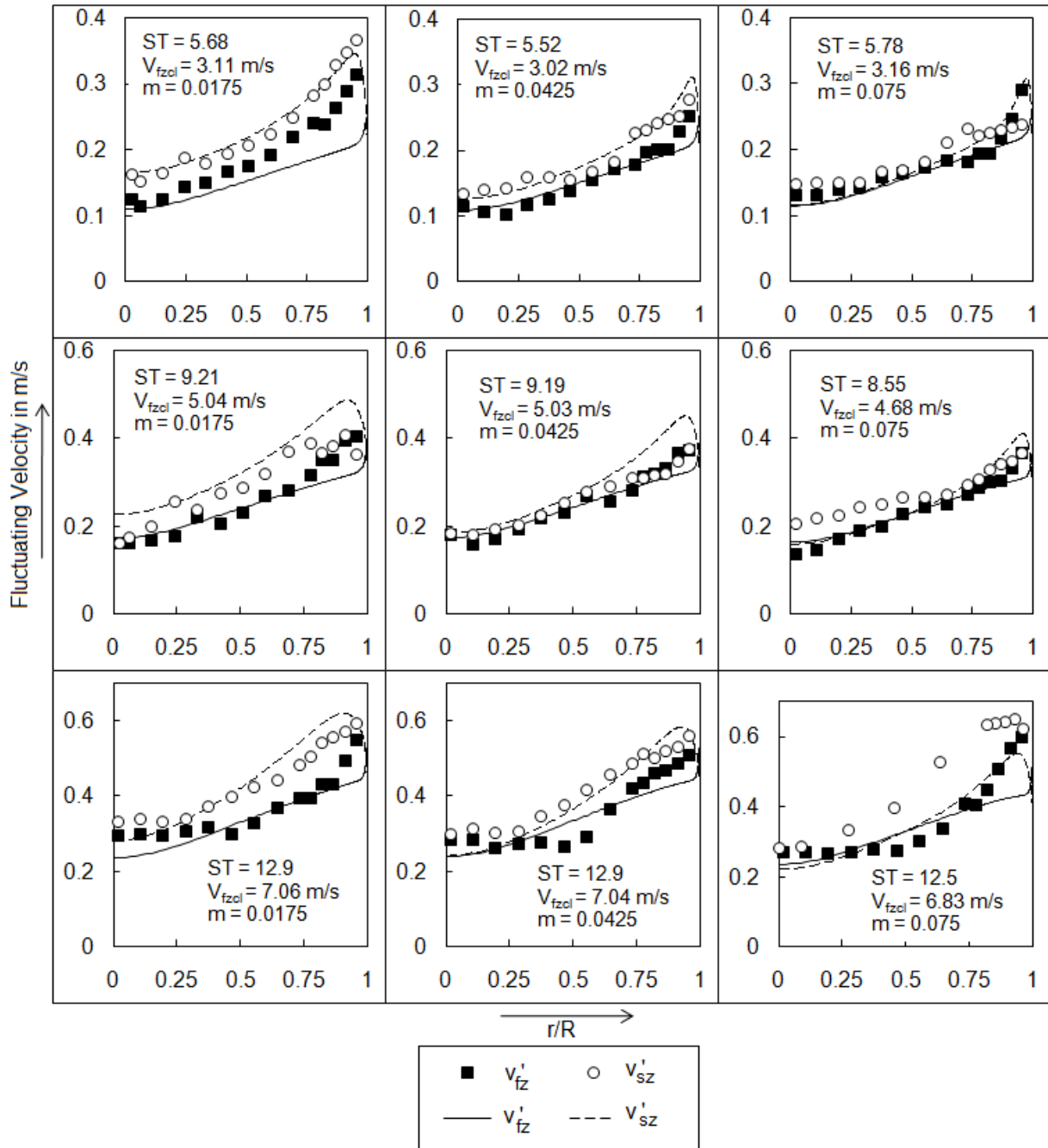


Figure 3-10. Fluctuating velocity (v'_{fz} and v'_{sz}) measurement for $d = 1 \text{ mm}$ ¹³ compared to flow predictions for intermediate ST case

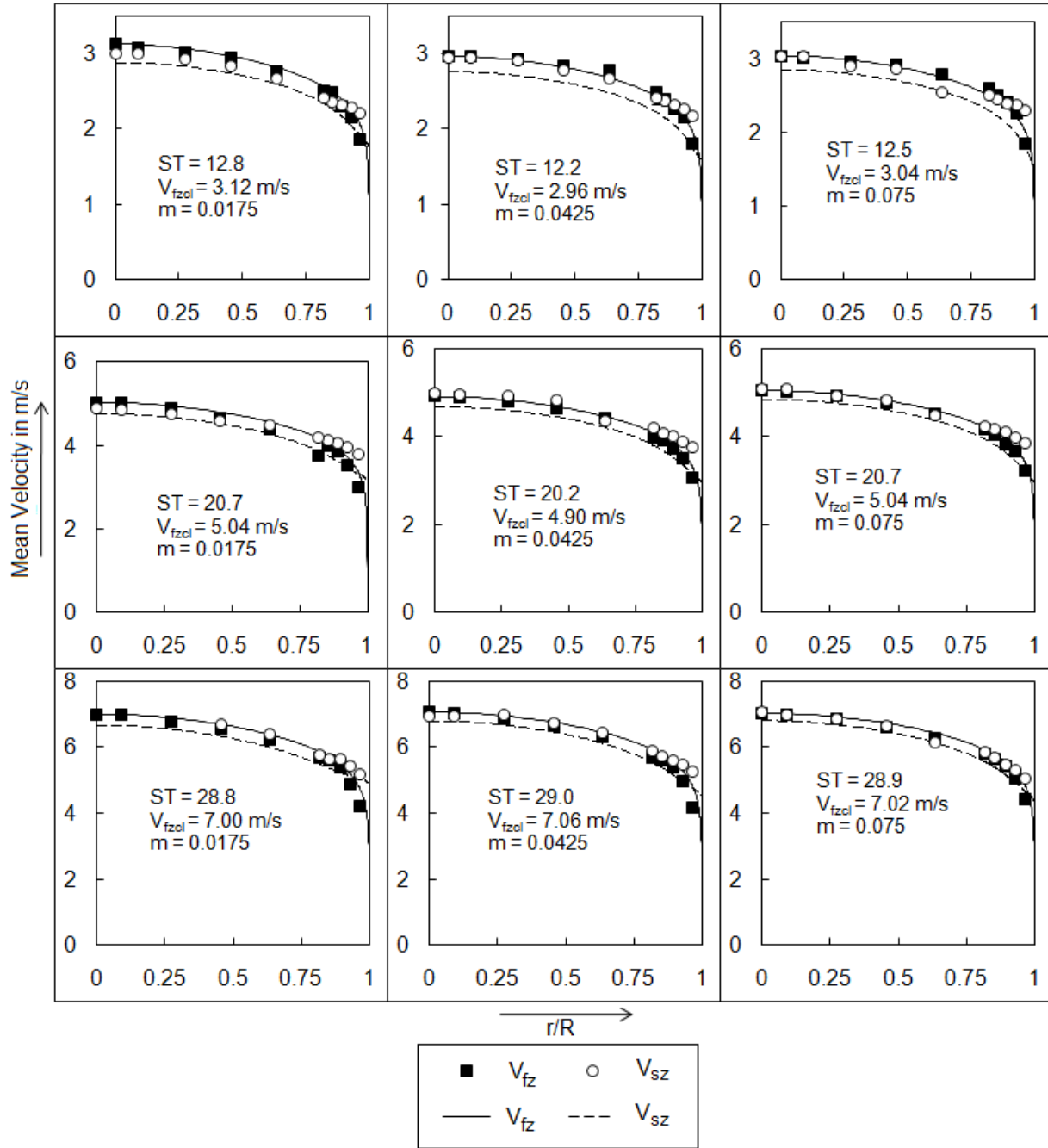


Figure 3-11. Mean velocity (V_{fz} and V_{sz}) measurement for $d = 1.5$ mm compared to flow predictions for intermediate ST case

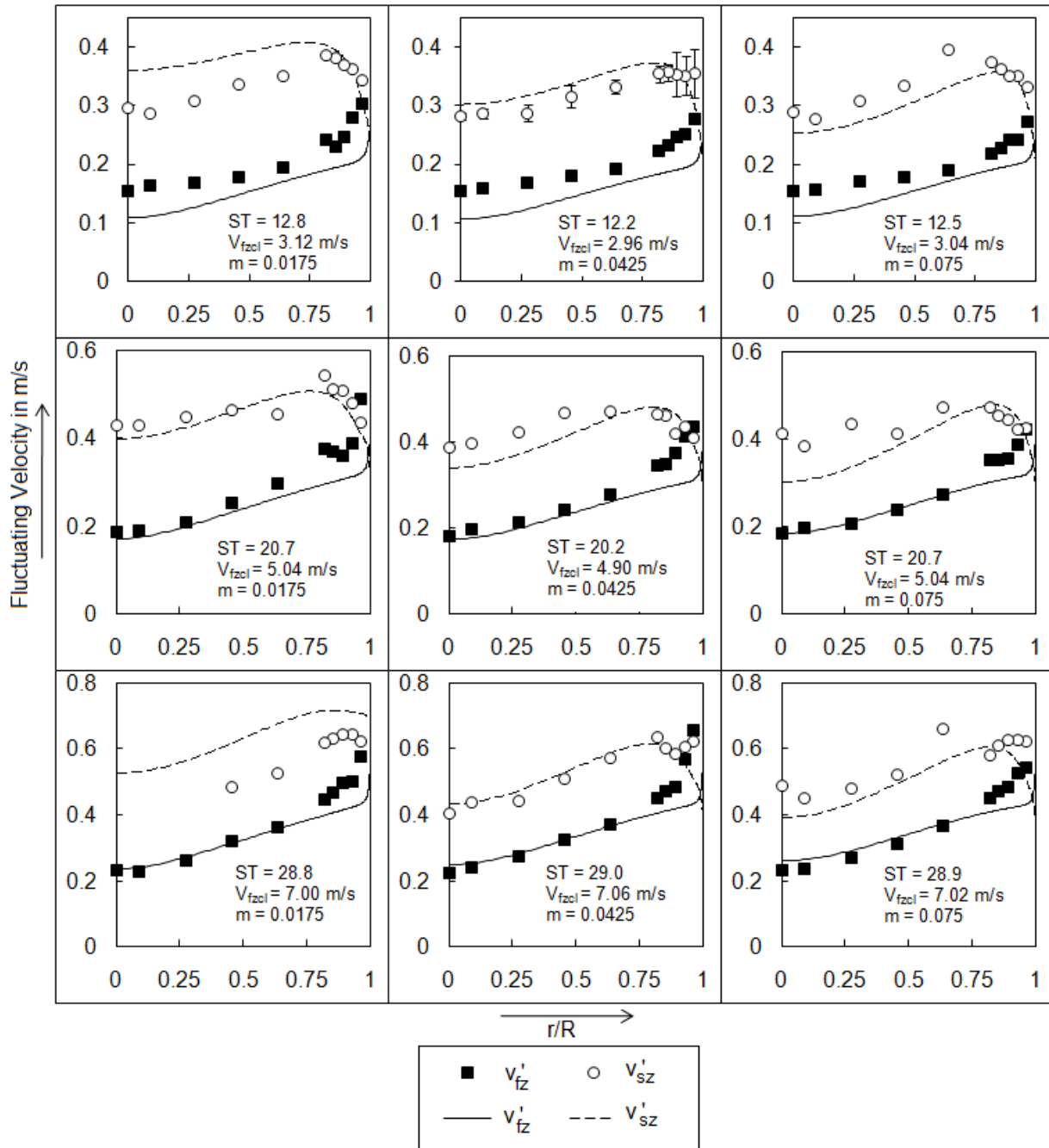


Figure 3-12. Fluctuating velocity (v'_{fz} and v'_{sz}) measurement for $d = 1.5$ mm compared to flow predictions for intermediate ST case

CHAPTER 4 BINARY SEGREGATION IN FLUIDIZED BED

Background

Fluidized bed with monosized particles have been studied in great detail ¹ in the recent past. Nevertheless, fluidized beds with multi-solid mixtures are not well understood. This is due to the fact, multi-solid fluidized beds on fluidization tend to segregate, thereby disturbing the flow patterns and leading to poor efficiencies. The phenomenon of particle segregation needs to be well understood in order to tackle the issue.

It is widely accepted that segregation in a gas fluidized binary mixture occurs due to gas bubbles that are generated as soon as the bed leaves the packed state. Rowe *et al.* ⁶² showed that one of components of the binary mixture is selectively dragged upwards in the wake of the bubble to form the upper layer of the bed. This component is termed the 'flotsam'. The second component, which sinks to the bottom of the column, is called the 'jetsam'. Despite the previous work, it is still not clear whether bubbling is responsible for the equilibrated segregation pattern, or if it is merely the mechanism that gives rise to segregation ¹⁶.

Nienow *et al.* ⁶³ experimentally studied the segregation behavior of nearly forty binary mixtures, although they reported on only a few of these. They concluded that mixtures with equal densities, but different sizes, mix easily. In addition, mixtures with equal sizes and with substantially different densities do not mix easily. They proposed a mixing index, M which is defined as the ratio of the average mass fraction of the jetsam in the uniformly mixed section to the average mass fraction of the jetsam through the

column (the exact definition of M is given in ^{63, 64}. M is a function of operating superficial gas velocity, U ,

$$M = \frac{1}{[1 + \exp(-Z)]}, \quad (4-1)$$

$$M = \frac{1}{[1 + \exp(-Z)]}, \quad (4-2)$$

where,

$$Z = \left(\frac{U - U_{TO}}{U - U_{mf-lower}} \right). \quad (4-3)$$

The parameter U_{TO} is the take-over velocity, *i.e.*, the superficial gas velocity at which the mixing index M is equal to 0.5, and $U_{mf-lower}$ is the smaller of the two minimum fluidization velocities of each individual material. Equation 4-1 works well for mixtures in which the volume fraction of jetsam is less than 50% (volume concentration), and for particle size ratios less than three. Hence, equation 4-1 cannot describe the behavior of extremely disparate mixtures. Also, these studies did not consider the pressure drop profile of the mixtures.

Nienow *et al.* ⁶⁴ presented experimental data for not only binary mixtures, but also tertiary and quaternary systems. They studied the effect of different gas distributors on segregation patterns. Their conclusions for binary mixtures were similar to those of Nienow *et al.* ⁶³.

Garcia *et al.* ²² studied the effect of particle density ratio, ρ_r , for a binary mixture while maintaining the particle size ratio (d_r) at unity. They observed that glass-alumina and alumina-polyethylene systems ($\rho_r = 1.5$ and 1.6 , respectively) mixed better than the glass-polyethylene system ($\rho_r = 2.39$).

Hoffmann *et al.*⁶⁵ and Huilin *et al.*²³ performed experiments as well as numerical simulations of binary mixtures, mostly with the same particle densities but different particle sizes. The mixture for which $d_r = 1.5$ ⁶⁵ mixed well whereas the other mixtures ($1.9 < d_r < 3.5$) mixed completely only at relatively high gas velocities.

The phenomenon of layer inversion in gas fluidized binary mixtures¹⁹ has also been observed with some particle mixtures involving smaller, denser particles and coarser, less dense particles. In such mixtures, the smaller, denser particles behave as jetsam at low velocities just above the point of fluidization, but at higher velocities the coarser, less dense particles behave as jetsam. The authors associated this phenomenon with the change in mixture bulk density as a function of composition and gas velocity.

Marzocchella *et al.*¹⁸ studied transient fluidization behavior of a mixture consisting of particles with the same density, but very different sizes ($d_r = 4$). The pressure drop profile from an initially mixed state for this system showed multiple peaks of fluidization (this phenomenon is described in more detail in the following sections) before the entire bed was completely fluidized and the pressure drop across the bed reached a steady value. The mixing index for this mixture initially increased as the gas velocity increased, but then reached a maximum value and decreased as the velocity of the gas further increased. In other words, the mixture started to segregate at relatively high velocities. Olivier *et al.*⁶⁶ investigated the transient fluidization behavior of less disparate mixtures. They observed that the pressure drop profile of these mixtures also had multiple peaks, but the degree of segregation reduced with an increase in velocity.

Formisani *et al.*^{16, 67} studied mixtures with intermediate ($1.8 < d_r < 4$) disparity and reported pressure drop profiles with multiple peaks when the mixtures were initially well mixed. The number of peaks reduced as the disparity between the two particle types diminished and, for two similar component systems, the pressure drop profiles showed a single peak before complete fluidization. The pressure drop profile from an initial segregated state of mixtures with intermediate disparity showed that the mixtures fluidized at two distinct points. In order to relate the behavior of all the mixtures, the authors defined two velocities, U_{if} , which is the point of incipient fluidization, and U_{ff} , the point at which the mixture completely fluidizes.

Joseph *et al.*¹⁷ performed experiments with mixtures having little disparity ($1 < d_r < 2$). These mixtures fluidized at a single velocity point and showed segregation behavior similar to mixtures with a single peak in their pressure drop profiles^{16, 67}.

The experiments performed in the present study involve both size segregating (d_r is varied from 1.4 to 6.6, in small increments) and density segregating ($\rho_r=3.1$ and 7.4) mixtures. Pressure drop profiles, from initially mixed and segregated states, are reported along with axial segregation profiles at different velocities. These experiments encompass all of the previously reported types of pressure drop profiles and segregation patterns.

Table 4-1 summarizes the work of previous researchers as well as the experiments performed in the present study. The table presents the mixture type, the parameters studied, and whether or not the pressure drop profiles are reported by the authors.

The variety of possible pressure drop profiles, *i.e.*, two point fluidization, multi-peak behavior, single-peak behavior, and single point fluidization, have made it difficult to define the minimum fluidization velocity for a particle mixture. In fact, the pressure drop profile is governed by the initial axial segregation profile. As a result, a variety of minimum fluidization velocities or incipient fluidization velocities can be defined based on the variety of pressure drop profiles. The complete fluidization velocity, U_c , is perhaps the only parameter which remains sufficiently independent of the initial segregation profile. So, it is preferable to define the fluidization velocity of a mixture by its U_c - the velocity at which the entire mixture, including both the jetsam and flotsam, is fluidized. Further, a parameter which would help categorize these different types of mixtures is also needed. Juxtaposing particle size ratio and particle density ratio is anticipated to be useful in predicting the fluidization behavior of these mixtures. As a result, parameters such as the ratio of the Archimedes numbers or the ratio of the minimum fluidization velocities of the individual components are expected to be of interest.

Experiments

Particles and Their Preparation

Experiments were performed with glass (Mo Sci Corporation), polystyrene (Norstone, Inc.), and steel particles (Ervin Industries) with mean diameters ranging from 83 μm to 550 μm and sizes following a log normal distribution. All of the particles are in the Geldart B class and on fluidization only exhibit either the bubbling or slugging flow regime. Thus, in all the cases when U_{mf} is being compared, U_{mb} (minimum bubbling velocity) is also being correspondingly compared. The particles were carefully sieved, dried in an oven for twelve hours and subject to an antistatic bar in order to eliminate

accumulated electrostatic charge. The particles were stored in a desiccator so that cohesive forces due to moisture and static effects were minimized. Table 4-2 summarizes the experimental materials and their properties. The notation used to represent the particle type has a letter indicating material type (G for glass, P for polystyrene, and S for steel) followed by the mean particle size in microns. The error in the measurement of the minimum fluidization velocities of all the particles was less than 10%.

Table 4-3 presents the studied mixtures and their properties (composition, size ratio, density ratio, Archimedes number ratio, and the ratio of the minimum fluidization velocities). The notation followed for the particle mixtures is in two parts. The first part describes the jetsam percentage composition (by mass), material type (glass, polystyrene and steel), and particle size. The second part of the notation describes all of the same properties, but for the flotsam.

Experimental Setup

A fluidization segregation unit (Jenike and Johanson, Fluidization Material Sparging – Segregation Tester, was used in the experiments. The tester has a column diameter of 1.6 cm and a height of 9.5 cm. There is a sliding disc assembly at the base of the column which can be used to divide the bed into multiple horizontal sections. Each of these sections may be transferred to a sampling container, one at a time, via a carousel arrangement. Details concerning the operation of the tester are given in Hedden *et al.*⁶⁸ and ASTM D-6941⁶⁹.

A schematic of the experimental set up is shown in Figure 4-1. A sintered metal plate with an average pore diameter of 40 μm was used as a gas distributor for the columns. The air enters the column from the bottom, with its flow rate controlled by a

mass flow controller. The pressure drop across the entire setup was measured using a pressure transducer. The instantaneous pressure drop and velocity data were recorded on a computer.

Experimental Procedure

Prior to running an experiment, air was passed through the empty column to get a background pressure drop due to the column, diffuser, and the filter sections.

In order to obtain the pressure drop profile for a segregated state, the material expected to be the jetsam was first weighed and a very small amount of antistatic powder (Larostat® HTS 905 S, BASF Corporation, approximately 2 mg) was mixed with the particles and loaded into the column from the top. Next, the material expected to be the flotsam was weighed and antistatic powder was mixed into it and loaded into the column. The height, H , to which the column was filled was recorded. The fixed bed height, H , was approximately 4 cm for all experiments. The velocity was slowly increased at a rate of 0.0833 cm/s^2 to a velocity much greater than that required to completely fluidize the mixture. The velocity was then decreased to zero at the same rate.

For the pressure drop profile measurements from a mixed state, fresh amounts of the jetsam and flotsam, along with the antistatic powder (approximately 5 mg), were completely mixed either manually for disparate mixtures (mixtures with 2-point fluidization), or for similar mixtures (mixtures with 1-point fluidization) complete mixing was obtained by maintaining the mixture at high air velocities (three times the complete fluidization velocity) for thirty minutes.

In order to obtain the segregation profiles for the mixture at different velocities, the mixture was first completely mixed by following the same procedure used in the

pressure drop profile measurements from a mixed state. The fluidized bed was then maintained at the intended velocity for thirty minutes. At the end of the thirty minutes, the velocity was suddenly set to zero, and the bed collapsed to a fixed bed state. Next, the bed was sectioned axially by using the sampling disc assembly at the base of the column. Each section was collected in a sampling container via the carousel arrangement and its composition was analyzed. The composition for mixtures with different sizes was obtained by sieving, while mixtures involving steel and glass or polystyrene were separated using magnets. Mixtures of glass and polystyrene were chosen such that they could be easily separated by sieves.

Segregation Index

Multiple definitions of an axial mixing index or segregation index for binary mixtures have been proposed^{17, 63}. The segregation index usually varies between zero and one, with zero indicating no segregation or uniform mixing and one indicating a completely segregated mixture.

In order to define a segregation index, the feed composition of the jetsam by weight, x_f , is first obtained as,

$$x_f = \frac{\text{mass of jetsam}}{\text{mass of jetsam} + \text{mass of flotsam}}. \quad (4-4)$$

In a similar manner, the final jetsam composition of the mixture, x_m , is defined as the weight fraction of the jetsam at the end of the segregation experiment. The two weight fractions are defined in order to account for the material losses (losses in the present work are approximately 5% by weight of the feed composition).

Next, the weight fraction of the jetsam for each axial section of the column, x_i , is determined. The segregation index, si_i , for the i^{th} axial section of the column is defined as,

$$si_i = \left(\frac{x_i - x_m}{1 - x_f} \right)^2, \quad (4-5)$$

for sections in which $x_i > x_f$ and,

$$si_i = \left(\frac{x_i - x_m}{x_f} \right)^2, \quad (4-6)$$

for sections in which $x_i < x_f$. Finally, the overall segregation index, SI , is computed as,

$$SI = \left[\sum_i si_i * \frac{\text{mass of section}}{\text{mass of the entire bed}} \right]^{1/2}. \quad (4-7)$$

Since SI is a function of velocity, segregation profiles were obtained at various velocities and the corresponding segregation indices were calculated for each profile.

It was observed that the reproducibility of the experiments increased as the disparity between the two components decreased, especially for size segregated mixtures. Hence, it was only necessary to conduct three replicate experiments for two of mixtures with the greatest disparity (mixture numbers 1 and 2 in Table 4-3). Only a single set of experiments was carried out for the other mixtures. The error in the value of SI was found to be between 5 and 10%.

Results and Discussion

Table 4-4 provides a detailed summary of the mixture parameters reported in the literature, as outlined in Table 4-1, as well as the results from the experiments performed in the present study, as outlined in Table 4-3. The mixtures are arranged in descending order with respect to the jetsam to flotsam minimum fluidization velocity

ratio. This velocity ratio, U_r , is a good measure of particle mixture disparity as discussed later in this section.

Throughout the published literature, as well as in this study, a wide variety of segregation behavior associated with different types of mixtures has been observed. Here, an attempt is made to qualitatively categorize these various mixtures based on the density ratio, size ratio, and the ratio of minimum fluidization velocities of the individual components.

Although all of the published studies provide information on segregation profiles, not all include pressure drop information. Hence, in some cases, categorizing the mixtures involves hypothesizing some aspects of the mixture behavior based on other reported behavior for those and similar mixtures. By analyzing the pressure drop, flow, and segregation behavior of the various mixtures, seven different mixture types can be identified (and are listed in Table 4-4). In general, for binary mixture types A-D, both the particle size and density ratios are equal to or greater than one ($d_r \geq 1$ and $\rho_r \geq 1$). This is not true for mixture types E-G, which have one of the ratios less than one with the other greater than one.

Mixture Types

Each mixture type is described using a typical example of that particular type. The rest of the figures are presented in Appendix C where figures (a) and (b) are the pressure drop profile of the fluidization and defluidization cycle for completely segregated and perfectly mixed states, respectively. Figure (c) represents the weight fraction of jetsam versus dimensionless height at different velocities and figure (d) shows how the SI varies as a function of velocity.

Type A mixtures

Mixtures with very large particle size ratio ($d_r > 4.5$; $U_r > 8$)

Type A mixtures fluidize at two distinct points when fluidized from a completely segregated state (Figure 4-2a). As the gas velocity is increased, the entire segregated bed remains in a fixed state and the pressure drop linearly increases. Eventually, the flotsam becomes fluidized (point A in Figure 4-2a is the first point of fluidization), but the jetsam remains in a fixed bed state. At this point, the pressure drop curve follows a linear profile (as the velocity increases), but with a different slope. This change in slope is due to the partial fluidization of the bed. It is important to note that the velocity required to fluidize the flotsam is slightly greater than the minimum fluidization velocity of the flotsam alone. As the velocity is further increased, a point is reached at which both the jetsam and flotsam are fluidized (point B in Figure 4-2a, which is the second point of fluidization). The pressure drop across the entire bed remains constant for larger velocities. The velocity required to fluidize both the jetsam and flotsam is slightly larger than the minimum fluidization velocity of the jetsam alone.

As the gas velocity is reduced, the bed height decreases and the jetsam settle at the bottom of the column (point C in Figure 4-2a is the first point of defluidization). The velocity at which point C occurs is generally smaller than both the velocity at point B and the minimum fluidization velocity of the jetsam. Upon further reduction of the gas velocity, the entire bed eventually settles (point D in Figure 4-2a is the second point of defluidization). The velocity at this point is greater than the minimum fluidization velocity of the flotsam. Points A and D occur at similar velocities.

When Type A mixtures are fluidized from an initial uniformly-mixed state, there are multiple peaks observed in the pressure drop profile (oval E in Figure 4-2b highlights

this peaked behavior). These peaks are a characteristic feature of mixtures with large particle size disparity and can be explained by the phenomenon of entrapment. As the gas velocity increases, the pressure drop across the bed increases linearly. At a certain velocity, only the flotsam in the topmost layer of the mixture which is entrapped by the jetsam, gains sufficient momentum to fluidize. The jetsam falls back to the bottom of the column, entrapping the remainder of the flotsam in the lower layers (Figure 4-3). This phenomenon is associated with the first peak in the pressure drop. Beyond the first peak, the pressure drop again increases linearly with velocity until a second layer of flotsam escapes. In this manner, as additional layers of the flotsam escape, multiple peaks in the pressure drop profile are observed. Eventually, a velocity is reached at which the entire amount jetsam fluidizes. At this point, the pressure drop across the bed stabilizes and the entire bed is completely fluidized as all of the flotsam is no longer entrapped. The number of peaks observed in the pressure drop profile corresponds to the number of escaping flotsam layers. The appearance of each peak corresponds very well with the visual observation of an escaping flotsam layer. Experiments were performed to determine that fewer peaks occur when the rate of increase of the gas velocity is higher. The magnitude of the pressure drop associated with each peak corresponds to the amount of flotsam escaping and the extent of each layer. The magnitude of the pressure drop of the successive peaks reduces as the velocity increases, implying that each successive escaping layer of flotsam decreases.

The nature of the defluidization curve for the mixture from an initially segregated or mixed state is the same (points F and G in Figure 4-2b are the first and second points of defluidization, respectively). In fact, the defluidization profile is independent of the initial

segregation profile (points C and D in Figure 4-2a coincide with F and G in Figure 4-2b). Hence, the defluidization curve is the most reproducible curve for a Type A mixture.

Type A mixtures are not only characterized by 2-point fluidization, but also by a minimum observed in the segregation index profile (Figure 4-2c). As the velocity increases beyond the complete fluidization velocity (points C and F in Figures 4-2a and 4-2b, respectively), the bed begins to mix and the S/I decreases. However, as the gas velocity increases further, the bed expansion due to the flotsam is greater than that for the jetsam and the bed begins to segregate with a corresponding increase in S/I . Thus, for Type A mixtures, there exists an optimum velocity at which the S/I is minimized.

Type B mixtures

Mixtures with significant level of disparity in particle size and density ($\rho_r > 3$ or $4.5 > d_r > 3.3$; $4.2 < U_r < 8$)

The pressure drop profiles for Type B mixtures are similar to those observed for Type A, where fluidization from a segregated state exhibits 2-point fluidization behavior, and fluidization from an initially mixed state exhibits peaked behavior (points A-D and E-G in Figures 4-4a and 4-4.b, respectively, have the same definitions as the corresponding points in Figures 4-2a and 4-2b). The key difference between a Type A and Type B mixture is the behavior of the segregation index. For Type B mixtures, the segregation index decreases as the gas velocity increases (Figure 4-4c) rather than exhibiting a minimum. For Type B mixtures, the mixing quality improves as the gas velocity increases, although complete mixing is difficult to achieve and can be attained only at very large fluidization velocities.

Type C mixtures

Mixtures with intermediate level of disparity ($2 < \rho_r < 3$ or $2 < d_r < 3.3$; $2.5 < U_r < 4.2$)

When Type C mixtures are fluidized from an initially segregated state, they exhibit 2-point fluidization (points A and B in Figure 4-5a are the first and second points of fluidization, respectively). However, when these mixtures are fluidized from a mixed state, they may either demonstrate single peak behavior (oval D in Figures 4-5b and 4-6) or single point fluidization behavior (shown in Figure 4-6). Single peak behavior is generally observed in either small diameter columns¹ or when the data acquisition system is sufficiently fast. It is this latter effect that is observed in the present study. When the mixtures were fluidized rapidly, fewer data points were obtained since the data acquisition rate remained the same and some of the key features (such as the peaks) of the pressure drop profiles were lost. Thus, it was necessary to fluidize the material slowly (the rate of velocity increase was 0.0833 cm/s²). The mixtures that have a single point or a single peak in their pressure drop profile show similar patterns.

As an example, Figure 4-6 compares pressure drop profiles for the same mixture (75G231-25G116) obtained in two different fluidized bed systems. One of the profiles is from the fluidized bed system used in the present study (column diameter is 1.6 cm), which has a very high data acquisition rate, and the other profile was obtained using the Joseph *et al.*¹⁷ fluidized bed system (column diameter is 12 cm) with a lower data acquisition rate. The pressure drop profile exhibits single pressure peak behavior, while the Joseph *et al.*¹⁷ system shows single fluidization point behavior. Some combination of the effect of the data acquisition rate and column diameter is thought to have caused this difference in the behavior.

The segregation index profile (Figure 4-5c) shows that at low velocities the segregation index is large, but at higher velocities (approximately twice the complete fluidization velocity), the mixture mixes completely.

Type D mixtures

Mixtures with minimal disparity in particle size and density ($1 < \rho_r < 2$ or $1 < d_r < 2$; $1 < U_r < 2.5$)

These mixtures behave like single component particle beds and fluidize at a single point from both the initially segregated or well mixed state (Figures 4-7a and 4-7b).

Type D mixtures also tend to mix easily at low velocities (Figure 4-7c). Furthermore, they do not exhibit segregation even at low velocities which are slightly above the complete fluidization velocity.

Type E mixtures

Mixtures with smaller, denser component as jetsam ($\rho_r > 2$ and $d_r < 1$)

Type E mixtures contain smaller, denser particles and coarser, less dense particles such that the size difference opposes the density difference. Generally, the smaller, denser component behaves as jetsam when the density ratio is large. The pressure drop profile may show multiple peaks or a single peak depending upon the disparity level based on U_r ^{16, 17}. Additionally, the segregation index decreases as the velocity increases.

Type F mixtures

Mixtures exhibiting layer inversion ($1 < \rho_r < 1.5$, $0.3 < d_r < 1$)

Mixtures with smaller, denser particles and coarser, less dense particles having a low density ratio and a low to intermediate size ratio may exhibit the phenomenon of layer inversion. At lower velocities, the smaller, denser component behaves as jetsam.

However, at higher velocities, the coarser, lighter component behaves as jetsam. For these mixtures, pressure drop data and segregation index are not readily available in the literature and were not examined here.

Type G mixtures

Mixtures with Coarser, lighter component as jetsam ($1 < \rho_r < 2$, $d_r < 0.3$)

For mixtures with smaller, denser particles and coarser, less dense particles having a low density ratio and a large size ratio, the coarser, less dense components behave as jetsam. As an example, mixture number 15 from Table 4-4 exhibits this kind of behavior. When mixture number 15 was fluidized from an initially segregated state, it had two points of fluidization, and when it was fluidized from an initially mixed state, it showed multiple peaks. The segregation index of mixture number 15 reduced as the operating velocity was increased. Pressure drop and segregation index figures for all the binary mixture experiments performed in this study are provided in Appendix C.

Classification Diagram

Figure 4-8 summarizes all of the data presented in Table 4-4 in a more concise manner. A log-log plot is used to due to the significant amount of available data for mixtures of smaller, denser particles and coarser, less dense particles ($\rho_r > 1$ and $0.1 < d_r < 1$). In addition, there have been many experiments performed for purely size segregating mixtures or density segregating mixtures. Hence, there are many data points along the x-axis and y-axis.

The various mixture types can be classified via a plot of particle density ratio (y-axis) versus particle size ratio (x-axis). The boundary lines give an approximate range of the particle properties associated with each mixture type. The segregation index minimum phenomenon is not present for mixtures with large density difference ($\rho_r =$

7.4). Since most practical cases involve density ratios less than this value, the boundary line for Type A mixtures is drawn as a straight line parallel to the y-axis.

As mentioned previously, the minimum fluidization velocity ratio is a useful measure characterizing the level of particle disparity in the mixture. Figure 4-9 shows how the ratio of the Archimedes number for the jetsam to flotsam,

$$Ar_r = \left(\frac{d_{jetsam}}{d_{flotsam}} \right)^3 \left(\frac{\rho_{s-jetsam} - \rho_g}{\rho_{s-flotsam} - \rho_g} \right), \quad (4-8)$$

which combines the effects of both the particle size and density ratios, is related to the minimum fluidization velocity ratio. For some mixtures, such as mixture numbers 15 and 34 in Table 4-4, Ar_r is less than one while U_r is greater one. In order to keep the data for all mixtures on a single plot, Ar_r is redefined as,

$$Ar_r = \left(\frac{d_{flotsam}}{d_{jetsam}} \right)^3 \left(\frac{\rho_{s-flotsam} - \rho_g}{\rho_{s-jetsam} - \rho_g} \right), \quad (4-9)$$

in Figure 4-9 so that Ar_r is always greater than one. Also, for mixture numbers 39 to 43 in Table 4-4, both Ar_r and U_r are less than one. In these cases, both Ar_r and U_r are redefined so that both ratios are always greater than one. The Archimedes number is given by equation 4-9 while the minimum fluidization velocity ratio is

$$U_r = \frac{U_{\min-flotsam}}{U_{\min-jetsam}}. \quad (4-10)$$

A simple correlation is developed between the two parameters (Ar_r and U_r),

$$U_r = 1.02 Ar_r^{0.49}, \quad (4-11)$$

which is shown in Figure 4-9. If $U_r > 8$, then the disparity level is extremely high (mixtures 1 to 8 in Table 4-4) and if $4.2 < U_r < 8$, then there is a high level of disparity

(mixtures 9 - 18 in Table 4-4). Further, mixtures having U_r between 2.5 and 4.2 have intermediate disparity level (mixtures 19 to 26 in Table 4-4). And finally, if U_r varies from 1 to 2.5, there is a low level of disparity (mixtures 27 - 43 in Table 4-4). Hence the correlation given in equation 4-11 allows one to predict U_r , based on Ar_r , and thus give an indication of the level of mixture disparity.

Figure 4-9 is a good fit for most mixtures except for numbers 5, 11, 14, and 18 in Table 4-4. Mixtures 5 and 14 are taken from the data of Nienow *et al.*⁶³ and Nienow *et al.*⁶⁴, respectively, who reported values for minimum fluidization velocity for glass that were smaller than predictions from various correlations and previously reported and the present study's measurements. The data for mixtures 11 and 18 are from the present study and have a higher minimum fluidization velocity for steel particles than expected from standard correlations like the Wen and Yu³⁹ correlation. Friction from the walls acting on the steel particles may be influencing these measurements. The friction coefficient between steel and acrylic (the column material) and the density of steel are both large which results in a large wall influence (Chapter 5). The minimum fluidization velocities of the other mixtures' materials (glass and polystyrene) in the present study are negligibly affected by wall effects.

For example, consider mixture number 22 (Table 4-4, *i.e.* 75G231-25G116). This mixture has been studied in the present column ($D = 1.6$ cm) as well as in a larger column, $D = 12$ cm¹⁷. The U_r obtained for this mixture is 3.15 ($U_r = \frac{U_{\min-jetsam}}{U_{\min-flotsam}} = \frac{6}{1.9}$) for the present column and 3.11 ($U_r = \frac{U_{\min-jetsam}}{U_{\min-flotsam}} = \frac{5.6}{1.8}$) for the 12 cm diameter column. The difference in U_r , between both columns is ~1% and, assuming that U_r is the principal

parameter required to characterize different mixtures, wall effects on segregation patterns are negligible. Experiments were performed to compare segregation patterns from the smaller column ($D = 1.6$ cm) to the segregation patterns from a wider column ($D = 12$ cm¹⁷) for mixture number 22. The segregation patterns for both columns were similar, validating that the wall has a minimal influence on mixture number 22.

Experiments Validating Minimal Wall Effects

It will be shown in Chapter 5 that it is possible for the minimum fluidization velocity of a single component system, U_{mf} , in a smaller column to be larger than in a wider column. The increase in U_{mf} depends upon the ratio of the particle size to column diameter, the ratio of the bed height to column diameter, the friction coefficient between the particles and the confining wall, and the Archimedes number. For most of the particles studied, the increase in U_{mf} was less than 14% with a bed height of 4 cm (Chapter 5). Additionally, this small increase in U_{mf} for the individual components results in a small increase in U_r when the ratio of the minimum fluidization velocities of the individual components (the primary parameter used to characterize mixtures) is calculated.

In addition, the segregation profiles are only minimally altered due to the wall effect. As an example, Figure 4-10 compares the segregation profiles of the same mixture in two columns – the column used in the present study ($D = 1.6$ cm) and a larger column ($D = 12$ cm¹⁷). In this figure, the operating velocity is scaled with the complete fluidization velocity, U_c , of the mixture and is denoted by V^* . Generally, segregation profiles are given as weight fraction (or volume fraction) of either jetsam or flotsam versus dimensionless height (instantaneous height, h , divided by the overall bed height). However, in this case, to compare data from two different columns, weight

fraction is plotted against h/D , and the zero of the dimensionless height, is defined to be at the center of the column. Although the segregation experiments were performed at different dimensionless operating velocities, the segregation profiles in the two columns match reasonably well. Similar results were also observed for mixture number 43 in Table 4-4 (30G116-70P275).

Effect of column H/D on Binary Segregation in Fluidized Bed

Experiments investigating the effect of the ratio fixed bed height to the column diameter (H/D) are also performed in this study. As the H/D increases, the complete fluidization velocity of the mixture also increases (especially in narrow columns). Hence to study the mixtures on the same platform the dimensionless velocity V^* (as defined in the previous section) is maintained constant.

Segregation behavior of four different mixtures namely 25G116-75G231 at $V^*=2.3$, 50G138-50G328 at $V^*=2.5$, 50G138-50G275 at $V^*=3$ and 70G116-30P275 at $V^*=3.1$, are presented in Figures 4-11, 4-12, 4-13 and 4-14 respectively. The four mixtures are from Type C category from a disparity point of view. Most of these experiments were carried out in a column with $D=1.6$ cm except for the curves for mixtures 25G116-75G231 at $H/D=2$ and 70G116-30P275 at $H/D=1.2$ which are from Joseph *et al.*¹⁷, $D=12$ cm). Again in these figures too the segregation profiles are plot against h/D instead of the conventional h/H and the zero is considered at the center of the fixed bed. This is done so that data from the two columns ($D=1.6$ cm and $D=12$ cm for Joseph *et al.*, 2007) can be plotted together. From Figures 4-11, 4-12, 4-13 and 4-14 it is observed that even at very high fluidization velocities, as the H/D ratio increases, segregated tail develop at the two ends of the column. At the center however, the two components remain completely well mixed. Thus, for an infinitely tall column which is being fluidized

by a very high velocity, there will be three zones, the center zone where it will be perfectly mixed and two end zones, one with a high jetsam concentration in the bottom end zone and the other with a high flotsam concentration in the top end zone. The length of the center perfectly mixed zone will depend on the level of disparity (i.e. d_r , ρ_r and U_r) and the operating velocity.

Summary

Chapter 4 presents a new classification scheme for the pressure drop profiles, and segregation behavior of binary fluidized mixtures ($d_r < 7$ and $\rho_r < 8$). Seven mixture types are proposed. This classification scheme is based on the particle size and density ratio of the two components and incorporates new data as well as previously published data exhibiting a wide range of fluidization behavior.

The effect of H/D on segregation is also studied herein. It is observed that even mixtures with fairly low level of disparity being fluidized at high velocities, if the H/D ratio of the column is indefinitely increased, segregated tails start appearing at the ends of the column.

While conducting H/D experiments it was realized that as the height of the fixed bed was increased or the column diameter was reduced the minimum fluidization velocities of monosized particles were enhanced. Although the qualitative results presented in this Chapter are hardly influenced by the elevation in minimum fluidization velocity due to the wall, there may be adverse effects on parameters like heat and mass transfer. In Chapter 5 the wall effects are quantified and a new semi-correlation is proposed for the predicting the enhancement in minimum fluidization velocities, which include the wall effects.

Table 4-1. Summary of published work (details in Table 4-4)

Reference	Type of Mixture						Layer Inversion	Pressure Drop Profile	Parameters studied
	Size difference	Density difference	Larger Denser	Smaller Denser as jetsam	Smaller Denser as flotsam				
	$\rho_r=1, d_r>1$	$\rho_r>1, d_r=1$	$\rho_r>1, d_r>1$	$\rho_r>1, d_r<1$	$\rho_r<1, d_r>1$	$\rho_r>1, d_r<1$ or $\rho_r<1, d_r>1$			
Joseph <i>et al.</i> ¹⁷	yes	yes	no	yes	no	no	yes	V, C _{mix} , H, SI	
Formisani <i>et al.</i> ¹⁶	yes	yes	no	yes	yes	no	yes	V, C _{mix} , v, SI	
Formisani <i>et al.</i> ⁶⁷	yes	no	no	no	no	no	yes	V, C _{mix} , v, SI	
Marzocchella <i>et al.</i> ¹⁸	yes	no	no	no	no	no	yes	V, C _{mix} , v, SI	
Hullin <i>et al.</i> ²³	yes	no	no	no	no	no	yes	V, C _{mix} , v, SI	
Hoffmann <i>et al.</i> ⁶⁵	yes	no	no	yes	no	no	no	V, SI	
Nienow <i>et al.</i> ⁶³	yes	no	yes	yes	no	no	no	V, C _{mix} , SI	
Nienow <i>et al.</i> ⁶⁴	yes	no	yes	no	no	no	no	V, SI	
Olivieri <i>et al.</i> ⁶⁶	no	yes	no	yes	no	no	no	V, C _{mix} , SI	
Garcia <i>et al.</i> ²²	no	yes	no	no	no	no	no	V, C _{mix} , v, SI	
Rasul <i>et al.</i> ¹⁹	no	no	no	yes	no	yes	no	ρ_b	
Present study	yes	yes	no	yes	no	no	yes	V, H, SI	

Table 4-2. Experimental material and properties – present study

Material	Diameter (µm)	Density (kg/m ³)	Sphericity	Umin (cm/s)	Standard Deviation (cm/s)	Notation
Glass	75-89	2500	0.9	1.5	0.2	G083
	104-125	2500	0.9	1.9	0.05	G116
	125-152	2500	0.9	2.7	0.3	G138
	152-178	2500	0.9	3.6	0.3	G165
	178-211	2500	0.9	4.6	0.3	G195
	211-251	2500	0.9	6	0.6	G231
	251-297	2500	0.9	8	0.2	G275
	297-354	2500	0.9	11	0.3	G328
	354-422	2500	0.9	13	0.2	G385
	422-500	2500	0.9	19	0.3	G460
	500-600	2500	0.9	25	0.8	G550
Polystyrene	251-297	1250	0.9	4	0.3	P275
	297-354	1250	0.9	7	0.5	P328
Steel	297-354	7800	0.85	46	2	S328

Table 4-3. Experimental mixtures and their properties – present study

Type	Mixtures	Size Ratio	Density Ratio	Ar no. ratio	Umin Ratio
Size Segregation	50G550-50G083	6.6	1	291	16.7
	50G462-50G083	5.6	1	172	12.7
	50G550-50G116	4.7	1	107	13.2
	50G385-50G083	4.6	1	99.8	8.7
	50G462-50G116	4.0	1	63.2	10.0
	50G328-50G083	4.0	1	61.7	7.3
	50G275-50G083	3.3	1	36.4	5.3
	50G231-50G083	2.8	1	21.6	4.0
	50G195-50G083	2.3	1	13.0	3.1
	50G165-50G083	2.0	1	7.86	2.4
	50G138-50G083	1.7	1	4.60	1.8
	50G116-50G083	1.4	1	2.73	1.3
	Density Segregation	13S328-87P328	1	7.40	7.40
75S328-25G328		1	3.10	3.10	4.2
Size and density against each other	70G116-30P275	0.42	2.30	0.170	0.5

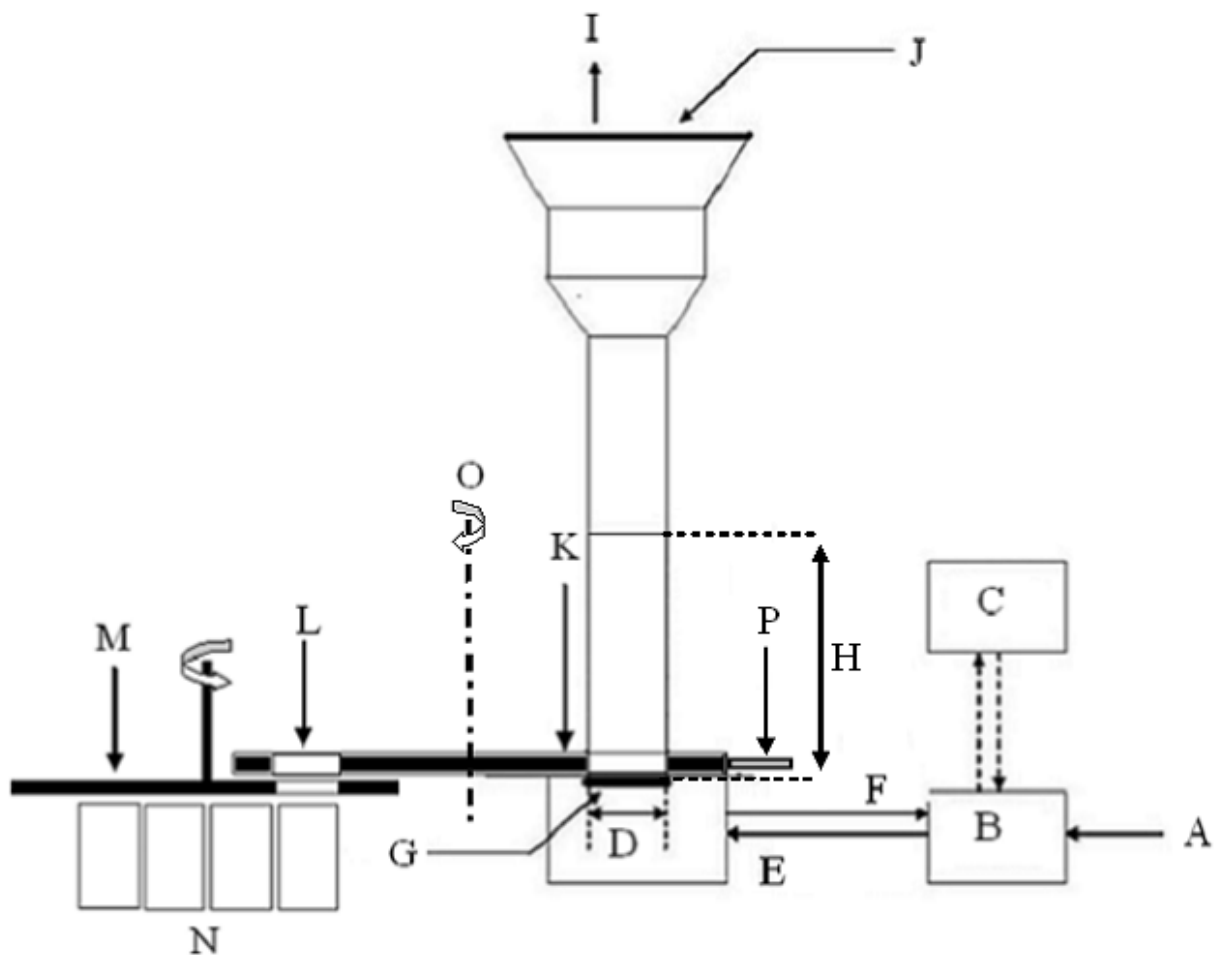


Figure 4-1. Schematic of the experiment: (A) air inlet, (B) mass flow controller and pressure transducer, (C) computer, (D) column diameter, (E) air flowing into the setup, (F) pressure signal, (G) diffuser, (H) bed height, (I) exiting air, (J) air filter, (K) sliding disc assembly, (L) slice of the bed, (M) carousel arrangement, (N) sampling containers, (O) axis of rotation of the sliding disc assembly, and (P) side handle to help rotate the sliding disc assembly about axis O.

Table 4-4. Details of mixtures and their properties – published work and present study

Sr no.	Type	Ur J/F	Mixtures			Size Ratio J/F	Density Ratio J/F	Ar # Ratio J/F	Reference
			Mixtures	Jetsam	Flotsam				
1	A	16.67	50G550-50G083	Glass	Glass	6.63	1.00	291	Present Study
2	A	13.16	50G550-50G116	Glass	Glass	4.74	1.00	107	Present Study
3	A	12.94	50G500-50Si125	Glass	Silica Sand	4.00	0.98	63	Marzocchella <i>et al.</i> ¹⁸
4	A	12.67	50G462-50G083	Glass	Glass	5.57	1.00	172	Present Study
5	B	11.61	10S324-90G165	Steel	Glass	1.96	2.52	19.10	Nienow <i>et al.</i> ⁶⁴
6	A	10.00	50G462-50G116	Glass	Glass	3.98	1.00	63.18	Present Study
7	A	8.67	50G385-50G083	Glass	Glass	4.64	1.00	99.80	Present Study
8	A	7.98	50G612-50G154	Glass	Glass	3.97	1.00	62.76	Formisani <i>et al.</i> ¹⁶
9	B	7.50	10G550-90G165	Glass	Glass	3.33	1.00	37.04	Nienow <i>et al.</i> ^{63, 64}
10	B	7.33	50G328-50G083	Glass	Glass	3.95	1.00	61.71	Present Study
11	B	6.57	13S328-87P328	Steel	Polystyrene	1.00	7.43	7.43	Present Study
12	B	6.00	50G499-50G172	Glass	Glass	2.90	1.00	24.42	Formisani <i>et al.</i> ⁶⁷
13	B	5.33	50G275-50G083	Glass	Glass	3.31	1.00	36.37	Present Study
14	B	5.30	10S273-90G231	Steel	Glass	1.18	2.52	4.16	Nienow <i>et al.</i> ⁶⁴
15	G	5.00	50MS624-50G154	Mol Sieves	Glass	0.25	1.70	0.03	Formisani <i>et al.</i> ¹⁶
16	B	4.57	10Cp461-90Q273	Copper Powder	Quartz	1.69	3.34	16.10	Nienow <i>et al.</i> ⁶³
17	B	4.35	10S390-90S138	Steel	Steel	2.83	1.00	22.57	Nienow <i>et al.</i> ⁶⁴
18	B	4.18	75S328-25G328	Steel	Glass	1.00	3.12	3.12	Present Study
19	C	4.00	50G231-50G083	Glass	Glass	2.78	1.00	21.56	Present Study
20	C	3.56	50G565-50G285	Glass	Glass	1.98	1.00	7.79	Hoffmann <i>et al.</i> ⁶⁵
21	C	3.33	55G5490-45G1590	Glass	Glass	3.45	1.00	41.16	Huilin <i>et al.</i> ²³
22	C	3.11	25G231-75G116	Glass	Glass	1.99	1.00	7.90	Joseph <i>et al.</i> ¹⁷
23	C	3.07	50G195-50G083	Glass	Glass	2.35	1.00	12.97	Present Study
24	C	3.00	50G499-50G271	Glass	Glass	1.84	1.00	6.24	Formisani <i>et al.</i> ^{16, 67}

Table 4-4. continued

Sr no.	Type	Ur J/F	Mixtures			Size Ratio J/F	Density Ratio J/F	Ar # Ratio J/F	Reference
			Mixtures	Jetsam	Flotsam				
25	C	2.53	50S439-50G428	Steel	Glass	1.03	3.06	3.31	Formisani <i>et al.</i> ¹⁶
26	C	2.50	55G4260-45G2300	Glass	Glass	1.85	1.00	6.35	Huilin <i>et al.</i> ²³
27	D	2.40	50G165-50G083	Glass	Glass	1.99	1.00	7.86	Present Study
28	D	2.11	50G565-50G365	Glass	Glass	1.55	1.00	3.71	Hoffmann <i>et al.</i> ⁶⁵
29	D	1.93	75G231-25P231	Glass	Polystyrene	1.00	2.33	2.33	Joseph <i>et al.</i> ¹⁷
30	D	1.86	46P328-54P231	Polystyrene	Polystyrene	1.42	1.00	2.86	Joseph <i>et al.</i> ¹⁷
31	D	1.80	50G138-50G083	Glass	Glass	1.66	1.00	4.60	Present Study
32	D	1.73	SS500-PP500	Silica sand	Polypropylene	1.00	2.89	2.89	Olivieri <i>et al.</i> ⁶⁶
33	D	1.67	50G3750-50PE3750	Glass	Polyethylene	1.00	2.39	2.39	Garcia <i>et al.</i> ²²
34	E	1.39	50S439-50MS800	Steel	Mol Sieves	0.55	5.21	0.86	Formisani <i>et al.</i> ¹⁶
35	E	1.35	50G593-50MS624	Glass	Mol Sieves	0.95	1.70	1.46	Formisani <i>et al.</i> ¹⁶
36	D	1.33	50G3750-50A3750	Glass	Alumina	1.00	1.57	1.57	Garcia <i>et al.</i> ²²
37	D	1.27	50G116-50G083	Glass	Glass	1.40	1.00	2.73	Present Study
38	D	1.25	50A3750-50PE3750	Alumina	Polyethylene	1.00	1.52	1.52	Garcia <i>et al.</i> ²²
39	E	0.96	10B273-90G461	Bronze	Glass	0.59	2.89	0.601	Nienow <i>et al.</i> ⁶³
40	E	0.69	80SG375-20SS125	Silica Sand	Silica Gel	0.33	4.33	0.160	Olivieri <i>et al.</i> ⁶⁶
41	E	0.67	50B235-50G565	Bronze	Glass	0.42	3.49	0.251	Hoffmann <i>et al.</i> ⁶⁵
42	F	0.52	FCC-Pumice	FCC	Pumice	0.65	1.12	0.311	Rasul <i>et al.</i> ¹⁹
43	E	0.45	70G116-30P275	Glass	Polystyrene	0.42	2.33	0.175	Joseph <i>et al.</i> ¹⁷
44	E		FCC-Bagasse	FCC	Bagasse	0.32	2.89	0.095	Rasul <i>et al.</i> ¹⁹
45	E		Bagasse-P2000	Bagasse	Polystyrene	0.10	2.46	0.002	Rasul <i>et al.</i> ¹⁹
46	E		PVC-Bagasse	PVC	Bagasse	0.32	1.93	0.063	Rasul <i>et al.</i> ¹⁹
47	F		Cenolyte-Bagasse	Cenolyte	Bagasse	0.32	1.40	0.046	Rasul <i>et al.</i> ¹⁹

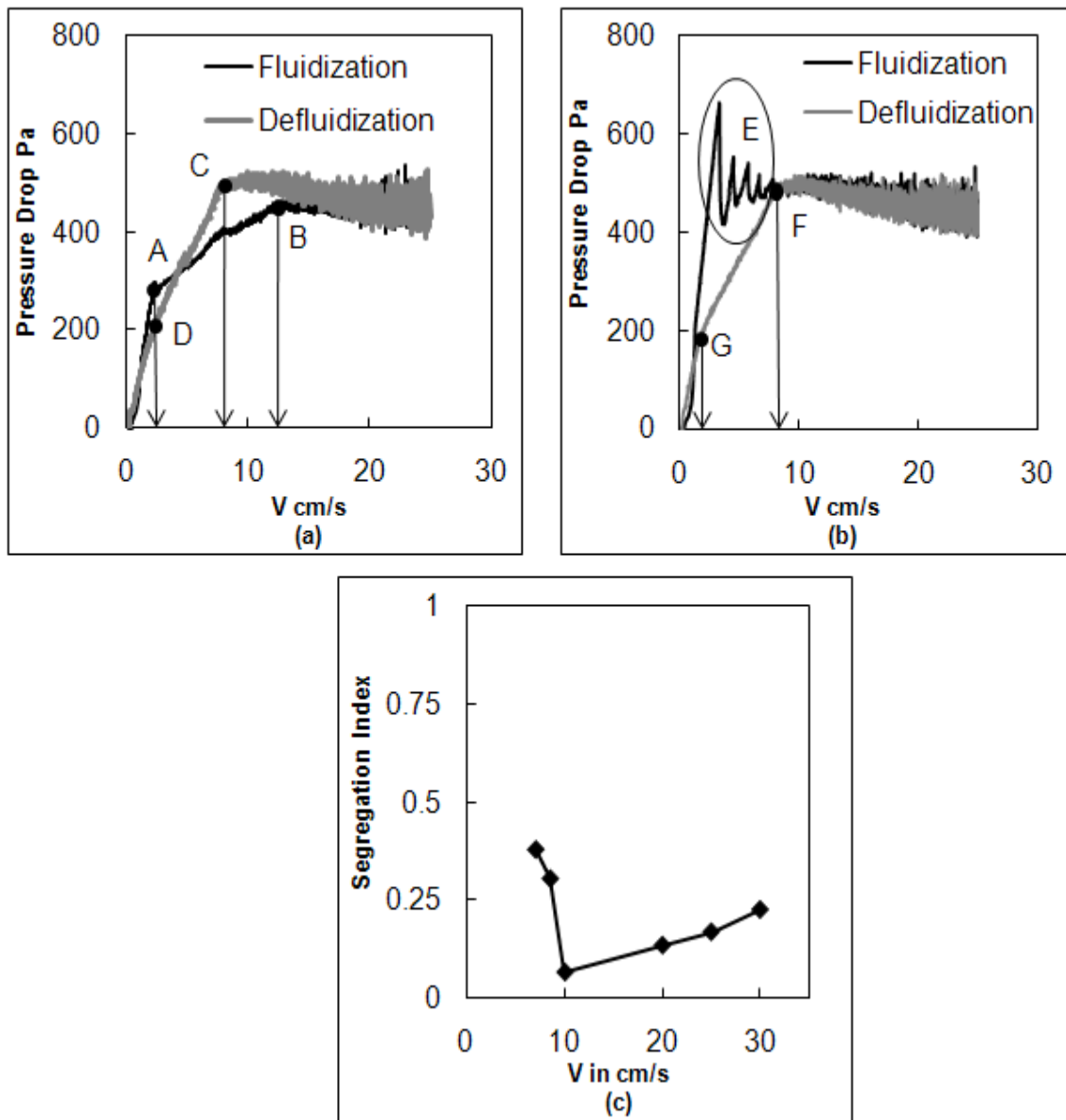


Figure 4-2. Typical pressure drop profiles and segregation index behavior for a Type A mixture 50G385-50G083. (a) Pressure drop profile, initially segregated state. (b) Pressure drop profile, initially mixed state. (c) Segregation index.

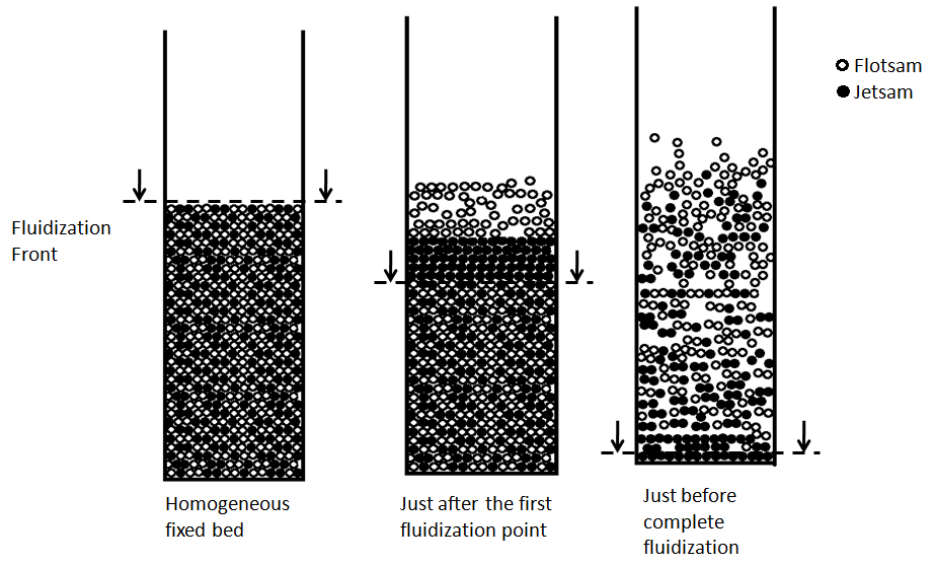


Figure 4-3. Process of fluidization for a homogeneous binary mixture which fluidizes at two points

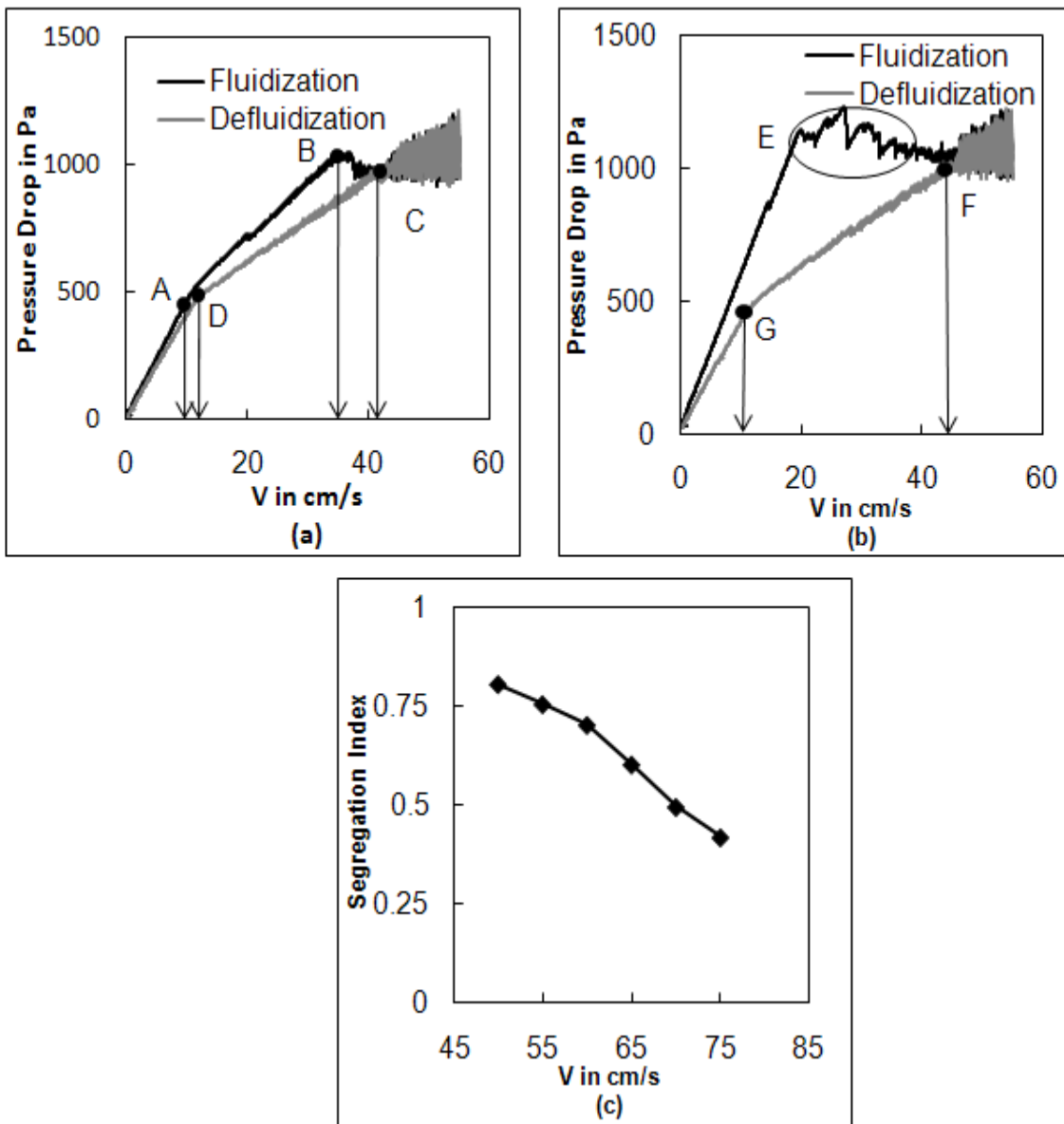


Figure 4-4. Typical pressure drop profiles and segregation index behavior for a Type B mixture 75S328-25G328. (a) Pressure drop profile, initially segregated state. (b) Pressure drop profile, initially mixed state. (c) Segregation index.

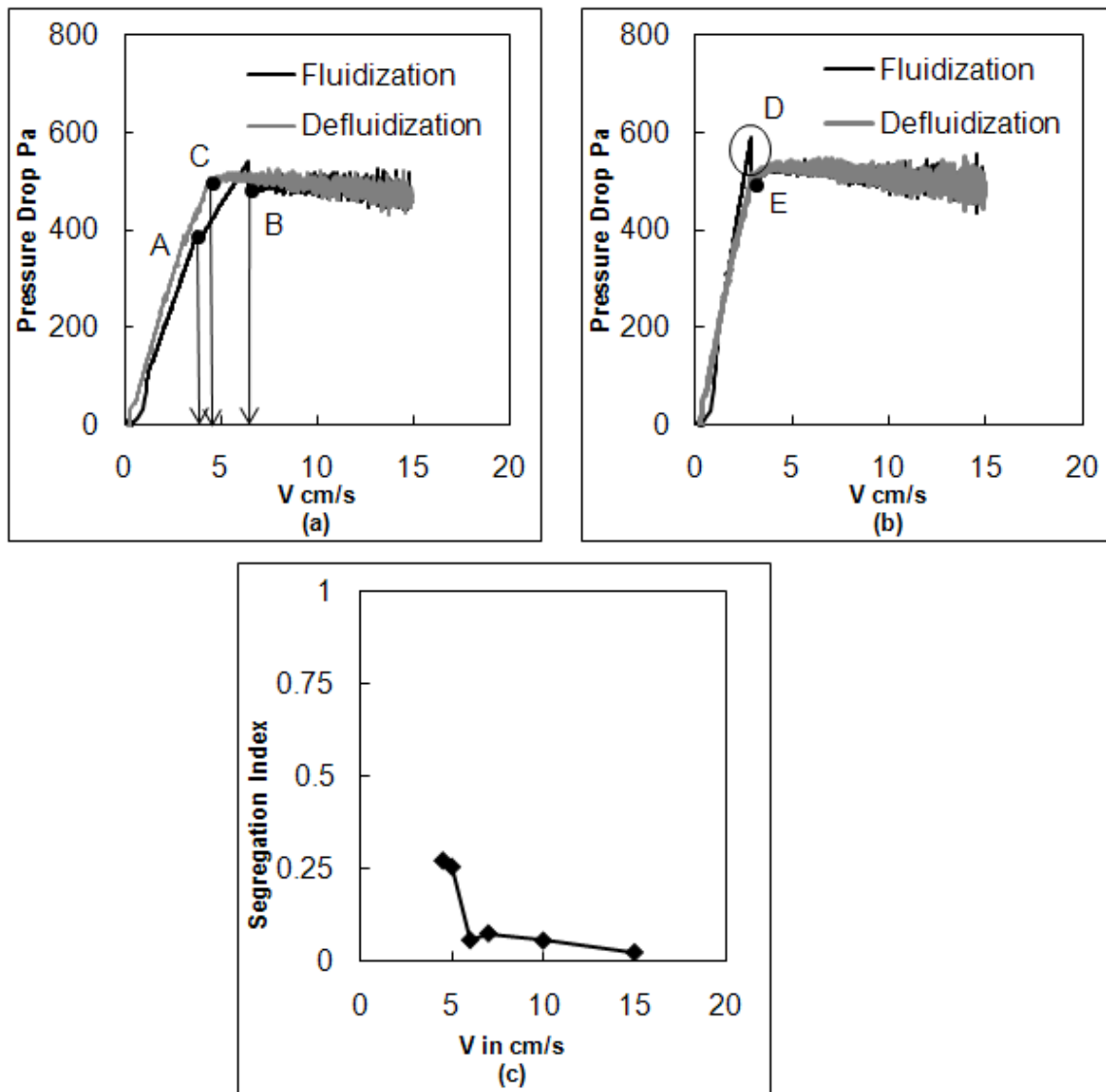


Figure 4-5. Typical pressure drop profiles and segregation index behavior for a Type C mixture 50G195-50G083. (a) Pressure drop profile, initially segregated state. (b) Pressure drop profile, initially mixed state. (c) Segregation index.

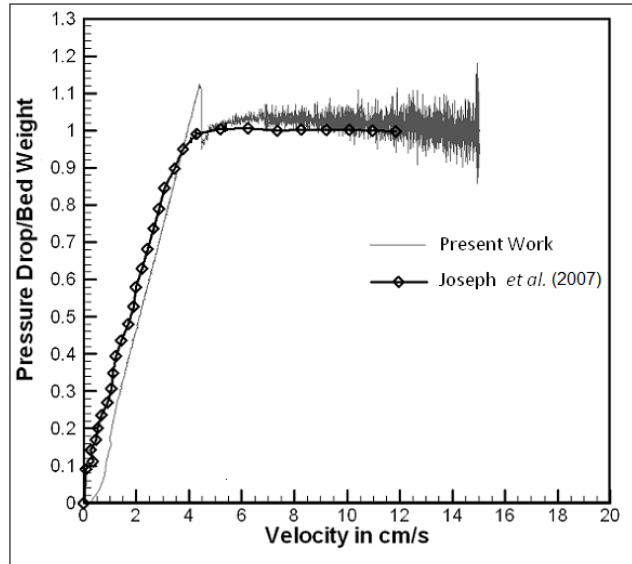


Figure 4-6. Pressure drop profiles for the mixture 75G231-25G116 from an initially mixed state. Comparison of the present work (column diameter is 1.6 cm) with the work of Joseph *et al.*¹⁷ (column diameter is 12 cm).

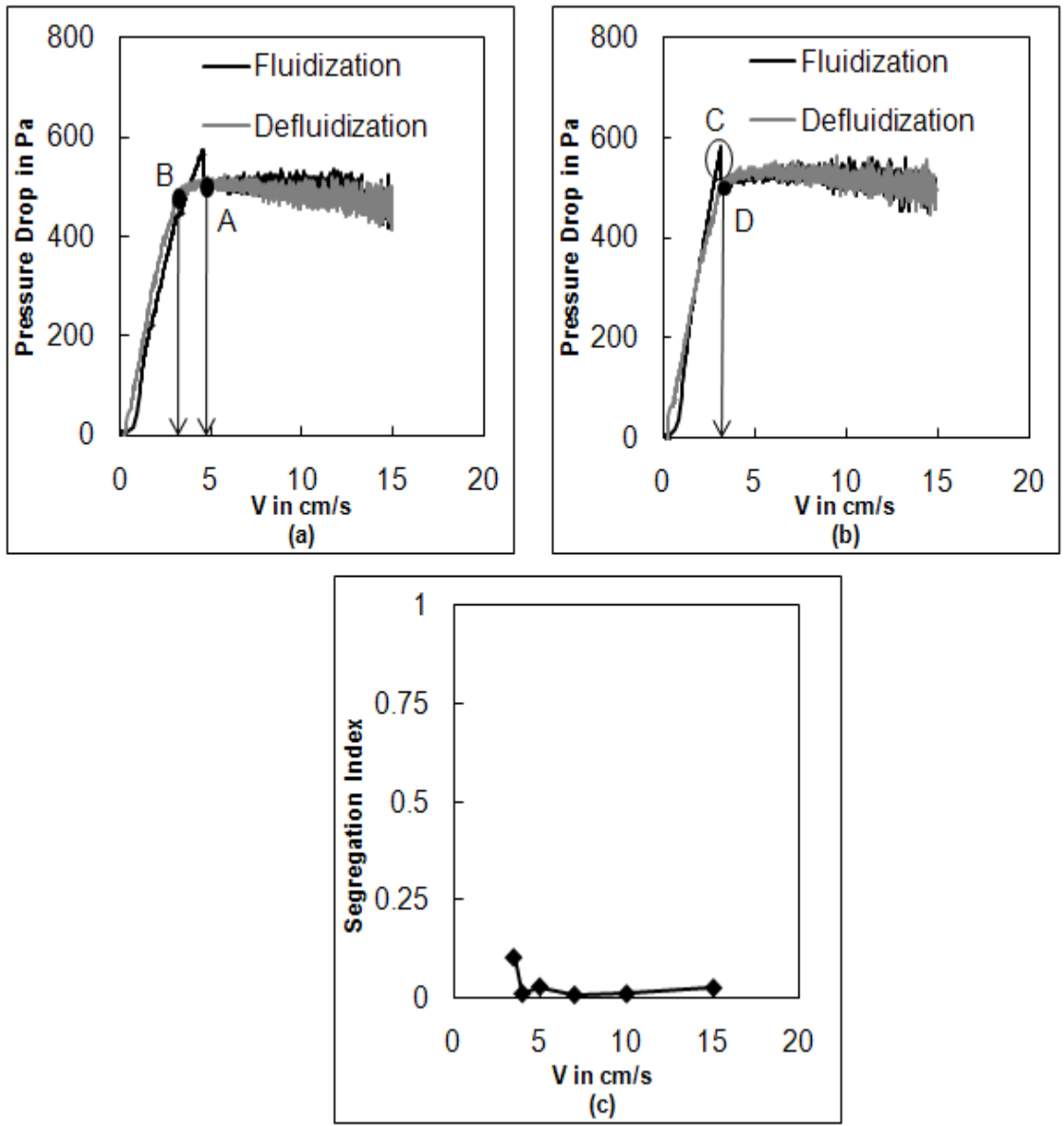


Figure 4-7. Typical pressure drop profiles and segregation index behavior for a Type D mixture 50G165-50G083. (a) Pressure drop profile, initially segregated state. (b) Pressure drop profile, initially mixed state. (c) Segregation index.

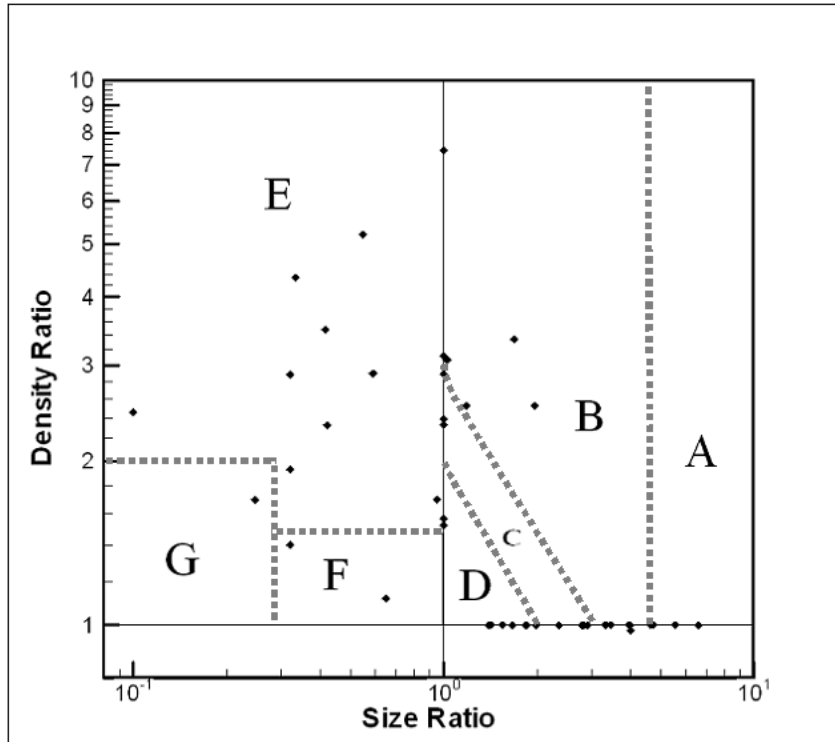


Figure 4-8. Mixture type diagram. Type A: Very large particle size ratio. Type B: Significant level of disparity in particle size and density. Type C: Intermediate level of disparity. Type D: Minimal disparity in particle size and density. Type E: Smaller, denser component as jetsam. Type F: Mixtures exhibiting layer inversion. Type G: Coarser, lighter component as jetsam.

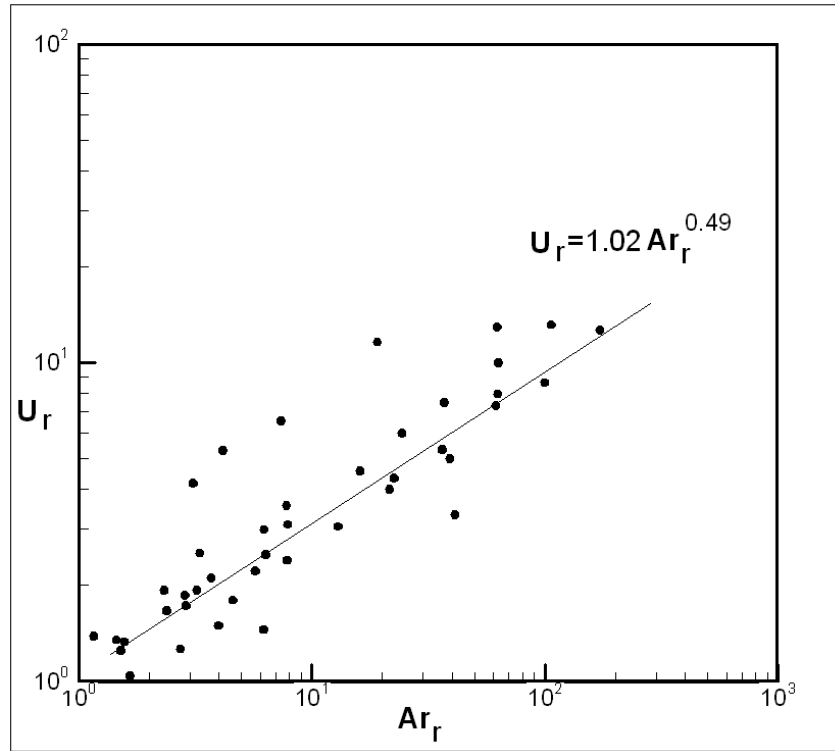


Figure 4-9. Correlation for the minimum fluidization velocity ratio and the Archimedes number ratio.

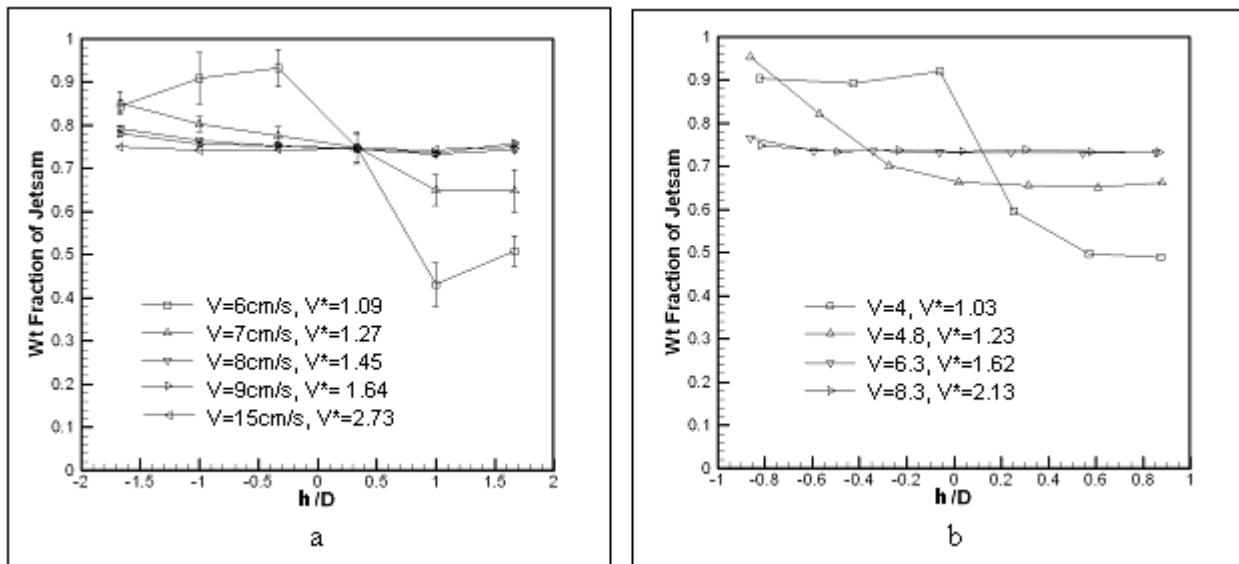


Figure 4-10. Segregation profiles for the mixture 75G231-25G116. (a) Present work ($D = 1.6$ cm). (b) Joseph *et al.*¹⁷ ($D = 12$ cm)

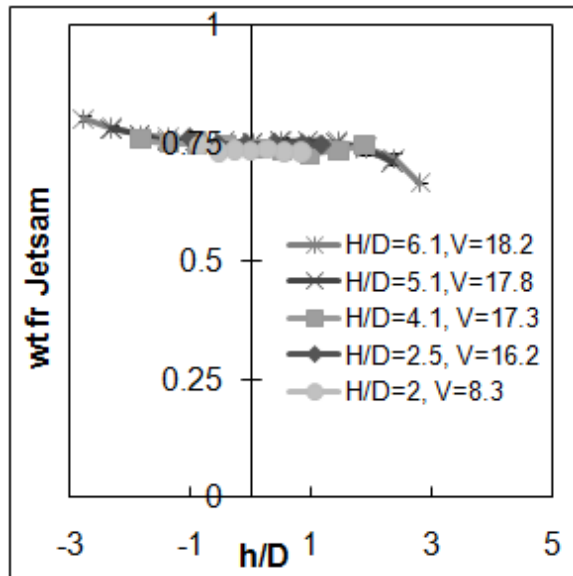


Figure 4-11. Segregation profiles of 25G116-75G231 at $V^* = 2.3$

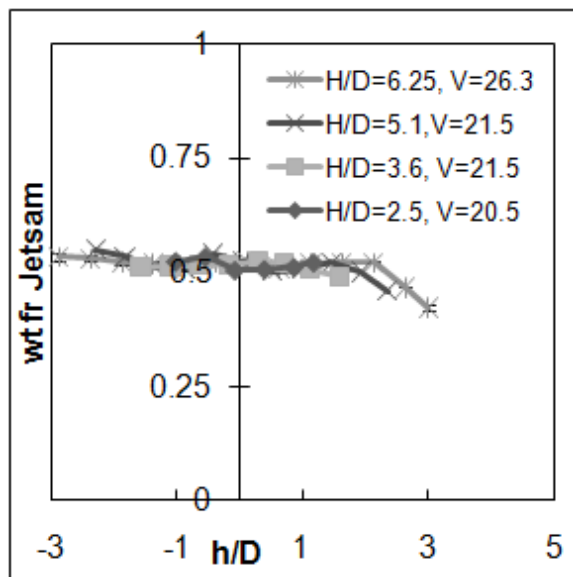


Figure 4-12. Segregation profiles of 50G138-50G328 at $V^* = 2.5$

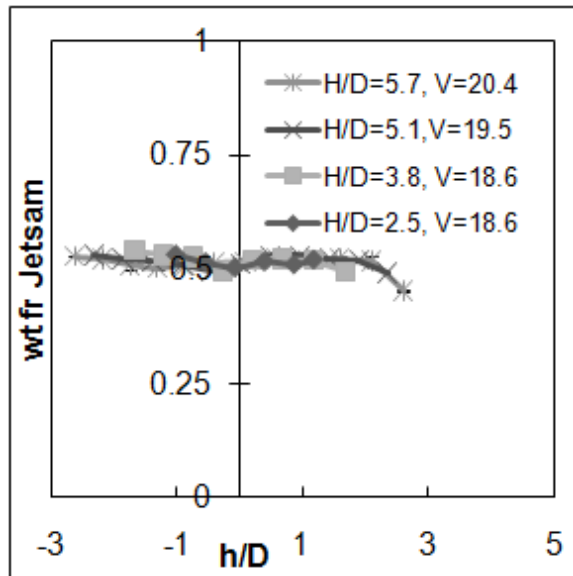


Figure 4-13. Segregation profiles of 50G138-50G275 at $V^*=3$

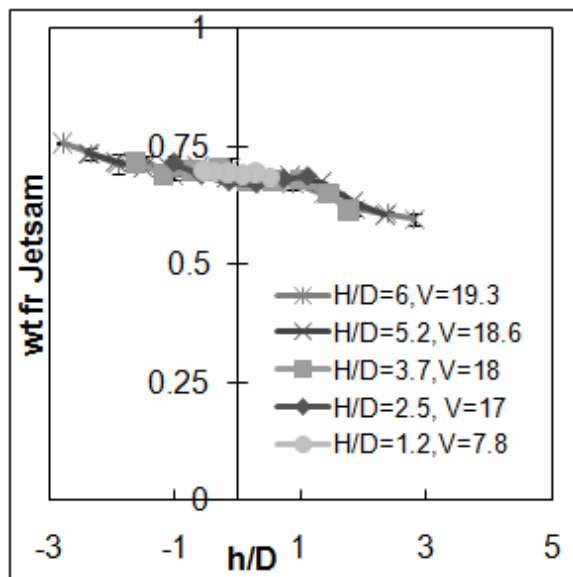


Figure 4-14. Segregation profiles of 70G116-30P275 at $V^*=3.1$

CHAPTER 5
EFFECT OF COLUMN DIAMETER AND BED HEIGHT ON MINIMUM FLUIDIZATION
VELOCITY

Background

MFBs are gaining interest as gas distribution issues are minimized and due to the reduction in the quantity of solids required. Nonetheless there is a pitfall that comes along with the MFBs, *i.e.* wall effects may influence the observed results. As stated in Chapter 1, there are several correlations that exist for calculating the minimum fluidization velocity²⁶⁻³⁹. None of the correlations include the effect of the bed height or diameter of the column, factors which are likely to be of interest when MFBs are considered.

The Wen and Yu³⁹ correlation, one of the more commonly used correlation for calculating the minimum fluidization velocity and is given as,

$$24.5 \left(\frac{\text{Re}_{p-mf}}{\mathcal{G}} \right)^2 + 1650 \left(\frac{\text{Re}_{p-mf}}{\mathcal{G}} \right) - \left(\frac{Ar}{\mathcal{G}^3} \right) = 0, \quad (5-1)$$

where

$$\text{Re}_{p-mf} = \frac{\rho_g (\mathcal{G}d) U_{mf}}{\mu_g}, \quad (5-2)$$

$$Ar = \frac{(\mathcal{G}d)^3 (\rho_s - \rho_g) \rho_g \mathcal{G}}{\mu_g^2}, \quad (5-3)$$

where Re_{p-mf} is Reynolds number at minimum fluidization velocity, Ar is the Archimedes number, \mathcal{G} is the sphericity, U_{mf} is the minimum fluidization velocity. Neither the Wen and Yu³⁹ nor any of the other correlations include the effect of the fixed bed height, H or diameter of the column, D , factors which are likely to be of interest when MFBs are considered.

Two recent investigations, however, have examined the influence of column diameter and bed height. Di Felice and Gibilaro⁷⁰ described a method for predicting the pressure drop across a particle bed, taking into account the effect of column diameter. They considered the column to be comprised of two sections: an inner core where the voidage remains nearly constant, and an outer annular section where the voidage varies due to the presence of the wall. Since there is a difference in the voidage over the cross-section of the column, the velocity also varies across the column's cross-section. This fact was used to develop a modified Ergun's equation, but this effect is only observed at very small column diameter (D) to particle diameter (d) ratios, *i.e.* $D/d < 15$.

Delebarre⁷¹ assumed that the fluidizing gas density is a function of the instantaneous bed height which in turn influences the minimum fluidizing velocity. This effect only occurs if the column is very tall. For micro fluidized beds, where the columns are short, this effect does not play much of a role.

As will be shown in the following section, experiments in which the bed height and column diameter are varied show that both parameters influence the bed's minimum fluidization velocity. Neither Di Felice and Gibilaro⁷⁰, nor Delebarre⁷¹ models are able to capture the experimental results. The remainder of this paper describes the theory and experiments in which a new mechanism is proposed for accounting for bed height and column wall effects.

Experimental Setup

Two fluidization segregation units (Jenike and Johanson, Fluidization Material Sparging – Segregation Tester and Fluidization Segregation Tester), were used in the experiments. The first tester has a column diameter of 1.6 cm and a height of 9.5 cm

and the latter tester has a 2.4 cm diameter column and an 18.5 cm height. Details concerning the operation of the testers are given in Hedden *et al.*⁶⁸ and ASTM D-6941⁶⁹.

A schematic of the experimental set up is shown in Figure 4-1. The experiments were carried out in both columns. A sintered metal plate with an average pore diameter of 40 μm was used as a gas distributor for both the columns. The air enters the column from the bottom, and its flow rate is controlled by a mass flow controller. The pressure drop across the entire setup was measured with a pressure transducer. The instantaneous pressure drop and velocity data were recorded on a computer.

Experiments were performed with glass and polystyrene particles of different sizes, ranging from 100 μm to 550 μm . These particles are in the Geldart B class. The particles were carefully sieved, then dried in an oven for twelve hours and finally subject to an antistatic bar (Takk industries) in order to eliminate accumulated electrostatic charge. The particles were stored in a desiccator so that cohesive forces due to moisture were minimized. To further reduce electrostatic charges that develop during fluidization, a very small amount (approximately 5 mg) of antistatic powder (Larostat® HTS 905 S, manufactured by BASF Corporation) was mixed with the particles, preceding the experiments. Table 5-1 summarizes the experimental materials and their properties. The notation used to represent the particle type is: G for glass and P for polystyrene, followed by the average particle size in microns. The values for the dynamic friction coefficients of glass and polystyrene on acrylic (the column wall material) are not readily available and so values of friction coefficients, for glass on

glass and polystyrene on polystyrene, obtained from Persson and Tosatti⁷² were used in the model calculations.

Prior to running an experiment, air was passed through the empty column to get the background pressure drop due to the column, diffuser, and the filter sections. Next, the particulate material was weighed and loaded into the column from the top. The height, H , to which the column was filled was recorded. The antistatic powder was mixed with the particles. The air velocity was slowly increased beyond the point of fluidization, and then decreased to zero to get the entire pressure drop profile. The point of intersection of the pressure drop line for the fixed bed and the horizontal line for the fully fluidized bed is typically defined as the minimum fluidization velocity. However, just before fluidization, the pressure drop across the bed overshoots the expected value and then decreases to a constant value. Such behavior is expected in columns with a small diameter. This overshoot was not observed during defluidization (Figure 5-1). Thus, the defluidization pressure drop curve was used to determine the point of fluidization^{25, 73}. A minimal of three cycles of fluidization and defluidization were carried out to determine an average minimum fluidization velocity. Each experiment was repeated twice and the procedure was repeated for all particle types. The maximum fluctuation observed in the value of U_{mf} was $\sim 7\%$ (for G550 in $D = 1.6$ cm and $H = 4.5$ cm; $U_{mf} = 24.5$ cm/s ± 0.9). The fairly consistent value of U_{mf} observed over the three cycles and two repetitions show that the trends in U_{mf} are not due to poor gas distribution but rather due to the wall effects. Additionally, gas channeling and maldistribution were not observed through the transparent columns during any of the experiments.

Figures 5-2 to 5-5 present the experimental data for the minimum fluidization velocity (U_{mf}), for the glass and polystyrene particles, obtained from both the columns. In these figures, the Reynolds number at U_{mf} , is plotted against the aspect ratio of the bed (H/D). In addition to the experimental data, the plots also include theoretical curves which will be described in the following section. The error bars represent the difference in the reading between two repetitions and not amongst different cycles.

The experimental data (Figures 5-2 – 5-5) show that minimum fluidization velocity monotonically increases as the height of the bed is increased. Further, wall effects on the minimum fluidization velocity are prominent when column diameter, $D = 1.6$ cm (Figure 5-2 and Figure 5-4). While, wall effects on minimum fluidization velocity are much less pronounced for column diameter, $D = 2.4$ cm (Figure 5-3 and Figure 5-5). Although the model proposed by Di Felice and Gibilaro⁷⁰ predicts this trend, their model is limited to column to particle diameter ratios of less than 15. In the experiments performed here, this ratio can be as large as 150, well outside the range of validity in Di Felice and Gibilaro⁷⁰ model.

As the height of the bed increases, the minimum fluidization velocity also increases. Delebarre⁷¹ model accounts for changes in the fluidizing gas density over the bed height and predicts at most a minimum fluidization velocity increase of approximately 0.5%, while the observed minimum fluidization velocity increase is greater than 20% in certain cases for the experiments examined here. Thus, this model does not predict the measured data.

Theory

Since existing correlations do not include the influence of column diameter or bed height, and because the recent models by Di Felice and Gibilaro⁷⁰ and Delebarre⁷¹ do

not predict the measured data, a new model is developed in this section in order to account for the observed trends. As will be presented, a key component of the model is the stress between the column wall and the bed.

The pressure drop, ΔP , for a fixed bed of height, H , is given by the semi-empirical correlation of Ergun¹ as,

$$-\frac{\Delta P}{H} = b_E V + a_E V^2, \quad (5-4)$$

where

$$a_E = 1.75 \frac{(1-\epsilon)}{\epsilon^3} \left(\frac{\rho_f}{g d} \right) \text{ and} \quad (5-5)$$

$$b_E = 150 \frac{(1-\epsilon)^2}{\epsilon^3} \left(\frac{\mu_f}{g^2 d^2} \right). \quad (5-6)$$

The parameter V is the superficial fluid velocity and ϵ is the bed voidage. The bed void fraction and fluid density are assumed to remain constant throughout the bed.

The pressure drop expression (equation 5-4) can be used to predict the minimum fluidization velocity of a mono-sized material by balancing the pressure force acting on the bed by the effective bed weight.

$$\left[1.75 \frac{(1-\epsilon)}{\epsilon^3} \right] Re_{p-mf}^2 + \left[150 \frac{(1-\epsilon)^2}{\epsilon^3} \right] Re_{p-mf} = [(1-\epsilon)Ar]. \quad (5-7)$$

Note that in the previous analysis, the stress between the wall and the bed has not been included.

In the case of a fixed bed with no interstitial fluid, a fraction of the bed weight is supported by the walls of the column. This phenomenon is known as Janssen's wall effect. To determine the wall force acting on the bed, consider a thin horizontal slice of the particle bed of thickness dz (Figure 5-6). The vertical stress, σ_v , acting on the top

face and the weight of the element are balanced by the vertical stress acting on the bottom face and the frictional forces applied by the wall. The resulting differential equation is,

$$\frac{d\sigma_v}{dz} + c_1\sigma_v = c_2, \quad (5-8)$$

where

$$c_1 = \frac{4\tan\phi k_J}{D} \text{ and} \quad (5-9)$$

$$c_2 = (1 - \epsilon)\rho_s g. \quad (5-10)$$

The parameter ϕ is the friction angle between the wall and particles. A horizontal frictional stress, σ_H , arises from the vertical stress, σ_v , producing a wall friction force of $\sigma_H \tan\phi$ ⁷⁴. It is assumed here that this horizontal stress is directly proportional to the vertical stress with k_J as the proportionality constant⁷⁴.

$$\sigma_H = k_J \sigma_v. \quad (5-11)$$

Solving equation 5-8 subject to the boundary condition that the stress at the top of the bed is zero gives,

$$\sigma_v = \frac{c_2}{c_1} (1 - e^{-c_1 z}). \quad (5-12)$$

The stress increases nearly linearly near the free surface, but asymptotes to a constant value deeper into the bed. These wall induced vertical stresses will affect the minimum fluidization velocity in narrow columns.

Now consider the situation when fluid is flowing through a fixed bed of solids with the same co-ordinate system as shown in Figure 5-6. At equilibrium, the force due to stress on the top face of the element, F_T , and the weight of the element, F_W , will be

balanced by the force due to the stress on the bottom face, F_B , the wall friction, F_F (Janssen's effect), the drag force on the solids, F_d , and the buoyancy force, F_{Bu} . Thus, a force balance on the solids yields:

$$F_B + F_F + F_d + F_{Bu} = F_T + F_W, \quad (5-13)$$

which, when expanded is

$$\begin{aligned} \frac{\pi}{4} D^2 (\sigma_v + d\sigma_v) + (\tan\phi\sigma_H) \pi D dz + \frac{\pi}{4} D^2 dp \\ = \frac{\pi}{4} D^2 \sigma_v + ((1-\epsilon)(\rho_s - \rho_g)g) \frac{\pi}{4} D^2 dz. \end{aligned} \quad (5-14)$$

In the above expression F_W and F_{Bu} have been combined to give the last term on the right hand side of equation 5-14. Simplifying and rearranging the previous equation gives,

$$\frac{d\sigma_v}{dz} + \frac{4\tan\phi\sigma_H}{D} = \left[(1-\epsilon)(\rho_s - \rho_f)g - \frac{dp}{dz} \right]. \quad (5-15)$$

If $\sigma_H = k_J\sigma_v$ is assumed, as in equation 5-11,

$$\frac{d\sigma_v}{dz} + \frac{4\tan\phi k_J\sigma_v}{D} = \left[(1-\epsilon)(\rho_s - \rho_f)g - \frac{dp}{dz} \right], \quad (5-16)$$

which may be written as

$$\frac{d\sigma_v}{dz} + c_1\sigma_v = c_2, \quad (5-17)$$

where

$$c_1 = \frac{4\tan\phi k_J}{D} \text{ and} \quad (5-18)$$

$$c_2 = \left[(1-\epsilon)(\rho_s - \rho_f)g - \frac{dp}{dz} \right]. \quad (5-19)$$

In equation 5-19 there are two additional terms as compared to equation 5-10: the drag term, represented by dp/dz and the buoyancy term.

The solution to equation 5-19 is equivalent to that of equation 5-8

$$\sigma_v = \frac{c_2}{c_1}(1 - e^{-c_1 z}), \quad (5-20)$$

but with different c_1 and c_2 .

Figure 5-7 presents equation 5-20 in graphical form. When the velocity is zero (*i.e.*, there is no gas flowing through the column), then equation 5-20 simplifies to Janssen's equation. As the velocity increases, the vertical contact stresses in the bed are smaller because the drag on the particles supports a fraction of the bed's weight. At and above the point of fluidization, the stresses in the column are zero (as contact does not exist amongst the particles), and thus $d\sigma_v/dz$ is also zero. This situation is only possible if $c_2=0$,

$$c_2 = \left[(1 - \epsilon)(\rho_s - \rho_f)g - \frac{dp}{dz} \right] = 0. \quad (5-21)$$

In equation 5-21, if Ergun's pressure drop expression is substituted (equation 5-4), the resultant expression will be the same as equation 5-7 and the wall effects will not be included in the analysis.

It is now assumed that the horizontal stress is not only a function of the downward vertical stress, but also a function the upward drag forces, caused by the gas flowing through the column. Since Ergun's pressure drop equation is used to calculate the pressure drop, it is assumed that the structure of these new terms on which the horizontal stress depends is similar in form to those given by Ergun's equation, but the

velocity terms are being scaled differently. These scales are chosen as they gave a favorable fit to the experimental data.

$$\sigma_H = k_J \sigma_v - k_1 H \left(\frac{\mu_f}{D g d} \right) V - k_2 H \left(\frac{\rho_f}{D} \right) V^2, \quad (5-22)$$

where k_1 and k_2 are constants.

Substituting equation 5-22 back into equation 5-15, yields:

$$\frac{d\sigma_v}{dz} + \frac{4 \tan \phi k_J \sigma_v}{D} = \left[\frac{4 \tan \phi k_2 (\rho_f) \left(\frac{H}{D} \right)}{D} \right] V^2 + \left[\frac{4 \tan \phi k_1 \left(\frac{\mu_f}{g d} \right) \left(\frac{H}{D} \right)}{D} \right] V + [(1 - \epsilon)(\rho_s - \rho_f)g] - \frac{dp}{dz}. \quad (5-23)$$

Comparing equation 5-23 to equation 5-16, there are two additional terms, proportional to V^2 and V , appearing on the right hand side of equation 5-23. These terms have come about due to the horizontal stress from the wall and the flow of the fluid through the bed.

Substituting Ergun's equation for pressure drop (equation 5-4) into equation 5-23:

$$\frac{d\sigma_v}{dz} + \frac{4 \tan \phi k_J \sigma_v}{D} = \left[\frac{4 \tan \phi k_2 (\rho_f) \left(\frac{H}{D} \right)}{D} - a_E \right] V^2 + \left[\frac{4 \tan \phi k_1 \left(\frac{\mu_f}{g d} \right) \left(\frac{H}{D} \right)}{D} - b_E \right] V + [(1 - \epsilon)(\rho_s - \rho_f)g]. \quad (5-24)$$

This equation is again of the form:

$$\frac{d\sigma_v}{dz} + c_1 \sigma_v = c_2. \quad (5-25)$$

where:

$$c_1 = \frac{4 \tan \phi k_J}{D} \text{ and} \quad (5-26)$$

$$\begin{aligned}
-c_2 = & \left[a_E - \frac{4 \tan \phi k_2 (\rho_f) \left(\frac{H}{D} \right)}{D} \right] V^2 \\
& + \left[b_E - \frac{4 \tan \phi k_1 \left(\frac{\mu}{g d} \right) \left(\frac{H}{D} \right)}{D} \right] V - [(1 - \epsilon)(\rho_s - \rho_f)g].
\end{aligned} \tag{5-27}$$

Setting $c_2=0$, the condition which is necessary for fluidization, and integrating over the length of the column:

$$\left[a_E - \frac{4 \tan \phi k_2' (\rho_g) \left(\frac{H}{D} \right)}{D} \right] V^2 + \left[b_E - \frac{4 \tan \phi k_1' \left(\frac{\mu_f}{g d} \right) \left(\frac{H}{D} \right)}{D} \right] V - [(1 - \epsilon)(\rho_s - \rho_f)g] = 0. \tag{5-28}$$

where k_1' and k_2' are lumped parameters which also include integration coefficients.

Substituting for a_E and b_E , which are Ergun's constants, yields;

$$\begin{aligned}
& \left[1.75 \frac{(1 - \epsilon)}{\epsilon^3} - 4 \tan \phi k_2' \left(\frac{g d}{D} \right) \left(\frac{H}{D} \right) \right] \frac{\rho_f V^2}{g d} + \\
& \left[150 \frac{(1 - \epsilon)^2}{\epsilon^3} - 4 \tan \phi k_1' \left(\frac{g d}{D} \right) \left(\frac{H}{D} \right) \right] \frac{\mu_f V}{(g d)^2} = [(1 - \epsilon)(\rho_s - \rho_f)g].
\end{aligned} \tag{5-29}$$

Multiplying throughout by the factor $\frac{\rho_f (g d)^3}{\mu_f^2}$ in order to make the equation

dimensionless gives:

$$\begin{aligned}
& \left[1.75 \frac{(1 - \epsilon)}{\epsilon^3} - 4 \tan \phi k_2' \left(\frac{g d}{D} \right) \left(\frac{H}{D} \right) \right] \text{Re}_{\rho-mf}^2 \\
& + \left[150 \frac{(1 - \epsilon)^2}{\epsilon^3} - 4 \tan \phi k_1' \left(\frac{g d}{D} \right) \left(\frac{H}{D} \right) \right] \text{Re}_{\rho-mf} = [(1 - \epsilon) Ar].
\end{aligned} \tag{5-30}$$

Equation 5-30 is a quadratic equation which can be easily solved for $\text{Re}_{\rho-mf}$, with k_1' and k_2' remaining constant. Rewriting equation 5-30 results in

$$a'' \left(\epsilon, \varphi, \left(\frac{\vartheta d}{D} \right), \left(\frac{H}{D} \right) \right) \text{Re}_{\rho-mf}^2 + b'' \left(\epsilon, \varphi, \left(\frac{\vartheta d}{D} \right), \left(\frac{H}{D} \right) \right) \text{Re}_{\rho-mf} - (1 - \epsilon) Ar = 0, \quad (5-31)$$

where a'' and b'' are functions not only of ϵ and φ , but also of $(\vartheta d/D)$ and (H/D) . Hence, both the ratio of particle size to column diameter $(\vartheta d/D)$ and the bed aspect ratio (H/D) play a role in determining U_{mf} .

Results and Discussion

The values of the universal constants k_1' and k_2' which give the minimum error for the experimental data set presented in this study were found out to be 610 and 30.1, respectively. In Figures 5-2 to 5-5 and Figures 5-8 and 5-9, the values of the universal constants k_1' and k_2' are kept at these values for all of the particle types, bed heights, and column diameters.

Figures 5-2 to 5-5 show that including the wall effects in the prediction of U_{mf} is successful in describing the effects of height versus column diameter (H/D) and the effect of particle size to column diameter (d/D) . The model only slightly under-predicts the increase in U_{mf} for very small sized particles ($d < 120 \mu\text{m}$) in the column with $D = 1.6$ cm, which is likely due electro-static cohesive and adhesive forces.

For a fixed column diameter, as the H/D ratio increases, U_{mf} increases (Figures 5-2 to 5-5). Hence, as the column becomes taller in comparison to its diameter, the wall effects are more prominent, making it more difficult to fluidize the particles. Also, for a constant particle size, as d/D ratio increases (due to changes in column diameter), U_{mf} increases (compare Figures 5-2 and 5-3 or Figures 5-4 and 5-5). As the column diameter decreases in comparison to the particle diameter, the ratio of wall contact surface area to the bulk volume increases, leading to a more significant wall effect. This wall effect reduces as the column increases in diameter relative to the particles, and

eventually becomes negligible as d/D becomes very small. The effect of H/D and d/D on U_{mf} are very similar; in fact, the increase in U_{mf} can be characterized by the product of H/D and d/D (equation 5-30). Additionally, as particle size increases and approaches the same order of magnitude as the column diameter ($d/D \sim O(1)$), then fluidization becomes difficult. Above a certain d/D ratio, the particle mixture is impossible to fluidize. This situation is predicted by the model, as the quadratic equation yields complex roots. Similarly, equation 5-30 breaks down for large H/D ratio predicting that at large H/D the gas may not fluidize the bed. For example, the model predicts that if glass particles of size 250 μm are fluidized in a 760 μm diameter column ($D/d \sim 3$) with $H/D = 1$, then the particles will not fluidize. Similarly, the model also predicts that if these particles are loaded into a 100 cm diameter column to a bed height of about 13 m ($H/D \sim 13$), the gas may not fluidize the bed.

Figure 5-8 compares the experimental data from Liu *et al.*²⁵ to the values predicted by the model. The data are plotted in the same dimensional form as given in the original work of Liu *et al.*²⁵. The model does not predict the increase in U_{mf} for the smaller particles ($d = 96.4 \mu\text{m}$), but it does give good predictions for the larger particle sizes. In this case also, the values of k_1' and k_2' are maintained at 610 and 30.1 respectively. For the largest particles ($d = 460 \mu\text{m}$), the prediction for the smallest diameter column is not that good, but this may be due to experimental error, which is not reported in Liu *et al.*²⁵. Also, the values of voidage were not clearly stated; only values of bulk density were given. In the model, the values of bulk density were kept constant with respect to the column diameter, but it has been observed that this value changes depending on the column diameter⁷³, particularly for small column diameters.

Figure 5-9 compares the model results to the average predictions of the Reynolds number at U_{mf} based on a large number of existing correlations²⁶⁻³⁹. The scatter bars on the correlation line represent the deviation in minimum fluidization velocity predictions using the different correlations. The experimental data obtained when the wall effects are minimum (at $H=2\text{cm}$ and $D=2.4\text{cm}$) are consistent with the model prediction and with the averaged correlation curve. On the other hand, only the new model is able to predict experimental data obtained when the wall effects are significant (at $H=10\text{cm}$, $D=1.6\text{cm}$), since the existing correlations for U_{mf} do not take wall effects into account.

Summary

Experiments show that wall effects influence the minimum fluidization velocity. Existing correlations fail to incorporate these wall effects. The model presented in this study attempts to include the wall influence by introducing Janssen's wall effect in the force balance during fluidization. This assumption leads to a modified Ergun's equation. The new model fits experimental data reasonably well for the minimum fluidization velocity over a range of particles sizes ($100\ \mu\text{m} - 500\ \mu\text{m}$), bed heights, and column diameters ($H/D > 6$). Some deficiencies in the model predictions are noted for smaller particles (around $100\ \mu\text{m}$ and smaller), but these deficiencies may be due to the significance of cohesive and adhesive forces at this scale.

Table 5-1. Experimental materials and properties

Material	Diameter (μm)	Density (kg/m ³)	Sphericity	Coefficient of friction	Notation
Glass	105 – 125	2500	0.9	0.4	G116
Glass	210 – 250	2500	0.9	0.4	G231
Glass	250 – 300	2500	0.9	0.4	G275
Glass	350 – 420	2500	0.9	0.4	G385
Glass	420 – 500	2500	0.9	0.4	G462
Glass	500 – 600	2500	0.9	0.4	G550
Polystyrene	250 – 300	1250	0.9	0.5	P275
Polystyrene	300 – 354	1250	0.9	0.5	P328

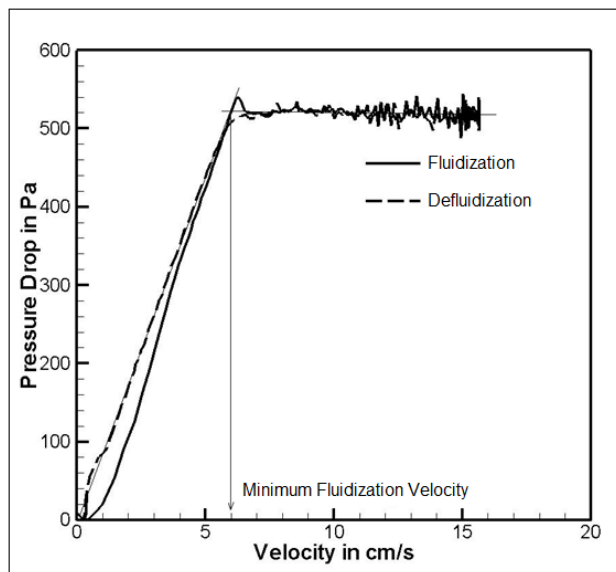


Figure 5-1. Example of a pressure drop profile (fluidization and defluidization) using G231 particles in the 1.6 cm diameter column. The minimum fluidization velocity is also shown in the figure

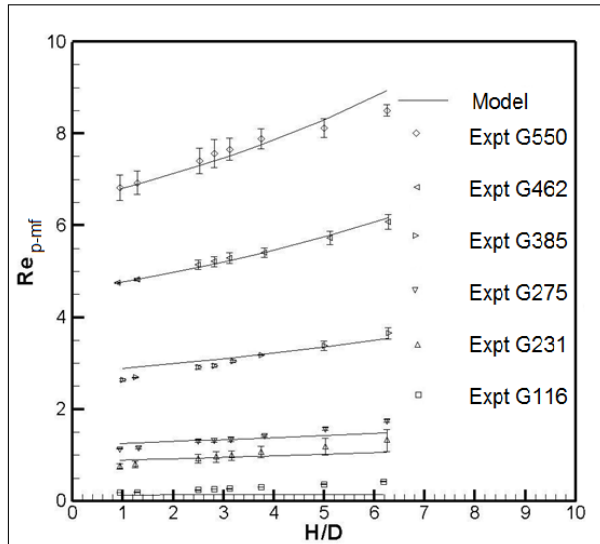


Figure 5-2. Re_{p-mf} as a function of H/D , for different glass particles in the column $D=1.6$ cm

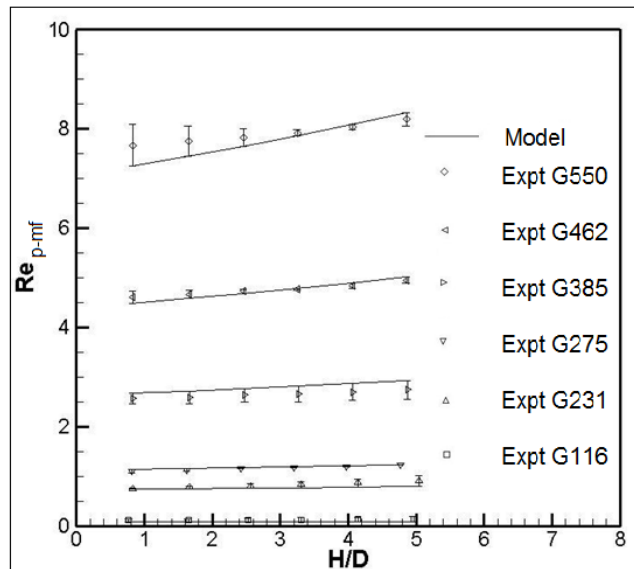


Figure 5-3. Re_{p-mf} as a function of H/D , for different glass particles in the column $D=2.4$ cm.

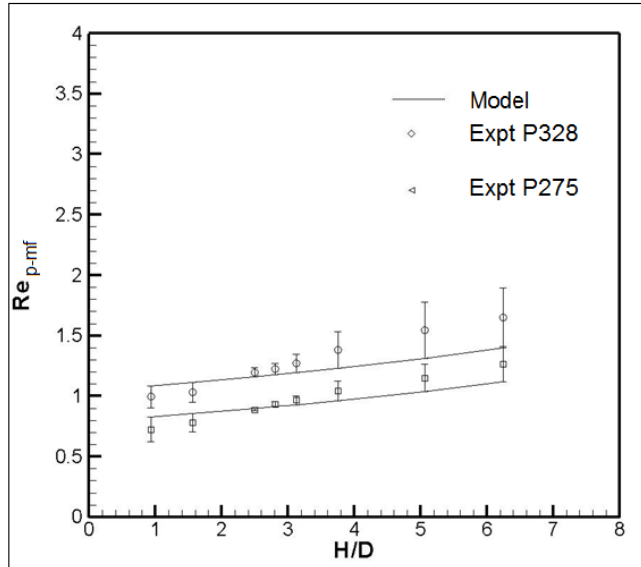


Figure 5-4. Re_{p-mf} as a function of H/D , for polystyrene particles in the column $D=1.6$ cm.

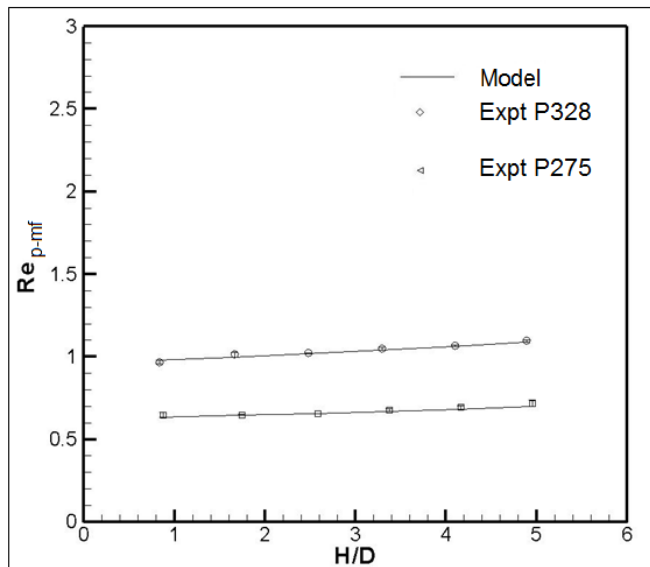


Figure 5-5. Re_{p-mf} as a function of H/D , for polystyrene particles in the column $D=2.4$ cm.

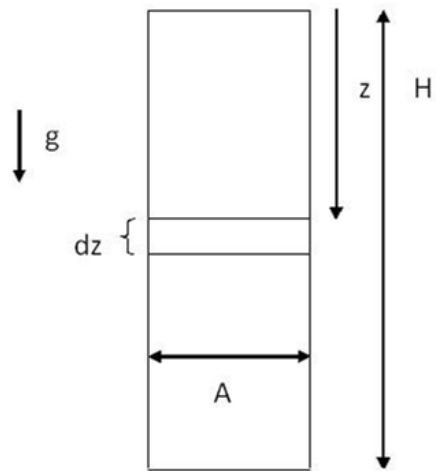


Figure 5-6. Sketch showing the fluidized bed coordinate system.

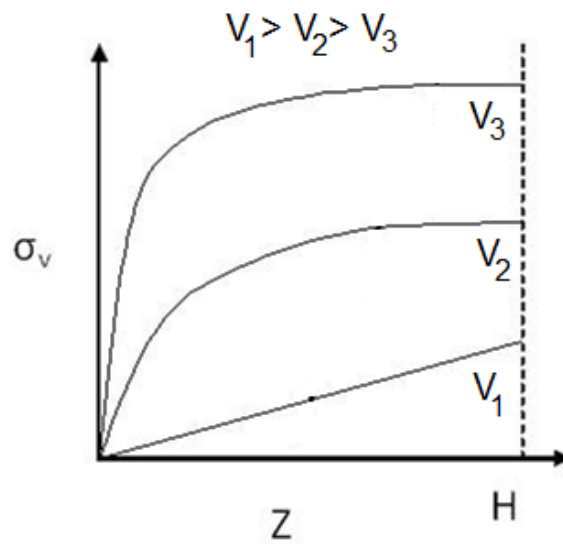


Figure 5-7. A schematic showing how the vertical stress in the bed varies with bed depth at different fluid velocity V_1 , V_2 and V_3 .

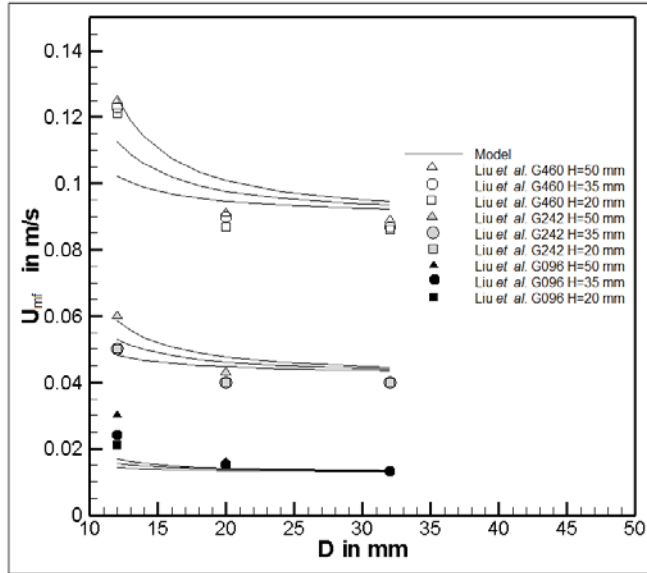


Figure 5-8. The minimum fluidization velocity as a function of the column diameter using the experimental data from Liu *et al.*²⁵. The curves are from equation 5-30.

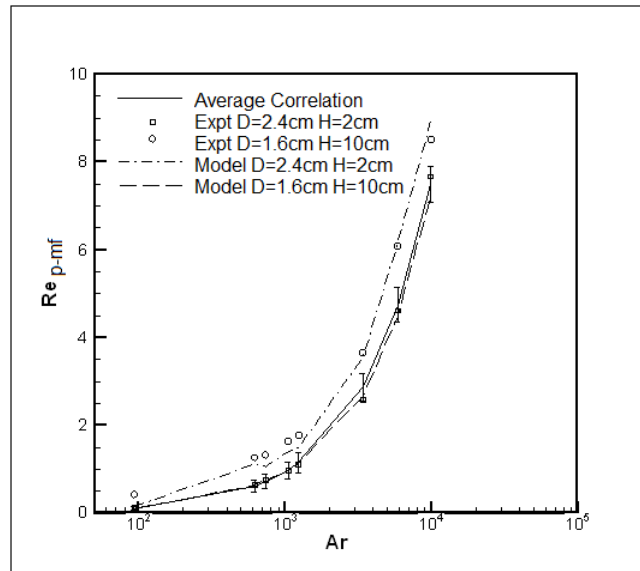


Figure 5-9. Comparison of the curves from equation 5-30 to the experimental data and existing correlations.

CHAPTER 6 CONCLUSIONS AND RECOMMENDATIONS

In this dissertation several aspects of fluid-solid fluidized systems are studied.

Models and co-relations are developed and many qualitative conclusions are drawn.

The most important contributions of the present study are:

- Development of a dilute, turbulent, gas-solid flow model which incorporates an improved description for interactions at the level of velocity fluctuations in both phases.
- Acquisition of detailed and non-intrusive flow data for dilute-phase liquid-solid flows in the transitional (intermediate ST) regime.
- Development of a dilute, turbulent, liquid-solid flow model for viscous, transitional and inertia flow regimes.
- Acquisition of axial segregation data of binary mixtures for gas fluidized beds and its qualitative analysis.
- Development of a semi-correlation to predict enhancement in minimum fluidization velocity in fluidized bed due to wall effects.

Dilute Turbulent Fluid-Solid Fluidized Flows

Experimental data for fully developed profiles of pneumatically conveyed solid particles in a vertical pipe ² have been available in the literature for more than twenty years. Many authors have proposed Eulerian based, dilute turbulent gas-solid flow models incorporating particle-particle interactions using a two-equation $k-\epsilon$ model to describe gas-phase turbulence ^{7, 8, 46, 9} to simulate these data. These Eulerian models have used various combinations of relations for drag, solid-phase stress, and fluctuating interaction terms to successfully predict for the gas-solid flow's mean velocities.

Unfortunately these models consistently under predict the gas turbulence and granular temperature. In the present study, the work of Bolio *et al.* ⁷ is advanced to include a new closure relation for the fluctuating velocity interaction.

The proposed new model (FET model along with Sinclair and Mallo, ⁴⁴ cross-correlation) for the fluctuating interaction term is formulated using an analogy with heat transfer. The time scales for the FET model depend on the Stokes number (ST) while activation of vortex shedding depends on Re_p . If $ST < 100$, particle drag is responsible for the energy transfer and if $ST > 100$, then particle collisions are responsible for energy transfer. These observations are consistent with the findings of Gore and Crowe ¹⁰ and Hestroni ¹¹.

The proposed new fluctuating interaction term model, along with the Wen and Yu ³⁹ drag relation, the Peirano and Leckner ⁵¹ solid stress closure which includes fluid effects, is evaluated against several benchmark experimental data sets. The new model predicts the mean velocity profiles and also the fluctuations velocity profiles of gas and solid for both small and large particles. For particles with $Re_p > 150$ vortex shedding is included in this model. It is also observed that the fluctuating interaction terms strongly influence the magnitude of gas turbulence away from the wall. Near the wall, turbulence generation and dissipation dominate over the fluctuating interaction term. In contrast, the predicted profiles are not sensitive to the choice of drag model or the solid-stress closure. Nevertheless, for liquid-solid flows the Peirano and Leckner ⁵¹ model for solid stress shows an improvement in the flow predictions because it takes the fluid effects into account. Also, the correlation of Syamlal and O'Brien ⁴⁹ predicts the slip velocity more accurately in the case of the liquid-solid cases.

The mean and fluctuation velocity data for 0.5 mm and 1 mm ¹³ and 1.5 mm (present study) particles obtained in a vertical pipe under dilute and highly turbulent conditions are benchmark data sets. The 2.32 mm particles ¹², with $ST > 40$,

demonstrate inertia-dominated flow regime. In this flow regime, particle-particle interactions dominate the flow behavior. The high ST model uses the Syamlal and O'Brien⁴⁹ drag relationship which predicts the velocity slip correctly, the Peirano and Leckner⁵¹ model for solid-phase stress and the FET model which predicts the shape and magnitude of the fluctuating velocities well, especially at the wall. The 0.5 mm particles¹³, with $ST < 5$, display viscous-dominated flow behavior, wherein the particles tend to mimic the fluid motion. Hence, the flow behavior for the liquid and solid are similar. The Chen and Wood¹⁵ model is used to describe the behavior for the low ST flows. Finally, the 1 mm¹³ and 1.5 mm particles, with $5 < ST < 40$, exhibit transitional behavior. There is sudden increase in the solid velocity fluctuations with increasing ST which may be due to the curved paths followed by the solids. The data obtained for some of the cases show non-monotonic relationships with the mass loading and operating velocity. For the intermediate ST model, the closures described for solid-phase viscosity and conductivity predict the shape of the fluctuating velocity profiles appropriately. In addition, the correlation developed for the time scale for fluctuating energy interaction term predicts the flow behavior of the transitional regime fairly well. To improve the predictions in the transitional regime, granular kinetic theory must be modified to include the effects of the deviations from the straight line paths followed by the solids.

Also, it is shown in the present study that models developed for gas-solid flows can be extended to liquid-solid flows. The models described herein give insight into how fluid-solid flows behave under various operating conditions and ST .

In industry, fluid-solid flows are often operated at higher mass loadings than the mass loadings of the experimental conditions seen in the present study. In the future efforts should be made to measure the detailed velocity profile of fluid-solid flows at higher mass loading using a non-intrusive measurement technique. Although it is difficult to measure velocities under higher mass loading conditions (due to signal attenuation and low data rate), matching refractive indices of the fluid and solid phases may help. The data acquired can be used to validate dense-phase flow models. Furthermore, models for prediction of drag forces on non-spherical particles are also available⁷⁵. If these models are used to close the drag relation in the Eulerian two-fluid model, potentially particle shape can also be included in the analysis.

Further, the flow loop experiments can be extended to study radial segregation of binary mixtures under dilute and turbulent flow conditions. For the segregation experiments, a PDPA system must be used as it not only measures velocities but also measures the diameter distribution. This information can be used to develop an Eulerian model to predict fluid-solid flows of binary mixtures. This model will also be useful because real situations deal with polydispered particle systems.

Fluidized Beds – Segregation of Binary Mixtures and Wall Effects

In this study, axial segregation of binary mixtures is studied in a fluidized bed. A new classification scheme for the pressure drop profiles and segregation behavior of binary fluidized mixtures is presented and seven mixture types are proposed. This classification scheme is based on the particle size and density ratio of the two components and incorporates new data as well as previously published data exhibiting a wide range of fluidization behavior.

In addition, based on the Archimedes number ratio for the mixture, the ratio of minimum fluidization velocities of the individual components can be estimated and the level of disparity can be identified. The knowledge of the mixture type and level of disparity in advance is a significant aid when one can select the size or density ratio in order to mitigate fluidization segregation and improve process efficiency. Further, identifying the jetsam and the flotsam in case of mixtures with a difference in size and density opposing each other may also help explain deviations from regular behavioral patterns due to layer inversion.

Additional experimentation will be necessary to further refine the boundaries for the seven mixture types. If the experiments are performed in a column with a large diameter (to minimize the influence of the wall), quantitative results can be obtained instead of qualitative observations, to precisely predict the segregation pattern.

The effect of H/D on segregation is also studied in the present work. It is observed that even at high fluidization velocities and with mixtures with fairly low level of disparity, if the H/D ratio of the column is indefinitely increased, segregated tails start appearing at the ends of the column.

Experiments show that wall effects influence the minimum fluidization velocity of monosized particles. If the H/D or the d/D ratio is increased the minimum fluidization velocity increases. Existing correlations fail to incorporate these wall effects and, hence, there is a need for a new model that can take these effects into consideration. The model presented in this study attempts to include the wall influence by introducing Janssen's wall effect in the force balance during fluidization. It is assumed that the horizontal stresses acting at the wall are not only a function of the local vertical stress,

but also are a quadratic function of velocity. These new terms have the same structure as that of the drag term, *i.e.*, the pressure drop, as given by the widely-accepted Ergun equation. This assumption leads to a modified Ergun's equation incorporating two universal constants. The new model fits experimental data reasonably well for the minimum fluidization velocity over a range of particles sizes, bed heights, and column diameters. This new model should greatly facilitate scaling results from micro fluidized beds to more traditional fluid bed sizes.

This model can be further improved to include of cohesive and adhesive effects due to electrostatic forces. This may help predict minimum fluidization velocity for smaller particles (around 100 μm and smaller).

APPENDIX A DILUTE-TURBULENT FLUID-SOLID FLOW PROGRAM

PhD_Data.m

```
%User Input File
%Operating Conditions
Re_center_line=yes;
m=0.0000001;
%Experimental set up
R=0.01525;
g=9.81;
%Fluid
muf=0.000018;
rhof=1.2;
Re=14.2*rhof*R^2/muf;
%Solid
rhos=1020;
d=2780*10^-6;
sphere=1;
nus0=0.65;
e=0.9;
ew=0.9;
fi=0.002;
%To specify a grid say yes
%To use default grid say no
User_Defined_Grid=no;
%Is the flow upward or downward
downward=no;
```

PhD_Model_Options.m

```
%Select Models
% 1)The Interaction terms
% 1.1)Drag Term description
Ding_Gidaspow_1990=yes;
% 1.1.1)Definition of CD
Wen_Yu=no;
Hill_Koch_Ladd=no;
Syamlal_OBrien=yes;
% 1.2)FKS & FKF description
FET=yes; %FET + Sinclair and Mallo
Louge_etal_1991=no; %TVBA + Louge
Sinclair_and_Mallo_1998=no; %TVBA + Sinclair and Mallo
Simonin_1996=no; %TVBA + Simonin
Koch_Sangani_1999=no; %TVBA + Koch & Sangani
Wylie_etal_2003=no; %TVBA + Wylie
Zhang_Reese_2003=no; %VBA + Zhang and Reese
Chen_Wood=no; %TVBA + Chen and Wood
% 1.3)Wake enhancement in k-E equation
Lun_Wake_term=yes;
% 2)Solid Stress Models
GKT=yes;
% 2.1)Description of diffusion coefficients for Vs and T
Lun=no;
Pierano_Leckner=yes;
% 3)Boundary Conditions
```

```

% 3.1)Vfzd Boundary Condition
Vfz_no_slip=yes;
Vfz_wall_Mfix=no;
% 3.2)Vszd Boundary Condition
Vsz_no_slip=no;
Johnson_Jackson_Vsz=yes;
Vsz_wall_Mfix=no;
fiw=0*pi/180;
% 3.3)Td Boundary Condition
Johnson_Jackson_T=yes;
Td_wall_Mfix=no;
fiw=0*pi/180;
% 3.4)kd Boundary Condition
k_no_slip=yes;
k_wall_Mfix=no;
% 3.5)Ed Boundary Condition
Bolio_equation_2_62=yes;
E_wall_Mfix=no;
% 4)muef model
Batchelor_Green=yes;

```

PhD_Model_Parameters.m

```

%Set Model Parameters and Weights
%Drag term parameters
wVfz(1)=-10; %weight of drag term on Vfz equation
wVsz(1)=10; %weight of drag term on Vsz equation
%Myung and Kasagi Parameters
sigmak=1.4;
sigmaE=1.3;
cT1=1.4;
cT2=1.8;
cT3=1.2;
cmu=0.09;
fT1=1;
%Mfix Parameters
% sigmak=1;
% sigmaE=1.3;
% cT1=1.44;
% cT2=1.92;
% cT3=1.22;
% cmu=0.09;
% fT1=1;
wk(1)=-20; %weight of Generation term on k equation
wE=[10 10]; %weight of 1)Generation; 2)Dissipation terms on E equation
%PTE parameters
wT=[-10 -10]; %weight of 1)Generation; 2)Dissipation terms on T equation
%Interacton terms parameters
wk(2)=-10; %weight of Interaction term on k equation
wT(3)=-10; %weight of Interaction term on T equation

```

PhD_Marching_Parameters.m

```

%Set Marching Parameters
%Setting Marching Parameters
%For Re Marching
n_Re_march=10000;

```

```

Re_jump=0.05;
n_Re_iterations=50000;
%For m Marching
n_m_march=10000;
if rhof<200
    %For Gas-Solid flows
    m_start=0.05;
    m_jump=0.05;
    lower_jump_limit=0.001;
else
    %For Liquid-Solid flows
    m_start=0.2;
    m_jump=0.2;
    lower_jump_limit=0.00001;
end
n_m_iterations=20000;
%output shows up after every n_m_working iterations
n_m_working=500;
%Tolerance Level
nus_tolerance=0.0000000001;
Vfzd_tolerance=0.0000000001;
Vszd_tolerance=0.0000000001;
Td_tolerance=0.0000000001;
kd_tolerance=0.0000000001;
Ed_tolerance=0.0000000001;
kTd_tolerance=0.0000000001;
%Guess Vsz/Vfz at Center-Line
%keep 0<Ratio_V<1
%Increase Ratio_V-->1 if code breaks down
Ratio_V=0.9;

```

PhD_ST_Classify.m

```

%Conditions for Low ST
Low_ST=no;
Mid_ST=no;
High_ST=no;
if ST<=5
    disp('*****!')
    disp('Running Low ST number case')
    disp('Running Chen and Wood')
    disp('Assuming k=T')
    disp('Assuming Vsz(r=R)=0')
    disp('*****!')
    Low_ST=yes;
    Chen_Wood=yes;
    FET=no;
    Louge_etal_1991=no;
    Sinclair_and_Mallo_1998=no;
    Simonin_1996=no;
    Koch_Sangani_1999=no;
    Wylie_etal_2003=no;
    Zhang_Reese_2003=no;
    Vsz_no_slip=yes;
    Johnson_Jackson_Vsz=no;
    Vsz_wall_Mfix=no;
end

```

```

if ST>5 && ST<=40
    disp('*****')
    disp('Running Mid ST number case')
    disp('*****')
    Mid_ST=yes;
end
if ST>40
    disp('*****')
    disp('Running High ST number case')
    disp('*****')
    High_ST=yes;
end

```

PhD_Guess_Profiles.m

```

%Guess Profiles
%Guess for Mfix wall conditions
if Vfz_wall_Mfix==yes || k_wall_Mfix==yes
    if Re<50001
        load Re_50000_wall
    end
    if Re>50000 && Re<100001
        load Re_100000_wall
    end
    if Re>100000 && Re<200001
        load Re_200000_wall
    end
    if Re>200000 && Re<300001
        load Re_300000_wall
    end
    if Re>300000 && Re<400001
        load Re_400000_wall
    end
    if Re>400000 && Re<500001
        load Re_500000_wall
    end
    if Re>500000
        load Re_500000_wall
    end
%Guess for No-slip condition
else
    if Re<50001
        load Re_50000
    end
    if Re>50000 && Re<100001
        load Re_100000
    end
    if Re>100000 && Re<200001
        load Re_200000
    end
    if Re>200000 && Re<300001
        load Re_300000
    end
    if Re>300000 && Re<400001
        load Re_400000
    end
    if Re>400000 && Re<500001

```

```

    load Re_500000
end
if Re>500000
    load Re_500000
end
end
end

```

PhD_Regridding.m

```

%Adjusting guess grid to User specified grid
clear temp
load User_Specified_Grid
[n,dummy]=size(r_User_Defined); %Finding number of new grid points
rdim_UD=r_User_Defined/R;
temp=zeros(3,n);
%Interpolating values for the new grid
for i=1:n
    temp(1,i)=interp1(rdim,Vfzd,rdim_UD(i));
    temp(2,i)=interp1(rdim,kd,rdim_UD(i));
    temp(3,i)=interp1(rdim,Ed,rdim_UD(i));
end
clear Vfzd kd Ed dummy
Vfzd=temp(1,:);
kd=temp(2,:);
Ed=temp(3,:);
rdim=rdim_UD;
clear temp rdim_UD %Clearing the unnecessary

```

PhD_1_Strain.m

```

%Calculating single phase strain
for i=1:n
    if i==1 || i==n
        if i==1
            dVfzdr(i)=0;
        else
            h1=drb(n);
            h2=drb(n)+drb(n-1);
            dVfzdr(i)=h1*h2/(h2-h1)*((Vfzd(i)-Vfzd(i-1))/h1^2-(Vfzd(i)-Vfzd(i-2))/h2^2);
        end
    else
        h1=drf(i);
        h2=drb(i);
        dVfzdr(i)=h1*h2/(h1+h2)*((Vfzd(i+1)-Vfzd(i))/h1^2+(Vfzd(i)-Vfzd(i-1))/h2^2);
    end
end
end

```

PhD_2_Strain.m

```

%Calculating two phase strain
for i=1:n
    if i==1 || i==n
        if i==1
            dVfzdr(i)=0;
            dVszdr(i)=0;
        else
            h1=drb(n);
            h2=drb(n)+drb(n-1);

```

```

    dVfzdr(i)=h1*h2/(h2-h1)*((Vfzd(i)-Vfzd(i-1))/h1^2-(Vfzd(i)-Vfzd(i-2))/h2^2);
    dVszdr(i)=h1*h2/(h2-h1)*((Vszd(i)-Vszd(i-1))/h1^2-(Vszd(i)-Vszd(i-2))/h2^2);
end
else
    h1=drf(i);
    h2=drb(i);
    dVfzdr(i)=h1*h2/(h1+h2)*((Vfzd(i+1)-Vfzd(i))/h1^2+(Vfzd(i)-Vfzd(i-1))/h2^2);
    dVszdr(i)=h1*h2/(h1+h2)*((Vszd(i+1)-Vszd(i))/h1^2+(Vszd(i)-Vszd(i-1))/h2^2);
end
end
end

```

PhD_1_Viscosity.m

```

%Calculating single phase viscosity
%Calculating dimensionless friction velocity
UTd=(-dVfzdr(n))^0.5;
%Calculating eddy viscosity
%Using Wall conditions from MFIX
if Vfz_wall_Mfix==yes || k_wall_Mfix==yes
    for i=1:n
        RT(i)=kd(i)^2/Ed(i);
        yplus(i)=UTd*(rd(n)-rd(i));
        fmu=1;
        muTd(i)=cmu*fmu*kd(i)^2/Ed(i);
        dmuTdkd(i)=(2*cmu*fmu*kd(i)/Ed(i));
        dmuTdEd(i)=(-cmu*fmu*kd(i)^2/Ed(i)^2);
    end
%Using the no-slip boundary conditions
else
    for i=1:n
        RT(i)=kd(i)^2/Ed(i);
        yplus(i)=UTd*(rd(n)-rd(i));
        %For no-slip at the wall
        if i==n
            fmu=0;
            muTd(i)=0;
        %for rest of the pipe
        else
            fmu=(1-exp(-yplus(i)/70))*(1+3.45/RT(i)^0.5);
            muTd(i)=cmu*fmu*kd(i)^2/Ed(i);
        end
        dRTdkd=2*kd(i)/Ed(i);
        dfmudkd=-(1-exp(-yplus(i)/70))*(3.45/2*(RT(i)^-1.5)*dRTdkd);
        dmuTdkd(i)=(2*cmu*fmu*kd(i)/Ed(i))+cmu*kd(i)^2/Ed(i)*dfmudkd; %Calculating dmuTd/dkd
        dRTdEd=-kd(i)^2/Ed(i)^2;
        dfmudEd=-(1-exp(-yplus(i)/70))*(3.45/2*(RT(i)^-1.5)*dRTdEd);
        dmuTdEd(i)=(-cmu*fmu*kd(i)^2/Ed(i)^2)+cmu*kd(i)^2/Ed(i)*dfmudEd; %Calculating dmuTd/dkd
    end
end

```

PhD_2_Viscosity.m

```

%Calculating two phase viscosities
UTd=(abs(dVfzdr(n)))^0.5; %Calculating Friction velocity
%Calculating muefd
if Batchelor_Green==yes
    for i=1:n
        muefd(i)=(1+2.5*nus(i)+7.6*nus(i)^2)*(1-nus(i)/nus0);
    end
end

```

```

end
end
%k-E model for muT
if Vfz_wall_Mfix==yes || k_wall_Mfix==yes
    for i=1:n
        RT(i)=kd(i)^2/Ed(i)/muefd(i);
        yplus(i)=UTd*(rd(n)-rd(i));
        fmu=1;
        muTd(i)=cmu*fmu*kd(i)^2/Ed(i);
        dmuTdkd(i)=(2*cmu*fmu*kd(i)/Ed(i));
        dmuTdEd(i)=(-cmu*fmu*kd(i)^2/Ed(i)^2);
    end
else
    for i=1:n
        RT(i)=kd(i)^2/Ed(i)/muefd(i);
        yplus(i)=UTd*(rd(n)-rd(i));
        if i==n
            fmu=0;
            muTd(i)=0;
        else
            fmu=(1-exp(-yplus(i)/70))*(1+3.45/RT(i)^0.5);
            muTd(i)=cmu*fmu*kd(i)^2/Ed(i); %Calculating muTd
        end
        dRTdkd=2*kd(i)/Ed(i)/muefd(i);
        dfmudkd=-(1-exp(-yplus(i)/70))*(3.45/2*(RT(i)^-1.5)*dRTdkd);
        dmuTdkd(i)=(2*cmu*fmu*kd(i)/Ed(i))+cmu*kd(i)^2/Ed(i)*dfmudkd; %Calculating dmuTd/dkd
        dRTdEd=-kd(i)^2/Ed(i)^2/muefd(i);
        dfmudEd=-(1-exp(-yplus(i)/70))*(3.45/2*(RT(i)^-1.5)*dRTdEd);
        dmuTdEd(i)=(-cmu*fmu*kd(i)^2/Ed(i)^2)+cmu*kd(i)^2/Ed(i)*dfmudEd; %Calculating dmuTd/dEd
    end
end
end
%Granular Kinetic Thoery Parameters
if GKT==yes
    PhD_mus_lambda_Models
end

PhD_mus_lambda_Models.m
%lambda_mus_models
%For Low Stokes number
if Low_ST==yes
    for i=1:n
        if i==n
            musdG(i)=muefd(i)+0;
            lambdadG(i)=muefd(i)+0;
        else
            temp1=Rep^2/18*rhos/rhof*2/3/cmu*Ed(i)/kd(i);
            musdG(i)=muefd(i)+muTd(i)/(1+temp1);
            lambdadG(i)=muefd(i)+muTd(i)/sigmak/(1+temp1);
        end
    end
end
end
%For Mid and High Stokes number
if Mid_ST==yes || High_ST==yes
    %High Stokes number relations
    if Lun==yes
        for i=1:n

```

```

musd(i)=5/96*pi^0.5*rhos/rhof*Rep*Td(i)^0.5; %Calculating musd
lambdad(i)=25/128*pi^0.5*rhos/rhof*Rep*Td(i)^0.5; %Calculating lambdad
w=(1+dR/6/2^0.5/nus(i))^-1;
g0=(nus0^(1/3))/(nus0^(1/3)-nus(i)^(1/3));
G1k(i)=(1+8/5*eta*nus(i)*g0*(3*eta-2))/(eta*(2-eta)*g0);
G1c(i)=(((1+8/5*eta*nus(i)*g0*(3*eta-2))*8*nus(i))/(5*(2-eta)))+(768*nus(i)^2*g0*eta/25/pi);
G2k(i)=nus(i);
G2c(i)=4*eta*nus(i)^2*g0;
G3k(i)=8*(1+12*eta^2*nus(i)*g0*(4*eta-3)/5)/eta/(41-33*eta)/g0;
G3c(i)=96*nus(i)*(1+12*eta^2*nus(i)*g0*(4*eta-3)/5+16*eta*nus(i)*g0*(41-33*eta)/15/pi)/5/(41-
33*eta);
alpha(i)=(w*G2k(i)+G2c(i)); %Calculating alpha
dwdnus=((1+dR/6/2^0.5/nus(i))^-2)*dR/6/2^0.5/nus(i)^2;
dg0dnus=(nus0^(1/3))/3/((nus0^(1/3)-nus(i)^(1/3))^2)/nus0^(2/3);
dalphadnus(i)=w+nus(i)*dwdnus+8*eta*nus(i)*g0+4*eta*nus(i)^2*dg0dnus; %Calculating
dalphadnus
dmusdT(i)=5/96*pi^0.5*rhos/rhof*Rep*(0.5*Td(i)^-0.5);
dmusdT(i)=dmusdT(i)*(w*G1k(i)+G1c(i)); %Calculating dmusd/dTd
musdG(i)=musd(i)*(w*G1k(i)+G1c(i)); %Calculating musd*(wG1k+G1c)
lambdadG(i)=lambdad(i)*(w*G3k(i)+G3c(i)); %Calculating lambdad*(wG1k+G1c)
end
end
if Pierano_Leckner==yes
cbeta=1.8-1.35;
for i=1:n
if i<n
zetar=3*(Vrd(i))^2/2/kd(i);
end
etat=3*cmu/2/(1+cbeta*zetar)^0.5*kd(i)/Ed(i)*rhof/rhos*(1-nus(i))/nus(i)*beta(i);
g0=(nus0^(1/3))/(nus0^(1/3)-nus(i)^(1/3));
dVTau1=(2*Rep*rhof/rhos*(1-nus(i))/nus(i)*beta(i)+(24*nus(i)*g0*(1+e)*(3-e)/5*(Td(i)/pi)^0.5);
dVTau2=(9/5*Rep*rhof/rhos*(1-nus(i))/nus(i)*beta(i)+(24*nus(i)*g0*(1+e)*(49-
33*e)/100*(Td(i)/pi)^0.5);
G1k(i)=nus(i)*rhof/rhof*Rep*(2/3*kTd(i)*etat+Td(i)*(1+2/5*(1+e)*(3*e-1)*nus(i)*g0))/dVTau1;
G1c(i)=8/5*nus(i)*g0*(1+e)^2*(G1k(i)+nus(i)*rhof/rhof*Rep*(Td(i)/pi)^0.5);
G2k(i)=nus(i);
G2c(i)=4*eta*nus(i)^2*g0;
G3k(i)=nus(i)*rhof/rhof*Rep*(9/10*kTd(i)*etat+3/2*Td(i)*(1+(1+e)^2*(2*e-
1)/100*nus(i)*g0))/dVTau2;
G3c(i)=18/5*nus(i)*g0*(1+e)^2*(G3k(i)+5/9*nus(i)*rhof/rhof*Rep*(Td(i)/pi)^0.5);
alpha(i)=(G2k(i)+G2c(i));
musdG(i)=G1k(i)+G1c(i);
lambdadG(i)=G3k(i)+G3c(i);
dg0dnus=(nus0^(1/3))/3/((nus0^(1/3)-nus(i)^(1/3))^2)/nus0^(2/3);
dalphadnus(i)=1+8*eta*nus(i)*g0+4*eta*nus(i)^2*dg0dnus;
end
end
%Using weighted average between high and low Stokes number
if Mid_ST==yes
for i=1:n
if i==n
temp2=muefd(i)+0;
temp3=muefd(i)+0;
else
temp1=Rep^2/18*rhos/rhof^2/3/cmud*Ed(i)/kd(i);
temp2=muefd(i)+muTd(i)/(1+temp1);

```

```

        temp3=muefd(i)+muTd(i)/sigmak/(1+temp1);
    end
    musdG(i)=(ST-5)/(40-5)*musdG(i)+(40-ST)/(40-5)*temp2;
    lambdadG(i)=(ST-5)/(40-5)*lambdadG(i)+(40-ST)/(40-5)*temp3;
end
end
end

```

PhD_Relative_Velocity.m

```

%Relative Velocity
Vrd=Vfzd-Vszd;
for i=1:n
    Vrd2(i)=(Vrd(i)^2+8*Td(i)/pi)^0.5;
end

```

PhD_Drag_Models.m

```

%Drag models for Ding & Gidspow type formulation
%Wen and Yu
if Wen_Yu==yes
    for i=1:n
        Red=(1-nus(i))*Rep*abs(Vrd(i));
        if Red>1000
            CD(i)=0.44;
        else
            CD(i)=24/Red*(1+0.15*Red^0.687);
        end
        beta(i)=3/4/Rep*CD(i)*nus(i)/(1-nus(i))^2.65*abs(Vrd(i));
    end
end
%Hill Koch and Ladd
if Hill_Koch_Ladd==yes
    for i=1:n
        Red=(1-nus(i))*Rep/2*abs(Vrd(i));
        w_HKL=exp(-10*(0.4-nus(i))/nus(i));
        if nus(i)<0.4
            F0=(1-w_HKL)*(1+3*(nus(i)/2)^0.5+135/64*nus(i)*log(nus(i))+17.14*nus(i))/(1+0.681*nus(i)-
8.48*nus(i)^2+8.16*nus(i)^3)+w_HKL*10*nus(i)/(1-nus(i)^3);
        else
            F0=10*nus(i)/(1-nus(i)^3);
        end
        if nus(i)<0.1
            F1=(2/nus(i))^0.5/40;
        else
            F1=0.11+0.00051*exp(11.6*nus(i));
        end
        if nus(i)<0.4
            F2=(1-w_HKL)*(1+3*(nus(i)/2)^0.5+135/64*nus(i)*log(nus(i))+17.89*nus(i))/(1+0.681*nus(i)-
11.03*nus(i)^2+15.41*nus(i)^3)+w_HKL*10*nus(i)/(1-nus(i)^3);
        else
            F2=10*nus(i)/(1-nus(i)^3);
        end
        if nus(i)<0.0953
            F3=0.09351*nus(i)+0.03667;
        else
            F3=0.0673+0.212*nus(i)+0.0232/(1-nus(i))^5;
        end
    end
end

```

```

end
F4=(F3+(F3^2-4*F1*(F0-F2))^0.5)/2/F1;
F5=(F2-1)/(3/8-F3);
if nus>0.01
    if Red>F5
        F=F2+F3*Red;
    else
        F=F0+F1*Red^2;
    end
else
    if Red>F4
        F=F2+F3*Red;
    else
        F=1+3/8*Red;
    end
end
end
CD(i)=4/3*(17.3/2/Red+0.336);
beta(i)=18*F/Rep^2*(1-nus(i))*nus(i);
end
end
%Syamlal and O'Brien
if Syamlal_O'Brien==yes
    for i=1:n
        Red=Rep*abs(Vrd(i));
        A_SO=(1-nus(i))^4.14;
        if (1-nus(i))>0.85
            B_SO=(1-nus(i))^2.65;
        else
            B_SO=0.8*(1-nus(i))^1.28;
        end
        Vrm=0.5*(A_SO-0.06*Red+((0.06*Red)^2+0.12*Red*(2*B_SO-A_SO)+A_SO^2)^0.5);
        CD(i)=(0.63+4.8*(Vrm/Red)^0.5)^2;
        beta(i)=3/4*nus(i)/Vrm^2/Rep*CD(i)*abs(Vrd(i));
    end
end
end

```

PhD_2_Generation.m

%Calculating Generation and corresponding slope terms

%Calculating Solid Stress

```

for i=1:n
    if GKT==yes
        sigmarzd(i)=-musdG(i)*dVszdr(i);
        dsigmarzdT(i)=-dmusdT(i)*dVszdr(i);
    end
end

```

end

%Compiling the Generation terms for all the equations

```

for i=1:n
    %The Pressure Drop / Gravity term is solved internaly
    G_Vfzd(i)=0;
    dG_Vfzd(i)=0;
    if downward==yes
        G_Vszd(i)=Ar/Rep^3*nus(i);
    else
        G_Vszd(i)=-Ar/Rep^3*nus(i);
    end
    dG_Vszd(i)=0;
end

```

```

G_Td(i)=-sigmarzd(i)*dVszdr(i);
dG_Td(i)=-wT(1)*dsigmarzdT(i)*dVszdr(i);
G_kd(i)=(1-nus(i))*muTd(i)*dVfzdr(i)^2;
dG_kd(i)=(1-nus(i))*wk(1)*dmuTdkd(i)*dVfzdr(i)^2;
if Vfz_wall_Mfix==yes || k_wall_Mfix==yes
    G_Ed(i)=(1-nus(i))*cT1*muTd(i)*dVfzdr(i)^2*Ed(i)/kd(i);
    dG_Ed(i)=(wE(1)*cT1*dVfzdr(i)^2/kd(i))*(1-nus(i))*(muTd(i)+Ed(i)*dmuTdEd(i));
else
    if i==n
        G_Ed(i)=0;
        dG_Ed(i)=0;
    else
        G_Ed(i)=(1-nus(i))*cT1*FT1*muTd(i)*dVfzdr(i)^2*Ed(i)/kd(i);
        dG_Ed(i)=(wE(1)*cT1*FT1*dVfzdr(i)^2/kd(i))*(1-nus(i))*(muTd(i)+Ed(i)*dmuTdEd(i));
    end
end
end
end

```

PhD_2_Dissipation.m

```

%Calculating Dissipation and corresponding slope terms
%Calculating Granular Temperature dissipation
for i=1:n
    if GKT==yes
        g0=(nus0^(1/3))/(nus0^(1/3)-nus(i)^(1/3));
        if Kunn_mod_diff_coef_table_4_1==yes
            gamma(i)=48/pi^0.5*etaf*(1-etaf)*g0*nus(i)^2/Rep*(rhos/rhof)*Td(i)^1.5;
            dgammatT(i)=48/pi^0.5*etaf*(1-etaf)*g0*nus(i)^2/Rep*(rhos/rhof)*1.5*Td(i)^0.5;
        else
            gamma(i)=48/pi^0.5*eta*(1-eta)*g0*nus(i)^2/Rep*(rhos/rhof)*Td(i)^1.5;
            dgammatT(i)=48/pi^0.5*eta*(1-eta)*g0*nus(i)^2/Rep*(rhos/rhof)*1.5*Td(i)^0.5;
        end
    end
end
if i==n
    fT2(i)=0;
else
    fT2(i)=(1-2/9*exp(-(RT(i)/6)^2))*(1-exp(-yplus(i)/5))^2;
end
end
%Compiling the dissipation terms for all the equations
for i=1:n
    D_Vfzd(i)=0;
    dD_Vfzd(i)=0;
    D_Vszd(i)=0;
    dD_Vszd(i)=0;
    if Low_ST==yes
        D_Td(i)=0;
        dD_Td(i)=0;
    end
    if Mid_ST==yes
        %D_Td(i)=(40-ST)/(40-5)*0+(ST-5)/(40-5)*gamma(i);
        D_Td(i)=0;
        dD_Td(i)=0;
    end
    if High_ST==yes
        D_Td(i)=gamma(i);
        dD_Td(i)=wT(2)*dgammatT(i);
    end
end

```

```

end
D_kd(i)=(1-nus(i))*Ed(i);
dD_kd(i)=0;
if Vfz_wall_Mfix==yes || k_wall_Mfix==yes
    D_Ed(i)=(1-nus(i))*cT2*Ed(i)^2/kd(i);
    dD_Ed(i)=-2*(wE(2)*cT2*(1-nus(i))*Ed(i)/kd(i));
else
    if i==n
        D_Ed(i)=0;
        dD_Ed(i)=0;
    else
        D_Ed(i)=(1-nus(i))*cT2*FT2(i)*Ed(i)^2/kd(i);
        dD_Ed(i)=-2*(wE(2)*cT2*FT2(i)*(1-nus(i))*Ed(i)/kd(i));
    end
end
end
end

```

PhD_2_Interaction.m

```

%Calculating Interaction and corresponding slope terms
%The Drag Term FD
if Ding_Gidaspow_1990==yes
    for i=1:n
        Fd(i)=beta(i)*(1-nus(i))*(Vrd(i));
        dbetadVfzd=3/4/Rep*CD(i)*nus(i)/(1-nus(i))^2.65;
        dFdVfzd(i)=beta(i);
        dbetadVsزد=3/4/Rep*CD(i)*nus(i)/(1-nus(i))^2.65;
        dFdVsزد(i)=-beta(i);
    end
end
%FET model + Sinclair & Mallo
if FET==yes
    for i=1:n
        kTd(i)=(6*kd(i)*Td(i))^0.5;
        dkTdT(i)=0.5*(6*kd(i))^0.5*Td(i)^-0.5;
        dkTdk(i)=0.5*(6*Td(i))^0.5*kd(i)^-0.5;
        g0=(nus0^(1/3))/(nus0^(1/3)-nus(i)^(1/3));
        if High_ST==yes
            if ST>100
                beta2(i)=24*nus(i)*g0/Rep*(Td(i)/pi)^0.5;
            end
            if ST<=100
                beta2(i)=(1-nus(i))*beta(i)*rhof/rhos/nus(i);
            end
        end
    end
    if Mid_ST==yes
        temp1=(1-nus(i))*beta(i);
        temp2=(1-nus(i))*beta(i)*rhof/rhos/nus(i);
        beta2(i)=(6.7*10^-7*Re-18.44*dR+0.62)*temp1;
    end
    if Low_ST==yes
        beta2(i)=(1-nus(i))*beta(i);
    end
    bkd(i)=beta2(i)*2*kd(i);
    bTd(i)=beta2(i)*3*Td(i);
    bkTd(i)=beta2(i)*kTd(i);
    FKS(i)=bkTd(i)-bTd(i);
end

```

```

dFKSdT(i)=-beta2(i)*(dkTdT(i)-3);
FKF(i)=bkd(i)-bkTd(i);
dFKFdK(i)=beta2(i)*(2-dkTdk(i));
if i==n
    dFKFdK(i)=0;
end
end
end
%TVBA + Louge
if Louge_etal_1991==yes
    for i=1:n
        kTd(i)=4/pi^0.5*rhof/rhos*Rep*beta(i)*(1-nus(i))/nus(i)*(Vrd(i))^2/Td(i)^0.5;
        %dkTdT(i)=0.5*(4/pi^0.5*rhof/rhos*Rep*beta(i)*(1-nus(i))/nus(i)*(Vrd(i))^2)*Td(i)^-1.5;
        dkTdT(i)=0;
        dkTdk(i)=0;
        bkd(i)=beta(i)*(1-nus(i))^2*kd(i);
        bTd(i)=beta(i)*(1-nus(i))^3*Td(i);
        bkTd(i)=beta(i)*(1-nus(i))*kTd(i);
        FKS(i)=bkTd(i)-bTd(i);
        dFKSdT(i)=-beta(i)*(1-nus(i))*(dkTdT(i)-3);
        FKF(i)=bkd(i)-bkTd(i);
        dFKFdK(i)=beta(i)*(1-nus(i))*(2-dkTdk(i));
        if i==n
            %FKF(i)=0;
            %FKS(i)=-bTd(i);
            dFKFdK(i)=0;
        end
    end
end
end
%TVBA + Sinclair & Mallo
if Sinclair_and_Mallo_1998==yes;
    for i=1:n
        kTd(i)=(6*kd(i)*Td(i))^0.5;
        dkTdT(i)=0.5*(6*kd(i))^0.5*Td(i)^-0.5;
        dkTdk(i)=0.5*(6*Td(i))^0.5*kd(i)^-0.5;
        bkd(i)=beta(i)*(1-nus(i))^2*kd(i);
        bTd(i)=beta(i)*(1-nus(i))^3*Td(i);
        bkTd(i)=beta(i)*(1-nus(i))*kTd(i);
        FKS(i)=bkTd(i)-bTd(i);
        dFKSdT(i)=-beta(i)*(1-nus(i))*(dkTdT(i)-3);
        FKF(i)=bkd(i)-bkTd(i);
        dFKFdK(i)=beta(i)*(1-nus(i))*(2-dkTdk(i));
        if i==n
            %FKF(i)=0;
            %FKS(i)=-bTd(i);
            dFKFdK(i)=0;
        end
    end
end
end
%TVBA + Simonin
if Simonin_1996==yes
    cbeta=1.8-1.35;
    for i=1:n
        if i==n
            if Vfz_wall_Mfix==yes || k_wall_Mfix==yes
                zetar=3*(Vrd(i))^2/2/kd(i);
            end
        end
    end
end

```

```

    etat=3*cmu/2/(1+cbeta*zetar)^0.5*kd(i)/Ed(i)*rhof/rhos*(1-nus(i))/nus(i)*beta(i);
    chi=nus(i)*rhos/rhof/(1-nus(i));
    kTd(i)=etat*(2*kd(i)+3*chi*Td(i))/(1+(1+chi)*etat);
else
    kTd(i)=0;
end
else
    zetar=3*(Vrd(i))^2/2/kd(i);
    etat=3*cmu/2/(1+cbeta*zetar)^0.5*kd(i)/Ed(i)*rhof/rhos*(1-nus(i))/nus(i)*beta(i);
    chi=nus(i)*rhos/rhof/(1-nus(i));
    kTd(i)=etat*(2*kd(i)+3*chi*Td(i))/(1+(1+chi)*etat);
end
bkd(i)=beta(i)*(1-nus(i))*2*kd(i);
bTd(i)=beta(i)*(1-nus(i))*3*Td(i);
bkTd(i)=beta(i)*(1-nus(i))*kTd(i);
FKS(i)=bkTd(i)-bTd(i);
dFKSdT(i)=-beta(i)*(1-nus(i))*(dkTd(i)-3);
FKF(i)=bkd(i)-bkTd(i);
dFKFdk(i)=beta(i)*(1-nus(i))*(2-dkTdk(i));
if i==n
    %FKF(i)=0;
    %FKS(i)=-bTd(i);
    dFKFdk(i)=0;
end
end
end
%TVBA + lgci
if Koch_Sangani_1999==yes
    for i=1:n
        g0=(nus0^(1/3))/(nus0^(1/3)-nus(i)^(1/3));
        Rdiss=1+(3*(nus(i)/2)^0.5)+(135/64*nus(i)*log(nus(i)))+(11.26*nus(i)*(1-5.1*nus(i)+16.57*nus(i)^2-
21.77*nus(i)^3)-(nus(i)*g0*log(0.01)));
        if nus(i)<0.4
            Rd=(1+(3*(nus(i)/2)^0.5)+(135/64*nus(i)*log(nus(i)))+(17.14*nus(i)))/(1+0.681*nus(i)-
8.48*nus(i)^2+8.16*nus(i)^3);
        else
            Rd=10*nus(i)/(1-nus(i))^3+0.7;
        end
        phi=Rd^2/(1+3.5*nus(i)^0.5+5.9*nus(i));
        bkd(i)=beta(i)*(1-nus(i))*2*kd(i);
        %bkd(i)=(36*nus(i)*muefd(i)*kd(i)*Rdiss/Rep^2);
        bTd(i)=beta(i)*(1-nus(i))*3*Td(i);
        %bTd(i)=(54*nus(i)*muefd(i)*Td(i)*Rdiss/Rep^2);
        bkTd(i)=(81*nus(i)*muefd(i)^2*(Vrd(i))^2/g0/(pi*Td(i))^0.5/Re^3*phi);
        FKS(i)=bkTd(i)-bTd(i);
        dFKSdT(i)=0.5*(81*nus(i)*muefd(i)^2*(Vrd(i))^2/g0/(pi)^0.5/Re^3)*Td(i)^-1.5+beta(i)*(1-nus(i))*3;
        FKF(i)=bkd(i)-bkTd(i);
        dFKFdk(i)=beta(i)*(1-nus(i))*2;
        if i==n
            %FKF(i)=0;
            %FKS(i)=-bTd(i);
            dFKFdk(i)=0;
        end
    end
end
end
%TVBA + Wylie

```

```

if Wylie_etal_2003==yes
    for i=1:n
        Red=Rep*abs(Vrd(i));
        ReT=Rep*Td(i)^0.5;
        phi=(1+2*ReT^2/Red^2-
ReT^4/Red^4)*erf(Red/2^0.5/ReT)+(2/pi)^0.5*ReT/Red*(1+ReT^2/Red^2)*exp(-Red^2/2/ReT^2);
        Kfb=0.0336+0.106*nus(i)+0.0116*(1-nus(i))^5;
        Rd0=(1+3/(2*nus(i)^0.5)^0.5+135/64*nus(i)*log(nus(i))+17.14*nus(i))/(1+0.681*nus(i)-
8.48*nus(i)^2+8.16*nus(i)^3);
        Rd=Rd0+Kfb*Red*phi;
        chi=(1+2.5*nus(i)+4.509*nus(i)^2+4.5154*nus(i)^3)/(1-(nus(i)/0.6436)^3)^0.6780;
        RS=(chi*(1+3.5*nus(i)^0.5+5.9*nus(i)))^1;
        bkd(i)=beta(i)*(1-nus(i))^2*kd(i);
        bTd(i)=beta(i)*(1-nus(i))^3*Td(i);
        bkTd(i)=(81*nus(i)*muefd(i)^2*(Vrd(i))^2*rhof/rhos/(pi*Td(i))^0.5/Re^3*RS*Rd^2);
        FKS(i)=bkTd(i)-bTd(i);
        dFKSdT(i)=0.5*(81*nus(i)*muefd(i)^2*(Vrd(i))^2*rhof/rhos/(pi)^0.5/Re^3*RS*Rd^2)*Td(i)^-
1.5+beta(i)*(1-nus(i))^3;
        FKF(i)=bkd(i)-bkTd(i);
        dFKFdk(i)=beta(i)*(1-nus(i))^2;
        if i==n
            %FKF(i)=0;
            %FKS(i)=-bTd(i);
            dFKFdk(i)=0;
        end
    end
end
%VBA + Zhang & Reese
if Zhang_Reese_2003==yes;
    for i=1:n
        g0=(nus0^(1/3))/(nus0^(1/3)-nus(i)^(1/3));
        kTd(i)=(pi^0.5/24/g0*rhof/rhos*Rep*beta(i)*(1-nus(i))/nus(i)^2*(Vrd2(i))^2/Td(i)^0.5);
        %dkTdT(i)=0.5*(pi^0.5/24/g0*rhof/rhos*Rep*beta(i)*(1-nus(i))/nus(i)^2*(Vrd2(i))^2)*Td(i)^-1.5;
        dkTdT(i)=0;
        dkTdk(i)=0;
        bkd(i)=beta(i)*(1-nus(i))^2*kd(i);
        bTd(i)=beta(i)*(1-nus(i))^3*Td(i);
        bkTd(i)=beta(i)*(1-nus(i))*kTd(i);
        FKS(i)=bkTd(i)-bTd(i);
        dFKSdT(i)=-beta(i)*(1-nus(i))*(dkTdT(i)-3);
        FKF(i)=-beta(i)*(1-nus(i))*Vrd(i)^2-bTd(i)+bkTd(i);
        dFKFdk(i)=beta(i)*(1-nus(i))*(2-dkTdk(i));
        if i==n
            %FKF(i)=0;
            %FKS(i)=-bTd(i);
            dFKFdk(i)=0;
        end
    end
end
%TVBA + Chen & Wood
if Chen_Wood==yes
    for i=1:n
        if i==n
            kTd(i)=0;
        else
            temp1=Rep^2/18/rhos/rhof*2/3/cmu*Ed(i)/kd(i);

```

```

    kTd(i)=2*kd(i)*exp(-0.0825*temp1);
end
dkTdT(i)=0;
dkTdk(i)=2;
bkd(i)=beta(i)*(1-nus(i))*2*kd(i);
bTd(i)=beta(i)*(1-nus(i))*3*Td(i);
bkTd(i)=beta(i)*(1-nus(i))*kTd(i);
FKS(i)=bkTd(i)-bTd(i);
dFKSdT(i)=-beta(i)*(1-nus(i))*(dkTdT(i)-3);
FKF(i)=bkd(i)-bkTd(i);
dFKFdK(i)=beta(i)*(1-nus(i))*(2-dkTdk(i));
if i==n
    %FKF(i)=0;
    %FKS(i)=-bTd(i);
    dFKFdK(i)=0;
end
end
end
%Wake modeling for vortex shedding
if Lun_Wake_term==yes
for i=1:n
    Redcl=Rep*abs(Vrd(1));
    Red=Rep*abs(Vrd(i));
    if rhof<200
    %For gas-solid flows
        if Redcl<=150
            temp1=1;
            temp2=0;
        end
        if Redcl>=150 && Redcl<310
            temp1=0.017*Red;
        end
        if Redcl>=310 && Redcl<610
            temp1=1.2+0.00005*Red^2;
        end
        if Redcl>=610 && Redcl<1560
            temp1=0.029*Red;
        end
        if Redcl>1560
            temp1=0.029*Red;
        end
        if Redcl>150 && Redcl<310
            temp2=10/3;
        end
        if Redcl>=310
            temp2=24/3;
        end
    end
else
    %For liquid solid flows
        if Redcl<500
            temp1=1;
            temp2=0;
        end
        if Redcl<=500
            temp1=0.017*Red;
            temp2=10/3;
        end
    end
end

```

```

        end
    end
    Ew(i)=12*nus(i)*temp1*temp2*kd(i)/Rep^2;
end
end
%Compiling the Interaction terms for all the equations
for i=1:n
    l_Vfzd(i)=-Fd(i);
    dl_Vfzd(i)=wVfz(1)*dFdVfzd(i);
    l_Vszd(i)=Fd(i);
    dl_Vszd(i)=wVsz(1)*dFdVszd(i);
    l_Td(i)=FKS(i);
    dl_Td(i)=wT(3)*dFKSdT(i);
    l_kd(i)=-FKF(i)+Ew(i);
    dl_kd(i)=wk(2)*dFKFdK(i);
    if Vfz_wall_Mfix==yes || k_wall_Mfix==yes
        l_Ed(i)=cT3*Ed(i)/kd(i)*(-FKF(i)+Ew(i));
        dl_Ed(i)=0;
    else
        if i==n
            l_Ed(i)=0;
            dl_Ed(i)=0;
        else
            l_Ed(i)=cT3*ft2(i)*Ed(i)/kd(i)*(-FKF(i)+Ew(i));
            dl_Ed(i)=0;
        end
    end
end
end
end

```

PhD_Thomas_Algorithms.m

```

%Forward reduction of matrix
for i=1:n
    if i==1
        A(i,3)=A(i,3)/A(i,2);
        A(i,4)=A(i,4)/A(i,2);
    else
        A(i,3)=A(i,3)/(A(i,2)-A(i-1,3)*A(i,1));
        A(i,4)=(A(i,4)-A(i-1,4)*A(i,1))/(A(i,2)-A(i-1,3)*A(i,1));
    end
end
%Back substitution to get new values
for i=1:n
    if i==1
        X(n+1-i)=A(n+1-i,4);
    else
        X(n+1-i)=A(n+1-i,4)-A(n+1-i,3)*X(n+2-i);
    end
end
end

```

PhD_1_Vfz_Eqn.m

```

%Solving the single phase Vfz equation
%Constructing the matrix, using principals of Finite Volume
%The matrix A is actually a tridiagonal matrix but is constructed in form
%of 4 columnar arrys. The first column is the sub-diagonal, the second
%column is a daigonal and the third is the super-diagonal, while the forth

```

```

%column is the B matrix in AX=B where A is the original tri-diagonal
variable=2;
for i=1:n
    C(i)=1+muTd(i); %Constructing Diffusion term
end
for i=1:n
    if i==1 || i==n
        if i==1 %Center Line Boundary Condition of Symmetry
            rd2=(((rd(i)+rd(i+1))/2)^2-(rd(i)^2))/2;
            a2=(((rd(i)+rd(i+1))/2)*(2*C(i)*C(i+1)/(C(i)+C(i+1))))/(rd(i+1)-rd(i))/rd2;
            A(i,1)=0;
            A(i,2)=a2;
            A(i,3)=-a2;
            A(i,4)=0;
            %Inserting operating condition
            %If the center-line velocity is known
            if Re_center_line==yes
                B1(i)=1;
            %Average velocity is known
            else
                B1(i)=rd(i)*drf(i)/Re^2;
            end
            %Inserting Pressure Drop as a variable
            B2(i)=1;
        end
        if i==n
            PhD_1_BC %Wall Boundary Condition
            %For operating condition
            %If the center-line velocity is known
            if Re_center_line==yes
                B1(i)=0;
            %Average velocity is known
            else
                B1(i)=rd(i)*drf(i-1)/Re^2;
            end
        end
    else
        rd2=(((rd(i)+rd(i+1))/2)^2-((rd(i)+rd(i-1))/2)^2)/2;
        a1=(((rd(i)+rd(i-1))/2)*(2*C(i)*C(i-1)/(C(i)+C(i-1))))/(rd(i)-rd(i-1))/rd2;
        a2=(((rd(i)+rd(i+1))/2)*(2*C(i)*C(i+1)/(C(i)+C(i+1))))/(rd(i+1)-rd(i))/rd2;
        A(i,1)=-a1;
        A(i,2)=a1+a2;
        A(i,3)=-a2;
        A(i,4)=0;
        %For operating condition
        %If the center-line velocity is known
        if Re_center_line==yes
            B1(i)=0;
        %Average velocity is known
        else
            B1(i)=rd(i)*(drf(i)+drf(i-1))/Re^2;
        end
        %Inserting Pressure Drop as a variable
        B2(i)=1;
    end
end
end

```

```

%Solving the velocity equation
temp3=0;
%For operating condition
%If the center-line velocity is known
if Re_center_line==yes
    temp4=1;
%Average velocity is known
else
    temp4=0.25;
end
%Modifying the system so that Thomas Algorithms can solve it
for i=1:n
    if i==n
        temp1=B1(i)/A(i,2);
        B1(i)=B1(i)-A(i,2)*temp1;
        temp4=temp4-A(i,4)*temp1;
        temp3=temp3-B2(i)*temp1;
    else
        temp1=A(i+1,1)/A(i,2);
        temp2=B1(i)/A(i,2);
        A(i+1,1)=A(i+1,1)-A(i,2)*temp1;
        A(i+1,2)=A(i+1,2)-A(i,3)*temp1;
        A(i+1,4)=A(i+1,4)-A(i,4)*temp1;
        temp4=temp4-A(i,4)*temp2;
        B1(i)=B1(i)-A(i,2)*temp2;
        B1(i+1)=B1(i+1)-A(i,3)*temp2;
        B2(i+1)=B2(i+1)-B2(i)*temp1;
        temp3=temp3-B2(i)*temp2;
    end
end
temp1=temp3;
temp3=temp3/temp1;
temp4=temp4/temp1;
for i=1:n
    temp1=B2(i);
    B2(i)=B2(i)-temp3*temp1;
    A(i,4)=A(i,4)-temp4*temp1;
end
%Solving the tri-diagonal system
PhD_Thomas_Algorithms
%Updating values
for i=1:n
    Vfzd(i)=X(i);
end

PhD_1_k_E_Eqn.m
%Solving the k-E equations for Single Phase flow
%Solving the k equation
for i=1:n
    C(i)=1+muTd(i)/sigmak; %Constructing the diffusion term
    D(i)=(muTd(i)*dVfzdr(i)^2)-Ed(i); %Constructing the source/sink terms
    S(i)=wk(1)*dmuTdkd(i)*dVfzdr(i)^2; %Constructing the slope of source/sink terms
end
%Constructing the matrix, using principals of Finite Volume
%The matrix A is actually a tridiagonal matrix but is constructed in form
%of 4 columnar arrys. The first column is the sub-diagonal, the second

```

```

%column is a diagonal and the third is the super-diagonal, while the forth
%column is the B matrix in AX=B where A is the original tri-diagonal
variable=5;
for i=1:n
    if i==1 || i==n %Inputing the Boundary Conditions
        if i==1 %Center Line Boundary Condition of Symmetry
            rd2=(((rd(i)+rd(i+1))/2)^2-(rd(i)^2))/2;
            a2=(((rd(i)+rd(i+1))/2)*(2*C(i)*C(i+1)/(C(i)+C(i+1))))/(rd(i+1)-rd(i))/rd2;
            A(i,1)=0;
            A(i,2)=a2-S(i);
            A(i,3)=-a2;
            A(i,4)=D(i)-S(i)*kd(i);
        else %Wall Boundary condition
            PhD_1_BC
        end
    else
        rd2=(((rd(i)+rd(i+1))/2)^2-((rd(i)+rd(i-1))/2)^2)/2;
        a1=((rd(i)+rd(i-1))/2)*(2*C(i)*C(i-1)/(C(i)+C(i-1)))/(rd(i)-rd(i-1))/rd2;
        a2=(((rd(i)+rd(i+1))/2)*(2*C(i)*C(i+1)/(C(i)+C(i+1))))/(rd(i+1)-rd(i))/rd2;
        A(i,1)=-a1;
        A(i,2)=a1+a2-S(i);
        A(i,3)=-a2;
        A(i,4)=D(i)-S(i)*kd(i);
    end
end
end
%Solving the tri-diagonal system
PhD_Thomas_Algorithims
%Updating values
kd=X;
%Solving the E equation
%if wall conditions are applied C, D & S are constructed differently at the wall as given in MFIX manual
if Vfz_wall_Mfix==yes || k_wall_Mfix==yes
    for i=1:n
        C(i)=1+muTd(i)/sigmaE; %Constructing the Diffusion term
        D(i)=(cT1*muTd(i)*dVfzdr(i)^2*Ed(i)/kd(i))-(cT2*Ed(i)^2/kd(i)); %Constructing the source/sink terms
        S(i)=(wE(1)*cT1*dVfzdr(i)^2/kd(i))*(muTd(i)+Ed(i)*dmuTdEd(i))-2*(wE(2)*cT2*Ed(i)/kd(i));
    end
end
%Constructing the slope of source/sink terms
%for all other conditions C, D & S are constructed as Bolio code
else
    for i=1:n
        C(i)=1+muTd(i)/sigmaE; %Constructing the Diffusion term
        if i<n
            fT2(i)=(1-2/9*exp(-(RT(i)/6)^2))*(1-exp(-yplus(i)/5))^2;
            D(i)=(cT1*fT1*muTd(i)*dVfzdr(i)^2*Ed(i)/kd(i))-(cT2*fT2(i)*Ed(i)^2/kd(i)); %Constructing the
            source/sink terms
            S(i)=
            (wE(1)*cT1*fT1*dVfzdr(i)^2/kd(i))*(muTd(i)+Ed(i)*dmuTdEd(i))-2*(wE(2)*cT2*fT2(i)*Ed(i)/kd(i));
        end
    end
end
D(n)=0;
S(n)=0;
end
end
%Constructing the matrix, using principals of Finite Volume
%The matrix A is actually a tridiagonal matrix but is constructed in form

```

```

%of 4 columnar arrys. The first column is the sub-diagonal, the second
%column is a daigonal and the third is the super-diagonal, while the forth
%column is the B matrix in AX=B where A is the original tri-diagonal
variable=6;
for i=1:n
    if i==1 || i==n %Inputing the Boundary Conditions
        if i==1 %Center Line Boundary Condition of Symmetry
            rd2=(((rd(i)+rd(i+1))/2)^2-(rd(i)^2))/2;
            a2=(((rd(i)+rd(i+1))/2)*(2*C(i)*C(i+1)/(C(i)+C(i+1))))/(rd(i+1)-rd(i))/rd2;
            A(i,1)=0;
            A(i,2)=a2-S(i);
            A(i,3)=-a2;
            A(i,4)=D(i)-S(i)*Ed(i);
        else %Wall Boundary condition Edwall=d^2(kd)/(d(rd))^2
            PhD_1_BC
        end
    else
        rd2=(((rd(i)+rd(i+1))/2)^2-((rd(i)+rd(i-1))/2)^2)/2;
        a1=(((rd(i)+rd(i-1))/2)*(2*C(i)*C(i-1)/(C(i)+C(i-1))))/(rd(i)-rd(i-1))/rd2;
        a2=(((rd(i)+rd(i+1))/2)*(2*C(i)*C(i+1)/(C(i)+C(i+1))))/(rd(i+1)-rd(i))/rd2;
        A(i,1)=-a1;
        A(i,2)=a1+a2-S(i);
        A(i,3)=-a2;
        A(i,4)=D(i)-S(i)*Ed(i);
    end
end
end
%Solving the tri-diagonal system
PhD_Thomas_Algorithims
%Updating values
Ed=X;

```

PhD_1_BC.m

```

%Boundary Conditions
%Boundary Condition for Vfz
if variable==2
    %No slip
    if Vfz_no_slip==yes
        A(i,1)=0;
        A(i,2)=1;
        A(i,3)=0;
        A(i,4)=0;
        B2(i)=0;
    end
    %Wall Function from Mfix
    if Vfz_wall_Mfix==yes
        h1=rd(i)-rd(i-1);
        h2=cmu^0.25*kd(i)^0.5*h1/2;
        rd2=(((rd(i)^2)-((rd(i)+rd(i-1))/2)^2)/2;
        a1=(((rd(i)+rd(i-1))/2)*(2*C(i)*C(i-1)/(C(i)+C(i-1))))/(rd(i)-rd(i-1))/rd2;
        A(i,1)=-a1;
        A(i,2)=a1+rd(i)/rd2*0.42*cmu^0.25*kd(i)^0.5/log(9.81*h2);
        A(i,3)=0;
        A(i,4)=0;
        B2(i)=1;
    end
end
end

```

```

%Boundary Condition for k
if variable==5
    %No slip
    if k_no_slip==yes
        A(i,1)=0;
        A(i,2)=1;
        A(i,3)=0;
        A(i,4)=0;
    end
    %Wall Function from Mfix
    if k_wall_Mfix==yes
        h1=rd(i)-rd(i-1);
        h2=cmu^0.25*kd(i)^0.5*h1/2;
        temp1=2*cmu^0.5*kd(i)*Vfzd(i)/h1/log(9.81*h2);
        temp2=2*cmu^0.75*kd(i)^1.5/0.42/h1;
        D(i)=temp1-temp2;
        S(i)=wk(1)*(2*cmu^0.5*Vfzd(i)/h1/log(9.81*h2))-10*1.5*(2*cmu^0.75*kd(i)^0.5/0.42/h1);
        rd2=((rd(i)^2)-((rd(i)+rd(i-1))/2)^2)/2;
        a1=((rd(i)+rd(i-1))/2)*(2*C(i)*C(i-1)/(C(i)+C(i-1)))/(rd(i)-rd(i-1))/rd2;
        A(i,1)=-a1;
        A(i,2)=a1-S(i);
        A(i,3)=0;
        A(i,4)=D(i)-S(i)*kd(i);
    end
end
%Boundary Condition for E
if variable==6
    %E at wall=muef/rhof*d^2k/dr^2
    if Bolio_equation_2_62==yes
        A(i,1)=0;
        A(i,2)=1;
        A(i,3)=0;
        h1=drb(n);
        h2=drb(n)+drb(n-1);
        A(i,4)=((kd(i)-kd(i-1))/h1-(kd(i)-kd(i-2))/h2)*(2/(h2-h1));
    end
    %Wall Function from Mfix
    if E_wall_Mfix==yes
        h1=rd(i)-rd(i-1);
        A(i,1)=0;
        A(i,2)=1;
        A(i,3)=0;
        A(i,4)=2*cmu^0.75*kd(i)^1.5/0.42/h1;
    end
end

```

PhD_2_nus_Eqn.m

```

%Solving nues equation for the Two Phase flow
%Constructing the matrix A
%The matrix A is constructed in form of 4 columnar arrys. The first column
%is unity representing a diagonal i.e. the variable itself. The second
%column is the slope term and the third is valuve from the previous
%iteration, while the forth column is the discretized mass conservation equation.
variable=1;
%Filling in the operating condition for center-line velocity is given
if Re_center_line==yes

```

```

for i=1:n
    if i==1 || i==n
        if i==1
            A(i,4)=(Vszd(i)+M*Vfzd(i))*rd(i)*drf(i);
        end
        if i==n
            A(i,4)=(Vszd(i)+M*Vfzd(i))*rd(i)*drf(i-1);
        end
    else
        A(i,4)=(Vszd(i)+M*Vfzd(i))*rd(i)*(drf(i)+drf(i-1));
    end
end
temp1=0;
temp2=0;
for i=1:n
    if i==1 || i==n
        if i==1
            temp2=temp2+Vfzd(i)*rd(i)*drf(i);
        end
        if i==n
            temp2=temp2+Vfzd(i)*rd(i)*drf(i-1);
        end
    else
        temp2=temp2+Vfzd(i)*rd(i)*(drf(i-1)+drf(i));
    end
end
temp2=M*temp2;
%Filling in the operating condition for average velocity is given
else
    for i=1:n
        if i==1 || i==n
            if i==1
                A(i,4)=(Vszd(i))*rd(i)*drf(i);
            end
            if i==n
                A(i,4)=(Vszd(i))*rd(i)*drf(i-1);
            end
        else
            A(i,4)=(Vszd(i))*rd(i)*(drf(i)+drf(i-1));
        end
    end
    temp1=0;
    temp2=M*Re^2/4;
end
%For Low Stokes number
if Low_ST==yes
    for i=1:n
        C(i)=(muefd(i)+muTd(i))/0.7; %Constructing the diffusion term
    end
    for i=1:n-1
        if i==1 %Inputing the Boundary Conditions
            a2=((rd(i)+rd(i+1))/2)*(2*C(i)*C(i+1)/(C(i)+C(i+1)))/(rd(i+1)-rd(i));
            A(i,1)=0;
            A(i,2)=a2;
            A(i,3)=-a2;
        else

```

```

        a1=((rd(i)+rd(i-1))/2)*(2*C(i)*C(i-1)/(C(i)+C(i-1)))/(rd(i)-rd(i-1));
        a2=((rd(i)+rd(i+1))/2)*(2*C(i)*C(i+1)/(C(i)+C(i+1)))/(rd(i+1)-rd(i));
        A(i,1)=-a1;
        A(i,2)=a1+a2;
        A(i,3)=-a2;
    end
end
%Using matrix properties to get tri-diagonal system
for i=2:n-1
    temp3=A(i,1);
    A(i,1)=A(i,1)/temp3;
    A(i,2)=A(i,2)/temp3;
    A(i,3)=A(i,3)/temp3;
    temp4=A(i-1,4);
    A(i-1,4)=A(i-1,4)-temp4*A(i,1);
    A(i,4)=A(i,4)-temp4*A(i,2);
    A(i+1,4)=A(i+1,4)-temp4*A(i,3);
end
A(n,1)=A(n-1,4);
A(n,2)=A(n,4);
A(n,3)=0;
for i=1:n
    if i==n
        A(i,4)=temp2;
    else
        A(i,4)=0;
    end
end
end
%Solving the tri-diagonal system
PhD_Thomas_Algorithms
%Updating values
nus=X;
end
%For Mid and High Stokes number
if Mid_ST==yes || High_ST==yes
    %Relations for High Stokes number
    for i=1:n
        D(i)=alpha(i);
        S(i)=dalphadnus(i);
        A(i,1)=1;
        A(i,2)=-1/S(i)/Td(i);
        A(i,3)=nus(i)-D(i)/S(i);
    end
    %Using matrix properties to get updated nus values
    for i=1:n
        temp1=temp1-A(i,2)*A(i,4);
        temp2=temp2-A(i,3)*A(i,4);
    end
    constant=temp2/temp1;
    for i=1:n
        X(i)=A(i,3)-constant*A(i,2);
    end
    %Updating the values of nus
    nus=X;
    %For Mid Stokes numbers
    if Mid_ST==yes

```

```

    %Taking a weighted average between high and low Stokes number
    for i=1:n
        nus(i)=(ST-5)/(40-5)*nus(i)+(40-ST)/(40-5)*M/(M+1);
    end
end
end
end

```

PhD_2_Vfz_Eqn.m

```

%Solving the Vfz equation for the Two Phase flow
%Constructing the matrix, using principals of Finite Volume
%The matrix A is actually a tridiagonal matrix but is constructed in form
%of 4 columnar arrys. The first column is the sub-diagonal, the second
%column is a daigonal and the third is the super-diagonal, while the forth
%column is the B matrix in AX=B where A is the original tri-diagonal
variable=2;
for i=1:n
    C(i)=muefd(i)+muTd(i); %Constructing Diffusion term
    D(i)=G_Vfzd(i)-D_Vfzd(i)+I_Vfzd(i); %Constructing the source/sink terms
    S(i)=dG_Vfzd(i)+dD_Vfzd(i)+dI_Vfzd(i); %Constructing the slope of source/sink terms
end
for i=1:n
    if i==1 || i==n
        if i==1 %Center Line Boundary Condition of Symmetry
            rd2=((rd(i)+rd(i+1))/2)^2-(rd(i)^2)/2;
            a2=((rd(i)+rd(i+1))/2)*(2*C(i)*C(i+1)/(C(i)+C(i+1)))/(rd(i+1)-rd(i))/rd2;
            A(i,1)=0;
            A(i,2)=a2-S(i);
            A(i,3)=-a2;
            A(i,4)=D(i)-S(i)*Vfzd(i);
            %Inserting operating condition
            %If the center-line velocity is known
            if Re_center_line==yes
                B1(i)=1;
            %Average velocity is known
            else
                B1(i)=(1-nus(i))*rd(i)*drf(i)/Re^2;
            end
            %Inserting Pressure Drop as a variable
            B2(i)=1;
        end
        if i==n
            PhD_2_BC %Wall Boundary Condition
            %For operating condition
            %If the center-line velocity is known
            if Re_center_line==yes
                B1(i)=0;
            %Average velocity is known
            else
                B1(i)=(1-nus(i))*rd(i)*drf(i-1)/Re^2;
            end
        end
    else
        rd2=((rd(i)+rd(i+1))/2)^2-((rd(i)+rd(i-1))/2)^2)/2;
        a1=((rd(i)+rd(i-1))/2)*(2*C(i)*C(i-1)/(C(i)+C(i-1)))/(rd(i)-rd(i-1))/rd2;
        a2=((rd(i)+rd(i+1))/2)*(2*C(i)*C(i+1)/(C(i)+C(i+1)))/(rd(i+1)-rd(i))/rd2;
        A(i,1)=-a1;
    end
end
end
end

```

```

A(i,2)=a1+a2-S(i);
A(i,3)=-a2;
A(i,4)=D(i)-S(i)*Vfzd(i);
%For operating condition
%If the center-line velocity is known
if Re_center_line==yes
    B1(i)=0;
%Average velocity is known
else
    B1(i)=(1-nus(i))*rd(i)*(drf(i)+drf(i-1))/Re^2;
end
%Inserting Pressure Drop as a variable
B2(i)=1;
end
end
%Solving the velocity equation
temp3=0;
%For operating condition
%If the center-line velocity is known
if Re_center_line==yes
    temp4=1;
%Average velocity is known
else
    temp4=0.25;
end
%Modifying the system so that Thomas Algorithms can solve it
for i=1:n
    if i==n
        temp1=B1(i)/A(i,2);
        B1(i)=B1(i)-A(i,2)*temp1;
        temp4=temp4-A(i,4)*temp1;
        temp3=temp3-B2(i)*temp1;
    else
        temp1=A(i+1,1)/A(i,2);
        temp2=B1(i)/A(i,2);
        A(i+1,1)=A(i+1,1)-A(i,2)*temp1;
        A(i+1,2)=A(i+1,2)-A(i,3)*temp1;
        A(i+1,4)=A(i+1,4)-A(i,4)*temp1;
        temp4=temp4-A(i,4)*temp2;
        B1(i)=B1(i)-A(i,2)*temp2;
        B1(i+1)=B1(i+1)-A(i,3)*temp2;
        B2(i+1)=B2(i+1)-B2(i)*temp1;
        temp3=temp3-B2(i)*temp2;
    end
end
temp1=temp3;
temp3=temp3/temp1;
temp4=temp4/temp1;
for i=1:n
    temp1=B2(i);
    B2(i)=B2(i)-temp3*temp1;
    A(i,4)=A(i,4)-temp4*temp1;
end
%Solving the tri-diagonal system
PhD_Thomas_Algorithms
for i=1:n

```

```

    Vfzd(i)=X(i);
end
%Updating the Pressure Drop
dPdZ=temp4;

PhD_2_Vsz_Eqn.m
%Solving the Vsz equations for Two Phase flow
variable=3;
for i=1:n
    C(i)=-musdG(i); %Constructing the diffusion term
    D(i)=G_Vszd(i)-D_Vszd(i)+l_Vszd(i); %Constructing the source/sink terms
    S(i)=dG_Vszd(i)+dD_Vszd(i)+dl_Vszd(i); %Constructing the slope of source/sink terms
end
%Constructing the matrix, using principals of Finite Volume
%The matrix A is actually a tridiagonal matrix but is constructed in form
%of 4 columnar arrys. The first column is the sub-diagonal, the second
%column is a daigonal and the third is the super-diagonal, while the forth
%column is the B matrix in AX=B where A is the original tri-diagonal
for i=1:n
    if i==1 || i==n %Inputing the Boundary Conditions
        if i==1 %Center Line Boundary Condition of Symmetry
            rd2=(((rd(i)+rd(i+1))/2)^2-(rd(i)^2))/2;
            a2=(((rd(i)+rd(i+1))/2)*(2*C(i)*C(i+1)/(C(i)+C(i+1))))/(rd(i+1)-rd(i))/rd2;
            A(i,1)=0;
            A(i,2)=a2+S(i);
            A(i,3)=-a2;
            A(i,4)=-D(i)+S(i)*Vszd(i);
        else
            PhD_2_BC
        end
    else
        rd2=(((rd(i)+rd(i+1))/2)^2-((rd(i)+rd(i-1))/2)^2)/2;
        a1=(((rd(i)+rd(i-1))/2)*(2*C(i)*C(i-1)/(C(i)+C(i-1))))/(rd(i)-rd(i-1))/rd2;
        a2=(((rd(i)+rd(i+1))/2)*(2*C(i)*C(i+1)/(C(i)+C(i+1))))/(rd(i+1)-rd(i))/rd2;
        A(i,1)=-a1;
        A(i,2)=a1+a2+S(i);
        A(i,3)=-a2;
        A(i,4)=-D(i)+S(i)*Vszd(i);
    end
end
end
%Solving the tri-diagonal system
PhD_Thomas_Algorithims
%Updating values
Vszd=X;

```

```

PhD_2_T_Eqn.m
%Solving the T equations for Two Phase flow
variable=4;
%Constructing the matrix, using principals of Finite Volume
%The matrix A is actually a tridiagonal matrix but is constructed in form
%of 4 columnar arrys. The first column is the sub-diagonal, the second
%column is a daigonal and the third is the super-diagonal, while the forth
%column is the B matrix in AX=B where A is the original tri-diagonal
%For the case of Low Stokes number
if Low_ST==yes

```

```

Td=kd;
end
%For the case of Mid and High Stokes number
if Mid_ST==yes || High_ST==yes
for i=1:n
C(i)=-lambdadG(i); %Constructing the diffusion term
D(i)=G_Td(i)-D_Td(i)+I_Td(i); %Constructing the source/sink terms
S(i)=dG_Td(i)+dD_Td(i)+dI_Td(i); %Constructing the slope of source/sink terms
end
for i=1:n
if i==1 || i==n %Inputing the Boundary Conditions
if i==1 %Center Line Boundary Condition of Symmetry
rd2=(((rd(i)+rd(i+1))/2)^2-(rd(i)^2))/2;
a2=
((rd(i)+rd(i+1))/2)*(2*C(i)*C(i+1)/(C(i)+C(i+1)))/(rd(i+1)-rd(i))/rd2;
A(i,1)=0;
A(i,2)=a2+S(i);
A(i,3)=-a2;
A(i,4)=-D(i)+S(i)*Td(i);
else
PhD_2_BC %Wall Boundary Condition
end
else
rd2=(((rd(i)+rd(i+1))/2)^2-((rd(i)+rd(i-1))/2)^2)/2;
a1=(((rd(i)+rd(i-1))/2)*(2*C(i)*C(i-1)/(C(i)+C(i-1)))/(rd(i)-rd(i-1)))/rd2;
a2=(((rd(i)+rd(i+1))/2)*(2*C(i)*C(i+1)/(C(i)+C(i+1)))/(rd(i+1)-rd(i)))/rd2;
A(i,1)=-a1;
A(i,2)=a1+a2+S(i);
A(i,3)=-a2;
A(i,4)=-D(i)+S(i)*Td(i);
end
end
end
%Solving the tri-diagonal system
PhD_Thomas_Algorithims
%Updating values
Td=X;
end

```

PhD_2_k_E_Eqn.m

```

%Solving the k-E equations for Two Phase flow
%Solving the k equation
variable=5;
for i=1:n
C(i)=(1-nus(i))*(muefd(i)+muTd(i)/sigmak); %Constructing the diffusion term
D(i)=G_kd(i)-D_kd(i)+I_kd(i); %Constructing the source/sink terms
S(i)=dG_kd(i)+dD_kd(i)+dI_kd(i); %Constructing the slope of source/sink terms
end
%Constructing the matrix, using principals of Finite Volume
%The matrix A is actually a tridiagonal matrix but is constructed in form
%of 4 columnar arrys. The first column is the sub-diagonal, the second
%column is a daigonal and the third is the super-diagonal, while the forth
%column is the B matrix in AX=B where A is the original tri-diagonal
for i=1:n
if i==1 || i==n %Inputing the Boundary Conditions
if i==1 %Center Line Boundary Condition of Symmetry
rd2=(((rd(i)+rd(i+1))/2)^2-(rd(i)^2))/2;

```

```

        a2=((rd(i)+rd(i+1))/2)*(2*C(i)*C(i+1)/(C(i)+C(i+1)))/(rd(i+1)-rd(i))/rd2;
        A(i,1)=0;
        A(i,2)=a2-S(i);
        A(i,3)=-a2;
        A(i,4)=D(i)-S(i)*kd(i);
    else %Wall Boundary condition
        PhD_2_BC
    end
end
else
    rd2=(((rd(i)+rd(i+1))/2)^2-((rd(i)+rd(i-1))/2)^2)/2;
    a1=(((rd(i)+rd(i-1))/2)*(2*C(i)*C(i-1)/(C(i)+C(i-1)))/(rd(i)-rd(i-1)))/rd2;
    a2=(((rd(i)+rd(i+1))/2)*(2*C(i)*C(i+1)/(C(i)+C(i+1)))/(rd(i+1)-rd(i)))/rd2;
    A(i,1)=-a1;
    A(i,2)=a1+a2-S(i);
    A(i,3)=-a2;
    A(i,4)=D(i)-S(i)*kd(i);
end
end
%Solving the tri-diagonal system
PhD_Thomas_Algorithms
%Updating values
kd=X;
%Solving the E equation
variable=6;
for i=1:n
    C(i)=(1-nus(i))*(muefd(i)+muTd(i)/sigmaE); %Constructing the diffusion term
    D(i)=G_Ed(i)-D_Ed(i)+I_Ed(i); %Constructing the source/sink terms
    S(i)=dG_Ed(i)+dD_Ed(i)+dl_Ed(i); %Constructing the slope of source/sink terms
end
%Constructing the matrix, using principals of Finite Volume
%The matrix A is actually a tridiagonal matrix but is constructed in form
%of 4 columnar arrys. The first column is the sub-diagonal, the second
%column is a daigonal and the third is the super-diagonal, while the forth
%column is the B matrix in AX=B where A is the original tri-diagonal
for i=1:n
    if i==1 || i==n %Inputing the Boundary Conditions
        if i==1 %Center Line Boundary Condition of Symmetry
            rd2=(((rd(i)+rd(i+1))/2)^2-(rd(i)^2))/2;
            a2=(((rd(i)+rd(i+1))/2)*(2*C(i)*C(i+1)/(C(i)+C(i+1)))/(rd(i+1)-rd(i)))/rd2;
            A(i,1)=0;
            A(i,2)=a2-S(i);
            A(i,3)=-a2;
            A(i,4)=D(i)-S(i)*Ed(i);
        else
            PhD_2_BC %Wall Boundary condition
        end
    end
else
    rd2=(((rd(i)+rd(i+1))/2)^2-((rd(i)+rd(i-1))/2)^2)/2;
    a1=(((rd(i)+rd(i-1))/2)*(2*C(i)*C(i-1)/(C(i)+C(i-1)))/(rd(i)-rd(i-1)))/rd2;
    a2=(((rd(i)+rd(i+1))/2)*(2*C(i)*C(i+1)/(C(i)+C(i+1)))/(rd(i+1)-rd(i)))/rd2;
    A(i,1)=-a1;
    A(i,2)=a1+a2-S(i);
    A(i,3)=-a2;
    A(i,4)=D(i)-S(i)*Ed(i);
end
end
end

```

```

%Solving the tri-diagonal system
PhD_Thomas_Algorithms
%Updating values
Ed=X;

```

PhD_2_BC.m

```

%Boundary Conditions
%Boundary Condition for Vfz
if variable==2
    %No slip
    if Vfz_no_slip==yes
        A(i,1)=0;
        A(i,2)=1;
        A(i,3)=0;
        A(i,4)=0;
        B2(i)=0;
    end
    %Wall Function from Mfix
    if Vfz_wall_Mfix==yes
        h1=rd(i)-rd(i-1);
        h2=cmu^0.25*kd(i)^0.5*h1/2;
        rd2=((rd(i)^2)-((rd(i)+rd(i-1))/2)^2)/2;
        a1=((rd(i)+rd(i-1))/2)*(2*C(i)*C(i-1)/(C(i)+C(i-1)))/(rd(i)-rd(i-1))/rd2;
        A(i,1)=-a1;
        A(i,2)=a1-S(i)+rd(i)/rd2*0.42*cmu^0.25*kd(i)^0.5/log(9.81*h2);
        A(i,3)=0;
        A(i,4)=D(i)-S(i)*Vfzd(i);
        B2(i)=1;
    end
end
%Boundary Condition for Vsz
if variable==3
    %No slip
    if Vsz_no_slip==yes
        A(i,1)=0;
        A(i,2)=1;
        A(i,3)=0;
        A(i,4)=0;
    end
    if Johnson_Jackson_Vsz==yes
        rd2=((rd(i)^2)-((rd(i)+rd(i-1))/2)^2)/2;
        a1=((rd(i)+rd(i-1))/2)*(2*C(i)*C(i-1)/(C(i)+C(i-1)))/(rd(i)-rd(i-1))/rd2;
        A(i,1)=-a1;
        A(i,2)=a1+S(i)-(rd(i)/rd2*pi*(rhos/rhof)*fi*Td(i)^0.5/(2*3^0.5)/(nus0/nus(i)-(nus0/nus(i))^(2/3)));
        A(i,3)=0;
        A(i,4)=-D(i)+S(i)*Vszd(i);
        ADiff(i,i-1)=-a1;
        ADiff(i,i)=a1-(rd(i)/rd2*pi*(rhos/rhof)*fi*Td(i)^0.5/(2*3^0.5)/(nus0/nus(i)-(nus0/nus(i))^(2/3)));
    end
    %Wall Boundary condition: from MFIX, Jenkins condition
    if Vsz_wall_Mfix==yes
        g0=(nus0^(1/3))/(nus0^(1/3)-nus(i)^(1/3));
        rd2=((rd(i)^2)-((rd(i)+rd(i-1))/2)^2)/2;
        a1=((rd(i)+rd(i-1))/2)*(2*C(i)*C(i-1)/(C(i)+C(i-1)))/(rd(i)-rd(i-1))/rd2;
        A(i,1)=-a1;
        A(i,2)=a1+S(i);
    end
end

```

```

A(i,3)=0;
A(i,4)=-D(i)+S(i)*Vszd(i)+(rd(i)/rd2*nus(i)*rhos/rhof*Td(i)*(1+2*(1+ew)*nus(i)*g0)*tan(fiw));
ADiff(i,i-1)=-a1;
ADiff(i,i)=a1;
end
end
%Boundary Condition for T
if variable==4
if Johnson_Jackson_T==yes
rd2=((rd(i)^2)-((rd(i)+rd(i-1))/2)^2)/2;
a1=((rd(i)+rd(i-1))/2)*(2*C(i)*C(i-1)/(C(i)+C(i-1)))/(rd(i)-rd(i-1))/rd2;
A(i,1)=-a1;
A(i,2)=a1+S(i)-(rd(i)/rd2*3^0.5*pi*(rhos/rhof)*(1-ew^2)*Td(i)^0.5/(nus0/nus(i)-(nus0/nus(i))^(2/3)));
A(i,3)=0;
A(i,4)=-D(i)+S(i)*Td(i)-(rd(i)/rd2*pi*(rhos/rhof)*fi*(Vszd(i))^2*Td(i)^0.5/(2*3^0.5)/(nus0/nus(i)-
(nus0/nus(i))^(2/3)));
ADiff(i,i-1)=-a1;
ADiff(i,i)=a1-(rd(i)/rd2*3^0.5*pi*(rhos/rhof)*(1-ew^2)*Td(i)^0.5/(nus0/nus(i)-(nus0/nus(i))^(2/3)));
end
%Wall Boundary condition: from MFIX, Jenkins condition
if Td_wall_Mfix==yes
rd2=((rd(i)^2)-((rd(i)+rd(i-1))/2)^2)/2;
a1=((rd(i)+rd(i-1))/2)*(2*C(i)*C(i-1)/(C(i)+C(i-1)))/(rd(i)-rd(i-1))/rd2;
A(i,1)=-a1;
A(i,2)=a1+S(i)-
(rd(i)/rd2*nus(i)*rhos/rhof*(1+2*(1+ew)*nus(i)*g0)*(3*Td(i))^0.5*3/8*(7/2*(1+ew)*tan(fiw)^2-(1-ew)));
A(i,3)=0;
A(i,4)=-D(i)+S(i)*Td(i);
ADiff(i,i-1)=-a1;
ADiff(i,i)=a1;
end
end
%Boundary Condition for k
if variable==5
%No slip
if k_no_slip==yes
A(i,1)=0;
A(i,2)=1;
A(i,3)=0;
A(i,4)=0;
end
%Wall Function from Mfix
if k_wall_Mfix==yes
h1=rd(i)-rd(i-1);
h2=cmu^0.25*kd(i)^0.5*h1/2;
D(i)=(2*(1-nus(i))*cmu^0.5*kd(i)*Vfzd(i)/h1/log(9.81*h2))-(1-
nus(i))*(2*cmu^0.75*kd(i)^1.5/0.42/h1)+I_kd(i);
S(i)=wk(1)*(2*(1-nus(i))*cmu^0.5*Vfzd(i)/h1/log(9.81*h2))-10*1.5*(1-
nus(i))*(2*cmu^0.75*kd(i)^0.5/0.42/h1);
rd2=((rd(i)^2)-((rd(i)+rd(i-1))/2)^2)/2;
a1=((rd(i)+rd(i-1))/2)*(2*C(i)*C(i-1)/(C(i)+C(i-1)))/(rd(i)-rd(i-1))/rd2;
A(i,1)=-a1;
A(i,2)=a1-S(i);
A(i,3)=0;
A(i,4)=D(i)-S(i)*kd(i);
end
end

```

```

end
%Boundary Condition for E
if variable==6
    %E at wall=muef/rhof*d^2k/dr^2
    if Bolio_equation_2_62==yes
        A(i,1)=0;
        A(i,2)=1;
        A(i,3)=0;
        h1=drb(n);
        h2=drb(n)+drb(n-1);
        A(i,4)=muefd(i)*((kd(i)-kd(i-1))/h1-(kd(i)-kd(i-2))/h2)*(2/(h2-h1))+l_kd(i)/(1-nus(i));
    end
    %Wall Function from Mfix
    if E_wall_Mfix==yes
        h1=rd(i)-rd(i-1);
        A(i,1)=0;
        A(i,2)=1;
        A(i,3)=0;
        A(i,4)=2*cmu^0.75*kd(i)^1.5/0.42/h1;
    end
end
end

```

PhD_1_Convergence.m

```

%Calculating convergence for single phase
Vfzd_C(z)=norm(Vfzd-Vfzd_o)/norm(Vfzd);
kd_C(z)=norm(kd-kd_o)/norm(kd);
Ed_C(z)=norm(Ed-Ed_o)/norm(Ed);

```

PhD_2_Convergence.m

```

%Calculating convergence for two phase
nus_C(z)=norm(nus-nus_o)/norm(nus);
Vfzd_C(z)=norm(Vfzd-Vfzd_o)/norm(Vfzd);
Vszd_C(z)=norm(Vszd-Vszd_o)/norm(Vszd);
Td_C(z)=norm(Td-Td_o)/norm(Td);
kd_C(z)=norm(kd-kd_o)/norm(kd);
Ed_C(z)=norm(Ed-Ed_o)/norm(Ed);
kTd_C(z)=norm(kTd-kTd_o)/norm(kTd);

```

PhD_Re_March.m

```

%Iterating on Re for single phase
n1=n_Re_iterations;
for z=1:n1
    Z(z)=z;
    %Saving old profiles
    Vfzd_o=Vfzd;
    kd_o=kd;
    Ed_o=Ed;
    PhD_1_Strain %Calculating strain
    PhD_1_Viscosity %Calculating eddy viscosity
    PhD_1_Vfz_Eqn %Solving Vfz equation
    PhD_1_k_E_Eqn %Solving k-E equation
    PhD_1_Convergence %Calculating convergence
    %Checking if anything is negative
    negative_profiles=no;
    for i=1:n

```

```

    if Vfzd(i)<0
        disp('Warning: negative Vfz')
        negative_profiles=yes;
        z_negative_profiles=z
        break
    end
    if kd(i)<0
        disp('Warning: negative k')
        negative_profiles=yes;
        z_negative_profiles=z
        break
    end
    if Ed(i)<0
        disp('Warning: negative E')
        negative_profiles=yes;
        z_negative_profiles=z
        break
    end
end
if negative_profiles==yes
    break
end
%Testing if new solution has converged
if Vfzd_C(z)<Vfzd_tolerance
if kd_C(z)<kd_tolerance
if Ed_C(z)<Ed_tolerance
    t2=cputime;
    disp('*****')
    disp('Marching on Re')
    Re_achieved=Re
    Vfz_C=Vfzd_C(z)
    k_C=kd_C(z)
    E_C=Ed_C(z)
    Time=t2-t1
    disp('*****')
    break
end
end
end
end
end

```

PhD_m_March.m

```

%Iterating on m
n1=n_m_ iterations;
n2=n_m_working;
n3=n1/n2;
for z=1:n1
    %Setting up counter
    Z(z)=z;
    z1=z/n2;
    z2=int16(z1);
    %Saving old profiles
    nus_o=nus;
    Vfzd_o=Vfzd;
    Vszd_o=Vszd;
    Td_o=Td;

```

```

kd_o=kd;
Ed_o=Ed;
kTd_o=kTd;
PhD_Relative_Velocity
PhD_2_Strain %Calculating Strain
PhD_2_Viscosity %Calculating all the various viscosities
PhD_Drag_Models %Calculating Drag
PhD_2_Generation %Calculating all the various Generation terms
PhD_2_Dissipation %Calculating all the various Dissipation terms
PhD_2_Interaction %Calculating all the various Interaction terms
PhD_2_nus_Eqn %Solving the nus equation
PhD_2_Vfz_Eqn %Solving the Vfz equation
PhD_2_Vsz_Eqn %Solving the Vsz equation
PhD_2_T_Eqn %Solving the T equation
PhD_2_k_E_Eqn %Solving the k-E equation
PhD_2_Convergence %Calculating convergence
%Checking if anything is negative
negative_profiles=no;
for i=1:n
    if nus(i)<0
        disp('Warning: negative nus')
        negative_profiles=yes;
        z_negative_profiles=z
        break
    end
    if Vfzd(i)<0
        disp('Warning: negative Vfz')
        negative_profiles=yes;
        z_negative_profiles=z
        break
    end
    if Vsزد(i)<0
        disp('Warning: negative Vsz')
        negative_profiles=yes;
        z_negative_profiles=z
        break
    end
    if Td(i)<0
        disp('Warning: negative T')
        negative_profiles=yes;
        z_negative_profiles=z
        break
    end
    if kd(i)<0
        disp('Warning: negative k')
        negative_profiles=yes;
        z_negative_profiles=z
        break
    end
    if Ed(i)<0
        disp('Warning: negative E')
        negative_profiles=yes;
        z_negative_profiles=z
        break
    end
end
end

```

```

if negative_profiles==yes
    break
end
%Saying Work in Progress
if z2==z1
    t2=cputime;
    disp('*****')
    disp('Marching on m')
    disp('Solving for...')
    Re_achieved=Re
    m_achieved=m
    nu_C=nus_C(z)
    Vfz_C=Vfzd_C(z)
    Vsz_C=Vsزد_C(z)
    T_C=Td_C(z)
    k_C=kd_C(z)
    E_C=Ed_C(z)
    kT_C=kTd_C(z)
    Time=t2-t1
    Iteration=z
end
%Testing for convergence
if nus_C(z)<nus_tolerance
if Vfz_C(z)<Vfzd_tolerance
if Vsزد_C(z)<Vsزد_tolerance
if Td_C(z)<Td_tolerance
if kd_C(z)<kd_tolerance
if Ed_C(z)<Ed_tolerance
if kTd_C(z)<kTd_tolerance
    nus_n=nus;
    Vfz_n=Vfzd;
    Vsزد_n=Vsزد;
    Td_n=Td;
    kd_n=kd;
    Ed_n=Ed;
    kTd_n=kTd;
    t2=cputime;
    disp('*****')
    disp('Marching on m')
    Re_achieved=Re
    m_achieved=m
    nu_C=nus_C(z)
    Vfz_C=Vfzd_C(z)
    Vsz_C=Vsزد_C(z)
    T_C=Td_C(z)
    k_C=kd_C(z)
    E_C=Ed_C(z)
    kT_C=kTd_C(z)
    Time=t2-t1
    Iteration=z
    disp('*****')
    if m==m_target
        m_march_complete=yes;
        disp('*****')
        disp('Completed March on m')
        disp('*****')

```



```

        drf(i)=rd(i+1)-rd(i); %Getting foward difference
        drb(j)=rd(j)-rd(j-1); %Getting backward difference
    end
    PhD_Re_March %iterating on Re
    if negative_profiles==yes
        disp('Terminating Code')
        break
    end
    if Re==Re_target
        break
    end
end
else %Similar as above
for q=1:n_Re_march
    Re=Res*exp(Re_jump*q);
    if Re>Re_target
        Re=Re_target;
    end
    r=R*rdim;
    V=Re*muf/rhof/2/R;
    rd=Re/2*rdim;
    for i=1:n-1
        j=i+1;
        drf(i)=rd(i+1)-rd(i);
        drb(j)=rd(j)-rd(j-1);
    end
    PhD_Re_March
    if negative_profiles==yes
        disp('Terminating Code')
        break
    end
    if Re==Re_target
        break
    end
end
end
end
if negative_profiles==yes
    break
end
for j=1:4
    for i=1:n
        if j==1
            Solution_Single_Phase(i,j)=r(i);
        end
        if j==2
            Solution_Single_Phase(i,j)=Vfzd(i)*V;
        end
        if j==3
            Solution_Single_Phase(i,j)=kd(i)*V^2;
        end
        if j==4
            Solution_Single_Phase(i,j)=Ed(i)*V^4*rhof/muf;
        end
    end
end
end
end

```

PhD_Definitions.m

%Pre-defining orders of matrices for Matlab optimization
%List is too long to be displayed

PhD_Two_Phase

```
%Main Code
clear all
clc
format compact
t1=cputime;
yes=1;
no=0;
PhD_Data %Taking in data from user
PhD_Model_Options %Selecting the models
PhD_Model_Parameters %Setting parameters and weights
PhD_Marching_Parameters %Setting Marching parameters
t2=cputime;
%Running the Single Phase code
disp('*****')
disp('Starting to March on Re')
Time=t2-t1
disp('*****')
PhD_Single_Phase
disp('*****')
disp('Completed March on Re')
disp('*****')
PhD_Definitions %Pre-Defining orders of matrices for Matlab optimization
for i=1:n
    N(i)=i; %Constructing a grid point matrix
end
r=R*rdim; %Defining the radius of the pipe
eta=(1+e)/2;
etaf=(1+ef)/2;
Ar=d^3*rhof*(rhos-rhof)*g/muf^2;
dR=d/R;
Rep=Re/2*dR;
ST=Rep/18*dR/2*rhos/rhof;
PhD_ST_Classify
m_target=m;
M1=R*rhof*m/d/rhos; %Defining M1=R*rhof*m/d/rhos
%M1 generally varies form 0 to 2 for most cases.
%Initiating M1 at 0.05 if necessary
if M1>m_start
    M1=m_start;
end
M=M1*dR;
m=M*rhos/rhof;
for i=1:n %Guessing Vs zd, Td & nus
    Vs zd(i)=Ratio_V*Vfzd(1);
    nus(i)=M/(Ratio_V+M);
    Td(i)=kd(1);
    kTd(i)=(6*kd(i)*Td(i))^0.5;
end
nus_n=nus;
Vfzd_n=Vfzd;
```

```

Vszd_n=Vszd;
Td_n=Td;
kd_n=kd;
Ed_n=Ed;
kTd_n=kTd;
t2=cputime;
disp('*****')
disp('Starting to March on m')
Time=t2-t1
disp('*****')
%Begining of the marching from M1=0.05 towards m_target
for q=1:n_m_march
    PhD_m_March
    if z==n_m_iterations %Give warning for overloading
        disp('*****')
        disp('Overloading of Solids')
        disp('*****')
    end
    if m_march_complete==yes %Breaking the loop
        break
    end
    if negative_profiles==yes || z==n_m_iterations
        disp('Reducing m_jump')
        m_jump=m_jump/2;
        if m_jump*d/R*rhos/rhof<lower_jump_limit
            disp('Code has reached its maximum solid loading')
            nus=nus_n;
            Vfzd=Vfzd_n;
            Vszd=Vszd_n;
            Td=Td_n;
            kd=kd_n;
            Ed=Ed_n;
            kTd=kTd_n;
            PhD_Post_Processing %Post Processing
            save('Output')
            break
        end
        M1=M1-m_jump;
        nus=nus_n;
        Vfzd=Vfzd_n;
        Vszd=Vszd_n;
        Td=Td_n;
        kd=kd_n;
        Ed=Ed_n;
        kTd=kTd_n;
    else
        M1=M1+m_jump; %Taking a linear jump in M1 towards m_target
    end
    M=M1*dR;
    m=M/rhof*rhos;
    if m>m_target %matching m and m_target
        m=m_target;
        M=m/rhos*rhof;
    end
end
disp('*****End Of Simulation*****')

```

```

if negative_profiles==yes || z==n_m_iterations
else
    PhD_Post_Processing %Post Processing
    save('Output')
end

```

PhD_2_nus_Residual.m

```

%Calculating nus Residual
variable=1;
%For Low Stokes number
if Low_ST==yes
    for i=1:n
        C(i)=(muefd(i)+muTd(i))/0.7;
    end
    %Constructing the diffusion matrix
    for i=1:n
        if i==1 || i==n %Inputing Boundary Conditions
            if i==1
                a2=
((rd(i)+rd(i+1))/2)*(2*C(i)*C(i+1)/(C(i)+C(i+1)))/(rd(i+1)-rd(i));
                ADiff(i,i)=a2;
                ADiff(i,i+1)=-a2;
            else
                a1=((rd(i)+rd(i-1))/2)*(2*C(i)*C(i-1)/(C(i)+C(i-1)))/(rd(i)-rd(i-1));
                ADiff(i,i-1)=-a1;
                ADiff(i,i)=a1;
            end
        else
            a1=((rd(i)+rd(i-1))/2)*(2*C(i)*C(i-1)/(C(i)+C(i-1)))/(rd(i)-rd(i-1));
            a2=((rd(i)+rd(i+1))/2)*(2*C(i)*C(i+1)/(C(i)+C(i+1)))/(rd(i+1)-rd(i));
            ADiff(i,i-1)=-a1;
            ADiff(i,i)=a1+a2;
            ADiff(i,i+1)=-a2;
        end
    end
end
%Calculating the Diffusion term
nus_Diff=ADiff*nus;
nus_Residual=nus_Diff;
end
%For Mid and High Stokes number
if Mid_ST==yes || High_ST==yes
    temp=constant;
    clear constant
    for i=1:n
        alphaTd(i)=alpha(i)*Td(i);
        constant(i)=temp;
        nus_Residual(i)=alpha(i)*Td(i)-constant(i);
    end
end

```

PhD_2_Vfz_Residual.m

```

%Calculating Vfz Residual
variable=2;
for i=1:n
    G_Vfzd(i)=-dPdZ; %letting Pressure Drop to be the generation term

```

```

C(i)=muefd(i)+muTd(i); %Calculating the Diffusion co-efficient
D(i)=G_Vfzd(i)-D_Vfzd(i)+I_Vfzd(i); %Compiling the source/sink terms
end
D(n)=0;
%Constructing the Diffusion matrix
for i=1:n
    if i==1 || i==n %Inputing the Boundary Conditions
        if i==1
            rd2=(((rd(i)+rd(i+1))/2)^2-(rd(i)^2))/2;
            a2=(((rd(i)+rd(i+1))/2)*(2*C(i)*C(i+1)/(C(i)+C(i+1))))/(rd(i+1)-rd(i))/rd2;
            ADiff(i,i)=a2;
            ADiff(i,i+1)=-a2;
        end
        if i==n
            ADiff(i,i)=1;
        end
    end
    else
        rd2=(((rd(i)+rd(i+1))/2)^2-((rd(i)+rd(i-1))/2)^2)/2;
        a1=(((rd(i)+rd(i-1))/2)*(2*C(i)*C(i-1)/(C(i)+C(i-1))))/(rd(i)-rd(i-1))/rd2;
        a2=(((rd(i)+rd(i+1))/2)*(2*C(i)*C(i+1)/(C(i)+C(i+1))))/(rd(i+1)-rd(i))/rd2;
        ADiff(i,i-1)=-a1;
        ADiff(i,i)=a1+a2;
        ADiff(i,i+1)=-a2;
    end
end
Vfz_Diff=ADiff*Vfzd; %Calculating the Diffusion term
Vfz_Residual=Vfz_Diff-D; %Calculating the Residual

```

PhD_2_Vsz_Residual.m

```

%Calculating Vfz Residual
variable=3;
for i=1:n
    C(i)=-musdG(i); %Calculating the Diffusion co-efficient
    D(i)=G_Vszd(i)-D_Vszd(i)+I_Vszd(i); %Compiling the source/sink terms
end
%Constructing the Diffusion matrix
for i=1:n
    if i==1 || i==n %Inputing Boundary Conditions
        if i==1
            rd2=(((rd(i)+rd(i+1))/2)^2-(rd(i)^2))/2;
            a2=(((rd(i)+rd(i+1))/2)*(2*C(i)*C(i+1)/(C(i)+C(i+1))))/(rd(i+1)-rd(i))/rd2;
            ADiff(i,i)=a2;
            ADiff(i,i+1)=-a2;
        else
            PhD_2_BC
        end
    end
    else
        rd2=(((rd(i)+rd(i+1))/2)^2-((rd(i)+rd(i-1))/2)^2)/2;
        a1=(((rd(i)+rd(i-1))/2)*(2*C(i)*C(i-1)/(C(i)+C(i-1))))/(rd(i)-rd(i-1))/rd2;
        a2=(((rd(i)+rd(i+1))/2)*(2*C(i)*C(i+1)/(C(i)+C(i+1))))/(rd(i+1)-rd(i))/rd2;
        ADiff(i,i-1)=-a1;
        ADiff(i,i)=a1+a2;
        ADiff(i,i+1)=-a2;
    end
end
Vsz_Diff=ADiff*Vszd; %Calculating the Diffusion term

```

```
Vsz_Residual=Vsz_Diff+D; %Calculating the Residual
```

PhD_2_T_Residual.m

```
%Calculating T Residual
```

```
varibale=4;
```

```
if Bolio_equation__36==yes
```

```
    rd2=((rd(n)^2)-((rd(n)+rd(n-1))/2)^2)/2; %Adding extra generation due to the wall
```

```
    G_Td(n)=
```

```
G_Td(n)+(rd(n)/rd2*pi*(rhos/rhof)*fi*Vszd(n)^2*Td(n)^0.5/(2*3^0.5)/(nus0/nus(n)-(nus0/nus(n))^(2/3)));
```

```
end
```

```
for i=1:n
```

```
    C(i)=-lambdadG(i); %Calculating the Diffusion co-efficient
```

```
    D(i)=G_Td(i)-D_Td(i)+I_Td(i); %Compiling the source/sink terms
```

```
end
```

```
%Constructing the Diffusion matrix
```

```
for i=1:n
```

```
    if i==1 || i==n %Inputing Boundary Conditions
```

```
        if i==1
```

```
            rd2=((rd(i)+rd(i+1))/2)^2-(rd(i)^2)/2;
```

```
            a2=((rd(i)+rd(i+1))/2)*(2*C(i)*C(i+1)/(C(i)+C(i+1)))/(rd(i+1)-rd(i))/rd2;
```

```
            ADiff(i,i)=a2;
```

```
            ADiff(i,i+1)=-a2;
```

```
        else
```

```
            PhD_2_BC
```

```
        end
```

```
    else
```

```
        rd2=((rd(i)+rd(i+1))/2)^2-((rd(i)+rd(i-1))/2)^2)/2;
```

```
        a1=((rd(i)+rd(i-1))/2)*(2*C(i)*C(i-1)/(C(i)+C(i-1)))/(rd(i)-rd(i-1))/rd2;
```

```
        a2=((rd(i)+rd(i+1))/2)*(2*C(i)*C(i+1)/(C(i)+C(i+1)))/(rd(i+1)-rd(i))/rd2;
```

```
        ADiff(i,i-1)=-a1;
```

```
        ADiff(i,i)=a1+a2;
```

```
        ADiff(i,i+1)=-a2;
```

```
    end
```

```
end
```

```
T_Diff=ADiff*Td; %Calculating the Diffusion term
```

```
T_Residual=T_Diff+D; %Calculating the Residual
```

PhD_2_k_E_Residual.m

```
%Calculating k-E Residual
```

```
%k Residual
```

```
variable=5;
```

```
for i=1:n
```

```
    C(i)=(1-nus(i))*(muefd(i)+muTd(i)/sigmak); %Calculating the Diffusion co-efficient
```

```
    D(i)=G_kd(i)-D_kd(i)+I_kd(i); %Compiling the source/sink terms
```

```
end
```

```
D(n)=0;
```

```
%Constructing the Diffusion matrix
```

```
for i=1:n
```

```
    if i==1 || i==n %Inputing Boundary Conditions
```

```
        if i==1
```

```
            rd2=((rd(i)+rd(i+1))/2)^2-(rd(i)^2)/2;
```

```
            a2=((rd(i)+rd(i+1))/2)*(2*C(i)*C(i+1)/(C(i)+C(i+1)))/(rd(i+1)-rd(i))/rd2;
```

```
            ADiff(i,i)=a2;
```

```
            ADiff(i,i+1)=-a2;
```

```
        else
```

```

        ADiff(i,i-1)=0;
        ADiff(i,i)=1;
    end
else
    rd2=(((rd(i)+rd(i+1))/2)^2-((rd(i)+rd(i-1))/2)^2)/2;
    a1=((rd(i)+rd(i-1))/2)*(2*C(i)*C(i-1)/(C(i)+C(i-1)))/(rd(i)-rd(i-1))/rd2;
    a2=((rd(i)+rd(i+1))/2)*(2*C(i)*C(i+1)/(C(i)+C(i+1)))/(rd(i+1)-rd(i))/rd2;
    ADiff(i,i-1)=-a1;
    ADiff(i,i)=a1+a2;
    ADiff(i,i+1)=-a2;
end
end
k_Diff=ADiff*kd; %Calculating the Diffusion term
k_Residual=k_Diff-D; %Calculating the Residual
%E Residual
variable=6;
for i=1:n
    C(i)=(1-nus(i))*(muefd(i)+muTd(i)/sigmaE); %Calculating the Diffusion co-efficient
    D(i)=G_Ed(i)-D_Ed(i)+I_Ed(i); %Compiling the source/sink terms
end
D(n)=0;
%Constructing the Diffusion matrix
for i=1:n
    if i==1 || i==n %Inputing Boundary Conditions
        if i==1
            rd2=(((rd(i)+rd(i+1))/2)^2-(rd(i)^2))/2;
            a2=((rd(i)+rd(i+1))/2)*(2*C(i)*C(i+1)/(C(i)+C(i+1)))/(rd(i+1)-rd(i))/rd2;
            ADiff(i,i)=a2;
            ADiff(i,i+1)=-a2;
        else
            ADiff(i,i-1)=0;
            ADiff(i,i)=1;
        end
    else
        rd2=(((rd(i)+rd(i+1))/2)^2-((rd(i)+rd(i-1))/2)^2)/2;
        a1=((rd(i)+rd(i-1))/2)*(2*C(i)*C(i-1)/(C(i)+C(i-1)))/(rd(i)-rd(i-1))/rd2;
        a2=((rd(i)+rd(i+1))/2)*(2*C(i)*C(i+1)/(C(i)+C(i+1)))/(rd(i+1)-rd(i))/rd2;
        ADiff(i,i-1)=-a1;
        ADiff(i,i)=a1+a2;
        ADiff(i,i+1)=-a2;
    end
end
E_Diff=ADiff*Ed; %Calculating the Diffusion co-efficient
E_Residual=E_Diff-D; %Calculating the Residual

```

PhD_Dimensions.m

```

%Giving dimensions oa all variables
%Giving dimensions to solution variables
Vfz=Vfzd*V;
Vsz=Vszd*V;
T=Td*V^2;
k=kd*V^2;
E=rhof*V^4*Ed/muf;
UT=UTd*V;
%Giving dimensions to all the terms in the equation
if Low_ST==yes

```

```

nus_Residual=V*rhof*nus_Residual;
Vfz_Diff=(V^2*rhof^2/muf)*V*Vfz_Diff;
G_Vfz=(V^2*rhof^2/muf)*V*G_Vfzd;
D_Vfz=(V^2*rhof^2/muf)*V*D_Vfzd;
I_Vfz=(V^2*rhof^2/muf)*V*I_Vfzd;
Vfz_Residual=(V^2*rhof^2/muf)*V*Vfz_Residual;
Vsz_Diff=(V^2*rhof^2/muf)*V*Vsz_Diff;
G_Vsz=(V^2*rhof^2/muf)*V*G_Vszd;
D_Vsz=(V^2*rhof^2/muf)*V*D_Vszd;
I_Vsz=(V^2*rhof^2/muf)*V*I_Vszd;
Vsz_Residual=(V^2*rhof^2/muf)*V*Vsz_Residual;
k_Diff=(V^2*rhof^2/muf)*V^2*k_Diff;
G_k=(V^2*rhof^2/muf)*V^2*G_kd;
D_k=(V^2*rhof^2/muf)*V^2*D_kd;
I_k=(V^2*rhof^2/muf)*V^2*I_kd;
k_Residual=(V^2*rhof^2/muf)*V^2*k_Residual;
E_Diff=(V^2*rhof^2/muf)*rhof/muf*V^4*E_Diff;
G_E=(V^2*rhof^2/muf)*rhof/muf*V^4*G_Ed;
D_E=(V^2*rhof^2/muf)*rhof/muf*V^4*D_Ed;
I_E=(V^2*rhof^2/muf)*rhof/muf*V^4*I_Ed;
E_Residual=(V^2*rhof^2/muf)*rhof/muf*V^4*E_Residual;
end
if Mid_ST==yes || High_ST==yes
alphaT=V^2*alphaTd;
constant=V^2*constant;
nus_Residual=V^2*nus_Residual;
Vfz_Diff=(V^2*rhof^2/muf)*V*Vfz_Diff;
G_Vfz=(V^2*rhof^2/muf)*V*G_Vfzd;
D_Vfz=(V^2*rhof^2/muf)*V*D_Vfzd;
I_Vfz=(V^2*rhof^2/muf)*V*I_Vfzd;
Vfz_Residual=(V^2*rhof^2/muf)*V*Vfz_Residual;
Vsz_Diff=(V^2*rhof^2/muf)*V*Vsz_Diff;
G_Vsz=(V^2*rhof^2/muf)*V*G_Vszd;
D_Vsz=(V^2*rhof^2/muf)*V*D_Vszd;
I_Vsz=(V^2*rhof^2/muf)*V*I_Vszd;
Vsz_Residual=(V^2*rhof^2/muf)*V*Vsz_Residual;
T_Diff=(V^2*rhof^2/muf)*V^2*T_Diff;
G_T=(V^2*rhof^2/muf)*V^2*G_Td;
D_T=(V^2*rhof^2/muf)*V^2*D_Td;
I_T=(V^2*rhof^2/muf)*V^2*I_Td;
T_Residual=(V^2*rhof^2/muf)*V^2*T_Residual;
k_Diff=(V^2*rhof^2/muf)*V^2*k_Diff;
G_k=(V^2*rhof^2/muf)*V^2*G_kd;
D_k=(V^2*rhof^2/muf)*V^2*D_kd;
I_k=(V^2*rhof^2/muf)*V^2*I_kd;
k_Residual=(V^2*rhof^2/muf)*V^2*k_Residual;
E_Diff=(V^2*rhof^2/muf)*rhof/muf*V^4*E_Diff;
G_E=(V^2*rhof^2/muf)*rhof/muf*V^4*G_Ed;
D_E=(V^2*rhof^2/muf)*rhof/muf*V^4*D_Ed;
I_E=(V^2*rhof^2/muf)*rhof/muf*V^4*I_Ed;
E_Residual=(V^2*rhof^2/muf)*rhof/muf*V^4*E_Residual;
end
PhD_Post_Processing.m
%Post Processing
disp('Post Processing...')

```

```

disp('*****')
ADiff=zeros(n,n);
PhD_2_Strain %Calculating Strain
PhD_2_Viscosity %Calculating various viscosities
PhD_2_Generation %Calculating Generation terms
PhD_2_Dissipation %Calculating Dissipation terms
PhD_2_Interaction %Calculating Interaction terms
%Calculating Residuals
PhD_2_nus_Residual
PhD_2_Vfz_Residual
PhD_2_Vsz_Residual
PhD_2_T_Residual
PhD_2_k_E_Residual
%Giving each term appropriate dimensions
PhD_Dimensions
%Calculating Pressure Drop and Friction velocity
if downward==yes
    %Vfz=-Vfz;
    %Vsz=-Vsz;
    %Solution_Single_Phase(:,2)=-Solution_Single_Phase(:,2);
    dPdz=-(V^2*rhof^2/muf)*V*dPdz-rhof*g;
    rhoavg=rhof*rhos*(m+1)/(rhos+m*rhof);
    Friction_Velocity=((dPdz+rhoavg*g)*R/2/rhoavg)^0.5;
else
    dPdz=(V^2*rhof^2/muf)*V*dPdz-rhof*g;
    rhoavg=rhof*rhos*(m+1)/(rhos+m*rhof);
    Friction_Velocity=(-dPdz-rhoavg*g)*R/2/rhoavg)^0.5;
end
%Calculating average Velocity and average nus
V_avg=0;
nus_avg=0;
for i=1:n-1
    V_avg=V_avg+(r(i)*(1-nus(i))*Vfz(i)+r(i+1)*(1-nus(i+1))*Vfz(i+1))*(r(i+1)-r(i))/R^2;
    nus_avg=nus_avg+(r(i)*nus(i)+r(i+1)*nus(i+1))*(r(i+1)-r(i))/R^2;
end
%Calculating various time scales
cbeta=1.8-1.35;
for i=1:n-1
    g0=(nus0^(1/3))/(nus0^(1/3)-nus(i)^(1/3));
    zetar=3*(Vrd(i))^2/2/kd(i);
    time_collision(i)=d/24/nus(i)/g0*(pi/T(i))^0.5;
    time_turbulent_eddy(i)=3/2*cmu*k(i)/E(i);
    time_fluid_integral(i)=time_turbulent_eddy(i)/(1+cbeta*zetar)^0.5;
    time_particle_relax(i)=nus(i)*rhos/(1-nus(i))/beta(i)/V^2/rhof^2*muf;
    ratio_c_r(i,1)=time_collision(i)/time_particle_relax(i);
    ratio_r_t(i,1)=time_particle_relax(i)/time_turbulent_eddy(i);
    ratio_c_t(i,1)=time_collision(i)/time_turbulent_eddy(i);
end
for j=1:7 %Compiling the Solution matrix
    for i=1:n
        if j==1
            Solution_Two_Phase(i,j)=r(i);
        end
        if j==2
            Solution_Two_Phase(i,j)=nus(i);
        end
    end
end

```

```
    if j==3
        Solution_Two_Phase(i,j)=Vfz(i);
    end
    if j==4
        Solution_Two_Phase(i,j)=Vsz(i);
    end
    if j==5
        Solution_Two_Phase(i,j)=T(i);
    end
    if j==6
        Solution_Two_Phase(i,j)=k(i);
    end
    if j==7
        Solution_Two_Phase(i,j)=E(i);
    end
end
end
end
```

APPENDIX B
RAW FLUID-SOLID DATA

Table B-1. Raw data for $d = 1.5$ mm, $m = 0.0175$ and $V_{fzcl} = 3.07$ m/s

r/R	V_{fz} m/s	v_{fz}' m/s	V_{sz} m/s	v_{sz}' m/s
0.96	1.86	0.357	2.21	0.405
0.93	2.15	0.330	2.28	0.426
0.89	2.30	0.291	2.31	0.434
0.85	2.48	0.271	2.36	0.449
0.82	2.50	0.285	2.40	0.455
0.64	2.76	0.228	2.67	0.413
0.45	2.94	0.209	2.83	0.395
0.27	3.02	0.199	2.92	0.361
0.09	3.07	0.192	3.00	0.337
0.00	3.12	0.182	3.00	0.347

Table B-2. Raw data for $d = 1.5$ mm, $m = 0.0425$, $V_{fzcl} = 2.96$ m/s and run 1

r/R	V_{fz} m/s	v_{fz}' m/s	V_{sz} m/s	v_{sz}' m/s
0.96	1.80	0.326	2.14	0.380
0.93	2.16	0.295	2.31	0.382
0.89	2.27	0.289	2.35	0.379
0.85	2.39	0.273	2.40	0.413
0.82	2.49	0.261	2.46	0.419
0.64	2.78	0.226	2.67	0.381
0.45	2.83	0.211	2.80	0.354
0.27	2.92	0.197	2.93	0.335
0.09	2.96	0.187	2.95	0.338
0.00	2.96	0.183	2.95	0.336

Table B-3. Raw data for $d = 1.5$ mm, $m = 0.0425$, $V_{fzcl} = 2.96$ m/s and run 2

r/R	V_{sz} m/s	v_{sz}' m/s
0.96	2.19	0.372
0.93	2.29	0.377
0.89	2.37	0.374
0.85	2.43	0.398
0.82	2.48	0.401
0.64	2.65	0.410
0.45	2.73	0.403
0.27	2.88	0.362
0.09	2.96	0.351
0.00	2.93	0.341

Table B-4. Raw data for $d = 1.5$ mm, $m = 0.0425$, $V_{fzcl} = 2.96$ m/s and run 3

r/R	V_{sz} m/s	v_{sz}' m/s
0.96	2.19	0.470
0.93	2.24	0.455
0.89	2.29	0.459
0.85	2.33	0.430
0.82	2.39	0.409
0.64	2.67	0.392
0.45	2.80	0.357
0.27	2.90	0.322
0.09	2.95	0.331
0.00	2.94	0.324

Table B-5. Raw data for $d = 1.5$ mm, $m = 0.0425$, $V_{fzcl} = 2.96$ m/s and run 4

r/R	V_{sz} m/s	v_{sz}' m/s
0.96	2.16	0.445
0.93	2.20	0.435
0.89	2.26	0.449
0.85	2.31	0.434
0.82	2.29	0.437
0.64	2.70	0.380
0.45	2.80	0.372
0.27	2.91	0.332
0.09	2.94	0.328
0.00	2.97	0.326

Table B-6. Raw data for $d = 1.5$ mm, $m = 0.075$ and $V_{fzcl} = 3.04$ m/s

r/R	V_{fz} m/s	v_{fz}' m/s	V_{sz} m/s	v_{sz}' m/s
0.96	1.86	0.322	2.30	0.390
0.93	2.26	0.285	2.38	0.414
0.89	2.41	0.284	2.40	0.412
0.85	2.51	0.268	2.45	0.426
0.82	2.60	0.256	2.51	0.441
0.64	2.78	0.224	2.54	0.466
0.45	2.92	0.211	2.87	0.393
0.27	2.96	0.201	2.90	0.364
0.09	3.00	0.184	3.04	0.327
0.00	3.04	0.181	3.03	0.339

Table B-7. Raw data for $d = 1.5$ mm, $m = 0.0175$ and $V_{fzcl} = 5.03$ m/s

r/R	V_{fz} m/s	v_{fz}' m/s	V_{sz} m/s	v_{sz}' m/s
0.96	2.99	0.574	3.79	0.512
0.93	3.52	0.455	3.95	0.565
0.89	3.86	0.424	4.05	0.599
0.85	4.00	0.433	4.11	0.600
0.82	3.77	0.442	4.19	0.637
0.64	4.40	0.348	4.49	0.533
0.45	4.67	0.297	4.59	0.546
0.27	4.90	0.247	4.75	0.527
0.09	5.02	0.222	4.85	0.507
0.00	5.03	0.221	4.87	0.506

Table B-8. Raw data for $d = 1.5$ mm, $m = 0.0425$ and $V_{fzcl} = 4.90$ m/s

r/R	V_{fz} m/s	v_{fz}' m/s	V_{sz} m/s	v_{sz}' m/s
0.96	3.07	0.506	3.75	0.476
0.93	3.50	0.481	3.89	0.506
0.89	3.73	0.434	4.01	0.488
0.85	3.93	0.404	4.07	0.536
0.82	3.99	0.402	4.20	0.541
0.64	4.42	0.322	4.37	0.550
0.45	4.63	0.281	4.83	0.545
0.27	4.78	0.249	4.93	0.492
0.09	4.89	0.231	4.96	0.463
0.00	4.90	0.212	4.97	0.451

Table B-9. Raw data for $d = 1.5$ mm, $m = 0.075$ and $V_{fzcl} = 5.04$ m/s

r/R	V_{fz} m/s	v_{fz}' m/s	V_{sz} m/s	v_{sz}' m/s
0.96	3.21	0.497	3.86	0.503
0.93	3.66	0.456	3.98	0.499
0.89	3.83	0.419	4.09	0.525
0.85	4.03	0.417	4.17	0.535
0.82	4.16	0.416	4.24	0.557
0.64	4.50	0.321	4.48	0.557
0.45	4.76	0.281	4.82	0.486
0.27	4.92	0.244	4.91	0.513
0.09	5.02	0.234	5.07	0.453
0.00	5.04	0.218	5.09	0.485

Table B-10. Raw data for $d = 1.5$ mm, $m = 0.0175$ and $V_{fzcl} = 7$ m/s

r/R	V_{fz} m/s	v_{fz}' m/s	V_{sz} m/s	v_{sz}' m/s
0.96	4.19	0.680	5.16	0.732
0.93	4.90	0.590	5.42	0.757
0.89	5.40	0.585	5.63	0.758
0.85	5.61	0.549	5.62	0.745
0.82	5.70	0.524	5.75	0.729
0.64	6.21	0.427	6.39	0.621
0.45	6.57	0.376	6.71	0.572
0.27	6.79	0.308		
0.09	6.97	0.268		
0.00	7.00	0.272		

Table B-11. Raw data for $d = 1.5$ mm, $m = 0.0425$ and $V_{fzcl} = 7.06$ m/s

r/R	V_{fz} m/s	v_{fz}' m/s	V_{sz} m/s	v_{sz}' m/s
0.96	4.16	0.772	5.26	0.732
0.93	4.97	0.671	5.47	0.712
0.89	5.40	0.570	5.60	0.687
0.85	5.61	0.553	5.73	0.709
0.82	5.69	0.530	5.87	0.746
0.64	6.33	0.438	6.43	0.672
0.45	6.62	0.382	6.74	0.601
0.27	6.85	0.325	6.98	0.521
0.09	7.04	0.283	6.95	0.513
0.00	7.06	0.263	6.94	0.474

Table B-12. Raw data for $d = 1.5$ mm, $m = 0.075$ and $V_{fzcl} = 7.02$ m/s

r/R	V_{fz} m/s	v_{fz}' m/s	V_{sz} m/s	v_{sz}' m/s
0.96	4.42	0.639	5.03	0.732
0.93	5.07	0.618	5.32	0.739
0.89	5.43	0.569	5.49	0.737
0.85	5.63	0.552	5.67	0.717
0.82	5.80	0.532	5.84	0.683
0.64	6.27	0.429	6.15	0.775
0.45	6.60	0.365	6.66	0.613
0.27	6.85	0.315	6.88	0.564
0.09	7.00	0.278	6.96	0.532
0.00	7.02	0.273	7.06	0.576

APPENDIX C
 FIGURES FOR FLUIDIZED BED BINARY MIXTURES

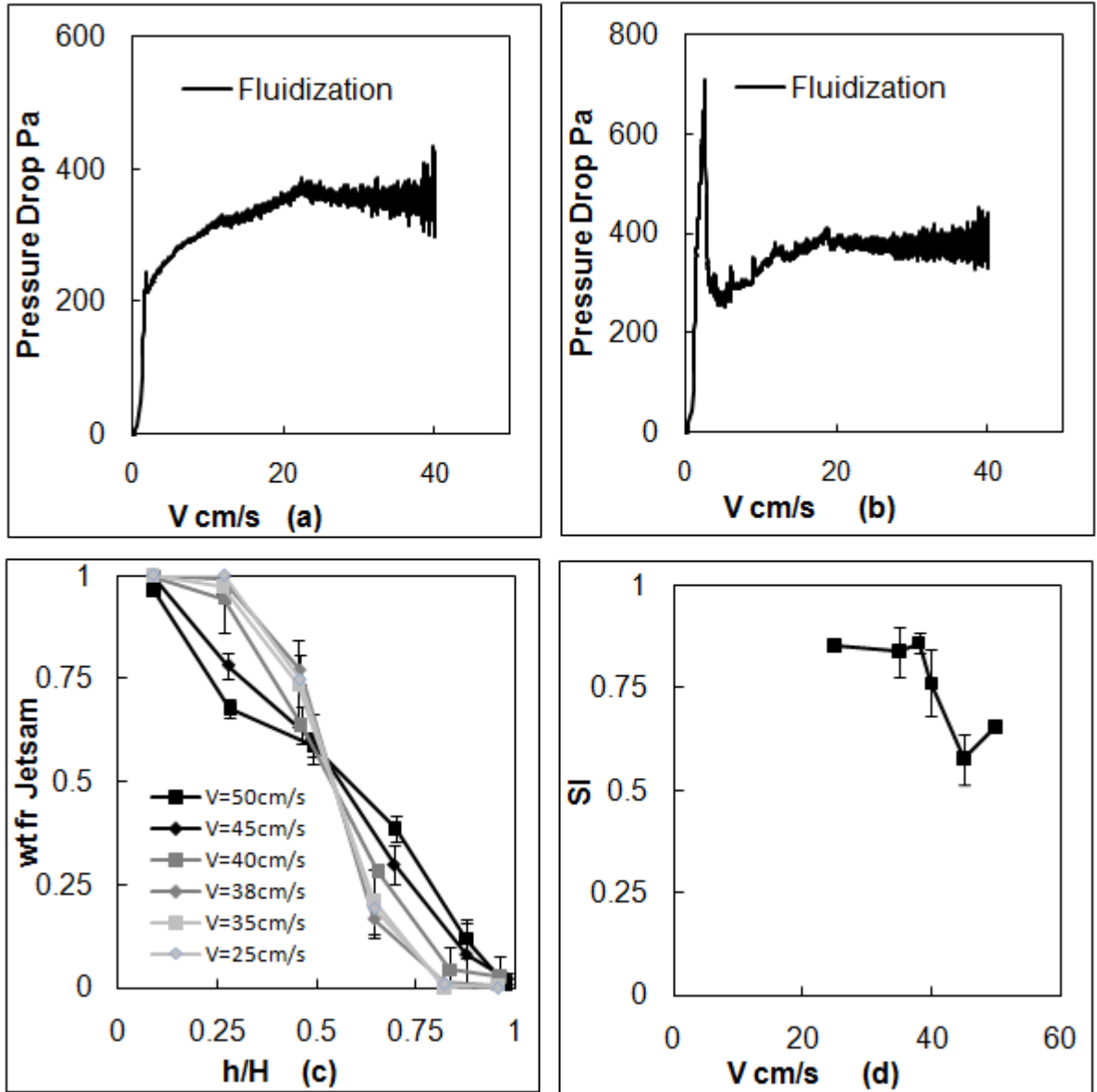


Figure C-1. Pressure drop profiles and segregation index behavior for a Type A mixture 50G550-50G083. (a) Pressure drop profile, initially segregated state. (b) Pressure drop profile, initially mixed state. (c) Segregation profiles. (d) Segregation index.

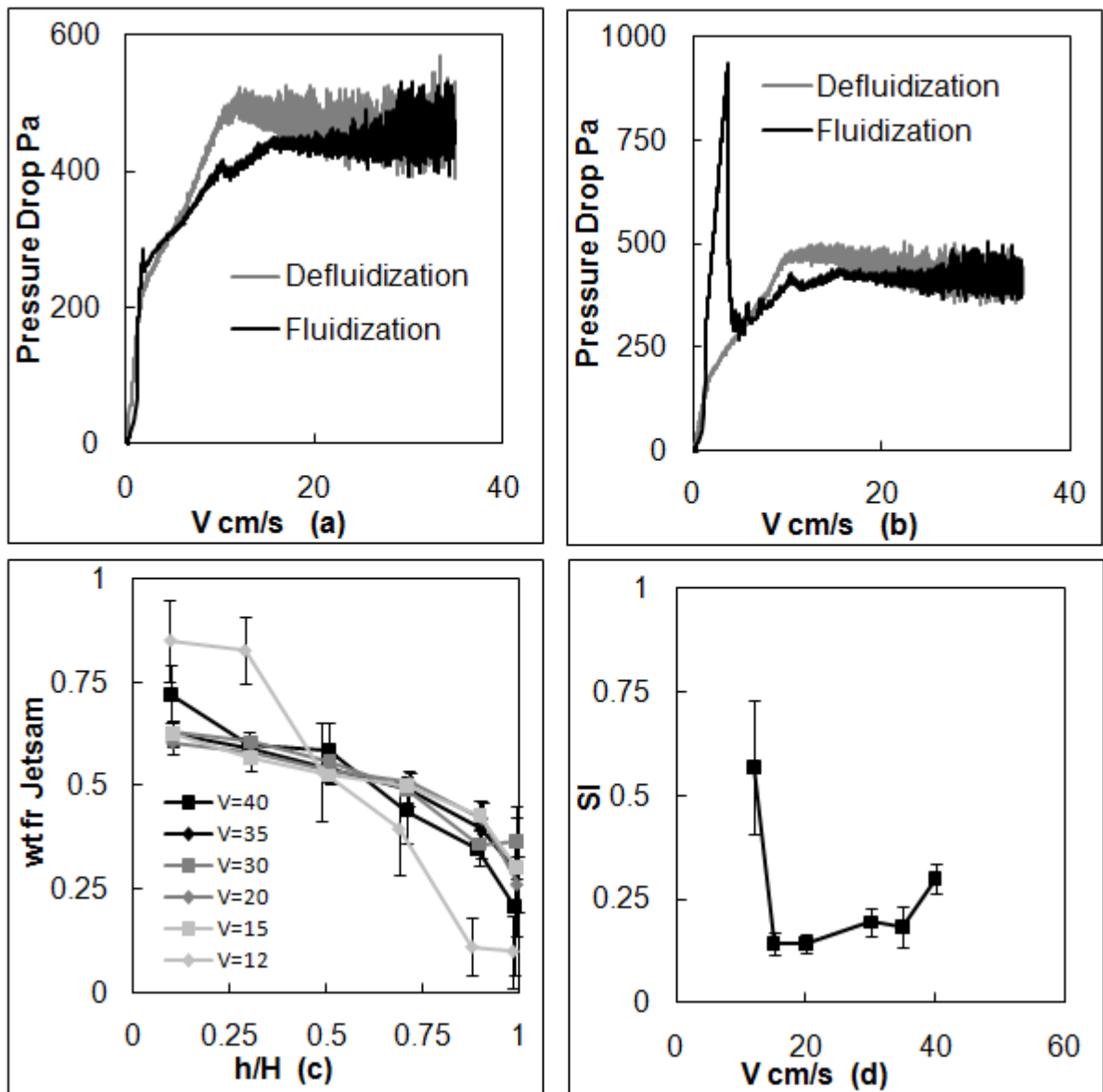


Figure C-2. Pressure drop profiles and segregation index behavior for a Type A mixture 50G462-50G083. (a) Pressure drop profile, initially segregated state. (b) Pressure drop profile, initially mixed state. (c) Segregation profiles. (d) Segregation index.

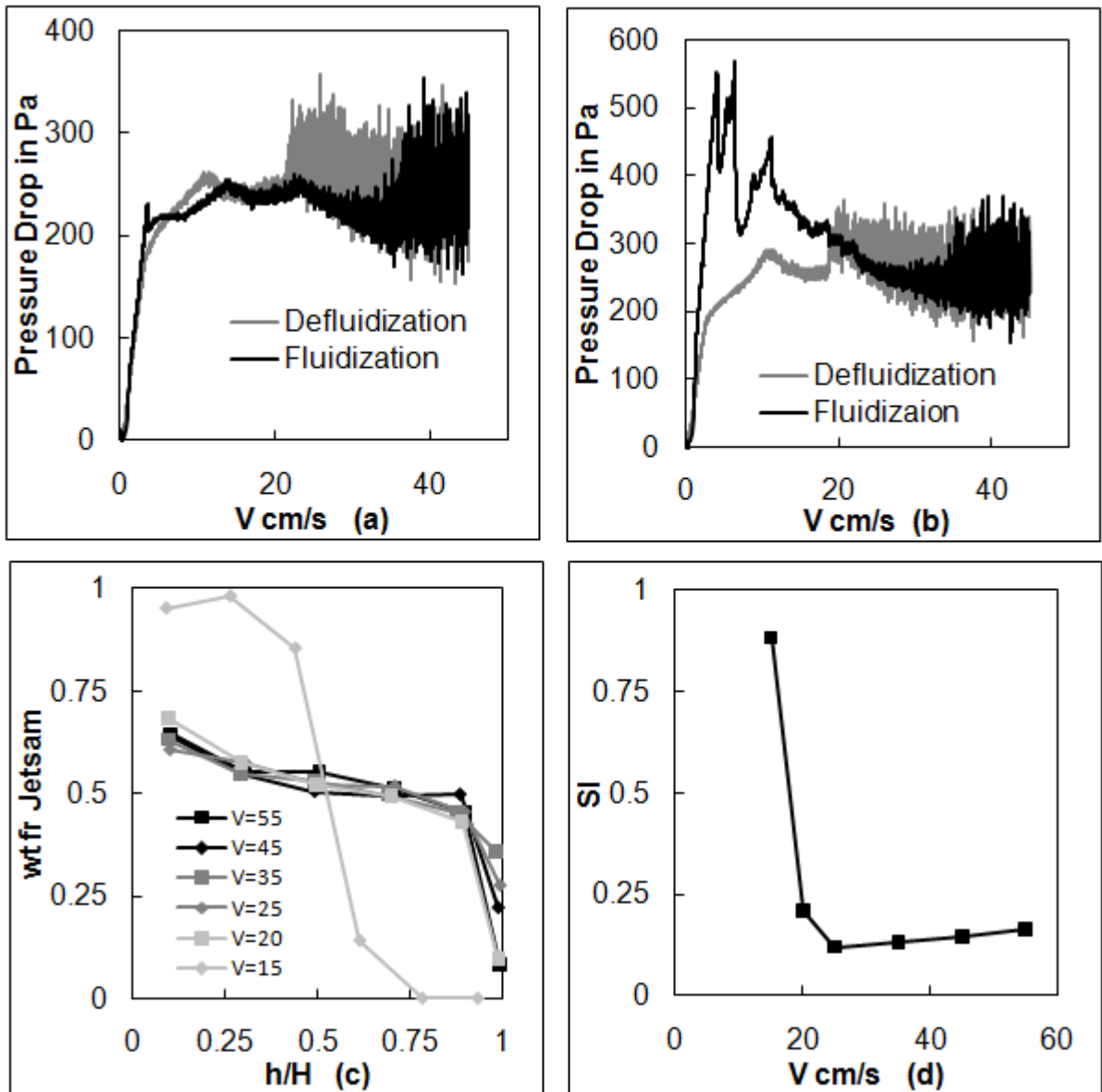


Figure C-3. Pressure drop profiles and segregation index behavior for a Type A mixture 50G550-50G116. (a) Pressure drop profile, initially segregated state. (b) Pressure drop profile, initially mixed state. (c) Segregation profiles. (d) Segregation index.

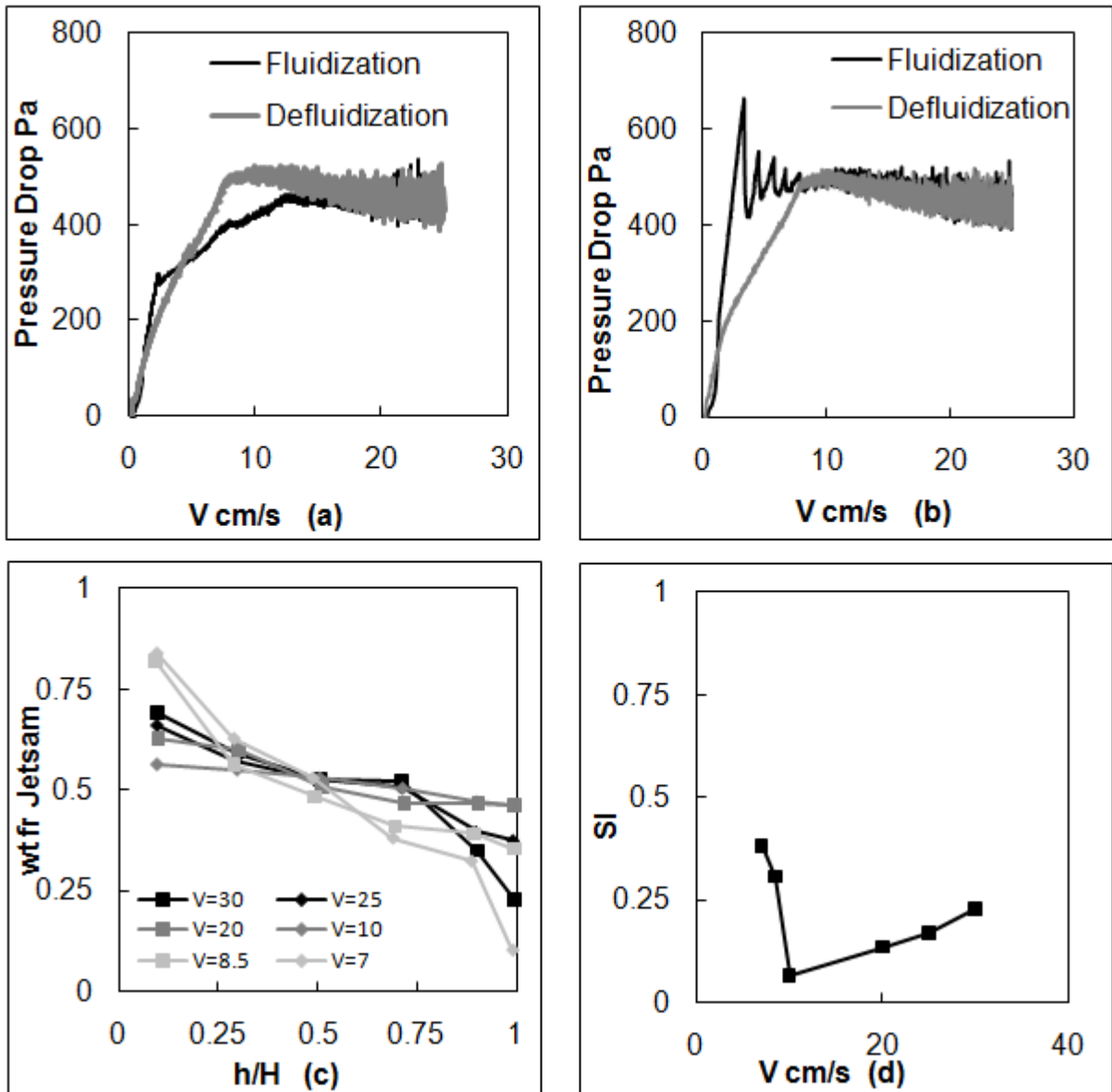


Figure C-4. Pressure drop profiles and segregation index behavior for a Type A mixture 50G385-50G083. (a) Pressure drop profile, initially segregated state. (b) Pressure drop profile, initially mixed state. (c) Segregation profiles. (d) Segregation index.

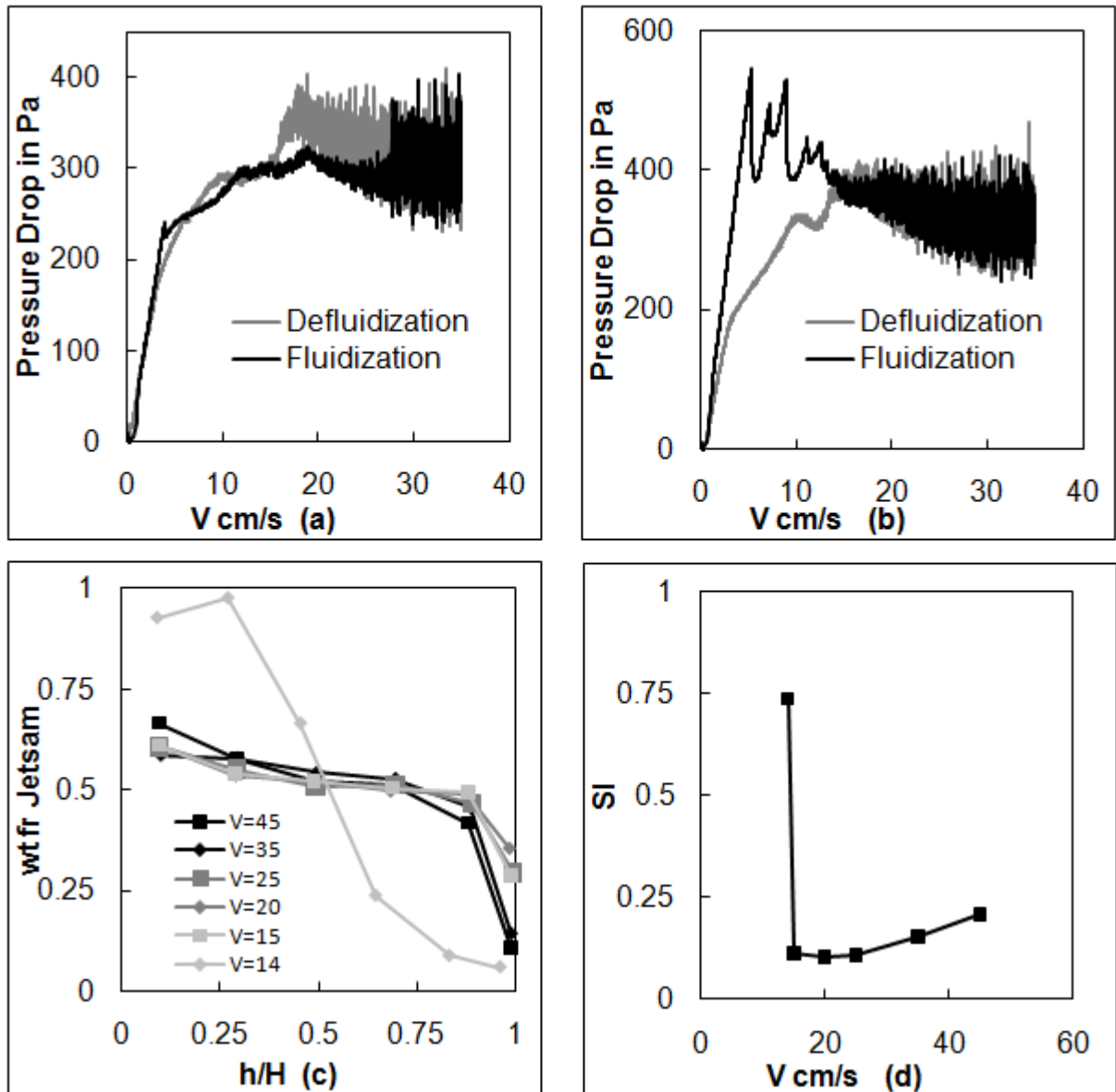


Figure C-5. Pressure drop profiles and segregation index behavior for a Type A mixture 50G462-50G116. (a) Pressure drop profile, initially segregated state. (b) Pressure drop profile, initially mixed state. (c) Segregation profiles. (d) Segregation index.

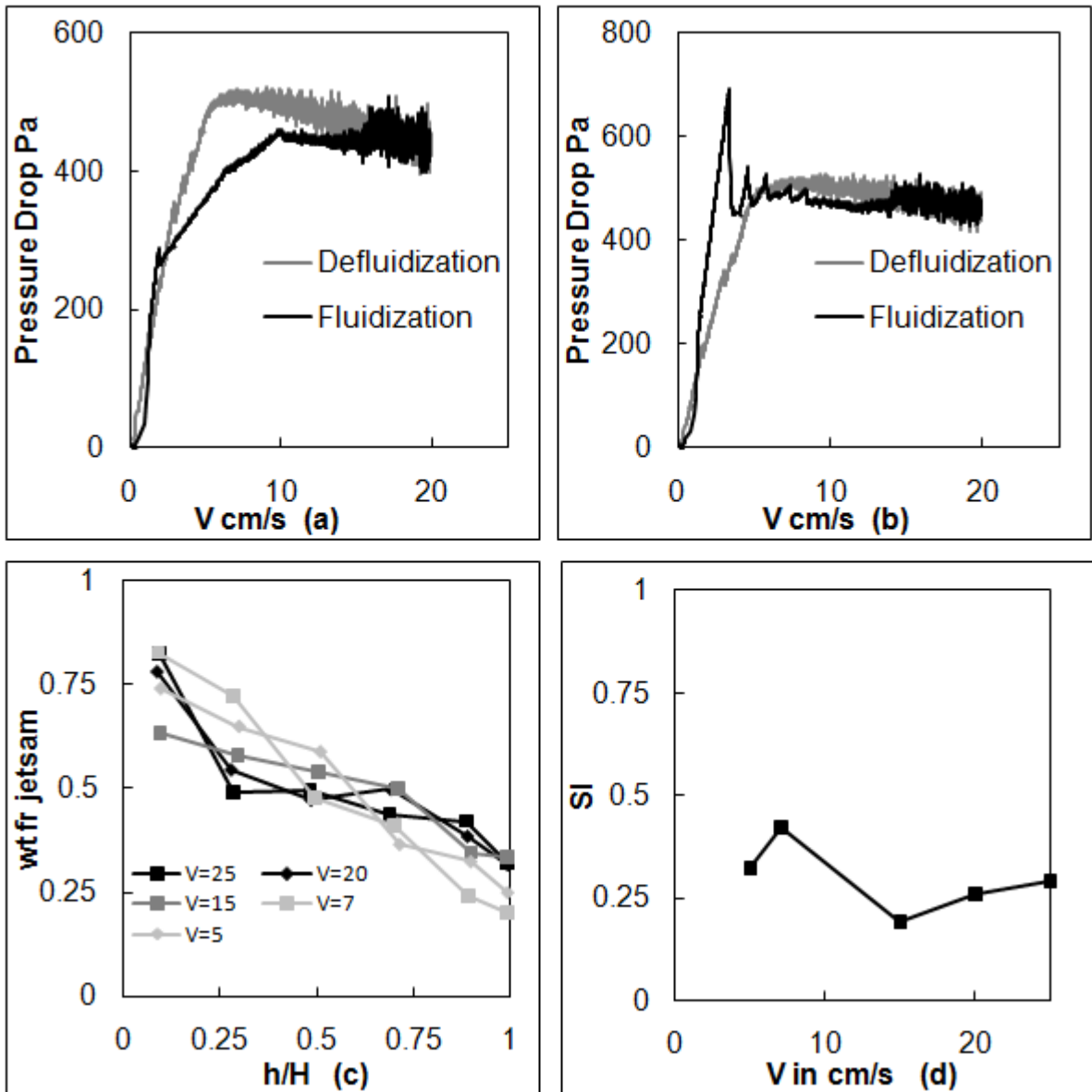


Figure C-6. Pressure drop profiles and segregation index behavior for a Type B mixture 50G328-50G083. (a) Pressure drop profile, initially segregated state. (b) Pressure drop profile, initially mixed state. (c) Segregation profiles. (d) Segregation index.

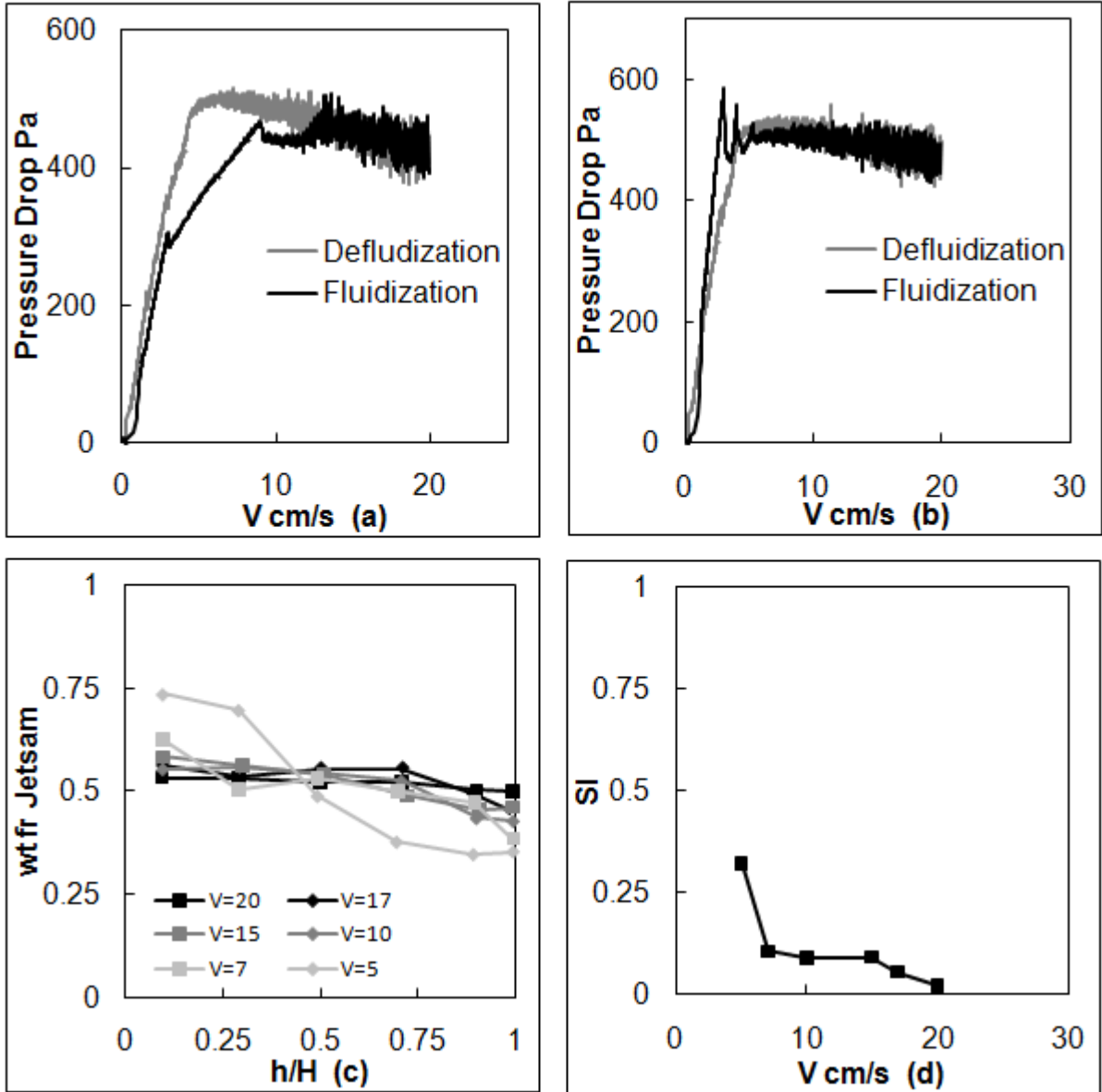


Figure C-7. Pressure drop profiles and segregation index behavior for a Type B mixture 50G275-50G083. (a) Pressure drop profile, initially segregated state. (b) Pressure drop profile, initially mixed state. (c) Segregation index.

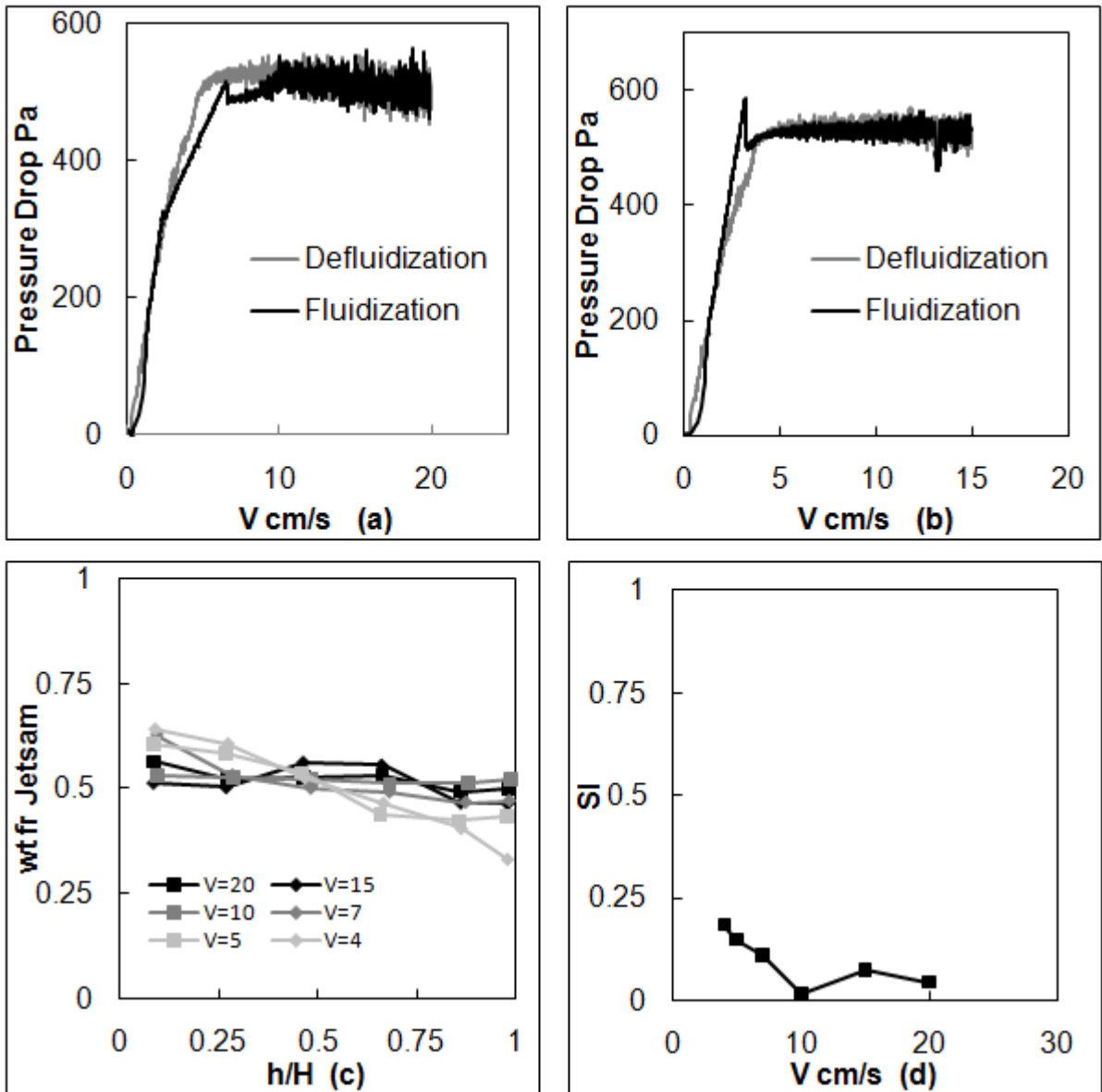


Figure C-8. Pressure drop profiles and segregation index behavior for a Type C mixture 50G231-50G083. (a) Pressure drop profile, initially segregated state. (b) Pressure drop profile, initially mixed state. (c) Segregation profiles. (d) Segregation index.

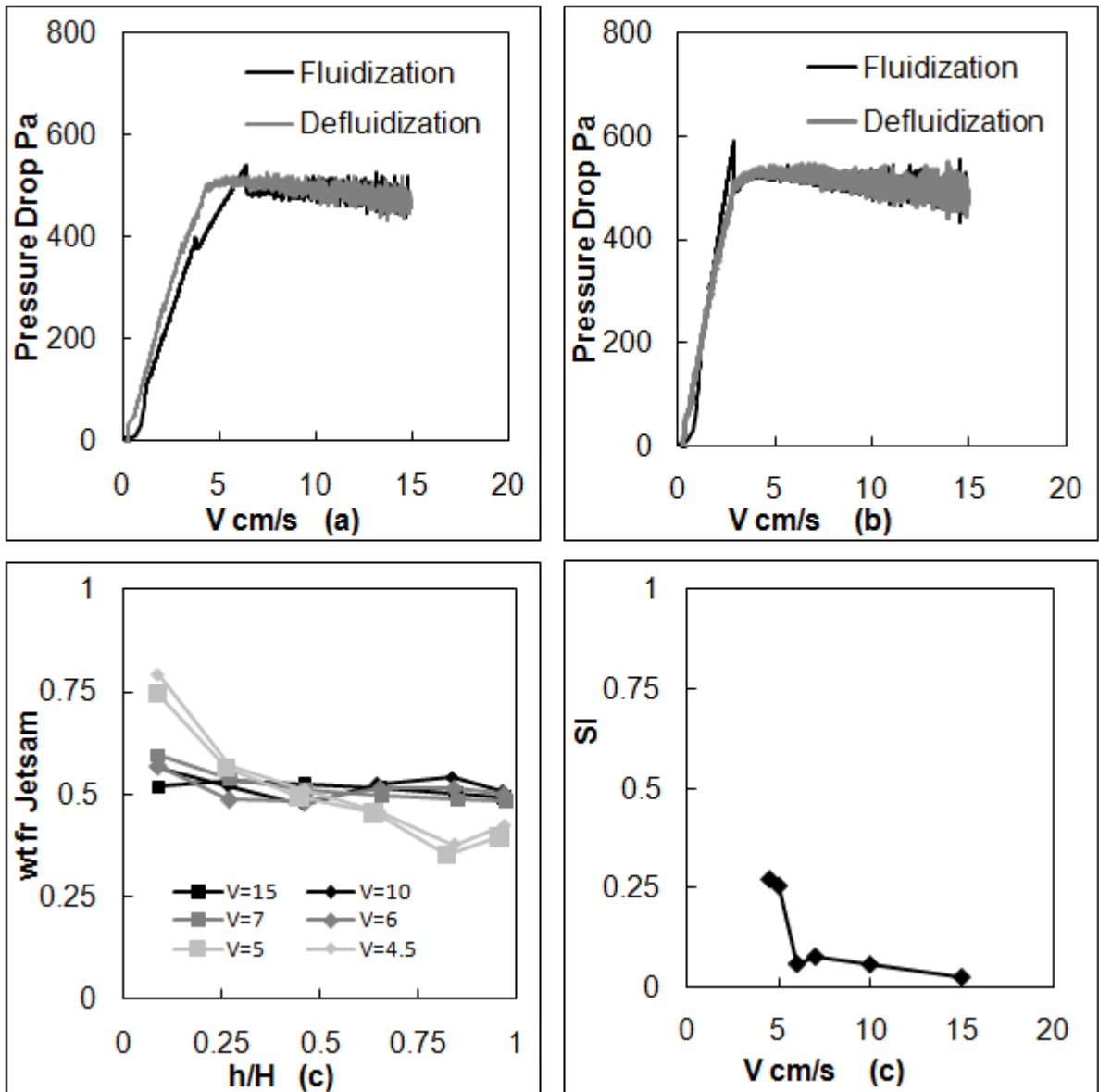


Figure C-9. Pressure drop profiles and segregation index behavior for a Type C mixture 50G195-50G083. (a) Pressure drop profile, initially segregated state. (b) Pressure drop profile, initially mixed state. (c) Segregation index.

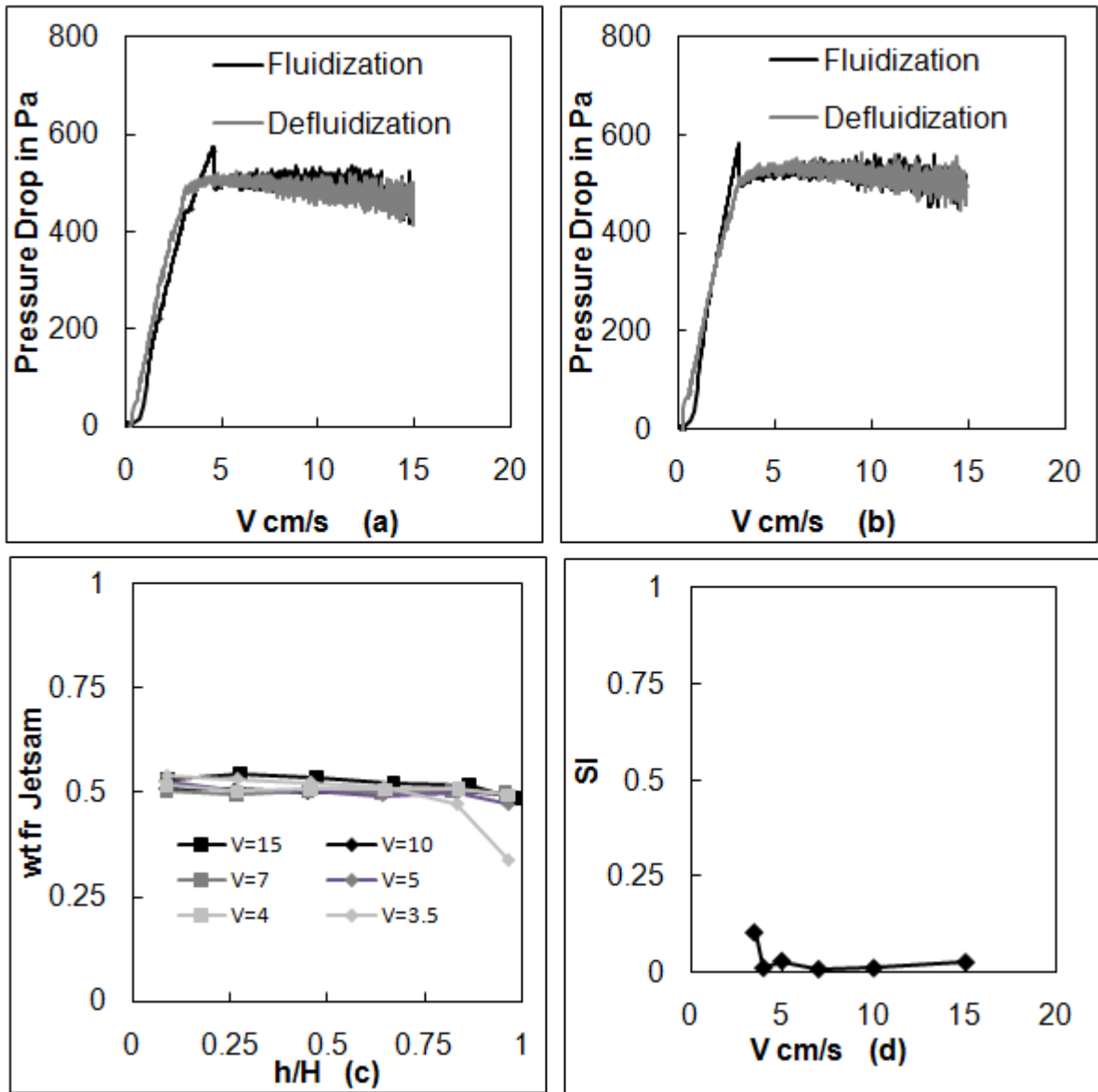


Figure C-10. Pressure drop profiles and segregation index behavior for a Type D mixture 50G165-50G083. (a) Pressure drop profile, initially segregated state. (b) Pressure drop profile, initially mixed state. (c) Segregation profiles. (d) Segregation index.

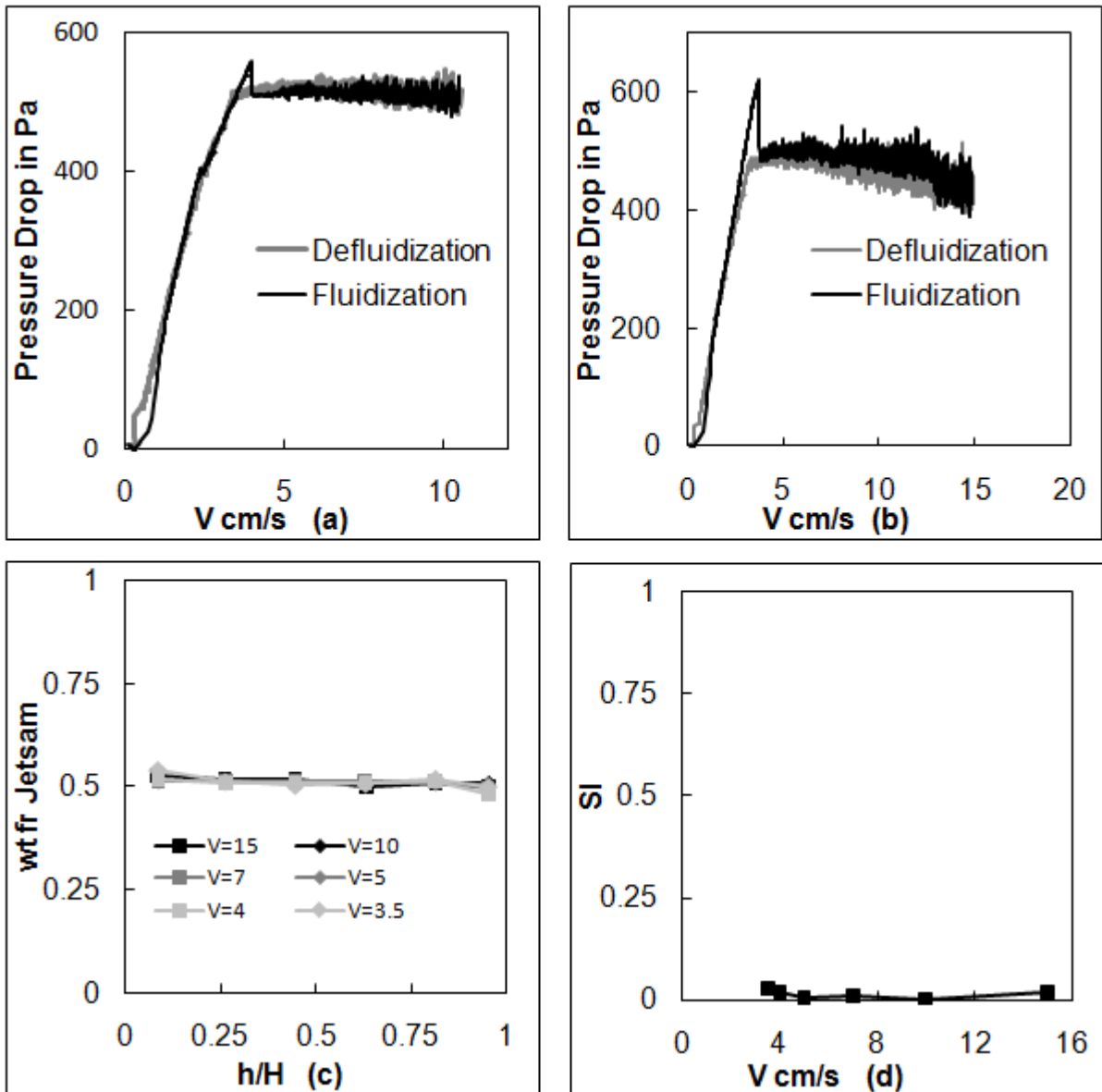


Figure C-11. Pressure drop profiles and segregation index behavior for a Type D mixture 50G138-50G083. (a) Pressure drop profile, initially segregated state. (b) Pressure drop profile, initially mixed state. (c) Segregation profiles. (d) Segregation index.

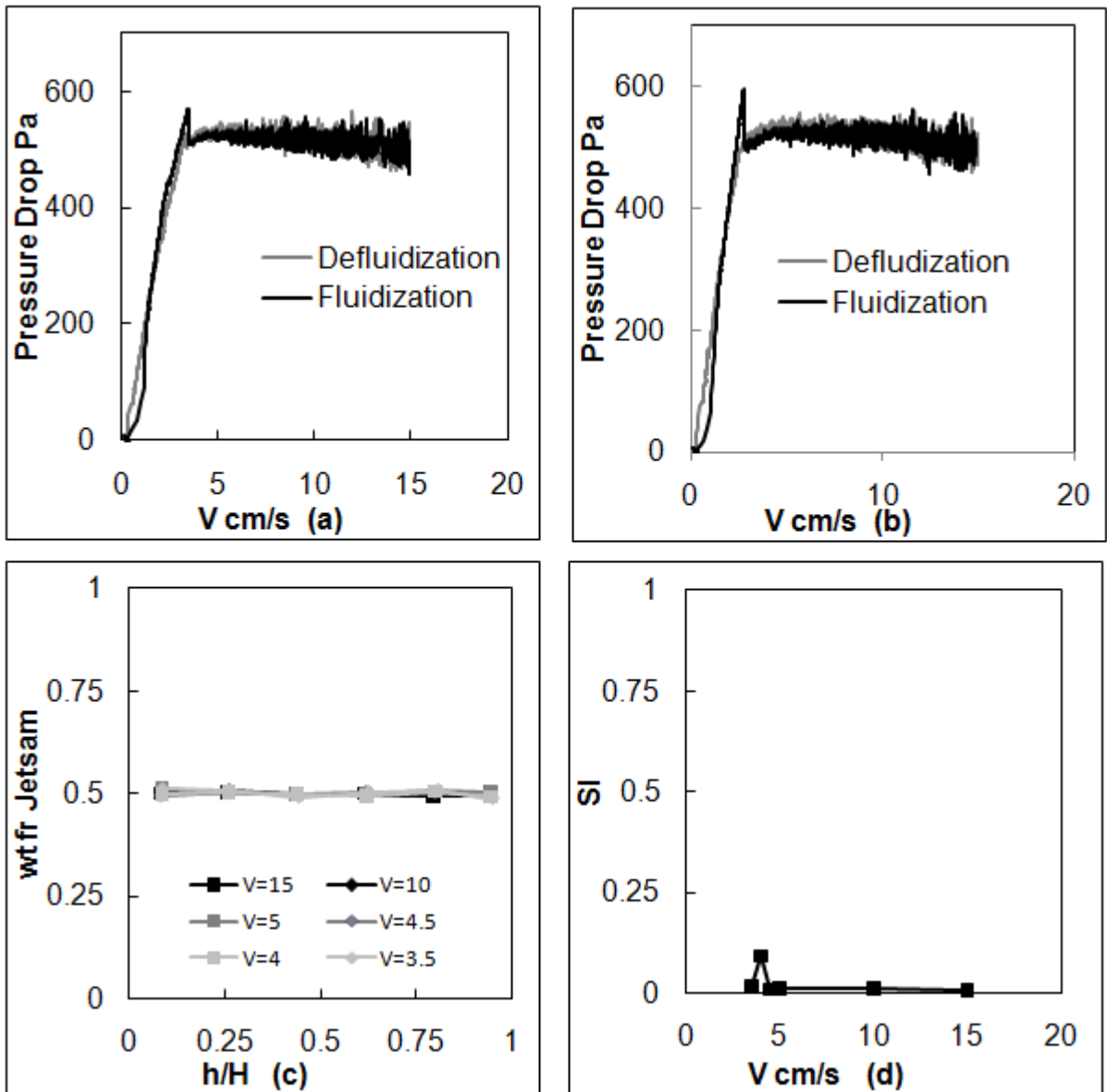


Figure C-12. Pressure drop profiles and segregation index behavior for a Type D mixture 50G116-50G083. (a) Pressure drop profile, initially segregated state. (b) Pressure drop profile, initially mixed state. (c) Segregation profiles. (d) Segregation index.

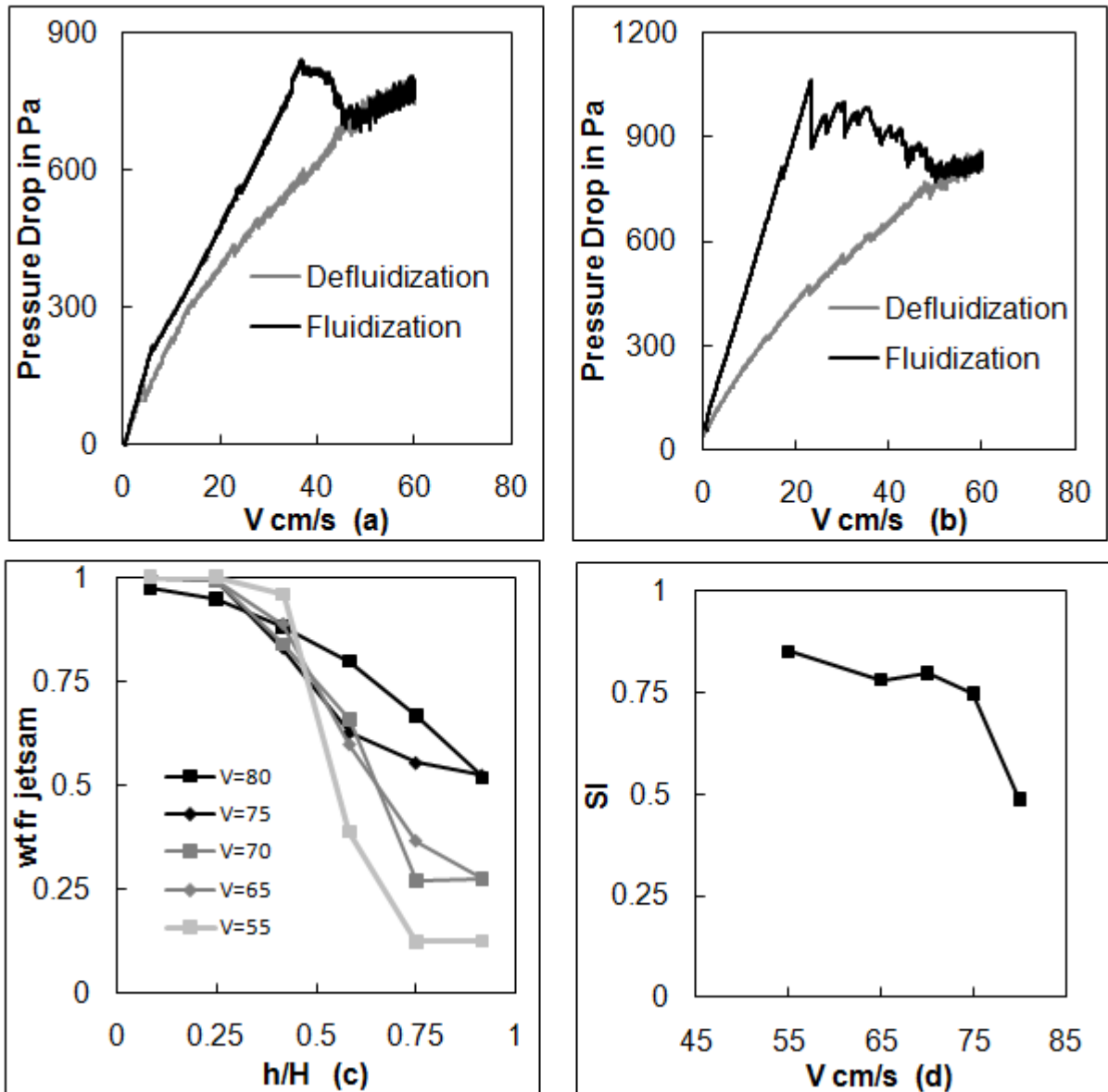


Figure C-13. Pressure drop profiles and segregation index behavior for a Type B mixture 13S328-87P328. (a) Pressure drop profile, initially segregated state. (b) Pressure drop profile, initially mixed state. (c) Segregation profiles. (d) Segregation index.

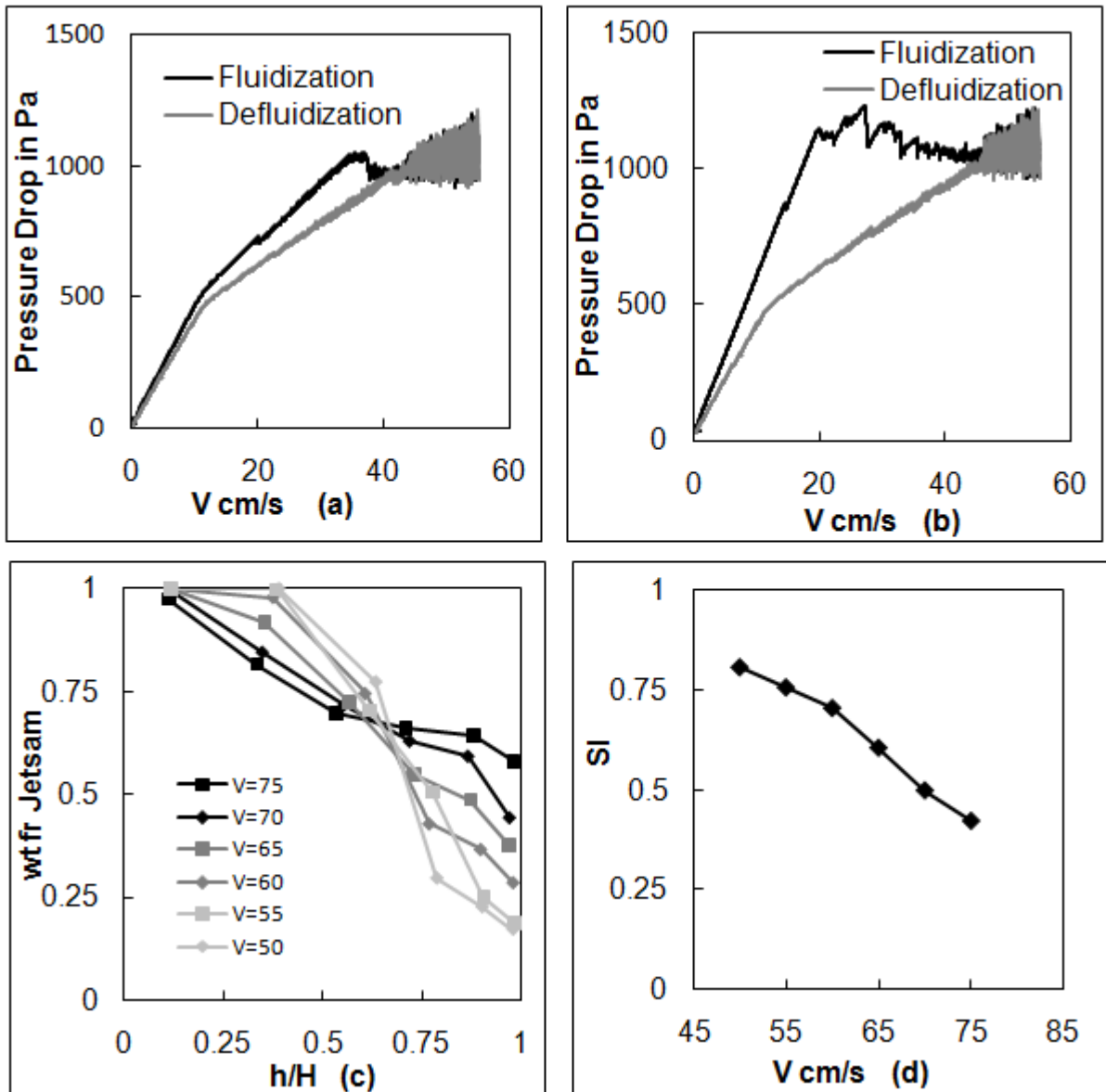


Figure C-14. Pressure drop profiles and segregation index behavior for a Type B mixture 75S328-25G328. (a) Pressure drop profile, initially segregated state. (b) Pressure drop profile, initially mixed state. (c) Segregation profiles. (d) Segregation index.

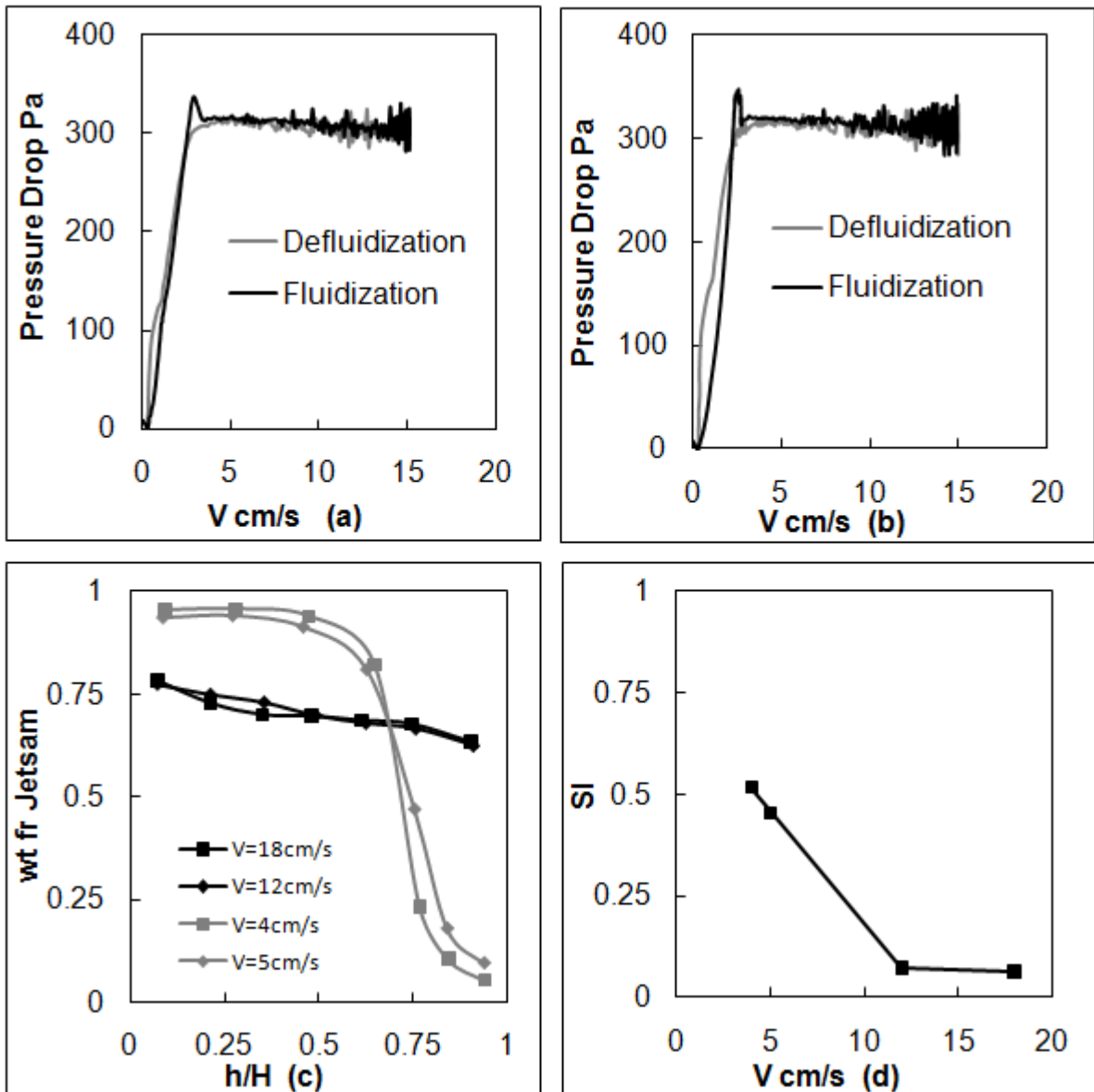


Figure C-15. Pressure drop profiles and segregation index behavior for a Type E mixture 70G116-30P275. (a) Pressure drop profile, initially segregated state. (b) Pressure drop profile, initially mixed state. (c) Segregation profiles. (d) Segregation index.

LIST OF REFERENCES

1. Kunii D, Levenspiel O. *Fluidization Engineering*, 2nd ed. Newton MA: Butterworth-Heinemann, 1991.
2. Tsuji Y, Morikawa Y, Shiomi H. LDV measurements of air-solid two-phase flow in a vertical pipe. *Journal of Fluid Mechanics*. 1984; 139: 417–434.
3. Jones E, Yurteri C, Sinclair J. Effect of mass loading on gas-solids motion and particle segregation patterns. *Handbook of Powder Technology*. 2001; 10: 843–849.
4. Sheen H, Chaing Y, Chaing Y. Two dimensional measurements of flow structure in a two phase vertical pipe flow. *Proceedings of National Science Council Republic of China (A)*. 1993; 17: 200–213.
5. Lee S, Durst F. On the motions of particles in turbulent duct flow. *International Journal of Multiphase Flow*. 1982; 8: 125–146.
6. Louge M, Mastorakos E, Jenkins J. The role of particle collisions in pneumatic transport. *Journal of Fluid Mechanics*. 1991; 231: 345–359.
7. Bolio E, Yasuna J, Sinclair J. Dilute turbulent gas-solid flow in risers with particle-particle interaction. *AIChE Journal*. 1995; 41: 1375–1388.
8. Simonin O. Continuum modeling of dispersed two-phase flow in combustion and turbulence in two phase flow. Von Karman Institute of Fluid Dynamics Lecture Series. 1996.
9. Benviades A, van Wachen B. Numerical simulation and validation of dilute turbulent gas-particle flow with inelastic collisions and turbulence modulation. *Powder Technology*. 2008; 182: 294–306.
10. Gore R, Crowe C. Effect of particle size on modulating turbulent intensity. *International Journal of Multiphase Flow*. 1989; 15: 279–285.
11. Hestroni G. Particles-turbulence interaction. *International Journal of Multiphase Flow*. 1989; 15: 735–746.
12. Alajbegovic A, Assad A, Bonetto F, Lahey R. Phase distribution and turbulence structure for solid/fluid upflow in a pipe. *International Journal of Multiphase Flow*. 1994; 20: 453–479.
13. Peppel M. Benchmark data and analysis of dilute turbulent fluid-particle flow in viscous and transitional regimes. PhD Thesis, University of Florida. 2010.

14. Hadinoto K, Curtis J. Numerical simulation of turbulent particle-laden flow with significant fluid to particle inertia ratio. *Industrial Engineering Chemistry Research*. 2009; 48: 5874–5884.
15. Chen C, Wood P. Turbulence closure model for dilute gas-particle flows. *The Canadian Journal of Chemical Engineering*. 1985; 63: 349–360.
16. Formisani B, Girimonte R, Longo T. Development of the approach based on the fluidization velocity interval. *Powder Technology*. 2008; 185: 97–108.
17. Joseph G, Leboreiro J, Hrenya C, Steven A. Experimental segregation profiles in bubbling gas fluidized bed. *AIChE Journal*. 2007; 53: 2804–2813.
18. Marzocchella A, Salatino P, Di Pastena V, Lirer L. Transient fluidization and segregation of binary mixtures of particles. *AIChE Journal*. 2000; 53: 2175–2182.
19. Rasul M, Rudolph V, Carsky M. Segregation potential in binary gas fluidized beds. *Powder Technology*. 1999; 103: 175–181.
20. Potic B, Kerstn S, Ye M, Van der Hoef M, van Swaaij W. Fluidization of hot compressed water in micro reactors. *Chemical Engineering Science*. 2005; 60: 5982–5990.
21. Chiba S, Nienow A, Chiba T, Kobayashi H. Fluidized binary mixtures in which denser component may be floatasam. *Powder Technology*. 1980; 26: 1–10.
22. Garcia F, Romero A, Villar J, Bello A. A study of segregation in a gas solid fluidized bed: Particles of different density. *Powder Technology*. 1989; 58: 169–174.
23. Huilin L, Yurong D, Gidaspow D, Lidan Y, Yukun Q. Size segregation of binary mixture of solid in bubbling fluidized bed. *Powder Technology*. 2003; 134: 86–97.
24. Geldart D, Baeyens J, Pope D, Van De Wijer P. Segregation in beds of large particles at high velocity. *Powder Technology*. 1981; 30: 195–205.
25. Liu X, Xu G, Gao S. Micro fluidized beds: Wall effects and operability. *Chemical Engineering Journal*. 2008; 137: 302–307.
26. Babu S, Shah B, Talwalker A. Fluidization correlation for coal gasification materials - minimum fluidization velocity and fluidized bed expansion. *AIChE Symposium Series*. 1978; 76: 176–186.
27. Baerg A, Klassen J, Gishler P. Heat transfer in a fluidized solid bed. *Can J Res Section F*. 1950; 28: 287–306.

28. Broadhurst T, Becker H. Onset of fluidization and slugging in beds of uniform particles. *AIChE Journal*. 1975; 21: 238–247.
29. Davies L, Richardson J. Gas interchange between bubbles and the continuous phase in a fluidized bed. *Trans Inst Chem Eng*. 1966; 44: 293–305.
30. Goroshko V, Rozenbaum R, Todes O. *Hydrodynamics and Heat Transfer in Fluidized Beds*. Cambridge MA: M I T Press, 1966.
31. Grewal N, Saxena S. Comparison of commonly used correlations for minimum fluidization velocity of small solid particles. *Powder technology*. 1980; 26: 229–234.
32. Johnson E. Institute of Gas Engineers Report, Publication No 318, London, 1949.
33. Kumar P, Sen Gupta P. Prediction of minimum fluidization velocity for multicomponent mixtures (short communication). *Indian Journal Technology* 1974; 12 (5): 225–251.
34. Leva M. *Fluidization*. New York NY: McGraw-Hill, 1959.
35. Miller C, Longwinuk A. Fluidization studies of solid particles. *Industrial and Engineering Chemistry*. 1951; 43: 1220–1226.
36. Pillai B, Raja Rao M. Pressure Drop and minimum fluidization velocities of air - fluidized bed. *Indian Journal Technology*. 1971; 9: 77–89.
37. Saxena S, Vogel G. The measurement of incipient fluidization velocities in a bed of coarse dolomite at temperature and pressure. *Trans Inst Chem Eng*. 1977; 55: 184–189.
38. van Heerdeem C, Nobel A, Krevelen V. Studies on fluidization II - heat transfer. *Chemical Engineering Science*. 1951; 1 (2): 51–66.
39. Wen C, Yu Y. Mechanics of fluidization. *Chemical Engineering Progress Symposium Series*. 1966; 62: 100–111.
40. Koch D. Kinetic theory for a monodispersed gas-solid suspension. *Physics of fluids*. 1990; 2: 1711–1722.
41. Igci Y, Andrew IV A, Sundaresan S, Pannala S, O'Brien T. Filtered two-fluid models for fluidized gas-particle suspensions. *AIChE Journal*. 2008; 54: 1431–1448.
42. Koch D, Sangani A. Particle pressure and marginal stability limits for homogeneous monodisperse gas-fluidized bed: kinetic theory and numerical simulations. *Journal of Fluid Mechanics*. 1999; 400: 229–263.

43. Wylie J, Koch D, Ladd A. Rheology of suspension with high particle inertia and moderate fluid inertia. *Journal of Fluid Mechanics*. 2003; 480: 95–118.
44. Sinclair J, Mallo T. Describing particle-turbulence interaction in a two-fluid modeling framework. *ASME Fluids Engineering Division Summer Meeting*. New York NY: Washington DC: ASME press. 1998; 4: 7–14.
45. Crowe C. On models for turbulence modulation in fluid-particle flows. *International Journal of Multiphase Flow*. 2000; 26: 710–727.
46. Zhang Y, Reese J. Gas turbulence modulation in a two-fluid model for gas-solid flows. *AIChE Journal*. 2003; 49: 3048–3065.
47. Hill R, Koch D, Ladd J. Moderate-Reynolds-number flows in ordered and random arrays of spheres. *Journal of Fluid Mechanics*. 2001; 448: 243–278.
48. Hill R, Koch D, Ladd J. The first effects of fluid inertia on flows in ordered and random arrays of spheres. *Journal of Fluid Mechanics*. 2001; 448: 213–241.
49. Benyahia S, Syamlal M, O'Brien T. Summary of MFIx equations. 2007, July Retrieved from www.mfix.org:
<https://www.mfix.org/documentation/MFIEquations2005-4-4.pdf>.
50. Lun C, Savage S, Jeffery D, Chepuriniy N. Kinetic theories for granular flow: inelastic particles in couette flow and slightly inelastic particles in general flow field. *Journal of Fluid Mechanics*. 1984; 140: 223–256.
51. Peirano E, Leckner B. Fundamentals of turbulent gas-solid applied to circulating fluidized bed combustion. *Progress in Energy and Combustion Sciences*. 1998; 24: 259–296.
52. Batchelor G, Green J. The determination of bulk stress in a suspension of spherical particle to order of c_2 . *Journal of Fluid Mechanics*. 1972; 56: 401–427.
53. Lun C. Numerical simulation of dilute turbulent gas-solid flows. *International Journal of Multiphase Flow*. 2000; 26: 1707–1736.
54. Benyahia S, Syamlal M, O'Brien T. Study of the ability of multiphase continuum models to predict core-annulus flow. *AIChE Journal*. 2007; 53: 2549–2569.
55. Johnson P, Jackson R. Frictional-collisional constitutive relations for granular materials with applications to plane shearing. *Journal of Fluid Mechanics*. 1987; 176: 67–93.
56. Patankar S, Spadling D. *Heat and Mass Transfer in Boundary Layers*. London: Morgan-Grampain Press, 1967.

57. Jones E. An experimental investigation of particle size distribution effect in dilute phase gas-solid flow. PhD Thesis, Perdue University. 2001.
58. Hrenya C, Bolio E, Chakrabarti D, Sinclair J. Comparison of low Reynolds $k-\epsilon$ turbulence model in predicting fully developed pipe flow. *Chemical Engineering Science*. 1995; 50: 1923–1941.
59. Pepple M, Curtis J, Yurteri C. Variation in mean turbulence intensity in fully developed pipe flow. *International Review of Chemical Engineering*. 2010; 2: 337–342.
60. Gondert P, Lance M, Petit L. Bouncing motion of spherical particles in fluids. *Physics of Fluids*. 2002; 14: 643–652.
61. Hadinoto K, Jones E, Yurteri C, Curtis J. Reynolds number dependence of gas-phase turbulence in gas-particle flows. *International Journal of Multiphase Flow*. 2005; 31: 416–434.
62. Rowe P, Nienow A, Agbim A. Preliminary quantitative study of particles segregation in gas-fluidised beds - binary systems of near spherical particles. *Trans Inst Chem Eng*. 1972; 50: 325–333.
63. Nienow A, Rowe P, Cheung L. A quantitative analysis of the mixing of two segregation powders of different densities in a gas fluidized bed. *Powder Technology*. 1978; 20: 89–97.
64. Nienow A, Naimer N, Chiba T. Studies of segregation/mixing in fluidised beds of different size particles. *Chem Eng Comm*. 1987; 62: 53–66.
65. Hoffmann A, Janssen L, Prins J. Particle segregation in fluidised binary mixtures. *Chemical Engineering Science*. 1993; 48: 1583–1592.
66. Olivieri G, Marzocchella A, Salatino P. Segregation of fluidized binary mixtures of granular solids. *AIChE Journal*. 2004; 50: 3095–3106.
67. Formisani B, De Cristofaro G, Girimonte R. A fundamental approach to the phenomenology of fluidization of size segregating binary mixtures of solids. *Chemical Engineering Science*. 2001; 56: 109–119.
68. Hedden D, Brone D, Clement S, McCall M, Olsofsy A, Patel P, Prescott J, Hancock B. Development of an improved fluidization segregation tester for use with pharmaceutical powders. *Pharmaceutical Technology*. 2006; 30: 54–64.
69. ASTM International. Standard practice for measuring fluidization segregation tendencies of powders, ASTM International, D6941–03.

70. Di Felice R, Gibilaro L. Wall effects for the pressure drop in fixed beds. *Chemical Engineering Science*. 2004, 59: 3037–3040.
71. Delebarre A. Does the Minimum Fluidization Exist? *Journal of Fluids Engineering* 2002; 124: 595–600.
72. Persson B, Tosatti E. *Physics of Sliding Friction (NATO Science Series E)*. New York: Springer Publishing Company, 1996.
73. Loezos P, Costamagna P, Sundaresan S. The role of contact stresses and wall friction on fluidization. *Chemical Engineering Science*. 2002; 57: 5123–5141.
74. Janssen H. Versuche uber getreidedruck in silozellen. *Z Ver Deutsch Ing* 1895; 39: 1045–1049.
75. Chhabra R, Agarwal L, Sinha N. Drag on non-spherical particles: an evaluation of available methods. *Powder Technology*. 1999; 101: 288–295.

BIOGRAPHICAL SKETCH

Akhil Rao was born in 1986 and brought up in Mumbai, India. He first studied at Bombay Scottish School (Indian Certificate of Secondary Education, Delhi board) and graduated from there in 2001. The same year, he enrolled in Ramnivas Ruia Junior College and two years later obtained the Higher Secondary Certificate (Maharashtra board). In 2003, he began his undergraduate studies at the Institute of Chemical Technology (Mumbai, India) and successfully graduated from there with a bachelor's in chemical engineering in 2007. In August 2007 he joined University of Florida (Gainesville, Florida) to pursue his PhD in chemical engineering.